DETECTION OF HAZARDOUS MATERIALS USING RAMAN SPECTROSCOPY

THESIS

Submitted to
Delhi Technological University
in partial fulfilment of the requirements for the degree of

DOCTOR OF PHILOSOPHY
IN
APPLIED PHYSICS

By

SANJAY
2K13/PHDAP/08

Under the Supervision of

Prof. RINKU SHARMA

**DEPARTMENT OF APPLIED PHYSICS
DELHI TECHNOLOGICAL UNIVERSITY
DELHI -110 042, INDIA**

SEPTEMBER 2021

Dedicated

To Supreme Mahadev Shankar, my family members and all teachers

CERTIFICATE

This is to certify that the thesis titled **"Detection of hazardous materials using Raman Spectroscopy"** is being submitted by Mr SANJAY with registration number 2K13/PHDAP/08 to Delhi Technological University, Delhi for the award of the degree of Doctor of Philosophy in Applied Physics. The work embodied in this thesis is a record of bonafide research work carried out by me at Laser Science and Technology Centre (LASTEC), DRDO, New Delhi and Department of Applied Physics, Delhi Technological University, New Delhi under the guidance of Prof. Rinku Sharma. It is further certified that this work is original and has not been submitted in part or fully to any other University or Institute for the award of any degree or diploma.

Sanjay
2K13/ PHDAP/08

This is to certify that the above statement made by the candidate is correct to the best of our knowledge.

Prof. Rinku Sharma
Supervisor
Department of Applied Physics
Delhi Technological University

ACKNOWLEDGEMENT

RESEARCH PUBLICATIONS

(Included in the thesis)

1. *A. Parmar,* **S. Gulia,** *S. Bajaj, V. Gambhir, R. Sharma and M. N. Reddy* "Signal processing of Raman signatures and realtime identification of hazardous molecules using continuous wavelet transformation (CWT)" *IEEE DOI: 10.1109/SPACES.2015.7058 275 pp. 323-325* **(2015).**

2. **Sanjay Gulia,** *Kamal K. Gulati, Vijayeta Gambhir, Rinku Sharma, M. N. Reddy* "Trace detection of explosive and their derivatives in stand-off mode using time-gated Raman spectroscopy" *Vibrational Spectroscopy 87 pp. 207-214* **(2016).**

3. **Sanjay Gulia,** *Kamal K. Gulati, Vijayeta Gambhir and Rinku Sharma* "Detection of explosive materials and their precursors through translucent commercial bottles using spatially offset Raman Spectroscopy using excitation wavelength in visible range" *Optical Engineering 58(12)* **(2019).**

4. *S.* **Gulia,** *Vijayeta Gambhir, M. N. Reddy, Rinku Sharma* "Stand-off Detection of p-nitrobenzoic acid through translucent plastic bottles using Spatially- offset Raman Spectroscopy (SORS)" *DAE-BRNS National Laser Symposium Dec. 3- 6,* **2014.**

5. *S.* **Gulia,** *Lalita Gupta, Vijayeta Gambhir, Rinku Sharma and M. N. Reddy* "Detection of explosive materials through transparent plastic and coloured glass bottles using normal Raman Spectroscopy" 4th International Conference on Current Developments in Atomic, Molecular & Optical Physics with Applications *(CDAMOP-2015) March 11th – 14th* **2015.**

6. *S.* **Gulia,** *Vijayeta Gambhir, Rinku Sharma and M. N. Reddy* "Detection of Explosive Materials at Low Concentrations in Soil using Normal Raman Spectroscopy" International Conference on Advances in Light Technologies and Spectroscopy of Materials *(ICALTSM-2016) Jan.16th – 18th* **2016.**

7. **Sanjay Gulia,** *Kamal K. Gulati, Vijayeta Gambhir and Rinku Sharma* "Computation of vibrational and thermal characteristics with their interpretation of [3,4-(methylenedioxy) phenyl]-2-methylaminopropane (MDMA) *(to be submitted).*

RESEARCH PUBLICATIONS
(Other than thesis work)

1. *Sanjay Gulia* "Laser spectroscopic techniques for explosive Detection" *DRDO Science Spectrum pp. 86-94* (**2015**).

2. *Kamal Kumar Gulati*, *Sanjay Gulia*, *Tanvi Gambhir, Nitesh Kumar, Vijayeta Gambhir and M.N. Reddy* "Stand-off detection and identification of explosives and Hazardous Chemicals in simulated real field scenario using time-gated Raman spectroscopy" *Defence Science Journal 69 (4) pp. 342-347* (**2019**).

3. *Kamal Kumar Gulati*, *Sanjay Gulia*, *Nitesh Kumar, Anil Kumar, Swaran Kumari, Vijayeta Gambhir and M.N. Reddy* "Real-time stand-off detection of improvised explosive materials using time-gated Raman spectroscopy" *Defence Science Journal 69 (4) pp. 342-347* (**2019**).

4. *S.Gulia*, *K.K. Gulati, V. Gambhir and M N Reddy "Stand-off detection of explosives using Gated-Raman Spectroscopy in visible and UV region" DAE-BRNS National Laser Symposium held at BARC, Feb. 6th – 9th* **2013**.

5. *M.N. Reddy*, *S. Gulia*, *Kamal K. Gulati, Vijayeta Gambhir* "Laser spectroscopic techniques for stand-off detection of explosives and IEDs" *ICOL-2013* (**2013**).

6. *M.N. Reddy*, *S. Gulia*, *Kamal K. Gulati, Vijayeta Gambhir* "Stand-off detection by Raman spectroscopy and LIBS." *First National Conference on "Trends & Applications in Laser Technology & Applications" (TALTO-1) Amity University, Noida* (**2013**).

7. *M.N. Reddy*, *S. Gulia*, *Kamal K. Gulati, Vijayeta Gambhir* "Stand-off identification of chemicals using time-gated Raman spectroscopy" *International Conference on Light and Light based Technologies (ICLLT-2016), Nov. 26th – 28th* **2016**.

8. *Sanjay Gulia* *and Vijayeta* Gambhir "Laser Spectroscopic Techniques for Bulk Explosive Detection" Nation Workshop on Explosive Detection (NWED-2020) March 1st – 2nd **2020**.

ABSTRACT

Hazardous materials have always been one of the most challenging threats to humanity and increasing with time. Hazardous materials cover a broad range of materials like industrial wastage, pollutant gases, poisonous compounds, biological agents causing diseases, narcotics, chemical & biological warfare agents, explosive materials etc. The management of hazardous materials requires monitoring of such materials. So the detection of hazardous threats always remains the top priority of law enforcing agencies. Along with the conventional threats of smuggled weapons & poisons and new threats like explosives, chemical and biological agents has surfaced and posed a serious challenge for society and particularly the law enforcement agencies. The explosive threats i.e. IED blasts, landmine blasts etc. are increasing day by day throughout the world and cause the loss of life of innocent people. Such incidents may be surely minimized by the development of reliable, portable and cost-effective explosive detectors; which is the motivational force for carrying the present study and contributing towards safeguarding innocent people and society as a whole against explosive threats. The detection of explosive threats focuses on the detection of bombs, bomb makers, and bomb placers. The constituents of a bomb or IED include ignition system, detonator, booster and main charge. The electronic components like battery, wires etc. may not be an indicator of bombs/IEDs exclusively as these components are used in ordinary items also. The detection of the presence of explosives material is the ultimate indicator of a bomb and may be helpful in preempting the explosion. Further detection of explosive materials plays a vital role in the field of post-blast investigations particularly in case of partial detonation which may take place, results in unburned residual quantities on the blast sites. Such unburned residuals of explosive materials may be found deposited on nearby surfaces especially metallic surfaces or mixed in the soil. The factors involved in the human-machine interface depend on the real scenario and should be incorporated at the design level in the process of the development of a particular explosive detector.

Laser spectroscopy techniques particularly Raman spectroscopy offers high potential in the identification of explosive materials with high specificity i.e. with a low false

rate. Raman spectroscopy involving laser as excitation source also promises with the detection of explosive material in the stand-off mode which is required to ensure the safety to the operator or human behind the machine. In the thesis, the potential of different types of Raman scattering based techniques has been investigated for the different real-field scenarios.

Chapter 1 provides a basic idea of hazardous materials and deals with the insight of the field of explosive detection in detail like the necessity of detection of hazardous materials especially explosives, different real scenarios etc. Further, the potential techniques for the detection of explosives both non-optical techniques like ion-mobility spectrometry, mass spectrometry, gas chromatography, surface-acoustic wave & nuclear-quadrupole resonance; and optical techniques like laser-induced breakdown spectroscopy, photo-dissociated laser-induced fluorescence, cavity-ring down spectroscopy, laser-based photoacoustic spectroscopy, THz spectroscopy and Raman spectroscopy have been discussed. Furthermore, different types of Raman scattering techniques like normal Raman spectroscopy, resonant Raman spectroscopy, time-gated Raman spectroscopy, surface-enhanced Raman spectroscopy, surface-enhanced resonant Raman spectroscopy and spatial-offset Raman spectroscopy have been covered.

Chapter 2 provides the theoretical and instrumental aspects of the field of Raman scattering. Classical theory and quantum theory have been described with their importance in the explanation of the nature of Raman scattering. The selection rules of Raman spectroscopy and IR absorption spectroscopy and their differences have been explained. Instruments used in the field of Raman spectroscopy have been discussed in detail. Different types of light sources both conventional light sources like mercury lamp, xenon lamp etc. and lasers have been discussed. Different optical schemes like 90-degree configuration and 180-degree configuration have been explained and correlated to the real scenarios. Further optical components like lenses, filters, mirrors, fibers etc. are discussed with specifying their roles in the field of Raman spectroscopy. Different types of wavelength selectors or spectrometers like monochromators, spectrographs and interferometers are discussed in terms of

application and corresponding detector. Finally, the frequency calibration of spectrometers is discussed.

Chapters 3 deals with the studies of explosive materials like ammonium nitrate and p-nitrobenzoic acid in soil samples and through the different types of plastic bottles. Raman spectra of soil samples of different concentrations of ammonium nitrate have been recorded and analysed in terms of the signal-to-noise ratio. Further the effect of integration time on the Raman spectra of these soil samples studied. The potential of the processing of the Raman spectra in terms of the background has been evaluated by recording Raman spectra of lower concentration soil samples with an improved signal-to-noise ratio. Further Raman spectra of p-nitrobenzoic acid through different plastic bottles have been recorded. The importance of the processing of Raman spectra in terms of background and fluorescence of plastic material have been investigated using plastic bottles of different materials.

Chapter 4 deals with the development of a customized algorithm for the identification of materials in real time. The real-time detection or identification of the materials in the field itself is one of the main required features of explosive detectors. The continuous wavelet transform (CWT) has been explained in detail. An algorithm has been developed based on CWT for the real-time identification of explosive materials. The Maxican Hat wavelet has been selected for its matching with the nature of the peaks of Raman spectra. Further, the methodology has been evolved and based on which algorithm has been developed represented in form of flow chart. The operational parameters have been sorted out and the graphic user interface is developed accordingly. Further, the developed algorithm and graphic user interface are evaluated by detecting and identifying very similar materials like 2,4,6-dinitrotolune, 1,3,5-trinitrobenze, 2,4,6-trinitrotoluene, ammonium nitrate, potassium nitrate, sodium nitrate, urea nitrate, barium nitrate etc.

Chapter 5 presents the trace detection of explosive materials and their derivatives using time-gated Raman spectroscopy. The instrumentation of the time-gated Raman spectroscopy techniques has been explained. The effect of different experimental parameters on the signal-to-noise ratio of peaks of Raman spectra has been

investigated. First, the potential of time-gated Raman spectroscopy over normal Raman spectroscopy has been demonstrated by recording Raman spectra of low-concentration sample of 1,3,5-trinitrobenzene using continuous mode and gated mode of intensified charged coupled device. Further, the effect of gain, pulse accumulation and pulse energy has been studied and found that the intensity i.e. sensitivity increases with an increase in any of these parameters. Finally, Raman spectra of low-concentration explosive samples like 100 ppm have been recorded successfully.

Chapter 6 deals with the detection of explosive materials through translucent plastic bottles using spatially offset Raman spectroscopy. The potential of the technique has been investigated with the excitation wavelength in the visible region. The capability of spatially offset Raman spectroscopy over the normal Raman spectroscopy is evaluated by recording Raman spectra of urea and sodium nitrate through their commercial translucent plastic bottles using both techniques. The effect of spatial offset inserted between incident laser spot and collection spot and integration time is investigated. The Spatially offset Raman spectroscopy ratio has been plotted with respect to spatial offset. Finally, the capability of spatially offset Raman spectroscopy technique has been studied for reduced collection of fluorescence from the container material.

Chapter 7 deals with the theoretical study of MDMA molecule for its structural, spectral and thermal characteristics. Geometry optimization of MDMA is performed using DFT and HF methods with different basis sets. Mulliken charge and MEP are studied for negative and positive sites of the molecule. Molecular orbital characteristics like HOMO-LUMO energies, energy gap, ionization potential, electron affinity, global hardness, chemical potential have been investigated. Thermal properties like SCF, zero-point energy, rotational constants, dipole moments are estimated. Enthalpy, specific heat and entropy are investigated in terms of temperature effect in the range 50 K – 700 K. Vibrational analysis are performed on optimized geometries of MDMA with different levels of theory. The vibrational frequencies are scaled and found in an excellent match with experimental values.

Chapter 8 represents the conclusion of the research work reported in the thesis. The main outcomes of the research work reported have been brought out clearly. Further, the future prospects of the work has been discussed.

The important findings and conclusions of the thesis are mentioned below:

- ✓ Simulated samples of post-blast scenarios have been successfully prepared and studied by recording their Raman spectra at different concentrations of explosive materials.

- ✓ The capability of detection through transparent plastic bottles is evaluated by recording Raman spectra of explosive materials successfully through transparent plastic bottles of different materials, thickness and transmission.

- ✓ Customised algorithm for real-time acquisition of Raman signal, its processing for background and fluorescence corrections and identification by peak matching with database has been developed and evaluated.

- ✓ The capability of time-gated Raman spectroscopy was evaluated by recording of Raman spectra of explosive samples of low concentrations i.e. 1000 ppm, 500 ppm and finally 100 ppm.

- ✓ The capability of SORS technique is successfully evaluated by recording Raman spectra of explosive materials through translucent-containers and effect of spatial offset on sensitivity was studied.

- ✓ Theoretical calculations on MDMA molecule have been performed and its structural, thermal and spectral characteristics were estimated and found in good agreement with experimental values.

The future prospective of the reported work has been summarized below:

- ✓ To carry out experimental work of SORS technique with SORS probes at 532nm and 785 nm.

- ✓ To enhance range and sensitivity of detection of explosive materials.

- ✓ To study the spectral signatures of hazardous molecules, both theoretically and experimentally, as per requirement of law-enforcement agencies.

CONTENTS

CHAPTER 2: Raman scattering: Theoretical treatment and instrumentation

LIST OF ABBREVIATIONS

AN	:	Ammonium nitrate
AoI	:	Angle-of-incidence
APD	:	Avalanche photodiode
B3LYP	:	Becke-3-parameter-Lee-Yang-Parr
BG	:	Background
CARS	:	Coherent anti-Stokes Raman Spectroscopy
CCD	:	Charge-coupled Device
cm	:	centimeter
CRDS	:	Cavity Ring-down Spectroscopy
CSA	:	chemical shift anisotropy
CW	:	Continuous wave
CWT	:	continuous wavelet transformation
DFT	:	Density Functional Theory
DNT	:	dinitrotoluene
GC	:	Gas Chromatography
GHz	:	gigahertz
GUI	:	Graphical User Interface
GW	:	giga watt
HDPE	:	high-density polyethylene
HF	:	Hartree–Fock
HMX	:	1,3,5,7-Tetranitro-1,3,5,7-tetrazocane
HOMO	:	Highest-occupied molecular Orbit
ICCD	:	Intensified Charge-coupled Device
IED	:	Improvised Explosive Device
IMS	:	like ion mobility spectrometry
IR	:	Infrared

LASER	:	Light Amplification by Stimulated Emission of Radiation
loD	:	Limit of detection
LPAS	:	Laser-based Photo Acoustic Spectroscopy
LPF	:	Longpass filter
LUMO	:	Lowest-unoccupied molecular orbit
MCP	:	Micro-channel plate
MDMA	:	[3,4-(methylenedioxy) phenyl]-2-methylaminopropane
MEP	:	Molecular electrostatic potential
MS	:	mass spectrometry
MW	:	Megawatt
NIR	:	Near Infrared
nm	:	Nanometer
NQR	:	Nuclear quadruple resonance
NRS	:	Normal Raman Spectroscopy
PAS	:	photo acoustic spectroscopy
PBI	:	Post-blast investigation
PETN	:	pentaerythritol tetranitrate
PMT	:	photo-multiplier tube
PNBA	:	p-nitrobenzoic acid
ppb	:	Parts-per billion
ppm	:	Parts-per million
PTI	:	Photo-thermal Imaging
QCC	:	Quadrupole coupling constant
QCL	:	quantum cascade laser
RDX	:	1,3,5-trinitroperhydro-1,3,5-triazine
RRS	:	Resonant Raman Spectroscopy
RS	:	Raman spectroscopy

SAW	:	Surface acoustic wave
SCF	:	self consistent field
SD	:	Standard deviation
SERS	:	Surface-enhanced Raman Scattering
SNR	:	signal-to-noise ratio
SORS	:	Spatial-offset Raman Spectroscopy
TATB	:	2,4,6-triamino-1,3,5-trinitrobenzene
TEC	:	Thermo-electric cooling
TED	:	Total Energy Distribution
TGRS	:	Time-gated Raman Spectroscopy
THz	:	terahertz
TNB	:	trinitrobenzene
TNT	:	trinitrotoluene
TR	:	Trans-receiver
TTL	:	Transitor-transitor logic
UV	:	Ultra-violet
UV RS	:	Ultra-violet Raman Spectroscopy
ZPV energy	:	Zero-point vibrational energy

LIST OF TABLES

LIST OF FIGURES

CHAPTER 1

INTRODUCTION

Explosive incidents have grown over the last few decades and become a global threat to humanity. Hence, reliable explosive detectors are need of the hour to preempt IEDs blasts, landmine blasts etc. Different potential non-optical and optical techniques for explosive detection have been discussed. Under optical techniques, laser spectroscopic techniques like LIBS, PD-LIF, LPAS, Raman spectroscopy etc. promise a great potential in the field of stand-off explosive detection. Being a finger-printing technique, Raman spectroscopy promises explosive detection with a low false alarm rate. Further different forms of Raman spectroscopy like normal Raman spectroscopy, TGRD, SERS, SORS etc. have been discussed in terms of their potential for different scenarios.
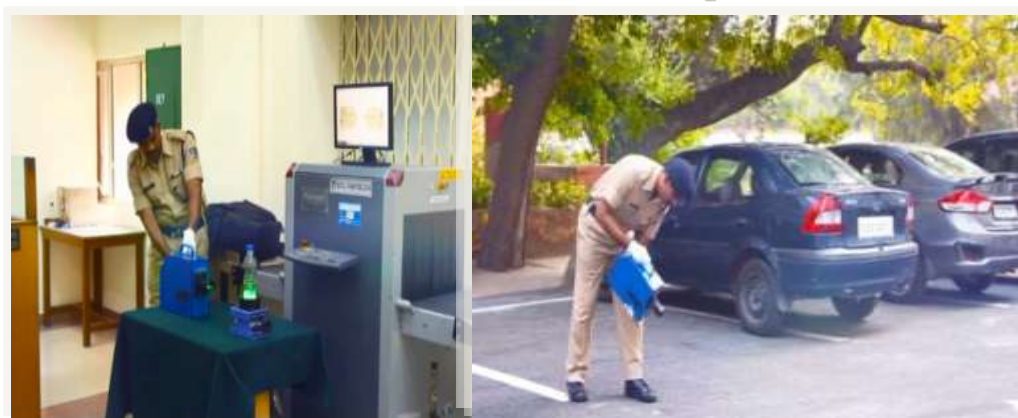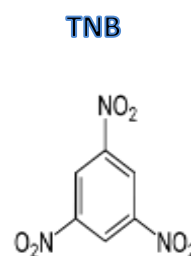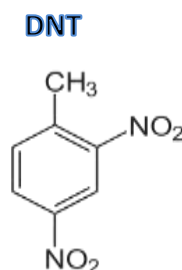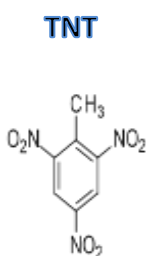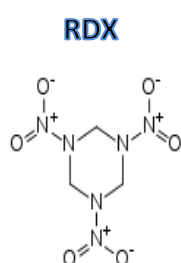
1.1 Hazardous materials

1.1.1 Classification of hazardous materials

The term "hazardous material" is vast and refers to any material, natural or man-created, in any form which results in harmful effects on human beings or any other creature including nature [1]. The hazardous materials may be broadly classified in the following categories:

a.   Industrial waste

b.   Pollutant gases

c.   Poisonous compounds

d.   Biological agents causing diseases

e.   Narcotics

f.   Chemical-biological warfare agents

g.   Explosive materials

Here onwards, explosive materials will be discussed in particular.

1.1.2 The necessity of detection of hazardous materials

During the last two decades, terrorism has emerged as a prominent threat to society. In every incident of terrorism, explosive materials are relatively more used in comparision to chemical and biological hazardous agents. Hence, explosive has been a greater cause of loss of the lives due to biological and chemical agents. In addition, explosive materials cause high infrastructural damage. Very frequently, explosive-based terror attacks take place in various forms like a car bomb attack, suicidal attack, planting of explosives at crowded or important public places many in parts of India and all-over world also. It becomes necessary to prevent, detect and neutralize these attempts of terrorists. These attacks can be prevented by legislating strong anti-terrorism laws and their enforcement and enforcing strong law. In addition, security agencies should be strengthened by developing state-of-art explosive detection systems. Hence, there is an urgent requirement of developing effective methods to detect the explosives at their pre-detonation stage. Therefore, the scientific

community has a great challenging but an interesting task that has to be accomplished at the earliest to defeat the intentions of terrorists.

1.2 Detection scenario

Detection of IEDs requires the development of new tools based on some analytical technique. The method used up to now still requires approaching the suspicious object to perform the analysis with great risk to the operator. A technique, to be used for such a purpose, should be capable of detecting and identifying targeted objects at a stand-off distance with an acceptable level of reliability maintaining a safe distance for the operator [2-5].

1.2.1 Accessibility-wise

The following approaches are adopted as far as accessibility to the target or test sample is concerned:

Point detection

If the detection process of any explosive detector requires sample preparation, placing of sample in the detector by touching etc., this process is called point detection and detector as point detector.

Remote sensing

If the detection process requires no sample preparation and detection is possible as it is available in the real scenario but the detector should be in the vicinity of the sample, this process is called remote sensing.

Stand-off detection

If the detection process requires no sample preparation and the sample can be detected from a distance, this process is called stand-off detection. Standoff explosive detection involves methods for sensing the presence of explosive devices when vital assets and those individuals monitoring, operating, and responding to the means of detection are physically separated from the explosive device. The zone of severe damage varies with the scenario and bomb type, it may vary from 10 m for a

pedestrian suicide bomber and 100 m for a vehicle-based bomb [6]. Standoff detection and identification is one of the most desirable capabilities. It is the very challenging task of developing stand-off explosive detectors. The larger range of detection poses several difficulties like reduction in the intensity of the Raman scattered light with the distance squared, wavelength-dependent losses due to absorption and wavelength-independent losses due to scattering in the air.

1.2.2 Quantity-wise

In different scenarios, the quantity available for the detection process varies tremendously as explained below:

1.2.2.1 Bulk detection

Bulk detection deals with the detection of macroscopic quantities of explosive materials. Such quantities could be visible to the naked eyes of the operator. Different phenomena like absorption, scattering, fluorescence, resonance etc. are used in distinguishing the explosive material from its surroundings.

1.2.2.2 Trace-detection

Traces of some materials refer here to the very low quantity which is invisible with naked eyes. The material may be on some surface or in the air as described below:

Particulate detection

It involves detection of confirmation of contamination of contaminated areas like contaminated car-door handle, briefcase handle etc. The amount of explosive materials can be as low as not visible by naked eyes i.e. microscopic quantities as may be a case of direct handling the explosive or indirectly through touching the person involved in handling explosives.

Vapour detection

It involves detecting vapours being emitted by explosive materials due to the vapourisation process. The level of concentration of vapours of explosive material in

its vicinity depends on the nature of the material itself like its vapour pressure, it's packaging, duration of the presence of explosive materials at the location under observation, environmental conditions like temperature, wind speed and direction etc. In addition, vapour detection is much difficult due to much less vapour pressures of explosive materials such as TNT, RDX, PETN etc. in naked form. The use of polymeric binders, plasticizers etc. further reduce the available concentration of vapours of explosive in air.

1.3 Detection techniques for Hazardous Materials

Different techniques have been used in the screening of explosive materials in different scenarios as explained below:

1.3.1 Non-optical techniques

Depending on the scenario and requirements of security agencies, explosive detectors based on different techniques are being used. Commercially available explosive detectors are based on different techniques like ion mobility spectrometry (IMS), mass spectrometry (MS), gas chromatography (GC), electrochemical detector/thermo-redox, surface acoustic wave detector, X-ray techniques, Nuclear quadrupole resonance (NQR), optical sensors etc. ***Ion mobility spectrometry and mass spectroscopy*** are very common techniques in commercial explosive detectors. These detectors are capable of detecting of explosives in both modes: vapour detection by sucking explosive vapours in the detector and particulate detection by swipe contaminated areas. IMS and MS-based detectors get saturated due to excess vapours of target materials. The saturation may be due to the presence of vapours of other chemicals present in the air. These detectors may get saturated due smell of flowers, newly painted objects etc. If the detector gets saturated, it has to be cleaned before scanning the next object. The process of cleaning takes approximately 30-60 minutes. Such detectors have to be calibrated very frequently as their performance is dependent on environmental conditions like temperature, pressure etc.

Gas chromatography is an analytical tool and is suitable particularly for mixture samples. The target materials i.e. explosive molecules are adsorbed on binder

substances and drift time increases for explosive molecules. Nowadays, GC and IMS/MS techniques are coupled together to enhance capabilities. Such GC based systems are analytical tools that are used in laboratory conditions and take a longer time in analysis and initial warm-up.

Surface acoustic wave (SAW) devices are based on the phenomenon of piezo-electricity and involve piezo-electric crystals with characteristic acoustic resonant frequencies. When the target molecule is adsorbed on crystal surfaces, this characteristic frequency of crystal changes. SAW detectors can respond to any molecule adsorbed on a crystal surface and therefore inherently less selective.

Nuclear quadrupole resonance (NQR) involves detecting the nitrogen nucleus due to its electric quadrupole moment. The ^{14}N nucleus possesses the large quadruple inherently and hence used for scanning the explosive materials. When nitrogen-based explosives are brought under the RF field of resonant frequency, ^{14}N nuclei are raised to a higher energy state. As the RF field is switched off, these nuclei come down to their initial lower energy state, by releasing energy in form of a weak signal in the radio-frequency domain. Only nitrogen-based explosives can be detected with NQR. NQR detector can detect when materials are in its proximity [2, 5].

1.3.2 Optical techniques

1.3.2.1 Introduction of optical techniques

Till today no technique is commercially available for reliable detection of explosive materials in required real scenarios. Globally many groups are working on the development of detection techniques for both scenarios: point detection and stand-off detection. The techniques discussed above are not suitable for stand-off detection at all. In addition, these techniques do not provide reasonable selectivity and hence suffers from false alarming. Laser-based spectroscopic techniques may provide solutions for both scenarios i.e. point detection and stand-off detection. These techniques also provide better selectivity and hence lesser false alarms [6, 7]. Laser-based spectroscopic techniques which are having good potential in the field of explosive detection are discussed below:

1.3.2.2 Laser-induced Breakdown Spectroscopy (LIBS)

This technique involves pulse laser, transmitting optics, receiving optics, spectrograph-coupled with CCD/ ICCD. It detects target material in its plasma form produced by a laser beam of the high power density of the order of GW/cm^2. This level of power density is achieved by tight focusing of the laser beam on target materials [6, 8]. The generated plasma results in the emission of characteristic frequencies from ions, atoms or small molecules present in it and these light signals are recorded by the spectrograph. The recorded spectrum provides lines corresponding to elements and their ions. This technique offers very good sensitivity. Its disadvantage is that it provides elemental information rather than molecular information as required in the field of explosive detection. A lot of research is globally going on to extract molecular information from the elemental spectrum.

1.3.2.3 Photo-dissociated Laser-induced Fluorescence (PD-LIF)

Photo-dissociated laser-induced fluorescence is a modified fluorescence technique. This technique involves pulsed UV laser, transmitting & receiving optics and spectrograph. In this technique, when NO_2-containing materials are exposed to UV laser pulse, NO ions are generated. These NO-ions have absorption in the UV region so the same laser is being used in exciting these ions and getting fluorescence. These generated ions are found at higher vibration levels of the ground state and hence provide fluorescence at the lower-wavelength side i.e. blue-shifted fluorescence [6, 9]. Most explosive materials contain nitro groups and this technique has constraints of detecting only such materials. There is always the possibility of false-positive alarms from non-explosive nitro compounds.

1.3.2.4 Cavity Ring-down Spectroscopy (CRDS)

In this technique, a short-duration laser pulse is transmitted through a resonant cavity made up of two mirrors of high reflectivity at both ends of the cavity. The intensity of pulse decay exponential manner w.r.t time. The decay time is measured in both cases i.e. empty-cavity and cavity filled with vapours of explosive materials and then compared for determining the concentration of vapours of target material inside the

cavity. This technique is an absorption technique and hence requires a tunable laser. Laser is tuned through a broad wavelength range. When we observe changes in decay time, the corresponding laser wavelength provides molecular information of vapours. This technique promises excellent sensitivity and selectivity for vapour detection as required in real scenarios of remote sensing [6, 10]. This technique is not suitable for bulk and particulate detection.

1.3.2.5 *Laser-based Photo Acoustic Spectroscopy (LPAS)*

Advancements in the field of quantum cascade lasers (QCLs) have led to significant enhancement in the sensitivity of the photo-acoustic process. Recently, photoacoustic spectroscopy (PAS) is being explored for stand-off detection of explosive materials. However, conventional PAS detections involve an enclosed container containing the sample. The acoustic signal is much weaker in the open condition than that in a closed one and hence not viable for stand-off detection of explosives or toxic gases detections [11-13]. LPAS used a pulsed QCL tunable laser in the mid-IR range. When the wavelength of the laser beam is tuned corresponding to the target material, the laser beam is absorbed and an acoustic wave is generated. This generated acoustic signal is proportional to the concentration of target material. This technique has good potential for explosive detection due to its good selectivity.

1.3.2.6 *Laser-based Photo-thermal imaging (PTI)*

Laser-based photo-thermal spectroscopy requires quantum cascade laser(s), transmitting and receiving optics, thermal camera, processing card. Quantum cascade lasers have emerged as an attractive tool due to their compactness and robustness. PTI is very similar to LPAS as both use QCL lasers for the excitation of samples. Due to absorption, the temperature will increase of the area of the surface where the target material is present. This temperature variation is recorded by a thermal camera [14]. This technique may prove very good for particulate detection like contamination by fingers etc. The temperature variation depends on the thermal characteristics of both the particle and the substrate. This technique also has good potential particularly for trace detection but still needs to be explored further.

1.3.2.7 THz Spectroscopy

Terahertz imaging/ spectroscopy is a relatively new technique and very promising for scanning of human beings for explosives during security check-ups at the entrance of airports etc. The novel advantage of this technique is that it can be used as a scanner like metal-detector gates. X-ray machines for scanning human beings at the airport or any other installation is not acceptable due to the harmful and irreversible biological effects of X-rays whereas THz waves are non-ionizing and hence involves no concern of any biological effect on human beings during screening. The terahertz refers to an electromagnetic region between 100GHz – 1THz [15]. In addition, THz waves can transmit through non-metallic materials cloths and packaging providing material-specific signatures in the THz range. THz is being explored for scanning purposes i.e. converting the THz technique in reflection mode as required in real scenarios. Processing of acquired images is also very critical for a clear view of any objects hidden below cloths etc. by the person under scanning.

1.3.2.8 Raman Spectroscopy

1.3.2.8.1 Normal Raman Spectroscopy

Raman spectroscopy is the most promising technique for explosive detection. In Raman spectroscopy, photon interacts with material; perturb molecules from their normal structure momentary. The scattered photon may have energy lower or higher depending on its interaction with molecules and provides stoke or anti-stoke line. The number of Raman peaks and their position depends on molecular structure. This technique is being used as an analytical technique and provides molecular information which is specific to molecular structure. The Raman signatures of a molecule/ material depend on the number of bonds, bond length, and angle between different bonds etc. which are very specific to the molecule. These characteristics cannot be the same between two molecules irrespective of their degree of similarity. Hence Raman spectroscopy is a finger-printing technique and promises unmatched selectivity. In addition, Raman spectroscopy does not require a tunable laser and a single-wavelength laser may generate Raman signatures of all kinds of materials like explosives, bioagents, chemical agents, narcotics etc. Due to the development in the

technology of lasers, CCD detectors, spectrometers, optical filters, it is easy to make a very compact and robust explosive detector. Many commercial explosive detectors are available based on Raman spectroscopy [6, 16]. Raman spectroscopy is a very promising tool in stand-off detection. Materials/ molecules in the path of beam/ near sample other than explosives will have different Raman signatures. In this way, this technique promises very low false alarming which is one of the critical requirements for an explosive detector.

1.3.2.8.2 Resonant Raman Spectroscopy

Though Raman spectroscopy provides excellent selectivity, it is not a very sensitive technique. Sensitivity is also a very critical parameter of any explosive detector. Though conventional Raman spectroscopy is not sensitive enough, developments in the field of light sources and detectors provide some means to enhance its sensitivity. If a laser of wavelength matching with/ near to absorption peak of material is used, Raman-scattering cross-section increases by $2 - 3$ orders and better sensitivity is achieved. Explosive materials have their absorption peaks in the UV range (190-230 nm). Also, the strength of the Raman signal is dependent on the wavelength of the incident beam in the inverse fashion of its fourth-power and hence higher with UV wavelengths. In literature, enhancement of Raman signal using excitation in the UV range is reported in comparison to that in visible/ NIR range [17]. For stand-off and low concentration detections, power incident on samples has to be increased. At low power, the Raman signal will not be generated and at higher power, materials start degrading due to heat and become black. This thermal degradation is a major problem making explosive detectors based on Resonance/ UV Raman spectroscopy.

1.3.2.8.3 Time-gated Raman Spectroscopy

Inherently Raman-scattering is a weak phenomenon and hence postures an insufficiency for trace detection. Being its broad spectral nature, Raman scattering co-exists with ambient light and fluorescence from the sample itself or other materials near to sample [18]. These problems can be overcome by using pulse laser and gating detection. Gating detection means the detection process should be only during optical

laser pulse but it should be OFF between two consecutive laser pulses. Raman signal is available only during the optical pulse and in between two consecutive pulses, no Raman signal is available. The only ambient background will be present between two pulses [19]. Fluorescence also occurs after few nanoseconds of optical pulses. Thus, detection only during an optical pulse will avoid ambient as well fluorescent signal resulting in much better sensitivity. This can be achieved using a gated intensifier detector (ICCD). The intensifier of ICCD also amplifies the Raman signal. Synchronizing the detector with an optical pulse is very critical in this technique. The enhancement in the sensitivity due to gated detection has been reported in literature particularly in stand-off detection.

1.3.2.8.4 Surface-enhanced Raman Scattering (SERS)

This technique is very promising and can have excellent potential in the detection of minute quantities of materials. SERS involves a laser, nanotextured metal surface for adsorption of target molecules, spectrograph and detector. The molecules of the target material are adsorbed on the SERS substrate. When the nanotextured surface is exposed by laser beam, plasmons are generated at nano-size sharp sites known as hot spots. The molecules which get absorbed at these sites, result in enhanced Raman scattering. These plasmons are responsible for the enhancement and the Raman cross-section is increased by order of $6 - 10$. This enhancement makes the SERS technique very sensitive [20, 21]. This technique may lead to a very compact and robust explosive detector having unmatched sensitivity as well selectivity. The main limitation of the technique is the localisation of enhancement effect i.e. at hot spots only and hence microscope is involved.

1.3.2.8.5 Spatial-offset Raman Spectroscopy

This technique is the most suitable technique for detecting explosive materials packaged in translucent packaging which poses a challenge to conventional Raman spectroscopy [22] usually preferred for scanning transparent or semitransparent containers. In real scenarios, bottles of diffused materials also have to be scanned. These diffused materials of container restrict recording of Raman signatures of content by conventional Raman spectroscopy due to very low transmission and fluorescence of container. SORS technique overcomes these limitations by limiting

the collection of Raman signal and fluorescence originating from the container and makes it possible to observe the Raman spectrum of the material inside the container by non-invasive means. This technique involves the same instrumentation but there is little offset between the transmitted laser beam and the optical axis of the receiver i.e. focusing the collection optics at spots which are spatially offset from incidence spot of laser beam [23-25]. As a result, the contribution of the Raman signal and fluorescence signal originating from container relative to Raman signal originating from content material is reduced remarkably by inserting offset between incidence spot and collection spot. In brief, the SORS technique overcomes the problem of fluorescence from the container. Due to the diffusion of light, the SORS technique enables the collection of Raman signals from content selectively through thick and coloured containers. One SORS based explosive detector has been reported in the literature and this system is under final trials.

Whereas **Chapter 1** provides a basic idea of hazardous materials, deals with the insight of the field of explosive detection and different non-optical and optical techniques having potential in the field of explosive detection, **Chapter-2** explains the theoretical aspects of the phenomenon of Raman scattering including selection rules and its instrumental aspects like types of light source both conventional light sources like mercury lamp, xenon lamp etc. and lasers; different optical schemes like 90-degree configuration and 180-degree configuration; optical components like lenses, filters, mirrors and optical fibers; and spectrometers like monochromators, spectrographs and interferometers are discussed in terms of application and corresponding detector. Finally, the frequency calibration of spectrometers is discussed. Further **Chapters 3** deals with the studies of explosive materials like ammonium nitrate and p-nitrobenzoic acid in soil samples and through the different types of plastic bottles using normal Raman spectroscopy. The importance of the processing of Raman spectra in terms of background and fluorescence of plastic material have been investigated using plastic bottles of different materials. **Chapter 4** deals with the development of a customized algorithm and then GUI for the identification of materials in real-time. **Chapter 5** presents the trace detection of explosive materials and their derivatives using time-gated Raman spectroscopy.

Raman spectra of low-concentration explosive samples like 100 ppm have been recorded successfully. **Chapter 6** deals with the detection of explosive materials through translucent plastic bottles using spatially offset Raman spectroscopy. The capability of spatially offset Raman spectroscopy over the normal Raman spectroscopy is evaluated by recording Raman spectra of urea and sodium nitrate through their commercial translucent plastic. **Chapter 7** deals with the theoretical study of the MDMA molecule for its structural, spectral and thermal characteristics. The geometrical parameters and vibrational frequencies estimated are found in an excellent match with experimental values. **Chapter 8** represents the conclusion of the research work reported in the thesis. The main outcomes of the research work reported have been brought out clearly. Further, the future prospects of the work has been discussed.

CHAPTER 2

RAMAN SCATTERING: THEORETICAL TREATMENT AND INSTRUMENTATION

In 1928, Sir C.V. Raman discovered a new type of scattering known as Raman scattering. The very simple instruments like sunlight as a light source, coloured glass filters, normal telescope etc. were only used in the discovery of the Raman scattering [26]. The effect observed was a true scattering rather than a normal fluorescence, was indicated in its first place by its feebleness in comparision with the normal scattering and secondly by its polarization which was in many cases quite strong and comparable with the polarization of normal scattering [27].
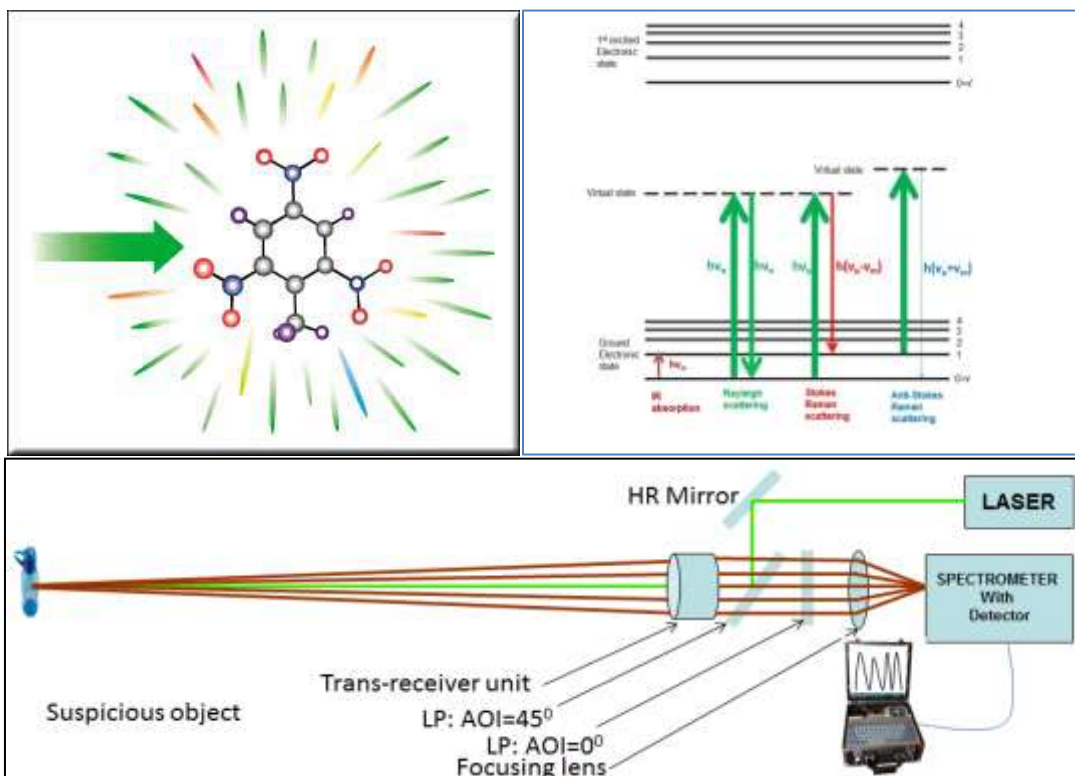
2.1　Origin of Raman spectrum

Raman scattering and infrared absorption both deals with vibrational transitions and rotational transitions occurring in the molecules. In IR absorption, the absorption of the incident beam in the sample is monitored in spectral domain. The intensity absorbed by the molecule obeys Beer-Lambert law as given below:

$$I = I_o e^{-\epsilon cd}$$

---------------------------------- 2.1

Where I_o and I are incident intensity and transmitted intensity of infrared beam; ϵ is molecular absorption coefficient; c is concentration and d is the path length of the beam through sample. Absorption A may be defined as:

$$A = log \frac{I_o}{I} = \epsilon cd$$

--------------------------------------- 2.2

Raman spectrum and IR absorption spectrum differs in terms of nature of their origin. For recording of Raman spectrum, monochromatic and intense incidence beam is used to interact with a sample and Raman-scattered light is collected in direction normal to incidence beam usually. But back-scattering and forward scattering configurations are also used in many studies. Raman spectrum consists of spectral lines at same frequency as that of incident beam and weak spectral lines at different frequencies. The spectral line at a frequency of incident beam is due to the Rayleigh scattering and spectral lines at shifted frequencies originate due to the Raman scattering and hence called Raman-scattering lines. Raman-scattering lines occur on both sides of the exciting line i.e. Rayleigh line and are called the Stokes lines on lower frequency side and anti-Stokes lines those at higher frequency side. Anti-stokes lines are found to be always much weaker compared to the Stokes lines [28]. The Raman spectra of the molecule CCl_4 is depicted in figure-2.1.
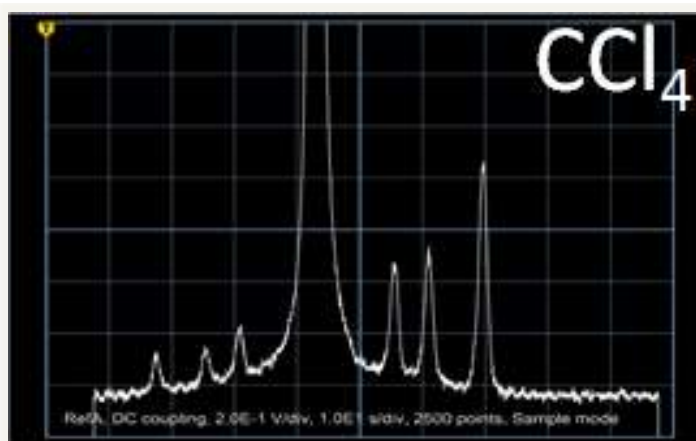
Figure-2.1. Raman spectra of CCl$_4$

The central broad peak represents the strong Rayleigh scattering which is elastic in nature. The peaks at right-hand sides i.e. at the higher-wavelength side are the Stokes lines. The peaks at left-hand sides i.e. at lower-wavelength are called anti-Stokes lines.

Under higher-resolution, broad Rayleigh peak is in fact found of consisting of equidistant lines very closely on both sides. This is the pure rotational Raman spectrum. The Stokes and anti-Stokes are also found to be bands composed of rotational fine-structure. These peaks constitute the vibrational (strictly rotational-vibrational) Raman spectrum of the molecules [29].

2.1.1   Classical theoretical treatment

An elementary explanation of the Raman Effect can be given from the classical theory. When a light beam interacts with a molecule, an electric dipole moment is induced in the molecule due to rapidly-oscillating electric field associated with the beam whether the molecule possesses an inherent dipole moment or not.

The electric field strength associated with a light beam is oscillating w.r.t. time and may be expressed as:

$$E = E_o \cos 2\pi \nu_o t$$
-------------------------------- 2.3

where **E$_o$** is the amplitude of electric field and **ν_o** is the frequency of the incident beam. The induced dipole moment in the molecule may be expressed as:

$$P = \alpha E = \alpha E_o \cos 2\pi \nu_o t$$
----------------------------- 2.4

Where $\boldsymbol{\alpha}$ is constant of proportionality known as molecular polarizability which is a measure of the ability of electrons to polarize. The oscillating molecule now radiates electromagnetic energy at frequency $\boldsymbol{\nu_o}$. This phenomenon is called Rayleigh scattering.

Now the molecule involves vibrational and rotation motion of its nuclei which in turn affects the molecular polarizability. This variation in the polarizability due to the vibrational motion of the nuclei may be expressed as:

$$\alpha = \alpha_o + \left(\frac{\partial \alpha}{\partial q}\right)_o q + \dotsb \qquad\qquad \text{------------------------------- 2.5}$$

where $\boldsymbol{\alpha_o}$ is the polarizability at the mean position and $\boldsymbol{(\partial\alpha/\partial q)_o}$ is the rate of variation of the polarizability w.r.t. the change in nuclear displacement i.e. $\mathbf{q}$ at the equilibrium position. The nuclear displacement q may be expressed as:

$$q = q_o \cos 2\pi \nu_m t \qquad\qquad \text{--------------------------------- 2.6}$$

where $\mathbf{q_o}$ and $\boldsymbol{\nu_m}$ are the amplitude and the frequency of molecular vibrational motion.

Using equations (2.5) and (2.6), equation (2.4) gives

$$P = \alpha_o E_o \cos 2\pi \nu_o t + \left(\frac{\partial \alpha}{\partial q}\right)_o q_o E_o \cos 2\pi \nu_o t \cos 2\pi \nu_m$$

$$= \alpha_o E_o \cos 2\pi \nu_o t + \frac{1}{2}\left(\frac{\partial \alpha}{\partial q}\right)_o q_o E_o \left[\cos\{2\pi(\nu_o + \nu_m)t\} + \cos\{2\pi(\nu_o - \nu_m)t\}\right] \text{ ---2.7}$$

From equation (2.7), the induced dipole moment changes not only with the frequency ν_o (Rayleigh scattering); with shifted frequencies $\nu_o + \nu_m$ (Stokes Raman scattering) and $\nu_o - \nu_m$ (anti-Stokes Raman scattering). If the slope of polarizability w.r.t. nuclear displacement at mean position is zero, the molecule will not be Raman-active. Thus the particular bond will be Raman active only when the slope at the mean position is non-zero at the equilibrium position. It is clear that the molecule need not have a permanent dipole moment for being the Raman active [28].

The classical explanation of the Raman-scattering has two main drawbacks [29]:

i.   According to the classical theory, both Stokes and anti-Stokes lines must be of same intensity. Experimentally it was observed that the anti-Stokes lines are drastically weaker than the Stokes lines.

ii. Classical theory cannot be applied to molecular rotations as it does not ascribe specific discrete rotational frequencies to the molecules.

2.1.2   Quantum theoretical treatment

Quantum mechanically, when an incident photon of frequency ν_o interacts with a molecule lying in a stationary level (v=0), there are following three possibilities:

i.   The energy of scattered photons may be same as that of incident photons i.e. $h\nu_o$, it is known as Rayleigh scattering.

ii. The incident photon may transfer some energy to the molecule during photon-molecule interaction. In this case, the molecule will transit to a higher energy level (v=1) and the energy of scattered photon will be lesser than that of incident photon i.e. $h(\nu_o-\nu_m)$ where $h\nu_m$ is difference in energy between energy levels v=0 and v=1. Such inelastic scattering is called Raman scattering and such spectral lines i.e. $h(\nu_o-\nu_m)$ is called Stokes Raman scattering lines. These lines occur at lower frequency i.e. at a higher wavelength in comparision to Rayleigh line.

iii. The molecule may transfer some energy to the incident photon during photon-molecule interaction. This may happen only when the molecule is initially at energy level v=1. In this case, the molecule will return to the lower energy level (v=0) and the energy of scattered photon will be greater than that of incident photon i.e. $h(\nu_o+\nu_m)$ where $h\nu_m$ is energy difference between energy levels v=0 and v=1. Such inelastic scattering is called Raman scattering and such spectral lines i.e. $h(\nu_o+\nu_m)$ are called anti-Stokes Raman scattering lines. These lines occur at higher frequency i.e. at lower wavelength in comparision to Rayleigh line.

The transitions corresponding to these three cases are depicted in figure-2.2.

18
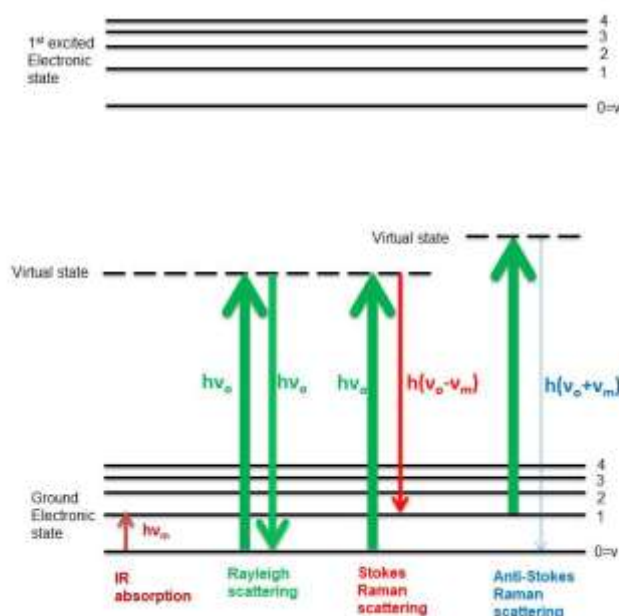
Figure-2.2. The transition of energy levels involved in IR absorption, Rayleigh scattering and Raman scattering (Stokes & anti-stokes both)

The Stokes and anti-Stokes Raman lines are located symmetrically on either side of the Rayleigh line.

2.1.2.1 Vibrational and Rotational Raman Spectra

The molecule may go under vibrational transition or only rotational transition and thus we can have two different kinds of Raman spectra namely vibrational Raman spectra and rotational Raman spectra respectively. Raman shift is found very less in the case of rotational lines in comparision to that of vibrational lines being the energy difference between rotational energy levels is much lesser than that between to vibrational energy levels. Therefore, higher resolution spectrometers are required to record the rotational Raman lines [29].

2.1.2.2 Raman scattering and virtual energy state

When an incident photon comes in the vicinity of target molecule, it transfers its energy to the molecule momentary resulting in distortion of electronic cloud around the nuclei. It can be considered as the formation of the molecule-photon complex during a very short period. This formation of the complex is very unstable and hence

the photon is released from the complex by either imparting some energy to the molecule (Stokes Raman lines) or taking some energy from the molecule (anti-Stokes lines). The complex between molecule and photon is very short-lived and does not represent any real state of the molecule and hence called the virtual state.

The shape and size of the distorted electronic cloud around the nuclei are determined by the amount of energy transferred to the molecule and hence on incident photon energy or frequency of the incident photon. The virtual level may be considered as the real state of short-lived 'molecule-photon' complex.

2.1.2.3 Explanation of relative intensities of Stokes and anti-Stokes lines

Experimentally it has been observed that the anti-Stokes lines are much weaker in comparision to the Stokes-lines. As discussed above, these lines occur only when the incident photon is scattered by the molecule in a higher energy level i.e. v=1. Most of the molecules are likely to be in the lowest energy level i.e. v=0 at room temperature. The ratio of intensities of anti-Stokes lines and Stokes lines is dependent on the ratio of their population in higher-energy level i.e. v=1 and that of ground energy level v=0 and hence governed by the Boltzmann equation as mentioned below:

$$\frac{N_1}{N_0} = \frac{g_1}{g_0} \exp\left[\frac{-(E_1 - E_0)}{kT}\right]$$

-- 2.8

where N_1 and N_2 are the number of molecules in the higher energy level v=1 and the ground energy level v=0 respectively; g is the degeneracy of these levels; E_1 and E_2 are energies of these levels; k is Boltzmann constant and T is temperature [30].

2.1.2.4 Selection rules for Infrared absorption and Raman scattering

Quantum mechanics explains whether the particular vibration will be infrared active, Raman active or active in both. If the change in dipole moment is exhibited during vibration, this will be an IR active vibration whereas if the change in polarizability is exhibited during vibration, this will be a Raman active vibration. So all the vibrational modes of a molecule are to be investigated to determine whether the molecule is IR active, Raman active or active in both. A molecule consists of 3N-6 number of

vibrational modes where N is the number of atoms constituting the molecule whereas 3N-5 in the case of a linear molecule.

In the case of small molecules, just inspection of the normal vibrational modes is sufficient to conclude whether the molecule is IR active or Raman active. The diatomic molecule has only one normal vibrational mode. The homopolar diatomic molecule like O_2, the possible vibration exhibits change in its polarizability during the vibration and hence such molecule is Raman active. But such molecule does not exhibit any change in dipole moment during the vibration and hence IR is inactive. Due to this, a spectral band can be observed in the Raman spectrum of oxygen gas but no band in its IR spectrum. The heteropolar diatomic molecule like NO exhibits changes in both polarizability and dipole moment during the vibration and hence both Raman active and IR active [31].

2.1.2.5 Raman versus Infrared spectroscopy

Though Raman scattering and infrared absorption both deals with transitions between vibrational levels, both differ from each other as described below [32, 33]:

i.   In Raman-scattering, incident photon distorts electronic cloud and degree of distortion depends on the energy or frequency of the incident photon. In other words, a photon of any energy or frequency can distort though up to different degrees of extent. Hence Raman scattering does not require photons of any particular frequency. In infrared absorption, an incident photon is absorbed taking the molecule to its higher energy state. The incident photon may be absorbed by molecule only when its energy matches with the energy difference between two consecutive energy levels. Hence infrared absorption requires photons of a particular frequency depending on the energy levels of the nature of the molecule.

ii.   As the 'molecule-photon' complex formed during Raman scattering is not a stable state and hence very short-lived whereas the molecule transit to a real higher vibrational level during infrared absorption and hence its lifetime is longer comparatively.

iii.   The polarization of Raman-scattered light is related to that of the incident beam which is not the case with infrared absorption.

iv.   Covalent bonds exhibit strong Raman scattering whereas ionic bonds exhibit strong infrared absorption.

v.   Raman-scattering is a good choice for aqueous samples like in medical lines being water is very weak in Raman-scattering whereas IR absorption is very strong in the water.

vi.   Being Raman-scattering is independent of the frequency of the incident photon, the single-wavelength laser is sufficient to generate the complete Raman spectrum. Whereas infrared absorption requires a tunable light source to cover the complete spectral region.

vii.   It is easy to record IR spectrum with high resolution whereas it is not easy to record high-resolution Raman spectrum due to its domain falling in UV-visible region.

viii.   Centro-symmetric molecules follow the rule of mutual exclusion which says either a normal vibrational mode of a molecule with centrosymmetric will be either Raman-active or IR active.

Any type of sample can be investigated with both Raman-scattering and IR spectroscopy whereas only crystalline samples with X-ray and liquid samples in NMR can be investigated.

2.1.2.6 **Polarisation of Raman-scattered light: Depolarisation ratio**

When a molecule goes under interaction with linearly polarized light, its electronic cloud around nuclei gets distorted. The extent to which it gets distorted will be decided by the ability of the molecule's electrons to polarize i.e. the polarizability of the molecule. Incident light is plane-polarised but it could affect election cloud in all directions. Thus the polarizability of the molecule is represented by a tensor and induced dipole moment can be expressed as

$$
\begin{bmatrix} \mu_x \\ \mu_y \\ \mu_z \end{bmatrix} = \begin{bmatrix} \alpha_{xx} & \alpha_{xy} & \alpha_{xz} \\ \alpha_{yx} & \alpha_{yy} & \alpha_{yz} \\ \alpha_{zx} & \alpha_{zy} & \alpha_{zz} \end{bmatrix} \begin{bmatrix} E_x \\ E_y \\ E_z \end{bmatrix}
$$

--------------------------------- 2.9

where α_{xx} is the tensor component in 1st and 2nd subscripts represent the direction of the polarizability of the molecule and polarization of the incident light respectively.

Thus polarization of the Raman scattered light is related to that of incident light [26, 27]. The intensity of the Raman scattered light may be measured for different polarisations using the analyser before the spectrometer. The analyser is an optical component that allows light to have polarization parallel to its optical axis only. Thus the light with different polarisations may be allowed to pass by changing the orientation of the analyser. The experimental scheme for studies of polarization of Raman scattering light is depicted in figure-2.3.
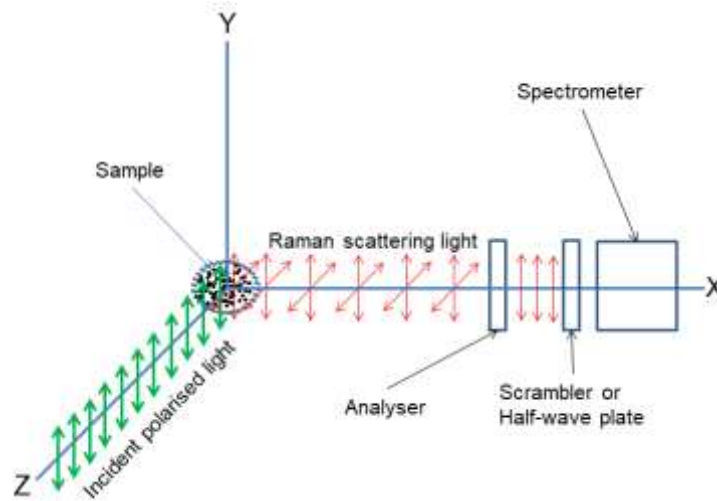
Figure-2.3: Experimental scheme for studies of polarization of Raman scattering light

The intensity ratio of Raman scattering light with polarization perpendicular to the direction of polarization of incident beam to that with polarization parallel to the incident is called the de-polarisation ratio [28]. The ratio of de-polarisation can be expressed as

$$
\rho_p = \frac{I_\perp}{I_\parallel}
$$

--------------------------------------- 2.10

where $I_\perp$ and $I_\parallel$ are intensities of Raman-scattered lights with polarization 90 degrees and with polarization parallel to the incident beam.

The measurement of the de-polarisation ratio has specific importance in assignment of the peaks. The value of de-polarisation ratio will be different for molecules with different symmetric nature as mentioned in table-2.1 below:

Table-2.1: Values of de-polarisation ratio for vibrations with different types of symmetries [34-36]

Nature of vibration	De-polarisation ratio
Totally symmetric vibration	$0 \leq \rho_d < \dfrac{3}{4}$
Non-totally symmetric vibration	$\rho_d = \dfrac{3}{4}$

Thus the value of de-polarisation ratio helps in assigning the peaks of Raman spectrum to different vibrational modes of the molecule. In case of IR absorption, we cannot get any such polarization specific information.

The efficiency of a grating of the spectrometer is polarisation dependent hence apparent de-polarisation ratio will not be correct. This problem can be minimized by using a half-wave plate between analyser and spectrometer. It rotates the polarization by 90° which ensures the polarization is the same before the spectrometer. The scrambler may also be used for scrambling the Raman-scatted light before entering the spectrometer [31].

2.2   Instrumentation

The experimentation work in the field of Raman spectroscopy generally involves the light source for incident beam, optical components, wavelength selectors, spectrum analyser, optical detector etc. [28, 31, 37, 38].

2.2.1 Excitation sources

Before the invention of the laser, mercury arc lamp and even sun light were the main choice as light source for experimentation work in the field of Raman scattering. Even the novel work carried out by Sir C.V. Raman in 1928 was also carried out using

these light sources only. The mercury arc lamp provides multiple intense peaks in UV-visible region.

With the invention of laser, it became the first choice as the light source in the field of Raman spectroscopy being its high intensity and monochromatic characteristics. He-Ne laser; Argon-ion laser; Excimer lasers; solid-state tunable lasers like Ti-Saphire laser, dye-laser; semi-conductor lasers are widely used in the field of Raman spectroscopy. The wavelengths of laser emission of the main lasers used in Raman spectroscopy are summarized below in table-2.2:

Table-2.2: Lasers used in different types of Raman spectroscopy [39]

Laser		Wavelength of emission	Type of Raman spectroscopy
He-Ne laser		632.8 nm	NRS
Excimer laser (KrF)		248 nm	UV RS
Dye laser		320-1200 nm	RRS, CARS
Ti:Sapphire laser		660-1180 nm	RRS, CARS
Diode lasers		785 nm	NRS, SERS
		810 nm	NRS
Nd:YAG laser	Fundamental	1064 nm	NRS, TGRS
	SHG	532 nm	NRS, TGRS, SERS
	THG	355 nm	UV RS, TGRS
	FHG	266 nm	UV RS, TGRS

NRS: Normal Raman Spectroscopy; UV RS: Ultra-violet Raman Spectroscopy; RRS: Resonant Raman Spectroscopy; CARS: Coherent anti-Stokes Raman Spectroscopy; SERS: Surface-enhanced Raman Spectroscopy; TGRS: Time-gated Raman Spectroscopy

2.2.2   *Optical configurations*

Optical configuration refers to the orientation of the transmitting axis and receiving axis. There are mainly two types of configurations [31] are used in the field of Raman spectroscopy:

i. 90° scattering configuration

ii.   Co-axial configuration

The optical configuration is selected as per the requirement of application as well as the nature of samples like solid, powder or liquid. 90° configuration is the most conventional configuration especially for a liquid sample as the Rayleigh scattering is minimum in this configuration. In this mode, the Raman scattering is collected in direction 90° to the incident beam i.e. transmitting axis and receiving axis are at 90° to each other. For field applications like the development of Raman scattering based detectors for explosive materials, narcotics etc., it is required that the sample should be scanned without taking a sample to the sample chamber. Such field-deployable detectors do not have a sample chamber rather the laser should come out from the system, interact with materials (under scan) and the Raman scattering should be collected through the same optics which transmits the laser i.e. transmitting axis and receiving axis is co-axial [40]. Such configuration is called co-axial configuration. This is also called 180^0 configuration and is also used in micro-Raman spectroscopy set-up, confocal-Raman spectroscopy set-up, Raman probes etc. [41]. Both 90° configuration and co-axial configuration are shown in figure-2.4.
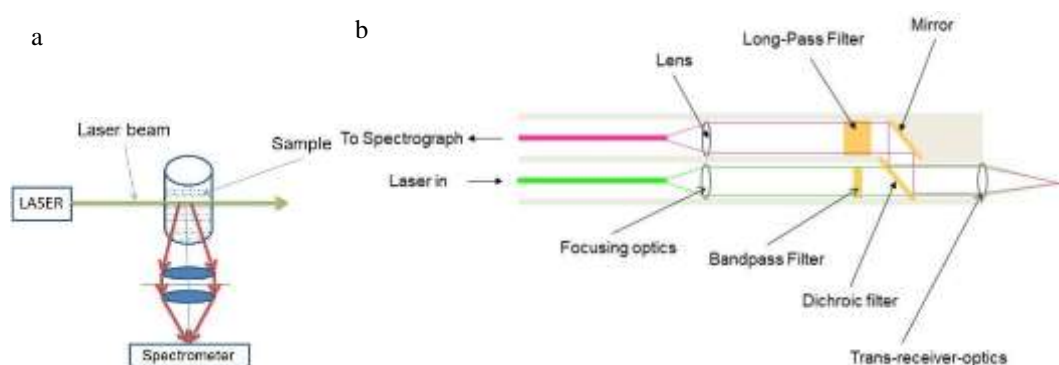
Figure-2.4. 90^0 configuration (b) 180^0 configuration

2.2.3 Optical components

2.2.3.1 Lenses & mirrors

In Raman spectroscopy, lenses and mirrors are used in guiding the monochromatic light beam to the sample from the light source and collecting the Raman scattered light and coupling it to spectrometer. Mirrors plays role in folding the beam usually by 90 degrees i.e. angle-of-incidence of such mirror is 45 degree. The lenses are used in focusing the laser beam on the material, collecting Raman-scattered beam &

making it parallel before the beam incident on the Rayleigh-rejection filter and finally focusing the scattered light beam at the slit of spectrometer. Usually, lens assembly rather than a single lens is used to remove aberrations.

2.2.3.2 Filters

Filters play important functions in the field of Raman spectroscopy. The first laser line filter is used in the path of an incident light beam to produce the highly monochromatic beam before the sample. Laser line filter passes the light of very narrow spectral width and reflects all the spectral lines out of spectral width. Notch filters or a long-pass filter is used in rejecting the strong Rayleigh-scattered light. Notch-filter rejects the Rayleigh line efficiently and exhibits good transmission at lower and higher wavelengths i.e. has a single narrow rejection spectral band centred at Rayleigh line. It ensures the recording of both Stokes and anti-Stokes Raman lines. In most applications recording of Stokes lines are sufficient like in the identification of materials and hence, a long-pass filter may be used instead of a notch filter being the low cost, narrower transition-width and better transmission in transmission band i.e. in Stokes lines region. In addition, a dichroic mirror is also used specially to implement the co-axial configuration. It is also a long-pass filter but with an angle of incidence of 45 degrees. All these filters are sensitive to the angle-of-incidence and hence be aligned carefully to avoid the losses in the intensity of incident beam as well as Raman-scattered light [42, 43].

2.2.3.3 Optical fibers

Optical fibers are light-guiding cavities based on total-internal reflection and do not require line-of-sight for the propagation of light. Fibers are used in a configuration where freedom of placing the spectrometers and lasers are required like developing compact systems. In Raman probes also the light from the laser to Raman-probe head and then coupling Raman-scattered light from focusing optics to spectrometers is executed using fibers. Single-mode fiber is used in carrying incident light from laser to optics whereas multi-mode fiber is used in coupling Raman-scattered light being a wide spectral band light.

2.2.4   Spectrometers

The spectrometer is an instrument that splits different wavelengths of the light beam in a different direction and ensures the measuring of the intensity of individual wavelengths using a photo-detector. There are different configurations used in spectrometers like Fastie-Ebert Configuration, Czerny-Turner Configuration Echelle configuration and interferometers [44, 45]. Prism and grating are the dispersing elements used in spectrometers. In the Echelle configuration, both grating and prism are used to achieve the higher resolution otherwise only grating is usually used as dispersing element. Different types of gratings like reflecting grating blazed grating, and holographic grating are used in spectrometers. With the modern fabrication techniques with high precision like lithography and holography, gratings with higher grating elements even 50000 lines per inch are possible ensuring excellent resolutions. The holographic type grating ensures the least stray light in the spectrometer.

As per the output of the spectrometer and so their nature of working, spectrometers may be divided into three broad categories:

2.2.4.1 Monochromators

In monochromators, the output beam comes out through the output slit and hence it is monochromatic. The grating is rotated to allow different wavelengths to come out through the output slit. Single-channel detectors like a photo-multiplier tube (PMT) are used in this configuration.

2.2.4.2 Spectrographs

In spectrograph, the output beam consists of the whole spectral band in dispersed form. It is made to fall on a multi-channel detector. The intensity of all the wavelength-constituents is measured simultaneously. Hence the grating does not need to be rotated. So the spectrographs require calibration rarely.

2.2.4.3 Fourier-transform interferometers

The interferometers also ensure the measurement of the intensity of different wavelength constituents. The position of the moving mirror is related to the wavelength reaching at the detector due to constructive interference and all the other

wavelengths cannot reach due to destructive interference. As the mirror moves on, the condition of constructive interference is satisfied for different wavelengths. Fourier-transformation is used to convert the intensity vs. time information to the intensity vs. frequency or wavelength. For the reference of wavelength for mirror position, He-Ne laser is used as a reference source.

2.2.5   Photo Detectors

The photo-detectors are used to read the output of the spectrometer. The intensity of the output beam is measured w.r.t. wavelength falling on the detector. Depending on the application, spectral region and configuration, different types of detectors are used as summarised in table-2.3 below:

Table-2.3: Photo-detectors used in Raman spectroscopy

Laser	Spectral region	Spectrometer configuration
Photo-Multiplier Tube (PMT)	350 - 800 nm	Monochromator
CCD 1D	200 - 1100 nm	Spectrograph
CCD 2D	200 - 1100 nm	Echelle spectrograph
Semiconductor detectors	700 - 2500 nm	Monochromators & interferometers

2.2.6   Frequency calibration

The accuracy of wavelengths or spectral lines read by the spectrometer depends on how well the spectrometer is calibrated. The calibration is a standard process that involves the standard light sources and their well-defined spectral lines. Neon lamps are used to achieve high-level calibration over a wide spectra range. Indene and Argon plasma laser are also used in calibrating the spectrometer with reasonable accuracy. Internal standards may also be used for the calibration process. Any material having several defined Raman spectral lines over a wide spectral range may be used as an internal standard.

CHAPTER 3

DETECTION OF EXPLOSIVE MATERIALS IN SOIL SAMPLES AND THROUGH PLASTIC BOTTLES USING NORMAL RAMAN SPECTROSCOPY

Post-blast investigation (PBI) of explosive materials and their identification through non-transparent containers are the mains required by intelligence agencies. In the post-blast scenario, residuals of unburned explosive materials available in the soil nearby the blast site are targeted. Identification of explosive materials through non-transparent containers is required at the airport and other vital installations. Here, soil samples of ammonium nitrate were prepared at different concentrations to simulate the scenario of post-blast investigation. These soil samples were investigated using normal Raman spectroscopy. In real scenarios, the target material may be in different types of containers particularly plastic bottles, coloured and thick glass bottles. In this work, we have reported Raman signatures of p-nitrobenzoic acid (PNBA), in plastic bottles and coloured glass bottles using normal Raman spectroscopy. The spectra have been analyzed in terms of parameters of a bottle like plastic-type, transmission etc.
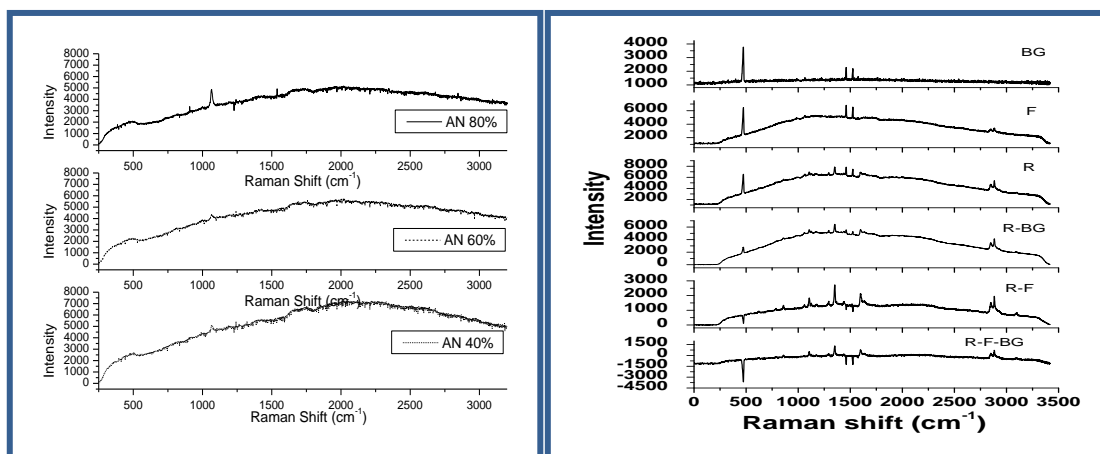
3.1 Introduction

Reliable detection of explosive materials is highly required by security agencies. Raman spectroscopy being a fingerprint technique is very reliable and suitable for the identification of unknown materials [46]. Post-blast identification of explosive materials is required by intelligence agencies. In the post-blast scenario, residuals of unburned explosive materials may be available in the soil nearby the blast site. Soil samples may be collected at the blast site and analysed for identification of explosive material used in the blast under investigation [47, 48]. In addition, Raman spectra of explosive materials have been earlier studied using glass bottles, which have very low interference in terms of fluorescence etc. [49, 50]. In real scenarios, the target material may be in different types of containers particularly plastic bottles, coloured and thick glass bottles.

Here, soil samples of ammonium nitrate were prepared at different concentrations to simulate the samples of real-scenario of post-blast investigation (PBI). These soil samples were investigated using normal Raman spectroscopy. In addition, Raman signatures of p-nitrobenzoic acid (PNBA) in plastic bottles of different colours were recorded using normal Raman spectroscopy. The spectra have been analyzed in terms of parameters of the bottle like plastic-type, transmission etc.

3.2 Experimental procedure

Material like p-nitrobenzoic acid $(C_6H_4(NO_2)CO_2H)$ and ammonium nitrate (NH_4NO_3) were procured from M/s Sigma-Aldrich. The soil samples were prepared with different concentrations of ammonium nitrate and urea to simulate the post-blast investigation scenario. In addition, p-nitrobenzoic acid (PNBA) was taken in different plastic bottles like A4 (white-transparent bottle), D8 (semi-transparent thick white bottle) and D1 (semi-transparent coloured bottle) for investigation of the effect of different types of bottles in recording Raman spectra of content material i.e. PNBA.

The experimental schematic used in these studies of explosive materials in soil samples and through plastic bottles is depicted in figure - 3.1.
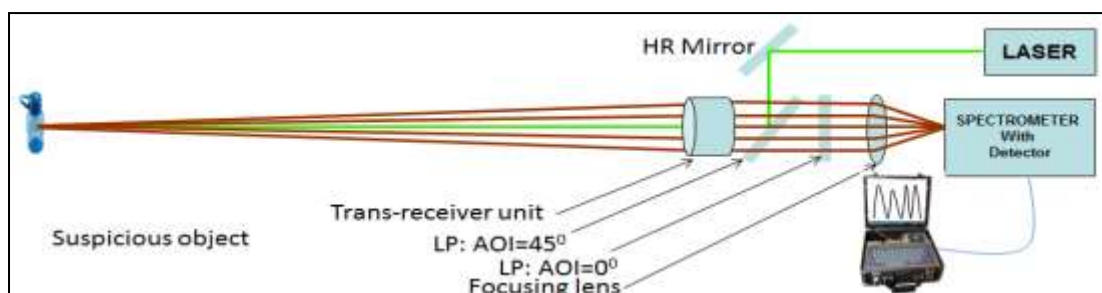
Figure-3.1: Experimental schematic used in the study of explosive materials in soil samples and through plastic bottles

It involves CW laser, CCD-coupled spectrograph, receiving optics etc. CW laser is 532nm 2nd harmonic of Nd:YAG. The receiving optics is of the diameter of 2 inches. It consists of HR mirror for the folding of laser beam, a long pass (LP) filter with an angle of incidence (AOI) of 45^0, a trans-receiver unit for transmission of laser beam towards target and collection of scattered photons. The Raman-scattered light beam was made parallel beam by trans-receiver optics. The parallel beam was passed through a long-pass filter with an angle of incidence of 0^0 for rejecting out the strong Rayleigh-scattering beam. Finally, the filtered Raman-scattering beam is focused by focusing optics at the slit of the spectrograph.

3.3 Results and discussion

The Raman spectra of the soil samples of ammonium nitrate with different concentrations were recorded at different integration times. First, the background i.e. solar noise was recorded in the same conditions as were used in acquiring Raman signal and then the background-subtracted Raman spectra of the samples were recorded. Raman spectra of PNBA were recorded through different bottles to investigate the effect of different types of plastic bottles. The spectra have been analyzed in terms of parameters of the bottle like plastic-type, transmission etc.

3.3.1 Detection studies in soil samples

Being one of the frequently used explosive materials in IEDs, ammonium nitrate was used in the studies of the scenario of post-blast investigation. After the blast, the residual of unburned explosive materials gets mixed in the soil. So the soil samples of ammonium nitrate were prepared for simulating the real scenario in the best way.

3.3.1.1 Raman spectra of ammonium nitrate at different concentration

Raman spectra of soil samples of ammonium nitrate of concentration 40%, 60%, 80% and pure were recorded at different integration times. Figure-3.2 shows Raman spectra of soil samples of ammonium nitrate of concentration of 40%, 60% and 80% recorded at an integration time of 20 s.
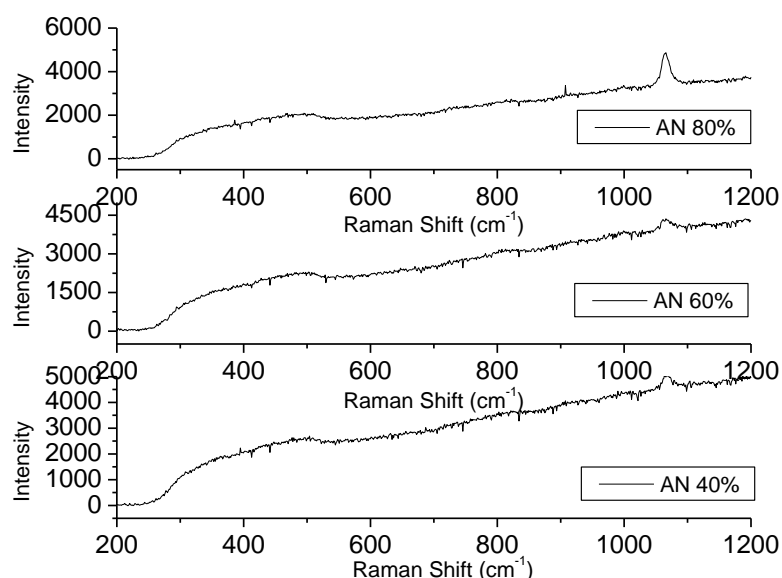
Figure-3.2. Raman spectra of soil samples of ammonium nitrate of concentration of 40%, 60% and 80% were recorded at an integration time of 20 s

As the concentration decreases from 80% to 40%, the decrease in signal-to-noise ratio (SNR) of Raman peak at 1050 cm^{-1} is observable. It is because the number of molecules interacting with the laser beam also decreases proportionally with the concentration.

3.3.1.2 Effect of background correction on the SNR of Raman peaks

The effect of background i.e. solar noise was studied by recording Raman spectra of soil samples in two ways: (i) without background correction and (ii) with background correction. It should be noted that the same integration time has been used in recording background (laser is kept OFF) as well as Raman spectra (laser is kept ON).

In this study, Raman spectra of pure ammonium nitrate and a soil sample of ammonium nitrate of concentration of 40% were recorded in both ways with integration time of 2 s and 20 s respectively as shown in figure-3.3.
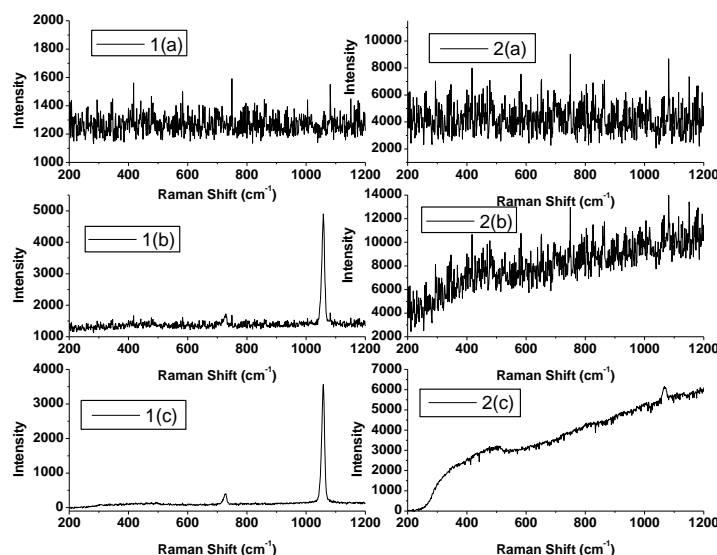
Figure-3.3. Raman spectra of pure ammonium nitrate and soil sample of ammonium nitrate of concentration of 40% were recorded in both ways with integration time of 2 s and 20 s respectively

The effect of background correction on the SNR of Raman peaks of ammonium nitrate in both samples can be observed. It can be observed that Raman peak of ammonium nitrate at 720 cm^{-1} is not observable even in the case of pure sample though it is observable in the Raman spectrum processed for background correction. It can also be observed that even the intense Raman peak at 1050 cm^{-1} is not observable without correction in the case of sample of concentration of 40%. Though it is observable when Raman spectrum is processed for the background correction.

3.3.1.3 Effect of integration time

The integration time refers to the time for which the signal is being collected by the spectrograph before giving the output. For observing the effect of integration, Raman spectra of soil samples of ammonium nitrate with a concentration of 40% were recorded with different integration times. Figure-3.4 shows Raman spectra of soil sample of 40% concentration recorded at an integration time of 10 s, 15 s, 20 s, 25 s

and 30 s. It could be easily observed that the SNR of Raman peak at 1050 cm^{-1} increased as the integration time was increased.
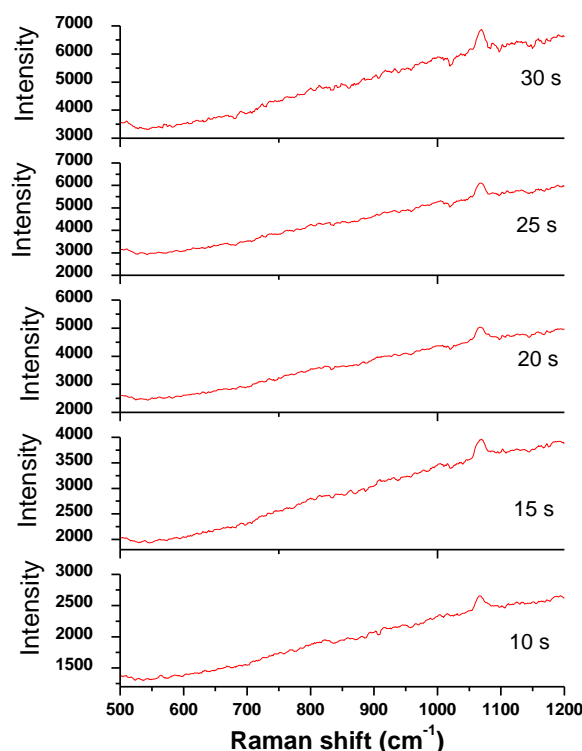
Figure-3.4: Raman spectra of soil sample of 40% concentration recorded at integration time of 10 s, 15 s, 20 s, 25 s and 30 s

3.3.2 Detection studies through plastic bottles

The scanning of materials through plastic bottles becomes unavoidable at the security gates at an airport or any other vital installation. The bottle carried by some person may be containing normal drinking water, medicine or some explosive material. The appearance of many explosive materials and their precursors is very similar to normal materials like water, sugar powder etc. So the investigation based on some scientific instruments becomes necessary.

3.3.2.1 Classification of plastic bottles

In this study, we simulated the real scenario by taking different materials like potassium nitrate, p-nitrobenzoic acid, nitromethane etc. in plastic bottles of different types as summarized in table-3.1.

Table-3.1: Details of sample materials and plastic bottles

Bottle Group	Bottle code	Transparency (material type)	Explosive material
	A	40- 70 % White Transparent	PNB A, Potassium Nitrate, Nitro methane
	B	30-65 % Thick White Transparent	PNBA, Potassium Nitrate
	C	10-50 % Colored Transparent	PNBA, Potassium Nitrate,
	D	1-10 % White Semi Transparent	PNBA, DNT, Potassium Nitrate,

3.3.2.2 Raman spectra of materials through different types of plastic bottles

Raman spectra of material through plastic bottles were processed for background correction and fluorescence correction. So spectra were recorded in different ways as described below:

Background or solar-noise (BG): The background was recorded with laser OFF but the spot of the collection was same as selected for recording Raman spectra i.e. spot of collection was on the content of bottle.

Fluorescence (F): The fluorescence of bottle material was recorded with laser ON but the spot of laser incidence & collection was above the content level i.e. no interaction of laser beam with content. So it contained fluorescence as well as background both i.e. F=Fluorecence +background

Raman spectrum (R): Raman spectrum of content was recorded with laser ON but the spot of laser incidence & collection was on the content of bottle. So background and fluorescence both were also collected while recording the Raman spectrum i.e. R=Raman+fluorescence+background

Raman corrected for background only (R-BG): In this case, Raman spectrum was processed for background correction only and correction for fluorescence was not implemented i.e. R-BG=Raman+fluorescence

Raman corrected fluorescence (R-F): In this case, Raman spectrum was processed for fluorescence correction which in turn also ensured background correction as fluorescence also contains the background i.e. R-F=Raman only.

i.   *Detection of PNBA in the white transparent bottle (A4)*

The bottle (A4), from group A (table-3.1), was used. The material p-nitrobenzoic acid (PNBA) was filled in the bottle as content as shown in figure – 3.5 (a). The bottle has very poor transparency less than 5 %. Background (BG), fluorescence (F) and Raman spectrum (R) of PNBA through the bottle were recorded and shown in figure – 3.5 (b). The Raman spectrum was also processed for background and fluorescence correction and shown as R-BG and R-F respectively and also shown in figure - 3.5 (b).

Raman peaks of PNBA were observed in Raman spectrum processed with background i.e. R-BG. Moreover, it was observed that Raman spectrum processed with fluorescence i.e. R-F did not provide any improvement further. It could be attributed to the fact that the container did not exhibit any appreciable fluorescence (ref spectrum F) and so fluorescence correction did not make any difference.

(a)   (b)
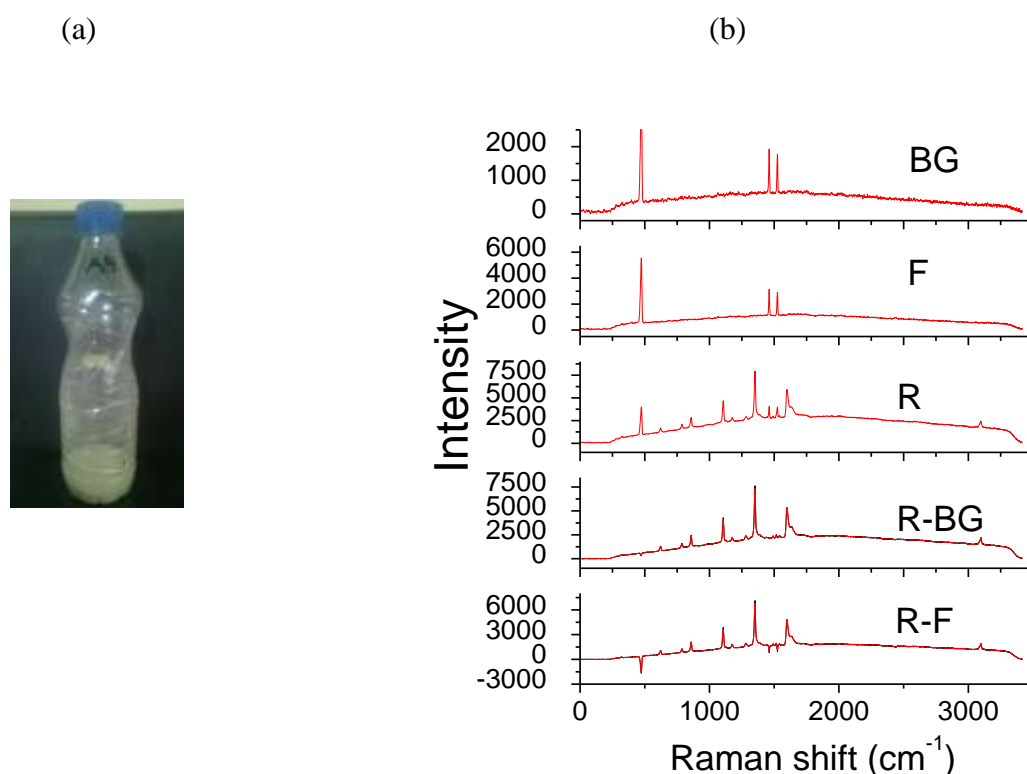
Figure-3.5. (a) PNBA filled in bottle (A4) and (b) the background recorded fluorescence & Raman spectrum of PNBA through bottle (A4) and processed Raman spectrum in terms of background and fluorescence.

ii.   Detection of PNBA in white semi-transparent thick bottle (D8):

The bottle (D8), from group D (table-3.1), was used. The material p-nitrobenzoic acid (PNBA) was filled in the bottle as content as shown in figure – 3.6 (a). The bottle has reasonable transparency around 70%. Background (BG), fluorescence (F) and Raman spectrum (R) of PNBA through the bottle were recorded and shown in figure – 3.6 (b). The Raman spectrum was also processed for background and fluorescence correction and shown as R-BG and R-F respectively and also shown in figure - 3.6 (b).

The improvement in SNR of Raman peaks of PNBA could be easily noticed in spectrum R-BG. Moreover, it was also observed that there was a further appreciable improvement in SNR of Raman peaks in processed Raman spectra R-F over that in the case of R-BG. It could be attributed to the fact that the bottle material exhibited strong fluorescence (ref spectrum F) and so fluorescence correction proved to be a better choice in such bottles.
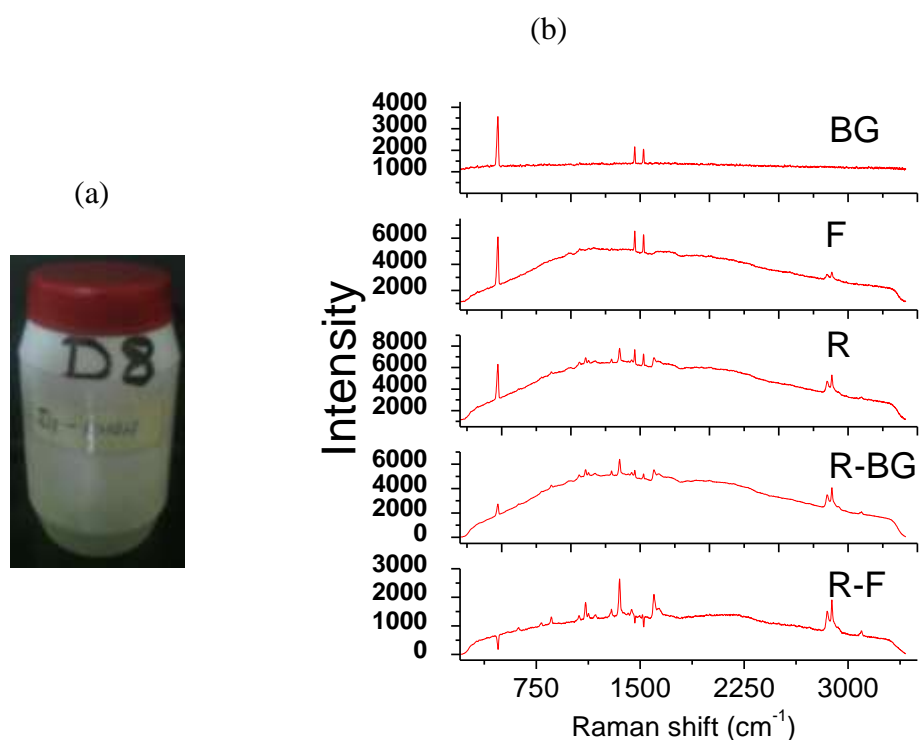
Figure-3.5. (a) PNBA filled in bottle (D8) and (b) the background recorded fluorescence & Raman spectrum of PNBA through bottle (D8) and processed Raman spectrum in terms of background and fluorescence.

iii.   Detection of PNBA in semi-transparent coloured bottle (A4):

The bottle (D1), from group D (table-3.1), was used. The material p-nitrobenzoic acid (PNBA) was filled in the bottle as content as shown in figure – 3.7 (a). The bottle has poor transparency around 10%. Background (BG), fluorescence (F) and Raman spectrum (R) of PNBA through the bottle were recorded and shown in figure – 3.7 (b). The Raman spectrum was also processed for background and fluorescence correction and shown as R-BG and R-F respectively and also shown in figure - 3.7 (b). The bottle exhibited very strong fluorescence (F) and the detector was saturated. Moreover, Raman peaks are not observable in Raman spectra (R) and it is attributed to the strong fluorescence exhibited by the bottle. Even Raman spectrum processed with background i.e. R-BG and with fluorescence i.e. R-F could not bring any difference. So it could be concluded that the processing methodology might be helpful only till the saturation did not occur.
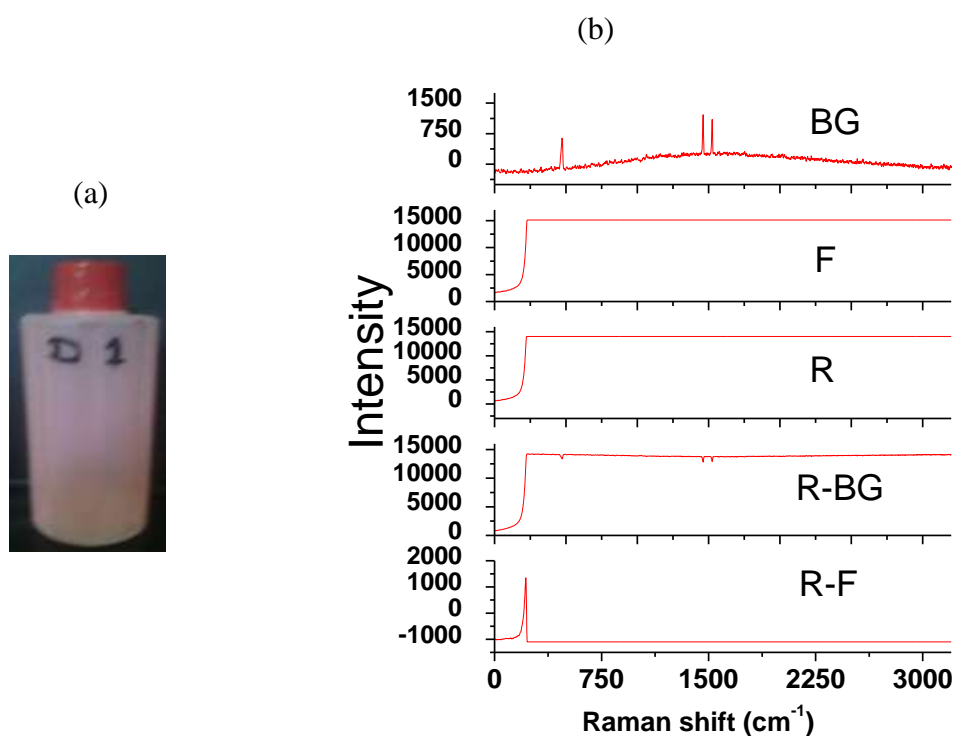
Figure-3.7. PNBA filled in bottle (D1) and (b) the background recorded fluorescence & Raman spectrum of PNBA through bottle (D1) and processed Raman spectrum in terms of background and fluorescence.

3.4   Conclusion

Soil samples of ammonium nitrate of different concentrations were studied. The effects of concentration and integration time on the intensity (or SNR) were studied. The improvement in the SNR of Raman peaks by processing Raman spectra by subtracting the background was also demonstrated. In addition, Raman spectra of material PNBA were recorded through plastic bottles of different materials in terms of transparency and colour. Raman spectra were processed by subtracting the background and fluorescence exhibited by the bottle materials. The processing of spectra improved the SNR of Raman peaks of the content material i.e. PNBA remarkably specially when the bottle exhibited appreciable fluorescence. However, the processing of Raman spectra did not provide any improvement in the situation of saturation in case of the strong fluorescence exhibited by the bottle.

CHAPTER 4

SIGNAL PROCESSING OF RAMAN SIGNATURES AND REAL-TIME IDENTIFICATION OF HAZARDOUS MOLECULES USING CONTINUOUS WAVELET TRANSFORMATION (CWT)

Implantation of bombs like IEDs by different terrorist groups all over the world has led to the development of reliable explosive detectors especially from a safe distance. Being a laser-based technique, Raman spectroscopy ensures a great deal in the field of developing such an explosive detector system. Though this technique ensures a fingerprint level discrimination of molecules, analysis of Raman signatures manually is time-consuming and cannot be afforded by security personal in a real scenario. So, automation of detection, acquisition and analysis of Raman signal is required for operations in a real scenario. In this work, we have developed software that caters to all these processes automatically and finally mentions the name of material under observation for stand-off detection. This is based on continuous wavelet transformation (CWT). This algorithm/ software is capable of identifications/ discrimination of very similar chemicals like trinitrobenzene (TNB), trinitrotoluene (TNT) and dinitrotoluene (DNT).
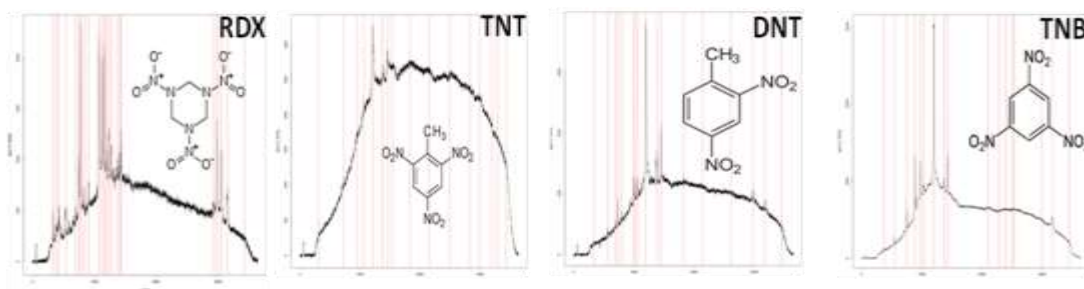
4.1   Introduction

In chapter 3, different types of real scenario samples like soil samples of explosive materials and explosive materials in plastic bottles were studied and different approaches of detection in terms of integration time, concentration, processing of Raman spectra with background and fluorescence were investigated. In the fieldable detection system, real-time acquisition and identification in automatic mode are one of the main requirements [51]. For this, the development of customized algorithms based on the field-specific methodology is of utmost importance. It also requires the development of a Graphical User Interface (GUI) ensuring ease of use of the detection system and should consist of all the parameters which have to be controlled during the acquisition and identification process [52, 53].

In this work, we have developed software that caters for all processes automatically and finally mentions the name of material under observation for stand-off detection. In the case of stand-off detection, the sample is not in closed-chamber so extra signal processing like background correction etc. is required. Software developed under this study is required to process Raman signals and based on continuous wavelet transform (CWT). This software is capable of identification/ discrimination of very similar chemicals like trinitrobenzene (TNB), trinitrotoluene (TNT) and dinitrotoluene (DNT).

4.2   Wavelet transform

Raman spectrum with adequate resolution gives unique signatures for various chemical compounds. Analysis and processing of these signatures help identification of various chemical compounds. Spectra peaks at various wavenumber for given spectrometer resolution are unique and can be considered fingerprints of that chemical. Thus peak detection is central to the algorithm for Raman spectroscopy based reliable chemical identification. Peak-width, peak-slopes, intensity, threshold, SNR, local maximum etc. could be different methodologies that may be used in the detection of peaks in Raman spectrum [54, 55]. Relative amplitude and intensity threshold-based algorithms are not very reliable for standoff detection due to fluctuation in spectra intensity and container effect and change in ambient conditions [56, 57].

The dimensionality of the functional signal is expanded in wavelet domain representation. Fourier domain representation deals with energy as a function of frequency for a one-dimensional time series [58] whereas wavelet domain representation facilitates the energy as a function of both scale and time axes.

Thus wavelet transform offers substantial advantages for analyzing nonlinear, transient responses and signals varying with time where the conventional approach of Fourier transform is not able to deal with reliable outcomes [59]. It provides a better result as it correlates the mother wavelet with pattern of Raman spectra for various scales and wave number positions. It localizes the peaks with wave numbers. Thus algorithm proposed uses CWT based ridge lines method and SNR reported in the literature.

4.3   Theory of Continuous wavelet transform (CWT)

Let x(t) be a continuous function then CWT of $x(t)$ may be given by the following integral considering a scale $a \in R$ and translational value $b \in R$

$$X_w(a,b) = \frac{1}{|a|} \int_{-\infty}^{\infty} x(t)\psi\left(\frac{t-b}{a}\right)dt$$

------------------- 4.1

where $\psi(t)$ represents a continuous function in both frequency domain and time domain and it is called mother wavelet. The main purpose of defining the mother wavelet is to have a source function to generate translated and scaled versions of the mother wavelet and simply called daughter wavelets. So CWT may be considered as the sum over all time of signal multiplied by scaled, shifted versions of wavelet function ψ [60, 61].

The wavelet transforms de-convolute signals and transform a continuous function into a highly redundant function. For analysis of Raman spectra, Mexican Hat wavelet was found the most suited mother wavelet [62] and can be expressed as follows:

$$\psi(x) = \left(\frac{2}{\sqrt{3}}\pi^{-1/4}\right)\left(1 - x^2\right)e^{-x^2/2}$$

--------------------------- 4.2

4.4   CWT based software developed for automated identification

CWT based peak detection method for analysis of Raman spectra computes CWT coefficients for various scales and wavenumber. CWT coefficients are associated with a local maximum around the peak centre at each scale. The local maximum increases with increasing CWT scale and attains its maximum when scaling corresponds exactly with peak width. To visualise CWT coefficients for various scales and wavenumber a ridge-like figure emerges resulting from graphs of 2D CWT coefficients obtained by considering their amplitudes as 3rd dimension. Peak detection is achieved by searching ridges through a 2D CWT coefficient matrix. Thus algorithm enabling peak detection algorithm may be considered consisting of the following three steps:

i.   computing 2D CWT for various scales

ii.   identifying ridges through 2D CWT coefficient matrix

iii.   identifying peaks based on ridges length threshold

In addition to CWT, analysis spectrum is preprocessed for background removal to nullify the effect of ambient conditions and translucent/transparent container for standoff detection of chemicals.

The algorithm is implemented on an atom-based Single board computer and code has been developed in QT on the Linux platform. GUI program controls the complete setup including spectrometer parameters, laser module, spectra data acquisition, background subtraction, peak identification, signature matching and thresholding. The complete process is automated and operates and logs data through a single button operation. Stand-off detection and identification from the sample at 30 cm takes about 10 sec.

4.4.1   Flow chart

The flow chart of the process for automatic identification of chemicals based on Raman signatures is depicted in figure-4.1. First, it checks interface communication with hardware like laser, spectrometer etc. If there is any lack of communication with

hardware it mentions the type of error. Then it takes background and then switches on the laser. Afterwards, Raman spectrum of the material under scan is acquired. Then it processes the Raman spectrum with the background. Finally, it matches the acquired spectrum with the database and mentions the name of the material in text, if the material under scan is in the database.
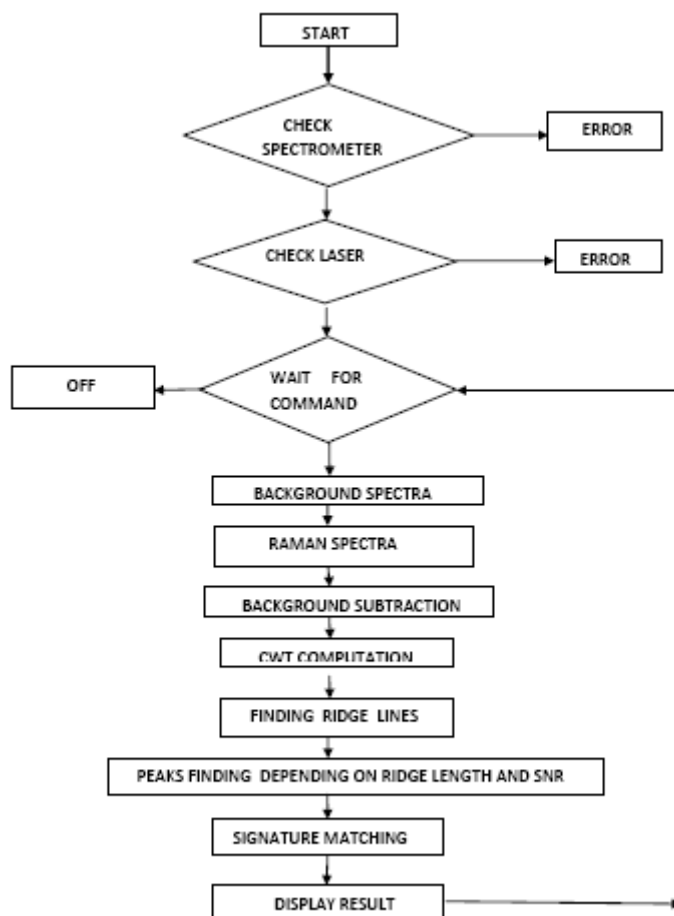
Figure-4.1: Flow chart of process for automatic identification of chemicals

4.4.2   GUI and parameter details

The Graphic User Interface (GUI) was developed as shown in figure – 4.2. It had all the parameters which had to be controlled in the process of acquiring and identifying the acquired spectra like integration time, laser ON-OFF option, data saving, library etc. After matching with database, the name of material was displayed along with the acquired spectrum.
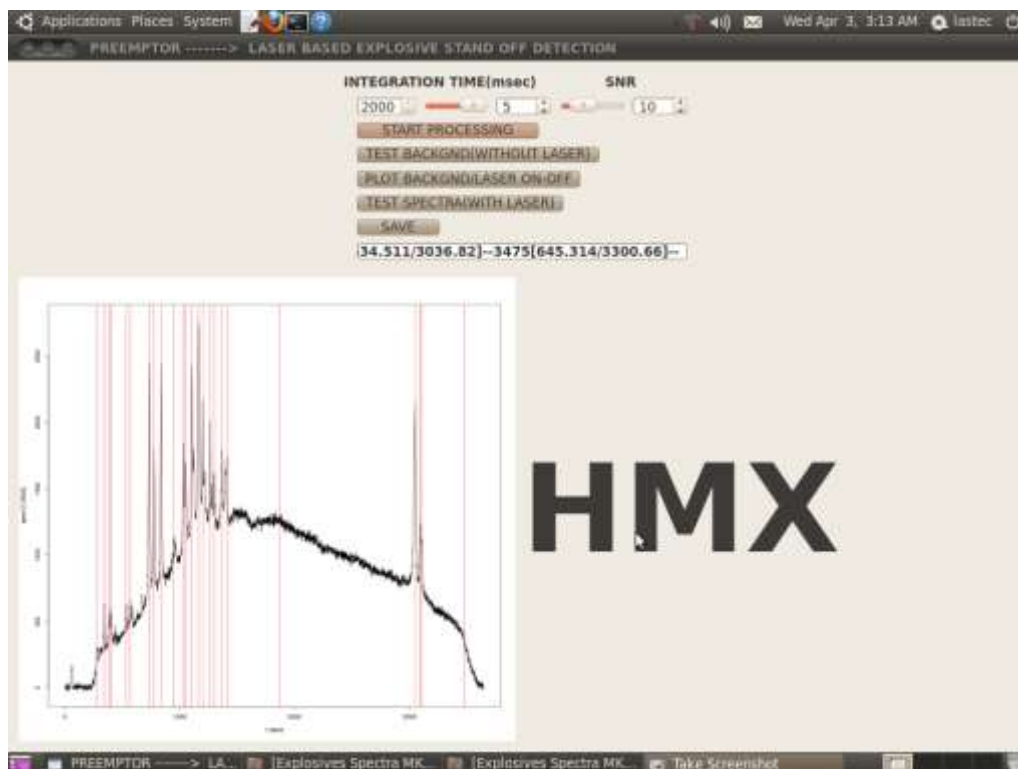
Figure-4.2: Graphic User Interface (GUI)

4.4.3   Identification of explosive materials

The capability of identification of the developed software was evaluated by identifying the very similar molecules. The materials with very similar chemical structures like DNT, TNT, TNB etc. were used in the evaluation of the identification potential of the developed software. These very similar molecules were successfully discriminated by the software. In addition, other materials like RDX, HMX, PETN, ammonium nitrate, Potassium nitrate, barium nitrate, sodium nitrate, urea nitrate etc. were used in the demonstration of the discrimination of very similar molecules. The snap shots of GUI showing the output result with Raman spectra in case of scanning of RDX, TNT, DNT and TNB are depicted in figure-4.3.
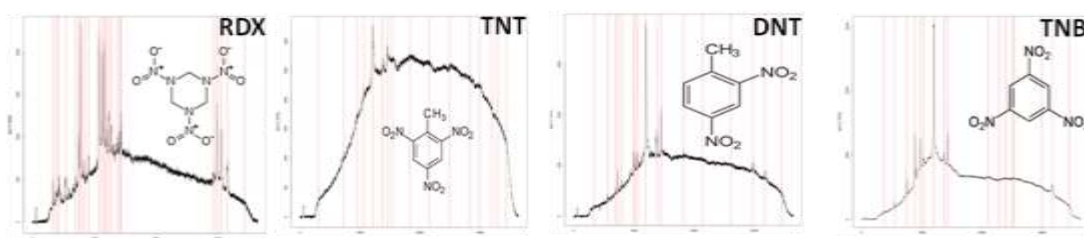
Figure-4.3: Snap shots of GUI showing the output result with Raman spectra in case of scanning of RDX, TNT, DNT and TNB

4.5   Conclusion

The continuous wavelet transform (CWT) based algorithm was developed using the Mexican Hat wavelet suitable for processing and picking peaks of Raman spectrum. The Graphical User Interface (GUI) was developed and parameters that were required to be controlled during the acquisition and identification process were incorporated in GUI. The output of the process is the name of material under scanning in text form if the material belongs to the database. Further discrimination capability of the software was demonstrated by identifying the very similar explosive materials. It resulted in a very low false alarm rate in the identification of explosive materials.

CHAPTER 5

STAND-OFF DETECTION OF EXPLOSIVES AND THEIR DERIVATIVES USING TIME-GATED RAMAN SPECTROSCOPY

Trace detection is of utmost importance for the detection of concealed explosive materials in form of IEDs. Surfaces of suspicious objects may be scanned for contamination of explosives. Sensitivity and selectivity are two main concerns in the field of explosive detection. Raman spectroscopy provides remarkable selectivity. Time-gated Raman spectroscopy also has the potential of providing sensitivity for trace detection. In the present study, time-gated Raman spectroscopy was investigated for the detection of ppm level concentration of explosives. To achieve better sensitivity, various parameters of the experimental set-up like gain of the intensifier, the number of pulses accumulated and pulse energy of laser were optimised. The trend of change in intensity of Raman scattering (background subtracted) was observed by varying values of these above-mentioned parameters. After optimising the parameters for better sensitivity, Raman spectra of RDX samples at lower concentrations (prepared by mixing RDX with KBr) were recorded. The corrected intensity increased linearly with an increase in gain of the intensifier, the number of pulses accumulated and pulse energy. After that, Raman spectra of RDX were recorded from a stand-off distance of 5m in backscattered mode with concentrations down to 100 ppm.
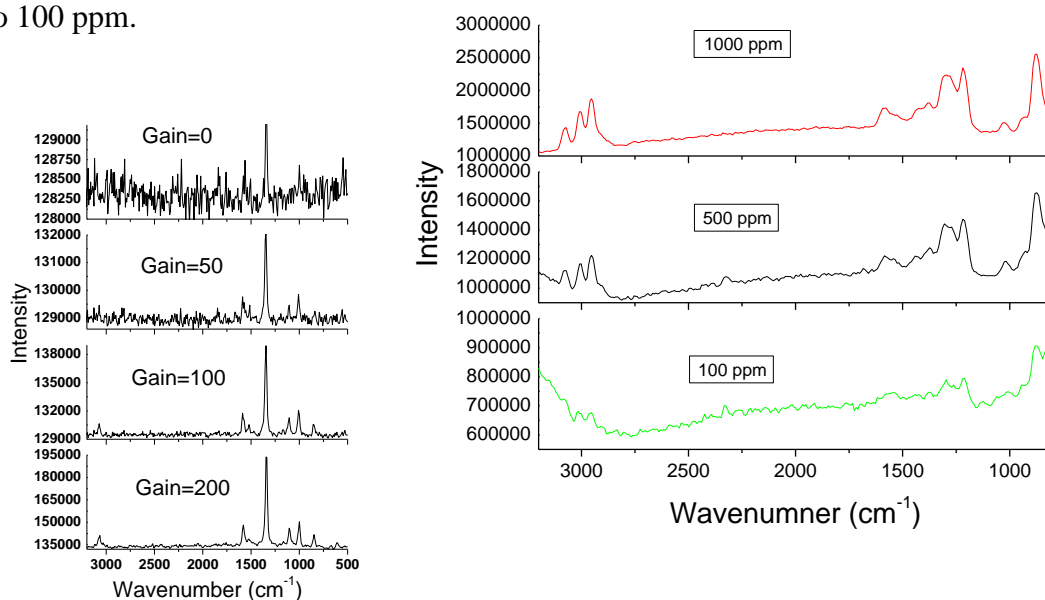
5.1   Introduction

In the detection of explosive materials including IEDs, the safety of the operator is one of the main concerns. It requires the development of stand-off detection methods for screening the area and interrogating the suspicious objects or materials from a safe distance. The safe area depends on the scenario and bomb type and so may vary from few meters to hundreds of meters [6]. Stand-off investigation of such explosive materials is one of the most unavoidable but greatest challenging tasks for researchers and engineers.

The detection at large distances involves physical difficulties like i. reduction of the intensity of the return signal with the distance and ii. Losses due to absorption & scattering in the air leading to significant compromise with sensitivity.

TGRS is a highly promising technique for detection of explosive materials from a large distance. It requires a pulse laser source and ICCD. ICCD is being synchronized with optical laser pulse with appropriate delay depending upon mainly stand-off distance [11, 20, 63].

In stand-off Raman spectroscopy, a pulsed laser source of nanosecond or shorter pulse is preferred as an excitation source as it provides high peak power (few MW). In addition, pulse laser enables gated-detection which in turn ensures the rejection of ambient light between consecutive laser pulses and collection of Raman photons (photons generated in inelastic scattering) only during the laser pulse. In this way, a high power pulse with gated detection results in a better signal-to-noise ratio (SNR). Raman photons are collected with receiving optics, and then coupled to dispersive spectrograph directly or using optical fiber. Intensified CCD coupled with spectrograph is used to detect and produce Raman spectrum of the sample under study. Dry sand samples having explosive concentrations of 4 – 8 % have been investigated using 532 nm as excitation laser wavelength [19]. Visibly excited stand-off detection may face fluorescence of samples and impurity. However, using pulse laser as excitation source and detection with gating ensures reduction of fluorescence and ambient light reasonably [64]. Random Raman lasing using 532 nm as excitation is being reported for stand-off explosive detection. The occurrence of Random Raman

laser depends on beam quality which is difficult to maintain at large stand-off distances [65].

Raman spectroscopy promises better sensitivity with visible wavelength as excitation compared to that in near-infrared range as the Raman scattering cross-section depends on wavelength in inverse fashion of its fourth power [30]. In literature, many research works in the field of stand-off detection of explosive materials using Raman spectroscopy in UV region have been reported [17, 66-70]. Though UV range excitation theoretically offers further better sensitivity, high energy UV photons exhibit potential risk of sample degradation and burning [30, 71-73]. The UV excitation which falls in absorption bands of explosives may cause photo-degradation and hence reduces concentration of the target molecules [66]. Explosives exhibit problems of sample burning remarkably due to their absorption in the deep UV range [71, 72]. Photo-degradation of sample with UV excitation may be reduced remarkably by following two methods: (a) either sample should be in motion like open-stream flow or magnetic stirring [70] so that point of interaction of laser with samples may be varied during investigating target material (not possible in real scenario) or (b) use of pulse energy of level of micro-joule (not sufficient for stand-off detection).UV excitation based methods do not promise the detection of explosives through normal transparent glass and plastic containers. Though UV excitation promises higher maximum energy permissible (MEP) for eye safety, it may generate other irreversible biological effects in operator body [73, 74]. Hence, UV excitation is not practical in a stand-off where high pulse energy has to be transmitted.

Despite several advancements in Raman spectroscopy that has been achieved in the area of explosive detection, however, Raman spectroscopy in the visible range remained to be investigated for trace detection of explosives. Trace detection targets surfaces of suspicious objects where contamination is probable like door handle of vehicles, handles of brief-case etc. The level of contamination may vary from a few ng/cm^2 to $\mu g/cm^2$ (i.e. ppm to ppb level) depending on the way of handling the explosives in making IED etc and the adhesive nature of explosives. In addition, the effect of various parameters of the set-up of time-gated Raman spectroscopy on the sensitivity remains to be explored. Here, the effect of various parameters like gain of

intensifier of intensified charge-coupled device (ICCD), number of pulses used in accumulation and pulse energy of laser on sensitivity was investigated thoroughly. After optimization of these parameters in terms of sensitivity, RDX was detected at lower concentrations. Raman spectra of 1,3,5-trinitroperhydro-1,3,5-triazine (RDX) was recorded in a stand-off with concentration level up to 100 ppm level using 532 nm as excitation wavelength.

5.2   Experimental procedure

In current study, 1,3,5-trinitrobenzene (TNB), p-nitro benzoic acid (PNBA) and 1,3,5-trinitroperhydro-1,3,5-triazine (RDX) were used. Samples of p-nitro benzoic acid and RDX were prepared by mixing with potassium bromide (KBr) at different ratios (w/w) in the form of pallets.1,3,5-trinitrobenzene was liquid sample and directly prayed on the aluminium sheet.

An experimental set-up used in the present study was developed according to the schematic depicted in Figure–5.1. This prototype mainly involves a pulse laser excitation source, ICCD-coupled spectrograph and compact receiving optics. A
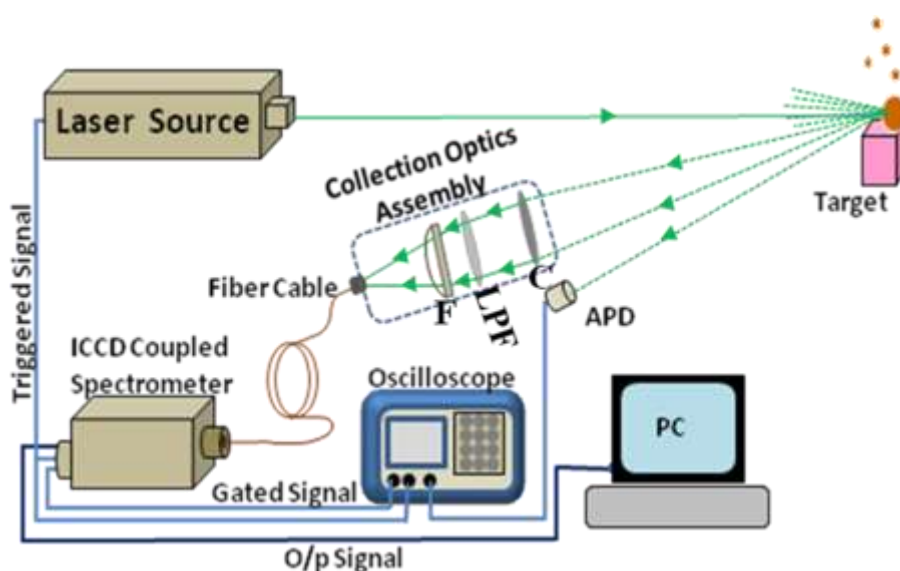
Figure–5.1: Schematic of ICCD based pulse Raman Stand-off detection system. C: Collimating optics, LPF: Longpass Filter, F: Focusing optics, ICCD: Intensified Charge Coupled Device, APD: Avalanche photodiode

Flashlamp-pumped Nd:YAG Pulse laser with 2nd harmonic (Make: Quantel, France, model: Brilliant) was used. It has maximum pulse energy of about 160 mJ at 532 nm, pulse duration of 6 ns and divergence of about 1mrad. It has a variable pulse repetition rate of 1-10 Hz. In these measurements, pulse repetition rate of 10 Hz was used.

The collection optics was very compact having a diameter of 1 inch and consisted of collimating optics (C), long-pass filter (LPF) and finally focusing optics (F). The revived backscattered Raman signal was collected and collimated with collimating optics (C). A long-pass filter (LPF) at 532 nm with a very steep transition width ~225 cm^{-1} and high optical density (O.D.) of the order of 6 (Make: Semrock, USA) was used to reject Rayleigh scattered photons. Finally focusing optics (F) was used to focus the remaining signal i.e. Raman signal at fiber-tip of an optical fiber bundle of core diameter of 200 μm (make: M/s ANDOR, USA & model: SR-OPT-8024. This bundle has 19 fibers arranged circularly at one end where Raman signal was focused, and linearly at the other end coupled to the spectrograph. The optical fiber bundle was used to couple the Raman signal to a spectrograph (Make: ANDOR, USA, model: SR303i) attached with the intensified charge-coupled Device (ICCD). The spectrograph has motorized entrance slit with a variable width varying from 10 μm - 2.5 mm. In present study, a silt width of 20 μm was used. This spectrograph has 303 mm focal length and f/4 aperture ratio. It consists of grating having 300 lines/mm blazed in the visible range having efficiency greater than 65 %. Its resulting spectral resolution is ~ 20 cm^{-1}.

Intensified charge-coupled device (ICCD) (make: ANDOR, USA and model: iStar 720-25-U) coupled with spectrograph (SR303) was used to record Raman spectra. The ICCD has a thermo-electrically cooling (TEC) mechanism and an array of 1024×256 pixels. The operational temperature of ICCD was set at -20 ^{0}C in these experiments. The ICCD may be gated 3 ns to 25 s with a resolution of 25 ps. Vertical binning was performed in the measurements. Its various parameters like intensifier gain, gate width, number of pulses to be accumulated were varied to observe their effects on intensity of Raman peaks. The present study was carried out in ambient conditions i.e. day-light conditions.

There are various sources of noise including solar noise, thermal noise of CCD and fluorescence of the samples as well as substrates. The samples like p-nitrobenzoic acid (PNBA), trinitrobenzene (TNB) and RDX mixed with KBr do not exhibit remarkable fluorescence. In addition, samples were prepared in form of pellets and hence no fluorescence from the substrate. Though the effect of other noise sources as mentioned above may be observed separately, the idea behind the current study was to simulate the experiment in the real scenario where all the noise sources may exist together.

Synchronizing of optical pulse with gate width

Matching the timings for optical pulse and gate width is one of the critical aspects in experiments of time-gated Raman spectroscopy. As Raman scattering takes place without any delay, the detector should be switched ON as soon as the optical pulse reaches the detector. But still, some delay has to be introduced to cater for the travelling time of incident photons from laser to sample and Raman photons from sample to detection end. The difference between the travelling time of photons from molecule to molecule or layer to layer (in order of sub ns) may be neglected as compared to longer laser pulses (6 ns) and gate widths ($\geq$ 10 ns) used in this work.

The triggering TTL signal of the laser system was fed to the ICCD detector. The laser pulse was detected using APD, which was kept near the receiver. The synchronization is achieved by monitoring gate output of ICCD and APD signal on an oscilloscope for accurate overlapping of both signals in the time-domain by inserting a proper delay. ICCD has an inbuilt electronic card that controls gate width, gate delay and gain of the intensifier of ICCD. These parameters may be varied by the user by inserting the required values in the software of ICCD.

5.3   Results and discussion

First, the experimental work was started using benzene and 1,3,5-trinitrobenzene (TNB) which have a common benzene ring with many explosives like 2,4,6-trinitrotoluene (TNT), 2,4-dinitrotoluene(DNT), 2,4,6-triamino-1,3,5-trinitrobenzene (TATB), picric acid, 2,4,6-trinitrophenylmethylnitroamine (commonly known as

tetryl) etc. [75, 76]. The effect of different parameters was studied by recording Raman spectra of RDX and PNBA from a distance of 5 m and for optimization of experimental set-up for better sensitivity. Finally, Raman spectra of low-concentration samples of RDX (diluted with KBr) with concentrations at 1000 ppm, 500 ppm and 100 ppm level in stand-off mode from 5 m using optimized experimental parameters. Table-5.1 shows peak assignments of the most intense peak of Raman spectra of TNB, PNBA and RDX.

Table-5.1: Assignment of the most intense peak of Raman spectra of TNB, PNBA & RDX

Molecule	Transition (most-intense)	Assignment	Intrinsic Raman scattering cross-section
TNB	1354 cm^{-1}	NO_2 symmetric stretching + NO_2i.p. deformation + CN stretching [77]	3.7×10^{-28} [78]
PNBA	1368 cm^{-1}	NO_2 symmetric stretching [79]	-----------
RDX	887 cm^{-1}	Ring-breathing mode [80, 81]	1.8×10^{-29} [82]

Raman scattering cross-section is wavelength-dependent e.g. it is 1.8×10^{-29}, 5.8×10^{-30} and 2.1×10^{-30} in case of 532 nm, 633 nm and 785 nm as excitation wavelength respectively for the peak at 887 cm^{-1} [82].

5.3.1   Gated-Raman signal and normal Raman signal

In the case of standoff detection, scattered Raman signal is accompanied by strong background noise available from other sources. This unwanted background noise can be solar or from any other light source near to targeted materials. Depending on conditions, this noise may be much strong and does not provide any information about targeted materials. Raman signal, having molecular information of targeted materials, may be easily obscured by this unwanted strong background noise. Gated detection opens the path to detect suspicious materials from stand-off distances in the daytime by reducing the effect of ambient light and fluorescence. This technique facilitates the recording of Raman spectra with enhanced SNR. Fluorescence rejection is also achieved at a reasonable level by gating detection due to their different time domains [17].

Gated-Raman spectroscopy where detector synchronized with a pulse laser was used in the current study and therefore weak Raman signal of 1,3,5-trinitrobenzene at low concentration ($\mu g/cm^2$) was measured from the stand-off distance of 5 m as shown in figure–5.2.
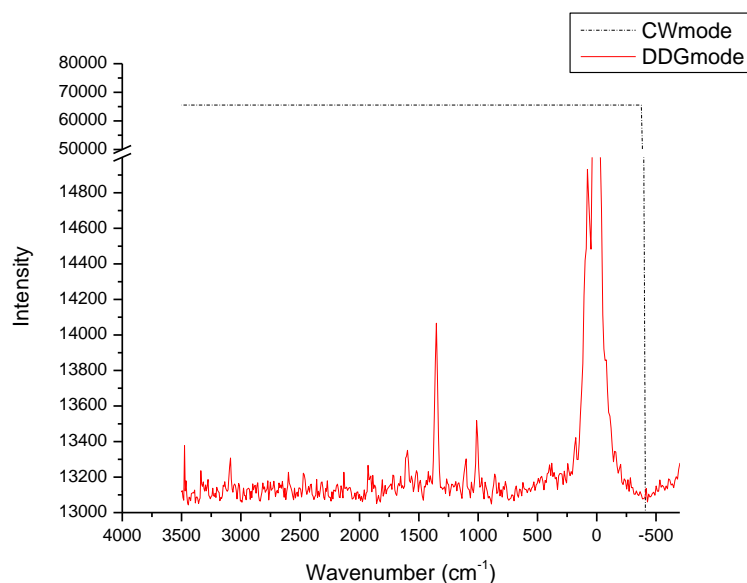
Figure–5.2. Raman spectra of 1, 3, 5 - trinitrobenzene at low concentration (100 μg/cm^2) were recorded using ICCD in CW mode and gate mode. Pulse energy of the laser, gain (G) of intensifier and gate width kept at 15 mJ, 100 and 20 ns respectively

Raman signal of 1,3,5-trinitrobenzene has recorded in stand-off backscattered mode from a distance of 5 m by using ICCD in CW mode as well as in synchronized mode. The aqueous sample of diluted concentration (100 mg of TNB in 1 litre of water) of 1,3,5-trinitrobenzene (TNB) was deposited uniformly on an aluminium sheet. The quantity of the chemical was approximately 100 $\mu g/cm^2$.   In the case of CW mode, intensifier of ICCD was kept continuously ON whereas it was synchronized with optical pulse of laser in synchronized mode. In both measurements pulse energy of laser, gain (G) of intensifier and gate width were kept at15 mJ, 100 and 20ns respectively. In CW mode, weak Raman signal (due to quantity at trace level ~ 100 $\mu g/cm^2$) was completely obscured by background noise which also gets amplified by intensifier continuously and hence molecular information cannot be extracted from scattered light collected at receiver (figure- 5.2). However, in synchronized mode, weak Raman signal easily detected and molecular information in terms of Raman stokes lines was observed as shown in figure- 5.2.

5.3.2 ICCD gain effect on Raman spectra

Photons entering an ICCD strike a photocathode plate where they are converted to electrons which are directed towards the micro-channel plate (MCP). At MCP, electrons are multiplied by applying a high voltage. Gain of the ICCD depends on this multiplication and hence the applied voltage to MCP. Therefore, by controlling the voltage at MCP, gain of ICCD can be controlled.

To analyze the effect of gain of intensifier on intensity of Raman scattering, Raman spectra of 1,3,5-trinitrobenzene was recorded from a distance of 5 m by varying the gain 0 to 200. The pulse energy of laser and gate width was kept at 15 mJ and 20 ns respectively. These Raman spectra were recorded with an accumulation of over 100 laser pulses.

Results of the study revealed a significant improvement in SNR of Raman peaks with an increased gain of intensifier as shown in figure-5.3.
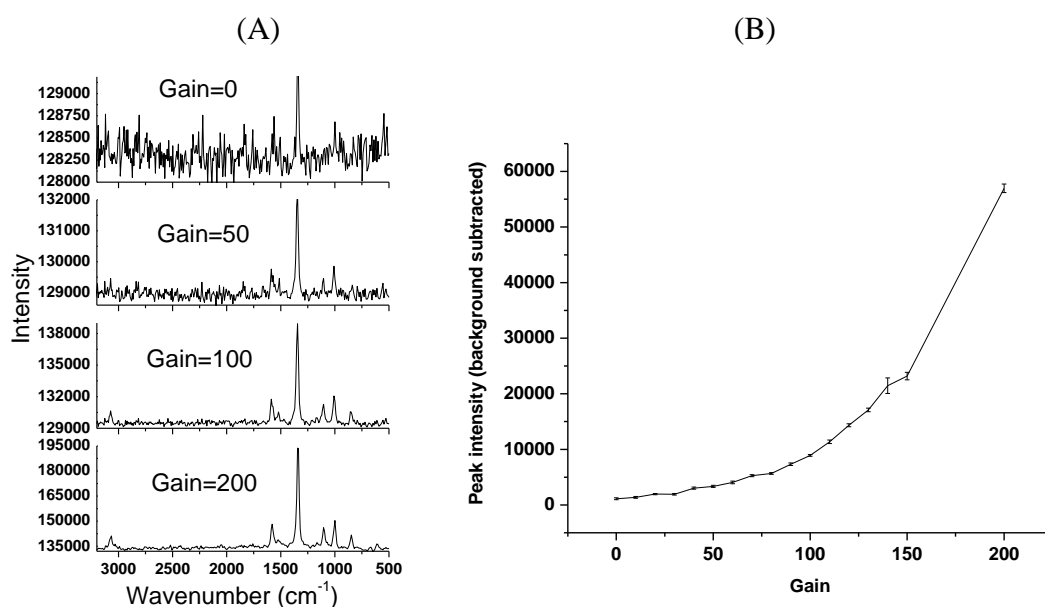
Figure-5.3: A: Raman spectra of 1, 3, 5 - trinitrobenzene recorded using gain of intensifier of ICCD detector at 0, 50, 100 and 200. In both measurements pulse energy of laser, gain (G) of intensifier and gate width were kept at 15 mJ, 100 and 20 ns respectively and B: Variation in peak intensity (background subtracted) of Raman peak at 1354 cm^{-1} w.r.t. gain of intensifier when gain value is varied 0 to 200. The error bars represent the standard deviation (SD) of the three-time measurement.

Raman spectra of 1,3,5-trinitrobenzene at gain of 0, 50, 100 and 200 are shown in Figure-5.3A.The improvement in SNR of Raman peak at 1354 cm^{-1} (corresponding to NO$_2$ symmetric stretching) can be easily visualized. In addition, due to an increase in sensitivity with increasing gain, less intense peaks e.g., peaks at 1007 cm^{-1} and 3076 cm^{-1} which did not exist with lower gain, start appearing in Raman spectra. It was observed that the intensity of Raman peak at 1354 cm^{-1} (NO$_2$ symmetric stretching) increased with an increase in gain as shown in figure-3B. The background-subtracted intensity of Raman scattering at 1354 cm^{-1} increased gradually with gain up to 80 and beyond it increased rapidly. The signal-to-noise ratio (SNR) of Raman peak at 1354 cm^{-1} was 30 and 85 in case of gain of intensifier at 50 and 200 respectively.

Raman signal and noise both go under the process of amplification. Raman signal appears in a phase-wise manner and keeps adding on during the accumulation of pulses. Whereas, noise is a random process and therefore can be averaged out when accumulated over several pulses and thus improved SNR was observed in the present study.

5.3.3 Pulse accumulation effect on Raman spectra

The effect of pulse accumulation was studied on Raman spectra by keeping pulse energy, gain (G) of intensifier and gate width at 30 mJ, 100 and 20 ns respectively. The test sample i.e. p-nitrobenzoic acid mixed with KBr at 1000 ppm (w/w) was in pellet form. Raman spectra of p-nitrobenzene were recorded from a distance of 5 m by accumulating a number of pulses in the range 10-2000. Raman spectra of p-nitrobenzoic acid mixed with KBr (at 1000 ppm) were recorded using the accumulation of 10, 100, 1000 and 2000 pulses in figure-5.4A. A significant increase in intensity of Raman signal was observed with increasing number of pulses accumulated. Experimental results indicated that less intense peaks i.e., 1368 cm^{-1} (corresponding to NO$_2$ symmetric stretching) that was almost invisible with 10 numbers of pulses started appearing at 100 numbers of pulses. Further, improvement in SNR of Raman peaks was observed visually as the pulses increased Figure-5.4B shows the trend of change in background-subtracted intensity of Raman peak at 1368 cm^{-1} with increase in accumulated pulse number.
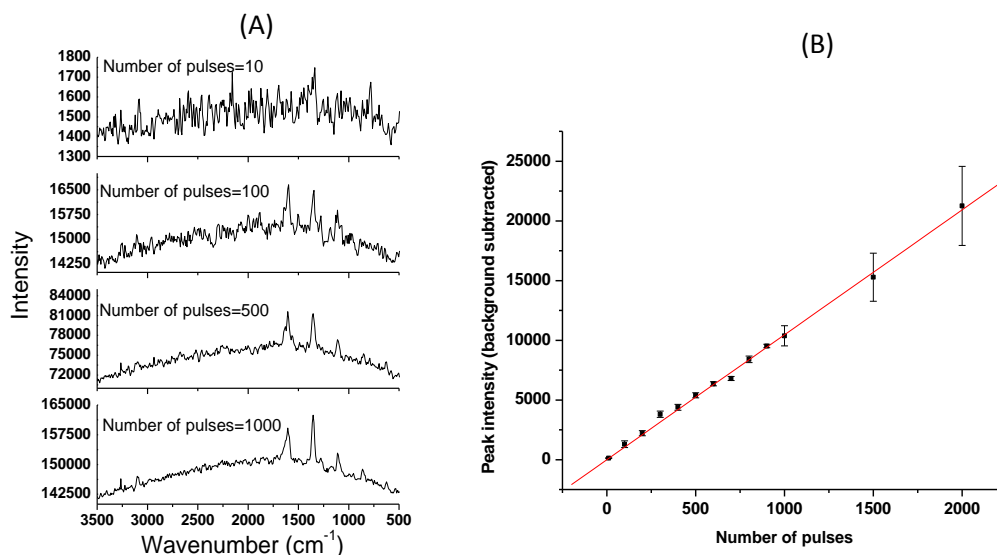
Figure-5.4 A: Raman spectra of p-nitrobenzoic acid recorded with accumulation of 10, 100, 1000 and 2000 pulses. Pulse energy of laser, gain (G) of intensifier and gate width at 30 mJ, 100 and 20 ns respectively and B: Variation of SNR of peak at 1368 cm^{-1} w.r.t. number of pulses accumulated. The error bars represent the standard deviation (SD) of the three-time measurement.

It was further observed that the intensity improves linearly with an increase in number of pulses accumulated. The signal-to-noise ratio (SNR) of Raman peak at 1368 cm^{-1} was 17 and 40 in case of number of pulses accumulated is 100 and 1000 respectively. These results reveal that better sensitivity is achievable by accumulating Raman spectra corresponding to more and more optical pulses of laser. However, at the same time, it is not possible to keep adding large number of pulses as this process is time-consuming. In real-time scenario, explosive detection and identification should be completed within a few seconds. This imposes a limit on the number of pulses to be accumulated. For example, it takes 100 s for the accumulation of 1000 pulses in case of a repetition rate of 10 Hz. The detection process can be made faster by using a laser of high repetition rate. However, it may induce thermal effects and damage the target material. So, there has to be a trade-off between number of pulses accumulated, detection-analysis time and pulse repetition rate.

5.3.4   *Pulse energy effect*

The pulse energy of the laser is one of the critical parameters which decide the maximum achievable sensitivity. The effect of pulse energy on the intensity of Raman peaks i.e., on sensitivity was carried out.
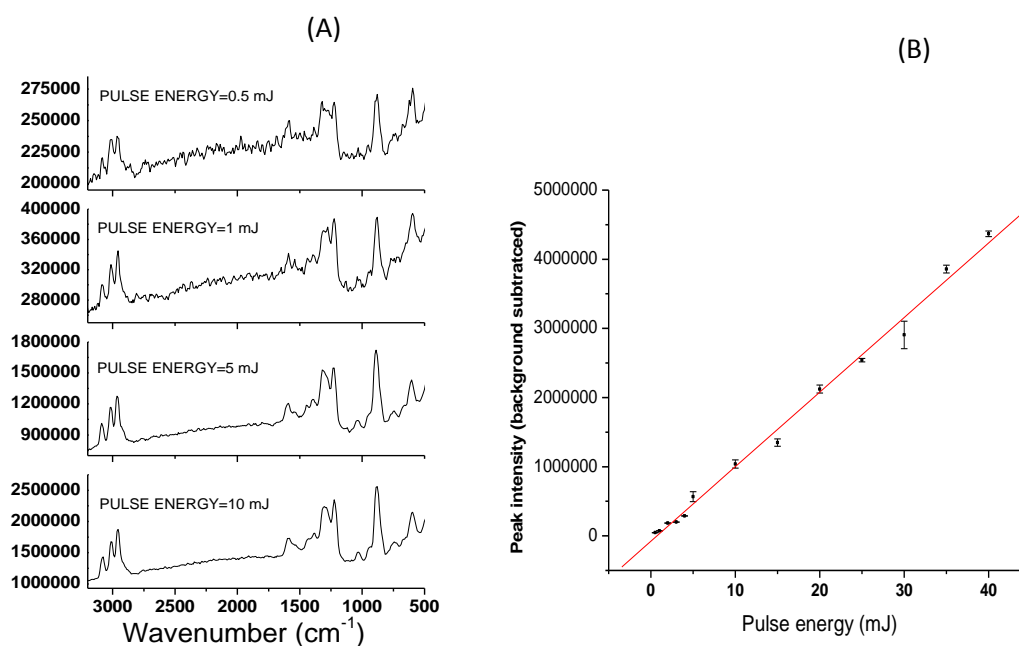
Figure-5.5. A: Raman spectra of RDX with pulse energy of 0.5 mJ, 1 mJ, 5 mJ and 10 mJ. Intensifier, gate width, pulses accumulated are kept at 100, 20 ns and 1000 respectively and B: Variation of SNR of peak at 887 cm⁻¹ w.r.t. pulse energy. The error bars represent the standard deviation (SD) of three-time measurement.

Gain of the intensifier, gate width and number of pulses accumulated were kept at 100, 20 ns and 1000 respectively. The sample was a pellet of RDX mixed with KBr at 1000 ppm (w/w). Figure-5.5A shows recorded Raman spectra of RDX mixed with KBr (at 1000 ppm) were recorded with pulse energy varying in the range 0.5-45 mJ. Raman spectra of RDX (at 1000 ppm) with pulse energy at 0.5 mJ, 1.0 mJ, 5.0 mJ and 10 mJ were shown in Figure-5.5A. Significant improvement in SNR of Raman peaks was easily observed when pulse energy increased. The background-subtracted intensity of Raman peak at 887cm^{-1} (ring stretching) was found to be increased linearly with an increase in pulse energy of laser as shown in fig. 5B. The signal-to-noise ratio (SNR) of Raman peak at 887 cm^{-1} was observed to be increases from 35 at a pulse energy of 1 mJ to 211 at a pulse energy of 10 mJ respectively.

5.3.5   *Raman spectra of explosives at ppm concentrations in stand-off mode*

The effects of experimental parameters like gain of intensifier; number of pulses used in accumulation and pulses energy on the sensitivity were studied. Raman spectra of

RDX mixed in KBr at concentrations 1000 ppm, 500 ppm and 100 ppm were recorded from a distance of 5 m as shown in figure-5.6. For achieving good sensitivity and recording of Raman spectra at these low concentrations, experimental parameters were set at optimized values. In recording these Raman spectra, a pulse energy of 20 mJ was used. The repetition rate and ICCD gain were set at 10 Hz and 200 respectively. The gate width of 100 ns was used and 1000 nos. of scans were accumulated. The pulse energy of 20 mJ was found sufficient for detection of RDX at a concentration of 100 ppm and hence higher pulse energy was not used. Raman spectra of RDX were successfully recorded at the lowest tested concentration level i.e. 100 ppm from distance of 5 m and shown in Figure-5.6. The intensity of Raman peaks decreased almost linearly as the concentration of sample came down from 1000 ppm to 500 ppm and then 100 ppm. Further, the limit of detection (LoD) was estimated using
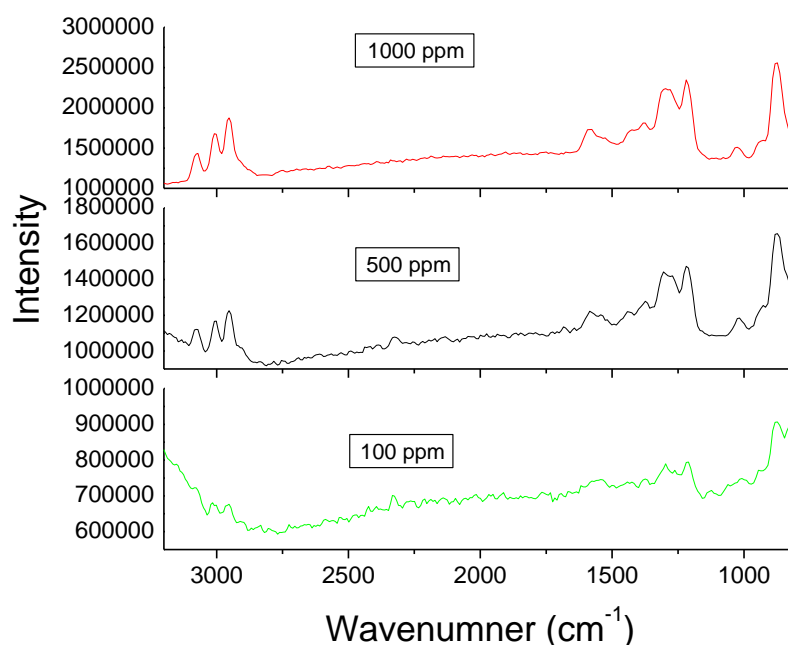
Figure-5.6. Raman spectra of RDX at concentrations 1000 ppm, 500 ppm and 100 ppm. Pulse energy of 20 mJ, repetition rate of 10Hz, ICCD gain at 200, gate width of 100 ns and accumulation of 1000 nos. of pulses.

Raman spectrum of RDX (peak at 887 cm^{-1}) of 100 ppm. In the estimation of the detection limit, the intensity has to be at least three times background in terms of the standard deviation (SD) [83]. The detection limit of RDX was estimated by estimating

background (standard deviation) and performing scaling factors. The detection limit was estimated at approximately 10 parts per million. As the background-subtracted Raman intensity is linear to pulse energy and number of pulses used in accumulations, the limit of detection reaches 1000 ppb using pulse energy of 100 mJ and accumulation of 2000 pulses.

5.4   Conclusion

The great potential of time-gated Raman spectroscopy was demonstrated in the field of trace detection of explosives in trace mode i.e. on contaminated surfaces. Different parameters i.e. repetition rate, pulse energy, intensifier gain and number of pulses on sensitivity were studied by observing their effect on Raman spectra recorded. Further, the experimental set-up was optimized by setting the values of different parameters to achieve sensitivity at lower concentrations in terms of intensifier gain, repetition rate, pulse energy as well as the number of pulses. Raman spectra of different explosives and their derivatives were recorded from a distance of 5 m. Raman spectra of RDX samples with different concentrations down to 100 ppm was recorded with optimised experimental set-up and limit of detection estimated at 10 ppm. The investigations carried out here provides an in-depth understanding of optimized values of different experimental parameters of TGRD set-up and envisages the design of compact and portable time-gated Raman spectroscopy-based explosive trace detector.

CHAPTER 6

DETECTION OF EXPLOSIVE MATERIALS AND THEIR PRECURSORS THROUGH TRANSLUCENT COMMERCIAL BOTTLES USING SPATIALLY OFFSET RAMAN SPECTROSCOPY USING EXCITATION WAVELENGTH IN VISIBLE RANGE

The detection and analysis of hazardous materials through opaque barriers is important for law-enforcement agencies. Conventional Raman spectroscopy provides fingerprint signatures of materials but lacks the ability to detect materials through opaque containers. Spatially offset Raman spectroscopy (SORS) overcomes the limitation of conventional Raman spectroscopy and allows the detection of materials through most commercial bottles and packaging materials. Moreover, SORS has the potential to detect hazardous materials through coloured glass bottles, high-density polyethylene (HDPE) bottles, Teflon layers, etc., which is required in the screening of commercial packaging at airports and other vital facilities. In the present study, SORS was investigated in the visible range with a 532nm excitation source for the detection of urea and sodium nitrate through commercial packaging, i.e.a white HDPE bottle with a thickness of 1 mm. The effects of the spatial offset and integration time on the Raman spectra of the content and container were evaluated. The trend of the change in the relative contributions from the content and container was studied by varying the offset and integration time. p-nitrobenzoic acid (PNBA) was detected through the coloured bottles in the study of reduction of fluorescence in SORS effect.
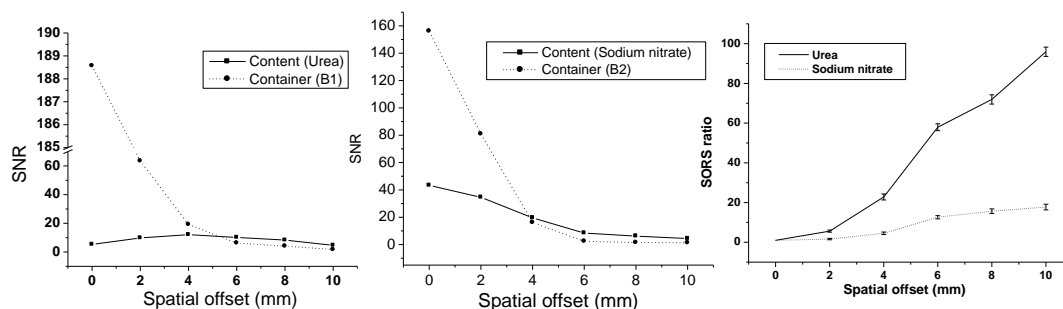
6.1 Introduction

Conventional Raman spectroscopy (RS) has been deeply investigated for bulk quantities, as it provides unique signatures of the target molecule, but has limitations for the detection of explosives through opaque containers [28, 30]. In the real scenario of screening of materials at airports, railway stations, and other checkpoints, materials must be detected through different types of containers and packages, such as coloured glass, transparent plastic bottles, high-density polyethylene (HDPE) bottles, and tetra packing. SORS offers a solution for investigating the explosive materials through most nonmetallic containers, such as coloured glass bottles, HDPE bottles, and teflon layers [84-89]. SORS involves collecting Raman scattered light from spatially offset illumination points, as depicted in Figure 1.
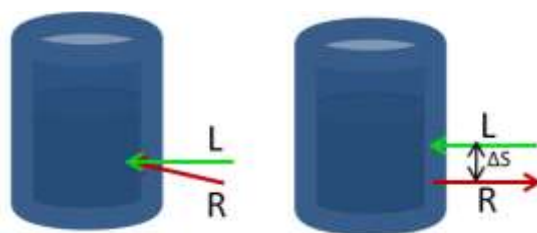
Figure-6.1: Geometrical configurations. Left: Conventional back-scattering Raman; Right: Spatially offset Raman spectroscopy (SORS)

The majority of photons in an excitation beam undergo multiple-Rayleigh scattering in the probed medium such as random walk, and produce Raman scattered photons which further travel in a random fashion [87]. Thus, a Raman scattering signal may be collected at a particular offset distance from the illuminating point, and the intensity of the Raman signal of the content and container depends on the offset distance. The spatial offset facilitates in reduction of collecting Raman and fluorescence signals from the container [90-98] which otherwise interfere with the signal originating from content. These interfering signals from the container are found to be the strongest at the illuminating point and decrease with an increasing offset of illuminating and collection points [24, 25].

The SORS technique has been investigated in the near-infrared region using different excitation wavelengths, e.g. 785 nm [25, 95-97], 830 nm [24, 84, 88, 90, 93, 94, 98], and 1064 nm [99, 100]. Though studies with excitation in the ultraviolet (UV) range were also reported for explosive detection [70-72, 101], no SORS study reported with UV

excitation, being low transmission of UV wavelengths through glass containers, translucent containers etc. [102]. The excitation wavelength of 532 nm in the visible region has also been employed for long-range standoff SORS using expensive pulsed lasers and intensified charge-coupled device (ICCD) detectors for depth profiling of target samples, which is important for medical applications [103-105]. However, detection using 532 nm as the excitation wavelength with a CCD has not been extensively investigated in SORS studies, to the best of our knowledge, and is avoided in conventional Raman spectroscopy owing to a fluorescence problem [106]. For small ranges, CW laser could be used with CCD without any appreciable effect of ambient light [107].

Commercial bottles, particularly those made of HDPE, exhibit no fluorescence or weak fluorescence, and in addition, explosives inherently exhibit hardly any fluorescence [108, 109] though different fluorescence-based techniques like Photodissociation-cum-Laser Induced Fluorescence technique [83], Amplified Fluorescence Polymers-based technique [110] etc. were reported for detection of explosive materials. Therefore, SORS may offer better sensitivity with excitation in the visible region compared with the near-infrared region, owing to the inversely proportional relationship of the Raman cross-section with the fourth power of the wavelength [28, 30] and the high quantum efficiency of CCD detectors in the visible region [111].

In the present study, we developed a standoff SORS spectroscopy system capable of detecting a variety of hazardous materials through commercial containers (i.e., an HDPE bottle) with an excitation wavelength of 532 nm using a continuous-wave (CW) laser and a CCD detector. The effects of the integration time and spatial offset on the Raman spectra of urea and sodium nitrate, which were recorded through a bottle, were examined. The intensities (background-subtracted) of the Raman spectra of the content (urea and sodium nitrate) and container were plotted with respect to the offset. The SORS ratio was also calculated and plotted for different offset values. The intensity of the peaks for both the content and container decreased with an increase in the offset. The photon diffusion in the container was smaller than that in the content owing to the large volume of the interaction of the content; therefore, the Raman signal decreased quickly in the case of the container. The effects of the diffusion

characteristics of the content materials on the SORS ratio were also investigated. Further, the variation of the peak intensity with respect to the integration time was examined while keeping the offset constant. PNBA was investigated through the coloured containers in carrying study fluorescence reduction in SORS.

6.2 Experimental procedure

A schematic of the SORS-based experimental setup is depicted in Figure-6.2(a). The setup included a CW laser, a CCD-coupled spectrometer, trans-receiver (TR) optics, a mirror, and filters. The laser was a commercially available CW 532nm 2nd-harmonic Nd:YAG laser (SDL-532-LN-400T, M/s Shanghai Dream Lasers Technology, China,) with variable optical power in range of 0–400 mW. Optical power of 150 mW was used for the experiments. The TR optics had a 70mm diameter. A long-pass filter (LPF, M/s Semrock, USA) was used to filter out the Rayleigh scattering at a 532nm wavelength.
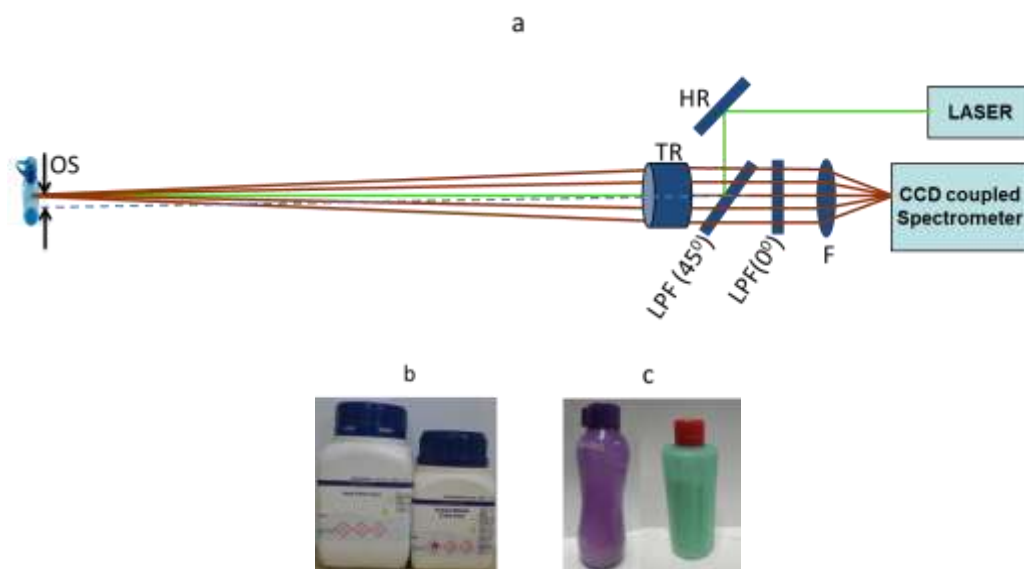
Figure-6.2: (a) Schematic of SORS-based experimental setup for stand-off detection through translucent containers. HR: High reflecting mirror with AOI=450, LPF (450): Longpass filter with AOI=450, TR: Trans-receiver optics, LPF (00): Longpass filter with AOI=00, F: Focusing optics, OS: Offset inserted. (b) Commercial bottles containing sample material urea (B1) and sodium nitrate (B2) (c) violet coloured bottle (C1) and green coloured bottle (C2) used for experiments of fluorescence reduction by SORS effect

The laser beam was guided to the sample container by a high reflective (HR) mirror, the LPF with an angle of incidence of 45°, and the TR optics. The backscattered

Raman signal was collected and collimated using the TR optics. The collimated beam comprised a Rayleigh-scattered optical signal (532 nm) and a Raman-scattered optical signal (>532 nm). The Rayleigh signal was filtered out by LPFs. The desired optical signal, i.e., the Raman scattered signal, was coupled to a spectrometer (HR4000, Ocean Optics, USA) by using focusing optics. The required offset between the laser beam and the receiving axis could be inserted by using the tilting mechanism in the mount of the HR mirror. The experiments were conducted in the standoff mode at a distance of 30 cm. SORS studies were performed on two content materials—urea and sodium nitrate (Loba Chemie Pvt. Ltd., India)—using their respective commercial containers (~1 mm thick HDPE bottles), as shown in Figure 6.2(b)). In addition, p-nitrobenzoic acid (PNBA) (Sigma Aldrich) was used in the study of fluorescence reduction by SORS effect.

6.3   Results and discussion

The standoff detection of the content materials was performed at a distance of 30 cm. The optical power of the laser was kept at 150 mW. The integration time and spatial offset used for recording the Raman spectra were varied, as described herein. Urea was used in this study because it is a precursor of explosive materials such as urea nitrate. Sodium nitrate was employed because it can be mixed with potassium nitrate to produce explosive materials [112]. First, the Raman spectra of pure urea and sodium nitrate were recorded, as shown in Figure-6.3.
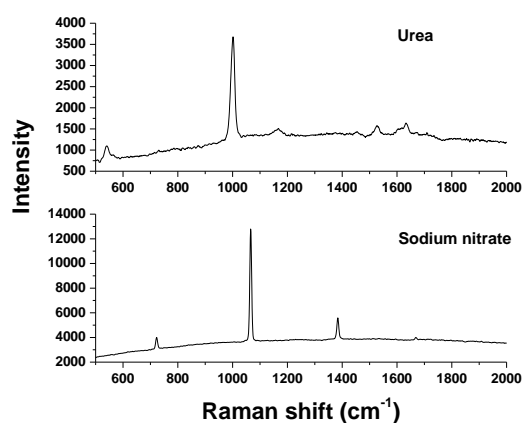
Figure-6.3: Raman spectra of pure urea and sodium nitrate recorded at integration times of 10 s and 2 s, respectively.

The potential of the SORS technique for detecting the materials through translucent containers was demonstrated. The effects of integration time and spatial offset on the Raman signatures recorded through the container were examined. Background-subtracted intensities of the most intense Raman peaks of content materials (1011 cm^{-1} and 1068 cm^{-1} for urea and sodium nitrate, respectively) and the container (peak at 2890 cm^{-1}) were plotted with respect to the spatial offset and integration time for both materials. Depending on the diffusion characteristics of urea and sodium nitrate, different trends were observed in the variation of the intensity with respect to the offset.

6.3.1   Spatially Offset Raman Spectroscopy Effect

The capability of SORS of detecting explosive materials confined in plastic containers was investigated, as shown in Figure 6.4.
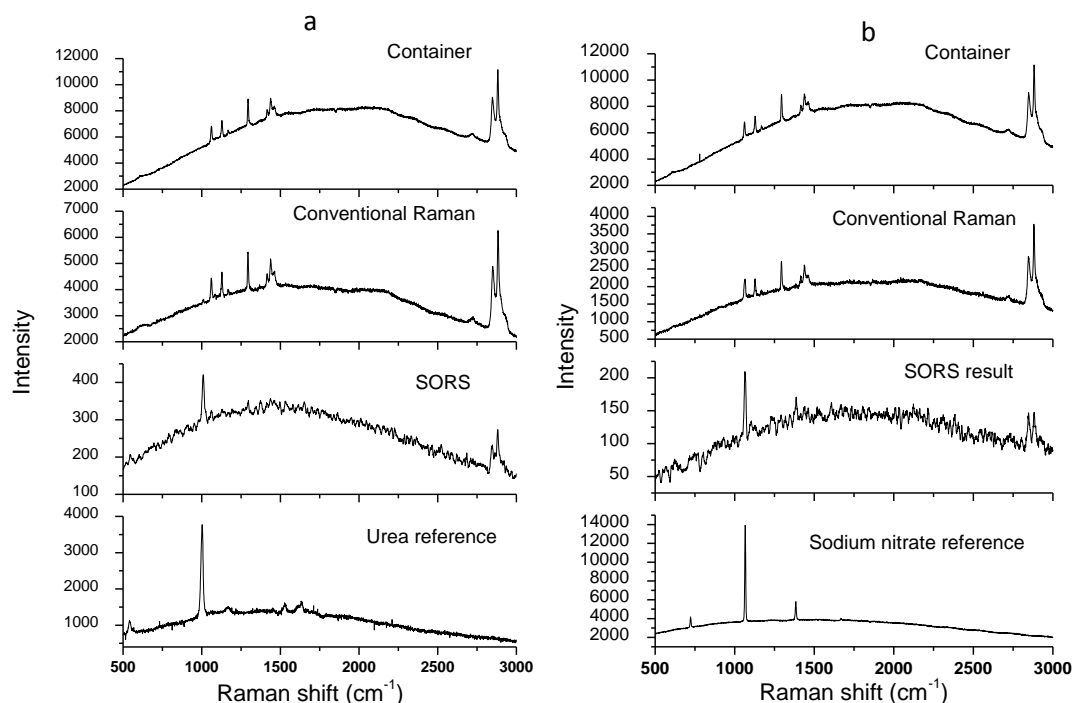
Figure-6.4: Conventional Raman and SORS spectra of (a) urea and (b) sodium nitrate in HDPE white bottles (B1 & B2) whereas the top and bottom show reference spectra of the container and pure (a) urea and (b) sodium nitrate, respectively.

Reference Raman spectra of the plastic containers and the content materials (urea and sodium nitrate) are shown at the top and bottom in Figures-6.4(a) and 6.4(b)

respectively. Both the reference spectra were recorded in the standoff mode with a distance of 30 cm and an integration time of 2 s. The Raman spectra of the content materials were recorded through the container in two modes: conventional Raman spectroscopy (laser incident spot and collection spot coinciding) and SORS (spatial offset of 6 mm between laser incident spot and collection point). The spectra recorded using conventional Raman spectroscopy were dominated by the Raman signatures of the container, and the signatures of the content materials were suppressed and not observable. In contrast, the Raman spectra recorded in the SORS mode exhibited the Raman signatures of urea and sodium nitrate, as shown in Figure 6.4. Thus, SORS facilitated the recording of the weak Raman signatures of the content materials by subtracting the strong Raman signatures of the containers.

6.3.2   Effect of Spatial Offset

The effect of spatial offset on Raman signatures of the content materials, i.e., urea and sodium nitrate, recorded through plastic containers (both containers had the same parameters), was examined, as shown in Figures-6.5 and 6.6, respectively. The Raman spectra were recorded while varying the spatial offset from 0 to 10 mm in steps of 2 mm for both content materials. The standoff distance and integration time were kept at 30 cm and 4 s, respectively. These spectra comprised the Raman signatures of the content materials and the container. However, their relative contributions changed with respect to the spatial offset. At zero spatial offset, the Raman signatures of the content were almost obscured by those of the container. As the spatial offset increased, all the Raman peaks of the container decreased significantly faster than those of the content materials, as shown in Figures-6.5(a) and 6.6(a). This was because of the diffusion of both excitation photons and Raman scattered photons in the content material, e.g., random walk, along the diffusion path [106]. Consequently, the interaction volume of the excitation photons and the distribution of "produced Raman photons" in the lateral direction in the content material increased, which was not the case for the container. Figures-6.5(b) and 6.6(b) show the trend of the change in the normalized intensity (background-subtracted) of the most intense Raman peaks of the content materials, i.e., the peak at 1011 cm^{-1}for urea and 1068 cm^{-1} for the sodium nitrate and container (2890 cm^{-1}), with an increase

in the spatial offset.
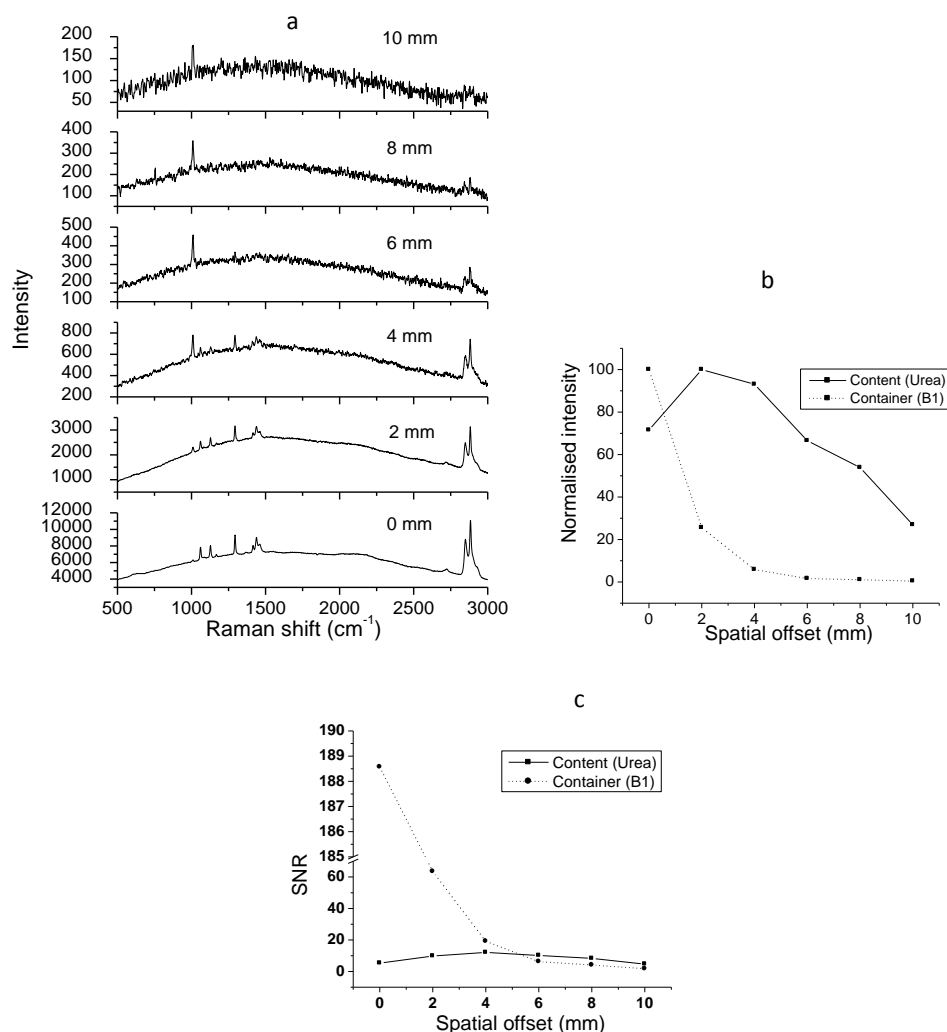
Figure-6.5: (a) SORS spectra of urea recorded through the plastic container in stand-off mode at different values of spatial offset. Spatial offset varied 0 to 10 mm in steps of 2 mm. Stand-off distance kept at 30 cm and integration at 4 s (b) The background-corrected intensity of Raman peaks of urea at 1011 cm^{-1} and container at 2890 cm^{-1} plotted w.r.t. spatial offset C. (c) The intensity of both bands normalised (maximum set to 100%) and plotted w.r.t. spatial offset.

The signal-to-noise ratios (SNRs) of the most intense peaks of urea and sodium nitrate were plotted with respect to the spatial offset, as shown in Figures-6.5(c) and 6.6(c), respectively. The plots of the normalized intensity revealed trends of the change in intensity of the Raman peaks of content and container. The SNR plots also indicated the sensitivity of the experimental setup for the Raman signatures of the content and container. The SNRs of the Raman peaks of the content were lower than that of the

container at zero offset. With an increase in the offset, this trend of the SNR of the Raman peaks for the content and container was reversed; i.e., the SNR was higher for the contents than for the container with an offset of > 4 mm (for sodium nitrate) and > 5 mm (for urea). The difference between the SNRs of the Raman peaks of the contents and container increased up to an offset of 10 mm and then started decreasing. The SNR of the Raman peaks was calculated by subtracting the baseline from peak intensity and then diving noise level in the flat portion of spectra.
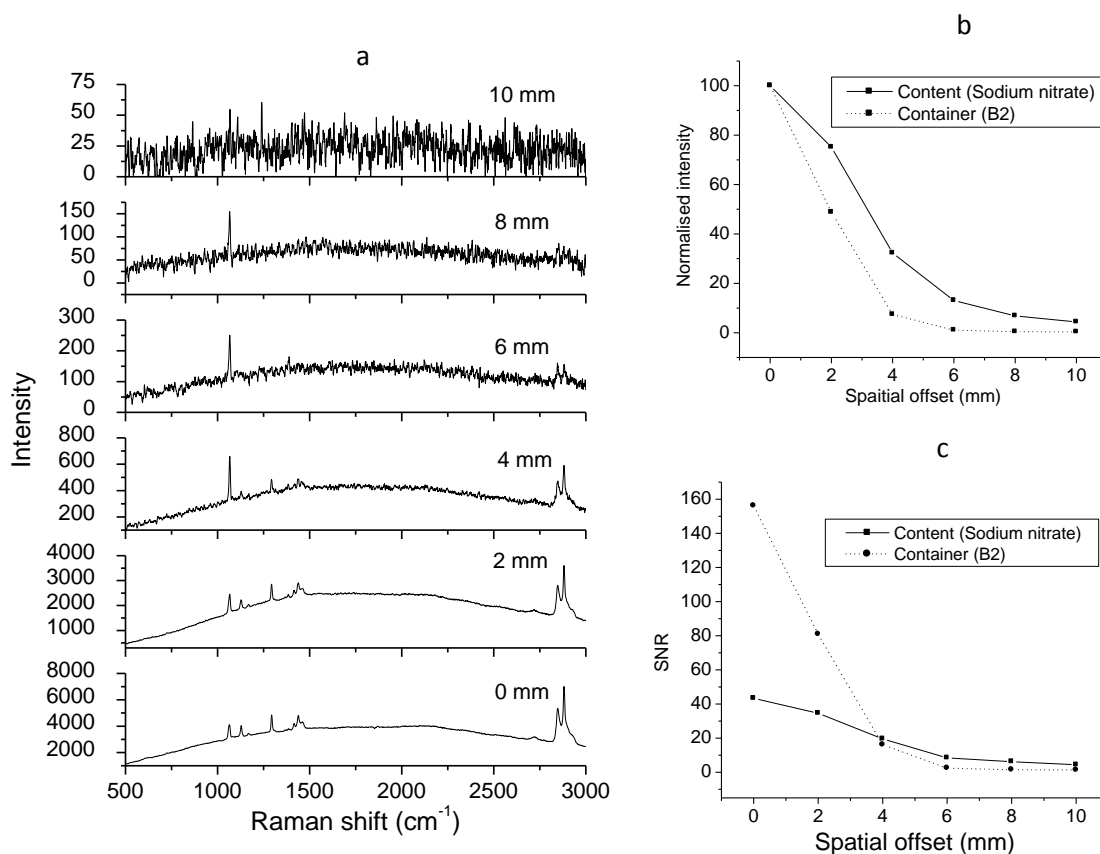
Figure-6.6: (a) SORS spectra of sodium nitrate recorded through plastic container in stand-off mode at different values of spatial offset. Spatial offset varied 0 to 10 mm in steps of 2 mm. Stand-off distance kept at 30 cm and integration at 4 s (b) The background-corrected intensity of Raman peaks of urea at 1068 cm^{-1} and container at 2890 cm^{-1} plotted w.r.t. spatial offset C. (c) The intensity of both bands normalised (maximum set to 100%) and plotted w.r.t. spatial offset.

6.3.3   *Diffusion-Dependent Trend in Intensity Variation with Respect to Spatial Offset*

The variations in the normalized intensities of the most intense Raman peaks of urea (at 1011cm^{-1}) and the container (at 2890 cm^{-1}), as well as sodium nitrate (at 1068 cm^{-}

[1]) and container (at 2890 cm^{-1}), were plotted w.r.t. the spatial offset, as shown in Figures-5(b) and 6(b), respectively. Intensities of the peaks of the content materials and container were normalized by setting the maximum intensity to 100%. The trend of the change in the intensity (normalized) was depicted for both content materials. There was a difference between the trends of the change in intensity with respect to the spatial offset for the two content materials. Intensity of the Raman peak of urea first increased and then decreased (Figure-5(b)) as spatial offset increased, whereas the intensity of the Raman peak of sodium nitrate only decreased (Figure-6(b)). The different trends of the variation in intensity were due to the different photon-diffusion efficiencies of the urea and sodium nitrate. The Raman peak intensity for urea initially increased owing to its higher diffusion efficiency. The intensity of the Raman peak of the container decreased continuously with an increase in the spatial offset. As the thickness of the container was significantly smaller than that of the content, the diffusion mainly occurred in the content, with no appreciable diffusion due to the container wall [113]. Thus, the intensity of the Raman peaks of the container decreased sharply with the increasing spatial offset.

6.3.4   Spatially Offset Raman Spectroscopy Ratio

The SORS ratio indicated the relative rate of decay of the intensities of Raman peaks of the content and container. It is defined as the ratio of the intensity of Raman peak of the content at a particular spatial offset(s) to that of the container at the same spatial offset(s) divided by the intensity ratio of the content to the container at zero spatial offsets [113] and is given by the following equation:

$$SORS\ ratio\ (s) = \frac{I_{content}\ (s)/I_{container}\ (s)}{I_{content}\ (0)/I_{container}\ (0)} \qquad \text{------------------------- 6.1}$$

Here, $I_{content}(s)$ and $I_{container}(s)$ are the Raman signal intensities of the content and container, respectively, at the spatial offset s, and $I_{content}(0)$ and $I_{container}(0)$ are those at zero offset.

The equation of SORS ratio shows that SORS ratio is dependent on the intensities of both content and container materials. The intensity of Raman peaks of the container

will again depend on its material and thickness mainly. Here we have used different content materials i.e. urea and sodium nitrate in the same type of container i.e. HDPE bottles. In calculations of the SORS ratio, the intensities (background-subtracted) of the Raman peaks of urea, sodium nitrate, and the containers at 1011 cm^{-1}, 1068 cm^{-1}, and 2890 cm^{-1}, respectively, were used. The SORS ratio was calculated for different values of the spatial offset in the range of 0–10 mm, with increments of 2 mm. The calculated SORS ratios were plotted w.r.t. the spatial offset, as shown in Figure-6.7.

With increasing spatial offset, the SORS ratio initially (up to 2 mm) increased slowly and subsequently increased almost linearly. At small spatial offsets, the diffusion was mainly due to the container; therefore, the relative contribution of the
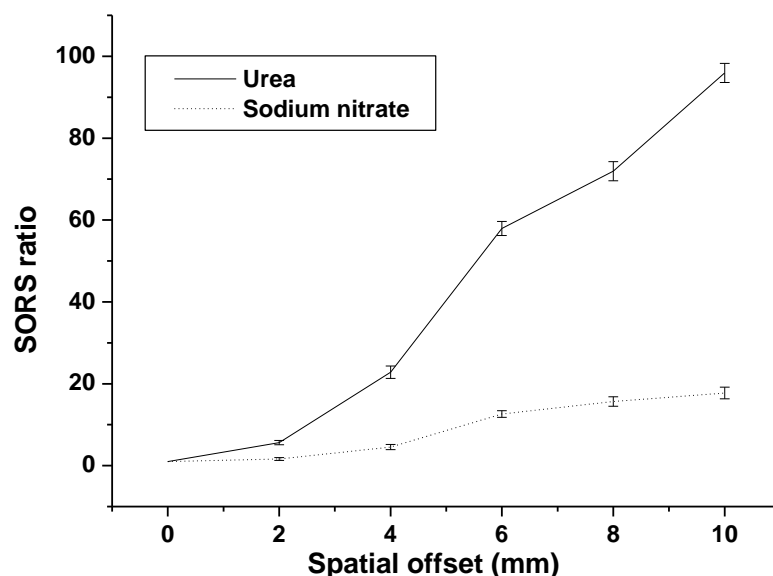
Figure-6.7: SORS ratio w.r.t spatial offset. SORS ratio calculated using the background-corrected intensity of Raman peaks of urea at 1011 cm^{-1}, sodium nitrate at 1068 cm^{-1} and container at 2890 cm^{-1}.

Raman signal from the content increased slowly with the increasing spatial offset. The SORS ratio increased at a higher rate for urea than for sodium nitrate. This is attributed to the higher diffusion efficiency of urea, which resulted in a slower intensity decay of the Raman peaks of urea compared with those of sodium nitrate. The slow increase in the SORS ratio with the increasing spatial offset was attributed to the thickness of the container [114].

6.3.5 Effect of Integration Time

The effect of integration time (i.e., time during which the Raman signal was acquired) on the Raman spectra of the content materials, i.e., urea and sodium nitrate, was examined in the range of 2–10 s with steps of 2 s, as depicted in Figures-6.8(a) and 6.9(a), respectively. The standoff distance and spatial offset were kept at 30 cm and 6 mm, respectively. The Raman peaks of the content materials were relatively strong compared with those of the container at spatial offset of 6 mm.
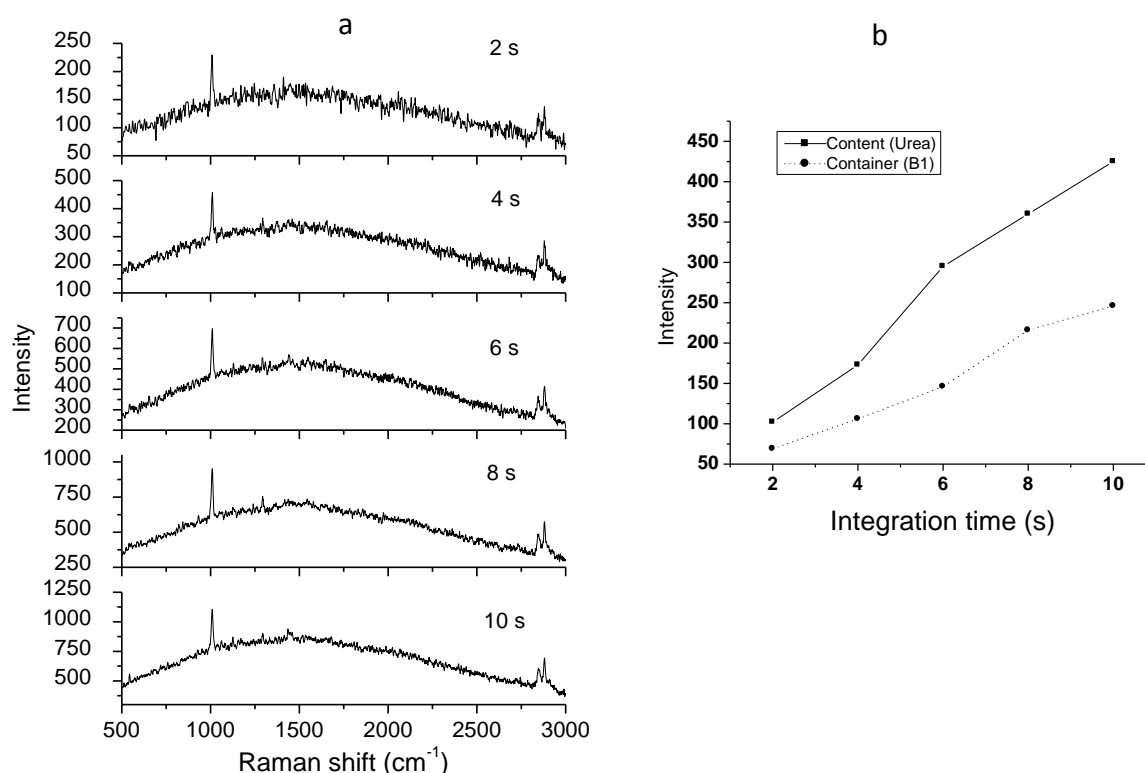
Figure-6.8: (a) SORS spectra of urea recorded through plastic container in stand-off mode at different integration times. Integration time varied 2 to 10 s in steps of 2 s. Stand-off distance kept at 30 cm and spatial offset at 6 mm (b). The background-corrected intensity of Raman peaks of urea at 1011 cm^{-1} and container at 2890 cm^{-1} plotted w.r.t. integration time spatial offset.

These spectra included Raman signatures of both the content and container. However, their relative contributions did not change as the integration time was varied; rather, the relative contributions were dependent on the spatial offset. The trends of the change in intensity (background-corrected) for the most intense Raman peaks of the content materials (at 1011 cm^{-1} for urea and 1068 cm^{-1} for sodium nitrate) and the container (2890 cm^{-1}) with an increase in the integration time are shown in Figures-

6.8(b) and 6.9(b). The intensities of the Raman signals of the content materials and container increased almost linearly with respect to the integration time.
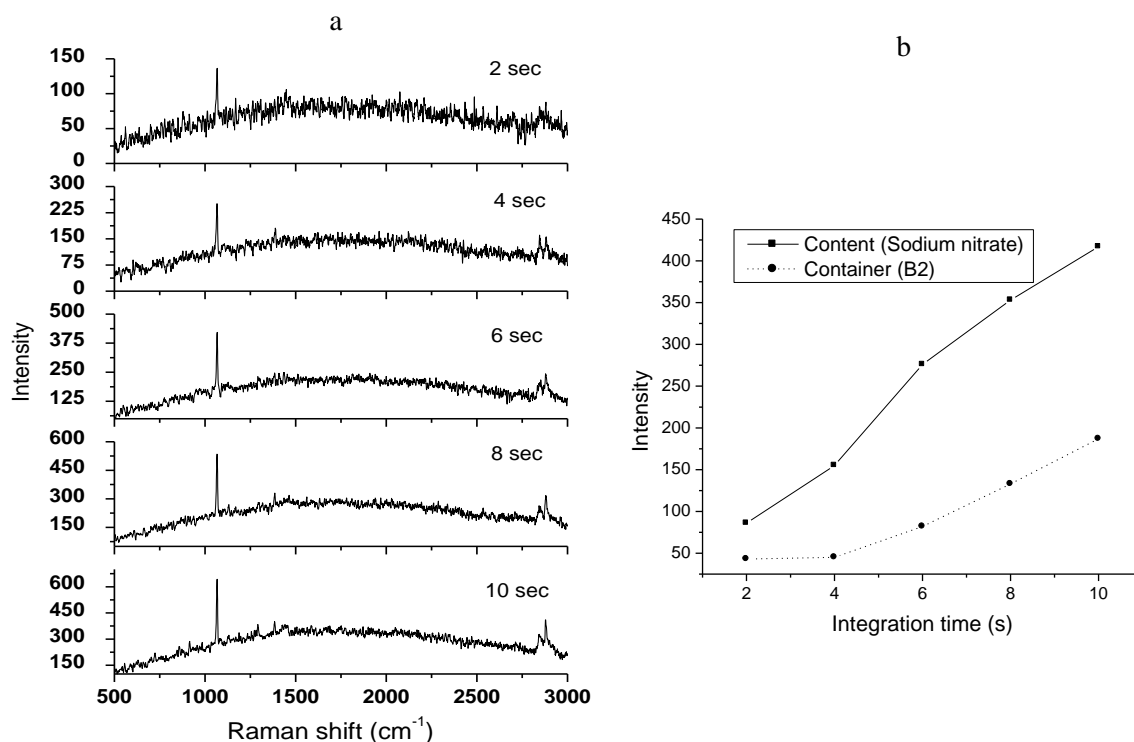
Figure-6.9 (a) SORS spectra of sodium nitrate recorded through plastic container in stand-off mode at different integration times. Integration time varied 2 to 10 s in steps of 2 s. Stand-off distance kept at 30 cm and spatial offset at 6 mm (b) the background-corrected intensity of Raman peaks of urea at 1068 cm^{-1} and container at 2890 cm^{-1} plotted w.r.t. integration time spatial offset.

At a large spatial offset, i.e., 6 mm, the Raman signal intensity of the content was not appreciable with a short integration time, i.e., 2 s, although it was higher than that of the container. Therefore, the spatial offset and integration time must be carefully optimized to achieve the desired result, and these parameters are related [115]. The optimized values of both parameters depend on the nature of the content and container.

6.3.6   Fluorescence Reduction by SORS

Being SORS is a potential technique of detecting explosives through translucent containers, it has to be explored for fluorescence reduction causing by the coloured containers as the explosive materials themselves do not exhibit the fluorescence. The coloured containers are used to exhibit the fluorescence in the case of conventional

74

Raman spectroscopy. The NIR excitation surely helps in the reduction of fluorescence in conventional Raman spectroscopy but at the cost of sensitivity [111].

Here the fluorescence reduction is explored with SORS technique even with excitation in the visible range (532 nm). In this study, conventional Raman spectra and SORS spectra of PNBA contained in two coloured bottles i.e. violet bottle (C1) and green bottle (C2) were recorded as shown in figure-6.10 (a) and 6.10 (b) respectively.
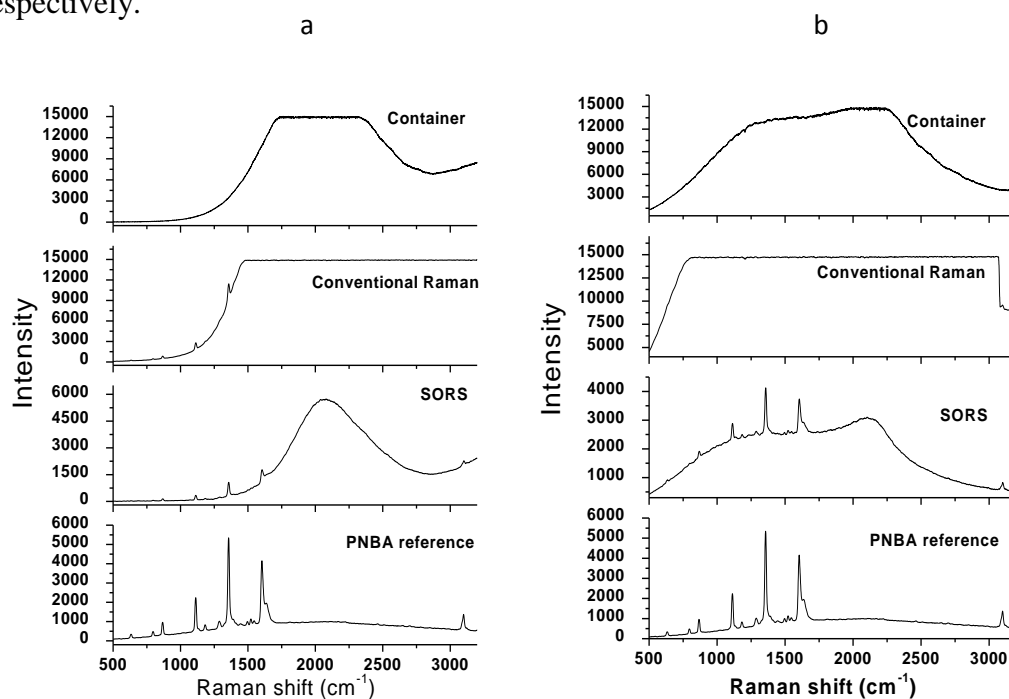
Figure-6.10: Conventional Raman and SORS spectra of PNBA in (a) violet colored bottle (C1) and (b) green coloured bottle (C2) whereas the top and bottom show reference spectra of container and pure PNBA respectively. SORS spectra of PNBA were recorded at offset of 10 mm and integration time of 6 s and 10 s in bottles C1 and C2 respectively.

In addition, reference Raman spectra of PNBA and both the coloured bottles were also recorded. Both the bottles (C1 and C2) exhibited intense fluorescence as could be observed in the spectra at the top of figures 10(a) and 10 (b). It could also be observed that the conventional Raman spectra recorded through both bottles C1 and C2 exhibited fluorescence too intense to observe the Raman lines of the content i.e. PNBA. The CCD of the spectrometer got saturated due to the high strength of fluorescence of the container and produced a flat portion in spectra due to the blooming effect of CCD [116]. Raman peaks of PNBA were obscured by the strong fluorescence. After inserting an offset of 10

mm, SORS spectra of PNBA were recorded through these fluorescent bottles i.e. C1 and C2 using an integration time of 6 s and 10 s respectively. SORS spectra exhibited an appreciable reduction in the fluorescence and all the intense Raman peaks could be observed. SORS spectra recorded by inserting the offset were generated from the depth of the content i.e. PNBA rather than from the container i.e. coloured fluorescent bottles C1 and C2 as the case with the conventional Raman spectra and hence exhibited the drastic decrease in the fluorescence. So it was exhibited that SORS itself could play the role in the reduction of fluorescence of containers even with excitation in the visible range and hence without compromising the sensitivity.

6.4   Conclusions

The potential of SORS technique was demonstrated for detecting explosives concealed in plastic commercial packages such as HDPE bottles and coloured bottles. The contribution of the Raman signatures of the content relative to that of the container increased with the spatial offset. This was confirmed by the variation in the SNRs of the Raman peaks of the content materials and the container. The SNR of the content materials improved over that of the container as the spatial offset increased. At a large spatial offset (~10 mm), the SNRs of the Raman peaks of the content approached those of the container. The changes in relative contributions of Raman signals of the content and container (and hence the SORS ratio) with an increase in the spatial offset were elucidated. For the first time, we experimentally investigated the effect of the diffusion efficiency of the content on the trend of the variation in intensity with respect to the spatial offset. The capability of SORS technique in the reduction of fluorescence was demonstrated by recording the Raman signatures of content material i.e. PNBA through coloured bottles in presence of strong fluorescence signal from the coloured bottles. This study gives fare idea about the potential of SORS techniques in the visible range and contributes towards the development of an effective SORS system for the detection of explosives concealed in plastic packages with excitation in the visible range and hence with reasonable better sensitivity.

CHAPTER 7

COMPUTATION OF VIBRATIONAL AND THERMAL CHARACTERISTICS WITH THEIR INTERPRETATION OF [3,4-(METHYLENEDIOXY) PHENYL]-2-METHYLAMINOPROPANE (MDMA)

Geometry optimization of MDMA was performed using DFT and HF methods with different basis sets. Mulliken charge and MEP were studied for negative and positive sites of the molecule. Molecular orbital characteristics like HOMO-LUMO energies, energy gap, ionization potential, electron affinity, global hardness, chemical potential were investigated. Thermal properties like SCF, zero-point energy, rotational constants, dipole moments were estimated. Enthalpy, specific heat and entropy were investigated in terms of temperature effect in the range 50 K – 700 K. Vibrational analysis was performed on optimized geometries of MDMA with different levels of theory. The vibrational frequencies were scaled and found in an excellent match with experimental values.

7.1 Introduction

Illicit drugs are common to be used for recreational ecstasy throughout the world [117]. MDMA is one of the main constituents in tablets sold for recreational ecstasy [118-121] and belongs to class of amphetamine compounds [122]. MDMA is also famous as a "club drug" due to its use in raves. However, it is also consumed at routine house parties with friends [123].

Its routine use causes different health issues including a reduction in memorisation, mental disturbance, mood swing, anxiety, sleep issues, abnormal body weight and tremors or twitches [124-127]. In addition, MDMA increases blood pressure, heart-pumping rate, and myocardial oxygen level [128, 129]. It was found that doses greater than 180 mg of MDMA caused only adverse health responses [124].

The sensitive, selective and real-time identification of illicit drugs is utmost required by the concerned agencies [130] to counter the challenges posed by the modern and organised crime era. Using vibrational spectroscopic techniques, different drugs can be easily identified even in presence of interfering material due to the fingerprint nature of the vibrational spectrum. Optical techniques, particularly Raman spectroscopy, have been reported in the literature for qualitative and quantitative analyses of illegal drugs [16, 131-133].

Experimentally spectral characteristics of MDMA have been well investigated using Raman spectroscopy [131, 134, 135]. In addition, theoretical studies have also been carried out on MDMA molecule [136-138]. Zapata-Torres, G et al. (2008) [138] investigated MDMA conformal structures whereas Z F Ebrahimi et al. (2016) [136] carried out estimation of molecular parameters like QCC, NQR, CSA etc. using HF method. Nuno Milhazes et al. (2007) [137] investigated theoretically the synthesis pathway of MDMA and its precursors. In addition, geometric optimization and frequency calculation of these molecules were performed using methods RHF/6-31G (d,p), B3LYP/6-31G(d,p) and B3LYP/ cc-pVDZ.

In the work reported here, the extensive theoretical studies of MDMA on estimation of molecular structure, spectral and thermal characteristics were performed. The structural optimization and estimation of vibrational frequencies were carried out

using methods HF and DFT. The basis set 6-31G(d,p) was used in HF method and 6-31G(d,p), 6-311G++(d,p) and cc-pVDZ along with DFT/ B3LYP. The calculated scaled values of vibrational frequencies were compared with that of vibrational spectrum recorded experimentally and also with theoretical values reported in literature [131, 134, 135, 137]. The values calculated with method B3LYP/ 6-311G++(d,p) were in better agreement with experimental values in comparision to the studies reported by Nuno Milhazes et al. (2007) [137]. Further, the thermodynamic properties like thermal energy, ZPV energy, enthalpy, specific heat capacity, entropy, rotational constants, and dipole moment of MDMA molecule were estimated. In addition, electronic structure of MDMA was also studied.

7.2   Quantum mechanical calculations

Quantum mechanical calculations have been carried out using HF method with 6-31G(d,p) basis set and DFT with 6-31G(d,p), 6-311++G(d,p) and cc-pVDZ basis sets on Gaussian 09 program. The calculations of vibrational frequencies were carried on the optimized structures with methods mentioned. True minimum of potential energy surface was obtained as no imaginary frequency mode appeared. The calculated values were scaled by 0.89 for HF/6-31G(d,p), 0.9668 for B3LYP/6-31G(d,p), 0.983 (for the range of wavenumbers up to 1700 cm^{-1}) & 0.958 (for above 1700 cm^{-1}) for B3LYP/6-311G++(d,p) [139] and 0.9721for B3LYP/cc-pVDZ [140]. The values of calculated frequencies, after scaling, were found in good match (10 cm^{-1}) with experimental values. The peak assignment of Raman spectrum was carried out based on the corresponding Total Energy Distribution (TEDs).

7.3   Results and discussion

7.3.1 Optimised molecular geometry

The optimised molecular geometry using B3LYP method with base set 6-311G++(d,p) and the scheme of numbering the atoms of MDMA is shown in figure-7.1. MDMA has nine C-C bonds, fourteen C-H bonds, four C-O bonds, two C-N bonds and one N-H bond.

The molecular structure of MDMA was optimized using HF method with 6-31G(d,p) and DFT with 6-31G(d,p), 6-311++G(d,p) and cc-pVDZ. The optimized bond lengths and bond angles estimated by various methods were summarized in Table-7.1. The relaxation of all parameters in calculation was used to ensure achieving of true energy minima as an indicator of optimized geometries and revealed by no imaginary frequency calculated.
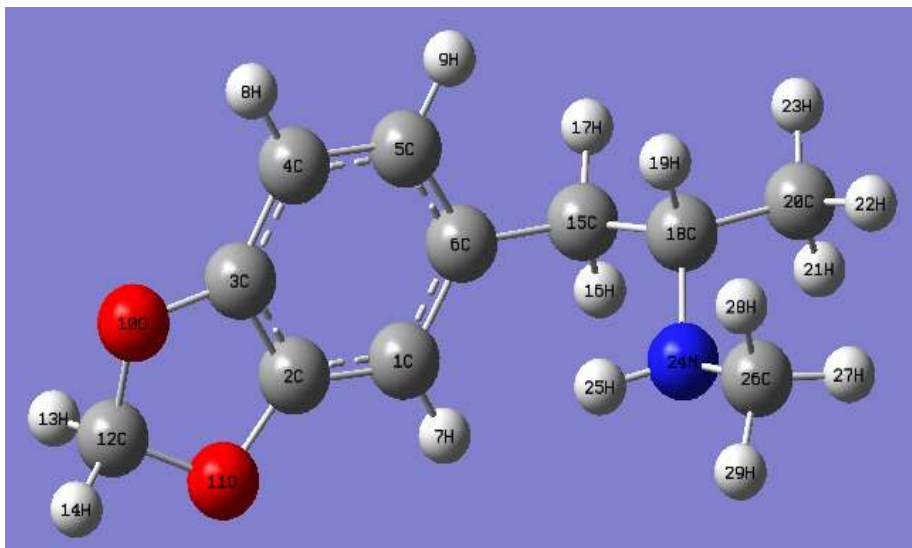
Figure-7.1: Optimised molecular structure of MDMA using B3LYP method with base set 6-311G++(d,p).

The comparison of estimated values of bond length and bond angles with experimental values reported in the literature [141]. The values estimated using B3LYP/6-311G++(d,p) are found in an excellent match. The values calculated using HF/6-31G(d,p) were found towards lower side whereas using B3LYP/6-31G(d,p) & cc-pVDZ towards higher side. The theoretical values of bond-length and bond-angles of MDMA have been already reported in literature [135] and included in table-1. When compared with experimental values, it could be easily observed that the estimated values in the present study clearly matched more precisely than reported values in literature.

Table-7.1: Optimized parameters of MDMA structure

	HF	B3LYP			Theoretical values (B3LYP; 6-31G+) [136]	Experimental values [141]
	6-31G (d,p)	6-31G (d,p)	6-311G ++(d,p)	cc-pVDZ		
Bond lengths (Å)						
C12H13	1.08501	1.09988	1.09773	1.10816		
C12H14	1.07981	1.09394	1.08904	1.10073		
C12O10	1.40765	1.43204	1.43226	1.43165	1.407	1.430
C12O11	1.40851	1.43252	1.43317	1.43221	1.408	1.429
O10-C3	1.35968	1.37671	1.37747	1.37594		1.385
O11-C2	1.35809	1.37615	1.37652	1.37540		1.373
C1C2	1.36708	1.38110	1.37908	1.38358	1.366	1.373
C2C3	1.37882	1.39159	1.38883	1.39413		1.384
C3C4	1.36580	1.38062	1.37817	1.38298		1.363
C4C5	1.39874	1.40580	1.40382	1.40835		1.408
C5C6	1.38629	1.40074	1.39924	1.40268		1.392
C6C1	1.40512	1.41381	1.41067	1.41608		1.402
C1H7	1.07437	1.08476	1.08331	1.09108		
C4H8	1.07395	1.08412	1.08261	1.09052		
C5H9	1.07605	1.08635	1.08465	1.09262		
C6C15	1.51659	1.51548	1.51482	1.51541		1.507
C15H16	1.08551	1.09593	1.09428	1.10229		
C15H17	1.08600	1.09606	1.09445	1.10224		
C15C18	1.53857	1.54646	1.54463	1.54583		1.535
C18H19	1.09612	1.10943	1.10705	1.11668		
C18C20	1.52827	1.53247	1.53140	1.53179		1.517
C20H21	1.08551	1.09503	1.09388	1.10258		
C20H22	1.08406	1.09368	1.09219	1.10061		
C20H23	1.08584	1.09498	1.09370	1.10194		
C18N24	1.45399	1.46492	1.46530	1.46437	1.456	1.497
N24H25	0.99915	1.01701	1.01452	1.02100	1.001	1.013
N24C26	1.44929	1.45969	1.46069	1.45849	1.447	1.490
C26H27	1.08363	1.09452	1.09247	1.10199		
C26H28	1.09349	1.10593	1.10397	1.11389		
C26H29	1.08418	1.09407	1.09219	1.10126		
Bond angle (°)						

	HF	B3LYP			Theoretical values (B3LYP; 6-31G+) [136]	Experimental values [141]
	6-31G (d,p)	6-31G (d,p)	6-311G ++(d,p)	cc-pVDZ		
H13C12H14	110.846	110.830	118.819	110.833		
H13C12O10	109.663	109.518	109.343	109.522		
H13C12O11	109.583	109.465	109.259	109.460		
H14C12O10	109.675	109.471	109.514	109.507		
H14C12O11	109.623	109.447	109.479	109.484		
O10C12O11	107.384	108.061	107.320	107.984	107.414	108.5
C12O10C3	106.211	105.433	104.822	105.280	106.192	105.6
C12O11C2	106.313	105.502	104.901	105.355	106.283	105.8
O10C3C2	109.169	109.719	109.540	109.642	109.155	109.5
C4C3O10						128.0
O11C2C3	109.087	109.628	109.460	109.540		110.2
C1C2C3	122.238	122.121	122.140	122.099		121.9
C1C2O11						127.9
C2C3C4	121.570	121.549	121.499	121.441		122.5
C3C4C5	116.860	116.841	116.886	116.946		116.3
C4C5C6	122.256	122.345	122.335	122.350		121.9
C5C6C1	119.412	119.451	119.383	119.351		120.3
C6C1C2	117.664	117.692	117.757	117.812		117.2
C2C1H7	120.996	121.118	121.000	120.928		
C6C1H7	121.340	121.189	121.243	121.259		
C3C4H8	121.454	121.363	121.410	121.263		
C5C4H8	121.685	121.795	121.704	121.790		
C4C5H9	118.571	118.681	118.584	118.618		
C6C5H9	119.171	118.972	119.078	119.030		117.9
C1C6C15	120.173	120.179	120.208	120.167		
C5C6C15	120.415	120.363	120.405	120.477		121.8
C6C15H16	109.607	109.877	109.765	109.755		
C6C15H17	108.896	109.389	109.324	109.303		
C6C15C18	114.476	114.425	114.522	114.612		111.1
H16C15C18	108.170	107.971	108.073	107.952		
H17C15C18	108.150	107.867	107.838	107.833		
C15C18H19	107.846	107.496	107.636	107.549		
C15C18C20	109.733	110.119	110.181	110.066		113.0
C15C18N24	109.486	109.271	109.513	109.287		

	HF	B3LYP			Theoretical values (B3LYP; 6-31G+) [136]	Experimental values [141]
	6-31G (d,p)	6-31G (d,p)	6-311G ++(d,p)	cc-pVDZ		
N24C18C20						107.9
H19C18C20	107.950	107.928	107.971	107.880		
H19C18N24	110.952	111.200	110.570	111.185		
C18C20H21	110.267	110.221	110.303	110.239		
C18C20H22	111.852	111.816	111.763	111.846		
C18C20H23	110.539	110.589	110.500	110.662		
H21C20H22	108.108	108.012	108.067	107.980		
H21C20H23	108.637	108.681	108.679	108.637		
H22C20H23	107.322	107.408	107.416	107.356		
C18N24H25	108.906	107.939	108.703	107.711	110.103	106.3
C18N24C26	115.598	114.775	115.115	114.804	116.339	115.3
N24C26H27	110.861	110.646	110.664	110.831		
N24C26H28	113.652	114.160	113.589	114.190		
N24C26H29	108.980	109.104	109.071	109.222		
H27C26H28	107.874	107.525	107.845	107.355		
H27C26H29	107.213	107.138	107.236	107.004		
H28C26H29	108.029	108.006	108.216	107.956		

7.3.2   Atomic Charges

Mulliken charge distribution plays an important role in the field of theoretical calculations based on quantum theories. Different properties of molecule like dipole moment, polarizability, electrostatic structure are influenced by Mulliken charge distribution. It has been calculated for MDMA molecule using HF and DFT at different levels and summarized in table-7.2. The structural charge distributions of MDMA, calculated at different levels, were shown in figure-7.2 and charge at each atomic site was summarized in table-2. It could be observed that the charge at C1, O10, O11 & N24 is negative whereas, at C3, H13, H14, H16, H17, H21, H22, H23, H25, H27 & H29 is positive with all methods of calculation. The charge at other sites of molecules shows change in polarity in case of different methods. The charge at C4, C5, C15, C20 & C26 and H7, H8, H9, H19 & H28 is found to be positive and

negative respectively whereas negative and positive respectively in case of other methods. The change in charge with the basis set is attributed to polarization.
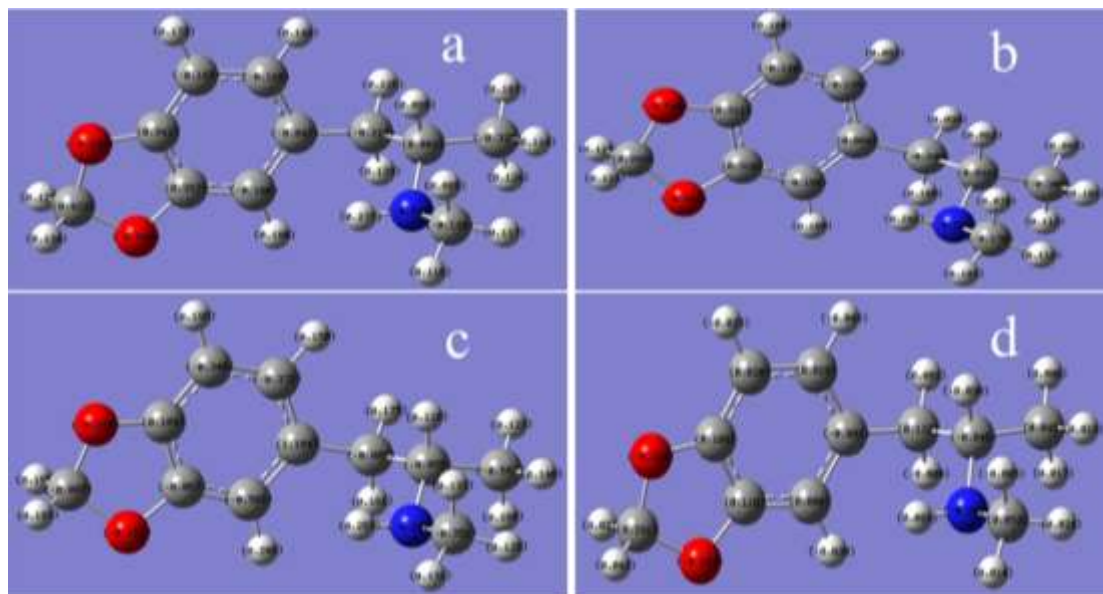
Figure-7.2: The Mulliken charge distribution molecular structure of MDMA by using (a)HF/6-31G(d,p) (b)B3LYP/6-31G(d,p) (c) B3LYP/6-311++G(d,p) and (d) B3LYP/cc-pVDZ

Table-7.2: Mulliken charges of MDMA with different basis sets.

Atom	HF	B3LYP		
	6-31G(d,p)	6-31G(d,p)	6-311G++(d,p)	cc-pVDZ
C1	-0.186	-0.169	-0.501	0.000
C2	0.357	0.318	-0.067	0.118
C3	0.342	0.311	0.104	0.109
C4	-0.165	-0.120	-0.346	0.020
C5	-0.165	-0.135	-0.372	0.029
C6	-0.047	0.084	1.104	-0.082
H7	0.180	0.105	0.205	-0.030
H8	0.173	0.100	0.195	-0.023
H9	0.148	0.081	0.150	-0.045
O10	-0.683	-0.540	-0.154	-0.284
O11	-0.682	-0.541	-0.151	-0.284
C12	0.423	0.289	-0.087	0.291
H13	0.122	0.114	0.195	0.031
H14	0.134	0.123	0.183	0.043
C15	-0.219	-0.240	-0.802	0.122
H16	0.133	0.105	0.161	0.000

Atom	HF	B3LYP		
	6-31G(d,p)	6-31G(d,p)	6-311G++(d,p)	cc-pVDZ
H17	0.126	0.099	0.175	0.003
C18	0.083	0.091	-0.059	-0.045
H19	0.089	0.062	0.118	-0.030
C20	-0.328	-0.306	-0.687	0.049
H21	0.124	0.112	0.168	0.017
H22	0.114	0.101	0.140	0.013
H23	0.107	0.095	0.123	0.008
N24	-0.641	-0.503	-0.100	-0.200
H25	0.277	0.241	0.263	0.083
C26	-0.135	-0.170	-0.351	0.053
H27	0.117	0.112	0.128	0.024
H28	0.085	0.079	0.133	-0.005
H29	0.116	0.103	0.131	0.014

7.3.3   *Estimation of Frontier molecular orbitals*

The calculation of HOMO and LUMO of MDMA was performed at level B3LYP/6-311G++(d,p). Further, their energy gap was estimated which was a measure of chemical activity of molecule. These orbitals were depicted in figure-7.3 along with their atomic orbital compositions. Further, the energy of HOMO-1 and LUMO+1 was estimated. In addition, different molecular characteristics like ionization energy, electron affinity, global hardness, chemical hardness, electrophilicity and dipole moment were estimated and summarized in table-7.3 including formulas used.
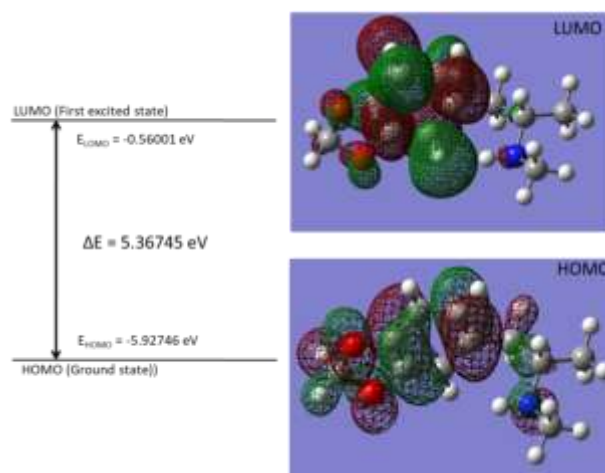
Figure-7.3: The frontier molecular orbitals and energies of HOMO and LUMO of MDMA calculated at B3LYP/6-311G++(d,p) level

Table-7.3: Estimated characteristics of MDMA in the gas phase at B3LYP/6-311G++(d,p) level

Parameter	Formula [142]	Value
E_{HOMO} (eV)		-5.92744
E_{LUMO} (eV)		-0.56001
$\Delta E_{HOMO-LUMO}$ (eV)		5.36743
E_{HOMO-1} (eV)		-6.18241
E_{LUMO-1} (eV)		-0.30885
$\Delta E_{(HOMO-1)-(LUMO+1)}$ (eV)		5.87356
Ionisation potential (I)	$I = -E_{HOMO}$	5.92744
Electron affinity (A)	$A = -E_{LUMO}$	0.56001
Global hardness (η)	$\eta = 1/2\ (\Delta E_{HOMO-LUMO})$	2.68372
Chemical potential (μ)	$\mu = 1/2(E_{HOMO} + E_{LUMO})$	-3.24373
Global electrophilicity (ω)	$w = \mu^2/2\eta$	1.96030

7.3.4 Molecular electrostatic potential (MEP)

MEP of MDMA molecule is depicted in figure-7.4. It helps to study molecular reactivity. In the MEPs, maximum negative region where an approaching electrophilic will be attached is represented as red colour whereas maximum positive region where a nucleophilic will be attached is represented as blue colour [143-145]. The value of potential ranges from -0.0385 a.u. (deepest red) to 0.02335 a.u. (deepest blue) and increases in the order red < orange < yellow < green < blue.
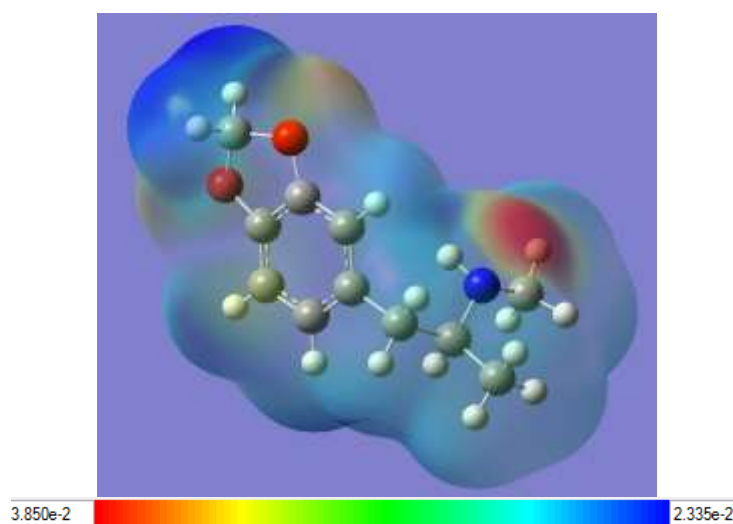
Figure-7.4: Molecular electrostatic potential (MEP) map of MDMA

7.3.5 Thermodynamic properties

Thermodynamic properties like SCF energy, vibrational energy, heat capacity (Cv), entropy (S), enthalpy (H), rotational constants, dipole moments and ZPV energy were computed at room temperature i.e. 298.15 K using methods HF and DFT at different levels and summarized in table-7.4. The minimum energy estimated for optimized MDMA structure was found to be -633 a.u. using DFT method at different levels and -629 a.u. (lower by 4 a.u.) using HF/6-31G(d,p). The heat capacity and entropy were also found to be lowest whereas vibrational energy, zero-point energy and rotational constants were highest in the case of HF method. The vibrational energy, zero-point energy, rotational constants and dipole moment showed trends of decrease with DFT method from lower to the higher basis set.

Table-7.4: The estimated thermodynamic parameters of MDMA

Thermodynamic parameters (298.15 K)	HF	B3LYP		
	6-31G(d,p)	6-31G(d,p)	6-311G++(d,p)	cc-pVDZ
SCF energy (a.u.)	-629.452645814	-633.395856449	-633.549888298	-633.406086164
Vibrational energy, E_{vib} (kcal mol^{-1})	172.000	161.335	160.473	160.254
Heat capacity at const. volume, Cv (cal mol^{-1} K^{-1})	40.770	44.636	44.805	44.786
Entropy, S (cal mol^{-1} K^{-1})	39.610	43.049	42.319	42.910
Zero-point vibrational energy, E_0 (kcal mol-1)	165.89543	154.70709	153.87833	153.62888
Rotational constants (GHz)				
A	1.58615	1.5429537	1.55984	1.54160
B	0.33855	0.3387186	0.33599	0.33821
C	0.31718	0.3158813	0.31694	0.31515
Dipole moment (Debye)				
μ_x	0.3192	0.7083	0.5450	0.8022
μ_y	-0.6297	-0.3851	-0.6115	-0.2158
μ_z	0.5542	0.4756	0.4178	0.3899
μ_{total}	0.8975	0.9360	0.9196	0.9177

The standard thermodynamic parameters i.e. Enthalpy changes (H), specific heat capacity (Cv) and Entropy (S) were studied at different temperatures in the range 50 K to 700 K at level B3LYP/6-311G++(d,p) and values obtained were summarized in table-7.5.

Table-7.5: Thermodynamic properties at different temperatures at level B3LYP 6-311G++(d,p)

Temp, T (K)	E(thermal) (kcal mol^{-1})	Specific heat, Cv (cal mol^{-1}K^{-1})	Entropy, S (cal mol^{-1}K^{-1})
50	154.044	7.36	5.319
100	154.608	15.154	12.823
150	155.548	22.35	20.355
200	156.842	29.465	27.751
250	158.503	37.068	35.123
298.15	160.473	44.805	42.319
350	163.015	53.227	50.162
400	165.875	61.086	57.786
450	169.116	68.458	65.412
500	172.711	75.243	72.982
600	180.844	87.035	87.777
700	190.049	96.757	101.947

The values of these parameters were found to be increased as temperature was increased from 50 K to 700 K. It is attributed to increased vibrational intensities with increase in temperature. The correlation equations of enthalpy changes (ΔH_m^o), heat capacities ($C_{p,m}^o$) and entropies (S_m^o) were derived in function of temperature by curve fitting of quadratic nature and corresponding fitting factors (R^2) was found to be 0.9999, 0.9986 and 0.9999, respectively. The derived relations were written below and the curve fitted graphs of corresponding parameters are shown in figure-7.4.

$$\Delta H_m^o = 153.70161 + 0.00148\,\text{T} + 7.24447 \times 10^{-5} T^2$$

$$C_{p,m}^o = -2.52611 + 0.17553\,\text{T} - 4.54168 \times 10^5 T^2$$

$$S_m^o = -2.37919 + 0.15164\,\text{T} - 3.06255 \times 10^{-6}\text{T}^2$$
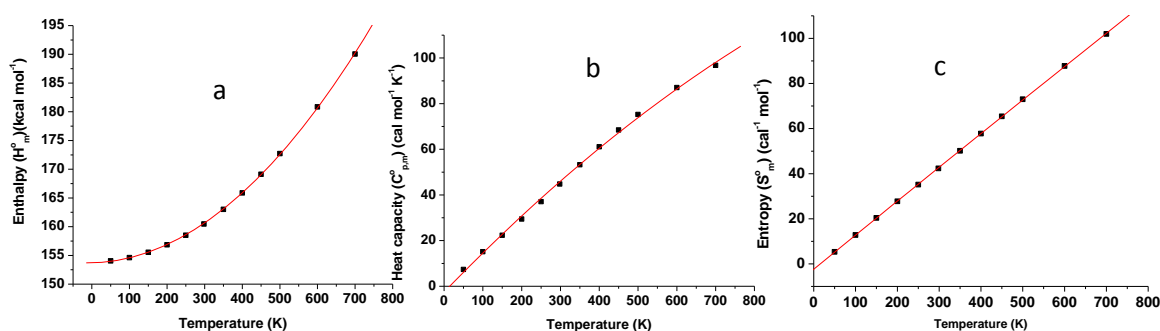
Figure-7.5: Curve fitted graphs of (a) enthalpy, (b) heat capacity and (c) entropy w.r.t. temperature for MDMA molecule

7.3.6 Vibrational analysis

The estimation of frequency of normal vibrations of MDMA molecules was estimated HF and DFT methods with basis set 6-31G(d,p) and basis sets 6-31G(d,p), 6-311G++(d,p) & cc-pVDZ respectively. Being consisting of 29 molecules, MDMA exhibited 81 numbers of normal modes of vibrations. The scaling of calculated vibrational frequencies was performed by 0.89 for HF/6-31G(d,p), 0.9668 for B3LYP/6-31G(d,p), 0.983 (up to 1700 cm-1) & 0.958 (above 1700 cm-1) for B3LYP/6-311G++(d,p) [139] and 0.9721 for B3LYP/cc-pVDZ [140]. The calculated frequencies after applying the scaling factor have been summarized in table-7.6 and compared with experimental values reported in literature.

Table-7.6: Comparision of estimated scaled frequencies with a different method and basis sets with experimental values.

Experimental values [137, 146, 147]	HF/ 6-31G(d,p)	B3LYP		
		6-31G(d,p)	6-311G++(d,p)	cc-pVDZ
346	346	336	341	340
521	521	523	533	525
716	715	709	717	720
774	787	756	766	762
812	799	812	811	806
1036	1037	1035	1041	1039
1102	1104	1107	1092	1100
1233	1220	1211	1224	1245
1253	1260	1253	1255	1254
1366	1377	1371	1362	1360
1444	1446	1442	1444	1439
1501	1512	1511	1499	1487
1607	1613	1606	1615	1609
Standard deviation	**68**	**93**	**46**	**61**

The scaled frequencies estimated at level B3LYP/6-31G++(d,p) have exhibited the lowest deviation when compared with the experimental values.

7.4 Conclusion

The geometry optimization of MDMA molecule was performed at different levels using methods HF and B3LYP. The estimated values of bond lengths and bond angles from optimized structure were found very close to the experimental ones. Mulliken charges on atomic sites and then MEP map revealed that negative potential sites were on oxygen atoms whereas positives potential sites were on hydrogen atoms. HOMO and LUMO molecular orbital energies and other properties of MDMA like ionisation potential, electronic affinity, molecular hardness, molecular potential and electrophilicity were estimated. Further thermodynamic properties of target molecule were studied and correlated relation between enthalpy; specific heat and entropy with temperature were derived. Finally, vibrational analysis was performed on MDMA optimized geometries using HF and DFT methods. The estimated values of vibrational frequencies were found matched with experimental ones in excellent agreement.

CHAPTER 8

CONCLUSION OF THE REPORTED WORK AND FUTURE PROSPECTIVE

This chapter provides the conclusions of the research work reported in the thesis and its future perspective. The main focus or outcome of this thesis was to work on developing experimental methodologies for developing explosive detection systems. Different techniques i.e. normal Raman spectroscopy, time-gated Raman spectroscopy and spatially offset Raman spectroscopy were evaluated in terms of the potential for screening of explosive materials keeping in mind the requirement of different real field scenarios. Theoretical treatment was also carried on MDMA molecule to study its structural, thermal and spectral characteristics.
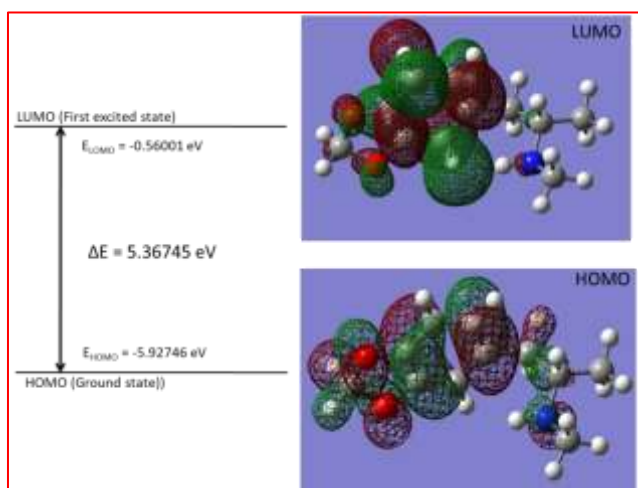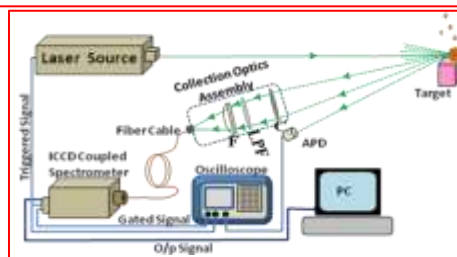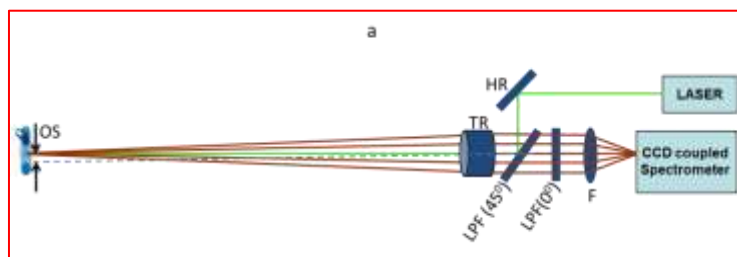
8.1   Conclusion of the work reported

Introduction to field of explosive detection and broad over-view on different potential techniques were covered in ***chapter-1***. Different scenarios of explosive detection, non-optical and optical techniques were elaborated further. The potential of different Raman spectroscopic techniques was also explained. ***Chapter-2*** covered the basics and theory of technique Raman spectroscopy. Both classical and quantum-theoretical treatments were explained and the generation of Raman lines i.e Stokes-lines and anti-Stokes lines and their relative intensities were discussed. Further selection rules of Raman spectroscopy and FTIR techniques and the difference between them were discussed. The importance of the depolarization ratio in the analysis/ assigning of Raman peaks were explained. Furthermore, instrumentation of Raman techniques like lasers, detectors, optical components including different types of filters, Raman-probes, geometrical configurations, spectrometers was explained.

In ***Chapters 3*** the studies of explosive materials like ammonium nitrate and p-nitrobenzoic acid in soil samples and through the different types of plastic bottles were studied. Raman spectra of soil samples of different concentrations of ammonium nitrate were recorded and analysed in terms of the signal-to-noise ratio. Further the effect of integration time on the Raman spectra of these soil samples studies. The potential of the processing Raman spectra in terms of background has was evaluated by recording Raman spectra of lower concentration soil samples with an improved signal-to-noise ratio. Further Raman spectra of p-nitrobenzoic acid through different plastic bottles were recorded. The importance of the processing of Raman spectra in terms of background and fluorescence of plastic material was studied using plastic bottles of different materials.

In ***Chapter 4*** the work on development of a customized algorithm and its evaluation for the identification of materials in real-time was carried out. The continuous wavelet transform was explained in detail based on which the algorithm was developed. The Mexican Hat wavelet was selected for its matching with the nature of the peaks of Raman spectra. Further, the methodology was evolved and based on which algorithm was developed represented in form of a flow chart. Further, the developed algorithm and graphic user interface were evaluated by detecting and identifying very similar

materials like 2,4,6-dinitrotolune, 1,3,5-trinitrobenze, 2,4,6-trinitrotoluene, ammonium nitrate, potassium nitrate, sodium nitrate, urea nitrate, barium nitrate etc.

In *Chapter 5* the trace detection of explosive materials and their derivatives using time-gated Raman spectroscopy was studied. Instrumentation of the time-gated Raman spectroscopy techniques was explained. The effect of different experimental parameters on the signal-to-noise ratio of peaks of Raman spectra was investigated. Further, the effect of gain, pulse accumulation and pulse energy was studied and found that the intensity i.e. sensitivity increases with an increase in any of these parameters. Finally, Raman spectra of low-concentration explosive samples like 100 ppm were recorded successfully.

In *Chapter 6* the detection of explosive materials through translucent plastic bottles using spatially offset Raman spectroscopy was studied. The potential of the technique was investigated with the excitation wavelength in the visible region. The capability of spatially offset Raman spectroscopy over the normal Raman spectroscopy was evaluated by recording Raman spectra of urea and sodium nitrate through their commercial translucent plastic bottles using both techniques. The effect of spatial offset inserted between incident laser spot and collection spot and integration time was investigated. The Spatially offset Raman spectroscopy ratio has been plotted with respect to spatial offset. Finally, the capability of spatially-offset Raman spectroscopy technique has been studied for reduced collection of fluorescence from the container material.

In Chapter-7, geometry optimization of MDMA was performed using DFT and HF methods with different basis sets. Mulliken charge and MEP were studied for negative and positive sites of the molecule. Molecular orbital characteristics like HOMO-LUMO energies, energy gap, ionization potential, electron affinity, global hardness, chemical potential were investigated. Thermal properties like SCF, zero-point energy, rotational constants, dipole moments were estimated. Enthalpy, specific heat and entropy were investigated in terms of temperature effect in the range 50 K – 700 K. Vibrational analysis was performed on optimized geometries of MDMA with different levels of theory. The vibrational frequencies were scaled and found in an excellent match with experimental values.

In brief, the important findings and conclusions of the thesis are mentioned below:

✓ Simulated samples of the post-blast scenario were successfully prepared and studied by recording their Raman spectra at different concentrations of explosive materials.

✓ The capability of detection through transparent plastic bottles was successfully evaluated by recording Raman spectra of explosive materials successfully through transparent plastic bottles of different materials, thickness and transmission.

✓ Customised algorithm for real-time acquisition of Raman signal, its processing for background and fluorescence corrections and identification by peak matching with database was developed and evaluated.

✓ The capability of time-gated Raman spectroscopy was evaluated by recording of Raman spectra of explosive samples of low concentrations i.e. 1000 ppm, 500 ppm and finally 100 ppm.

✓ The capability of SORS technique was successfully evaluated by recording Raman spectra of explosive materials through translucent containers and the effect of spatial offset on sensitivity was studied.

✓ Theoretical calculations on MDMA molecule were performed and its structural, thermal and spectral characteristics were estimated and found in good agreement with experimental values.

8.2 Future Prospective of the work

➢ To carry out experimental work of SORS technique with SORS probes at 532nm and 785 nm.

➢ To enhance the range and sensitivity of detection of explosive materials.

➢ To study the spectral signatures of hazardous molecules, both theoretically and experimentally, as per the requirement of law-enforcement agencies.

REFERENCES

1. Carson, P.A., *Hazardous chemicals handbook*. 2002: Elsevier.

2. Bielecki, Z., et al., *Sensors and systems for the detection of explosive devices-an overview*. Metrology and Measurement Systems, 2012. **19**(1): p. 3-28.

3. Brenner, D.J., *Are x-ray backscatter scanners safe for airport passenger screening? For most individuals, probably yes, but a billion scans per year raises long-term public health concerns*. Radiology, 2011. **259**(1): p. 6-10.

4. Caygill, J.S., F. Davis, and S.P. Higson, *Current trends in explosive detection techniques*. Talanta, 2012. **88**: p. 14-29.

5. Tourné, M., *Developments in explosives characterization and detection*. Journal of Forensic Research, 2013. **12**(002).

6. Wallin, S., et al., *Laser-based standoff detection of explosives: a critical review*. Analytical and bioanalytical chemistry, 2009. **395**(2): p. 259-274.

7. Johnson, J.B., et al., *Standoff methods for the detection of threat agents: A review of several promising laser-based techniques*. Journal of Spectroscopy, 2014. **2014**.

8. Gottfried, J.L. and F.C. De Lucia Jr, *Laser-induced breakdown spectroscopy: capabilities and applications*. 2010, ARMY RESEARCH LAB ABERDEEN PROVING GROUND MD WEAPONS AND MATERIALS RESEARCH ….

9. Wynn, C.M., et al., *A novel method for remotely detecting trace explosives*. Lincoln Laboratory Journal, 2008. **17**(2): p. 27-39.

10. Taha, Y.M., C.A. Odame-Ankrah, and H.D. Osthoff, *Real-time vapor detection of nitroaromatic explosives by catalytic thermal dissociation blue diode laser cavity ring-down spectroscopy*. Chemical Physics Letters, 2013. **582**: p. 15-20.

11. Chen, X., et al., *Quantum cascade laser based standoff photoacoustic chemical detection*. Optics express, 2011. **19**(21): p. 20251-20257.

12. Petra, N., et al., *Theoretical analysis of a quartz-enhanced photoacoustic spectroscopy sensor*. Applied Physics B, 2009. **94**(4): p. 673-680.

13. Waclawek, J., et al., *Quartz-enhanced photoacoustic spectroscopy-based sensor system for sulfur dioxide detection using a CW DFB-QCL.* Applied Physics B, 2014. **117**(1): p. 113-120.

14. Furstenberg, R., et al., *Stand-off detection of trace explosives via resonant infrared photothermal imaging.* Applied Physics Letters, 2008. **93**(22): p. 224103.

15. Appleby, R. and H.B. Wallace, *Standoff detection of weapons and contraband in the 100 GHz to 1 THz region.* IEEE transactions on antennas and propagation, 2007. **55**(11): p. 2944-2956.

16. Mogilevsky, G., et al., *Raman spectroscopy for homeland security applications.* International Journal of Spectroscopy, 2012. **2012**.

17. Gaft, M. and L. Nagli, *UV gated Raman spectroscopy for standoff detection of explosives.* Optical materials, 2008. **30**(11): p. 1739-1746.

18. Gulia, S., et al., *Trace detection of explosive and their derivatives in stand-off mode using time gated Raman spectroscopy.* Vibrational Spectroscopy, 2016. **87**: p. 207-214.

19. Carter, J.C., et al., *Standoff detection of high explosive materials at 50 meters in ambient light conditions using a small Raman instrument.* Applied Spectroscopy, 2005. **59**(6): p. 769-775.

20. Ehlerding, A., et al., *Resonance-enhanced Raman spectroscopy on explosives vapor at standoff distances.* International Journal of Spectroscopy, 2012. **2012**.

21. Ko, H., S. Chang, and V.V. Tsukruk, *Porous substrates for label-free molecular level detection of nonresonant organic molecules.* ACS nano, 2009. **3**(1): p. 181-188.

22. Gulia, S., et al., *Detection of explosive materials and their precursors through translucent commercial bottles using spatially offset Raman spectroscopy using excitation wavelength in visible range.* Optical Engineering, 2019. **58**(12): p. 127102.

23. **Gulia Sanjay**, et al. ***Stand-off Detection of p- nitrobenzoic acid in translucent plastic bottles using Spatially-offset Raman Spectroscopy (SORS)****. in *National Laser Symposium-23*. 2014. Sri Venkateswara University, Tirupati, AP.

24. Hargreaves, M.D. and P. Matousek. *Threat detection of liquid explosive precursor mixtures by Spatially Offset Raman Spectroscopy (SORS).* in *Optics and photonics for counterterrorism and crime fighting V.* 2009. International Society for Optics and Photonics.

25. Olds, W.J., et al., *Noninvasive, quantitative analysis of drug mixtures in containers using spatially offset Raman spectroscopy (SORS) and multivariate statistical analysis.* Applied spectroscopy, 2012. **66**(5): p. 530-537.

26. Raman, C.V. and K.S. Krishnan, *A new type of secondary radiation.* Nature, 1928. **121**(3048): p. 501-502.

27. Raman, C.V., *A new radiation.* Indian Journal of physics, 1928. **2**: p. 387-398.

28. Ferraro, J.R., *Introductory raman spectroscopy.* 2003: Elsevier.

29. Kumar, R., *Atomic and Molecular Spectra.* 2003: KEDAR NATH RAM NATH.

30. Smith, E. and G. Dent, *Modern Raman Spectroscopy A Practical Approach, John Wiley & Sons.* West Sussex, England, 2005.

31. Long, D.A., *The Raman effect: a unified treatment of the theory of Raman scattering by molecules.* 2002: Wiley.

32. Lewis, I.R. and H. Edwards, *Handbook of Raman spectroscopy: from the research laboratory to the process line.* 2001: CRC press.

33. P.G., C.J.a.G., *Handbook of Vibrational Spectroscopy.* 2001: John Wiley.

34. Allemand, C.D., *Depolarization ratio measurements in Raman spectrometry.* Applied Spectroscopy, 1970. **24**(3): p. 348-353.

35. Dijkman, F. and J. Van der Maas, *Dependence of bandshape and depolarization ratio on slitwidth.* Applied Spectroscopy, 1976. **30**(5): p. 545-546.

36. Fini, G. and P. Mirone, *Slitwidth Dependence of Depolarization Ratios.* Applied Spectroscopy, 1975. **29**(3): p. 230-232.

37. Shea, J., *Handbook of instrumental techniques for analytical chemistry.* IEEE Electrical Insulation Magazine, 1998. **14**(6): p. 42-42.

38.   Strommen, D.P. and K. Nakamoto, *Laboratory Raman Spectroscopy*. 1984: Wiley-Interscience.

39.   Li, Z., et al., *Raman spectroscopy for in-line water quality monitoring—Instrumentation and potential.* Sensors, 2014. **14**(9): p. 17275-17303.

40.   Gulati, K.K., et al., *Standoff detection and identification of explosives and hazardous chemicals in simulated real field scenario using time gated Raman spectroscopy.* Defence Science Journal, 2019. **69**(4): p. 342-347.

41.   *https://www.oceaninsight.com/products/fibers-and-probes/probes/raman-probes/general-purpose-raman-probes/.*

42.   *https://www.semrock.com/filter-types-for-raman-spectroscopy-applications.aspx.*

43.   Bumbrah, G.S. and R.M. Sharma, *Raman spectroscopy–Basic principle, instrumentation and selected applications for the characterization of drugs of abuse.* Egyptian Journal of Forensic Sciences, 2016. **6**(3): p. 209-215.

44.   Lerner, J. and A. Thevenon, *The optics of spectroscopy.* Jobin-Yvon Optical Systems/Instrumentss SA, 1988.

45.   Lerner, J.M., *Imaging spectrometer fundamentals for researchers in the biosciences—a tutorial.* Cytometry Part A: the journal of the International Society for Analytical Cytology, 2006. **69**(8): p. 712-734.

46.   Corfield, R., *Liquid explosives detectors entering service at airports.* Chemistry world, 2014.

47.   Ceco, E., et al. *Stand-off imaging Raman spectroscopy for forensic analysis of post-blast scenes: trace detection of ammonium nitrate and 2, 4, 6-trinitrotoluene.* in *Chemical, Biological, Radiological, Nuclear, and Explosives (CBRNE) Sensing XV*. 2014. International Society for Optics and Photonics.

48.   Fountain, A.W., et al., *Recent advances and remaining challenges for the spectroscopic detection of explosive threats.* Applied spectroscopy, 2014. **68**(8): p. 795-811.

49.   Iping Petterson, I.E., et al., *Noninvasive detection of concealed explosives: depth profiling through opaque plastics by time-resolved Raman spectroscopy.* Analytical chemistry, 2011. **83**(22): p. 8517-8523.

50. Ramírez-Cedeño, M.L., et al., *Remote detection of hazardous liquids concealed in glass and plastic containers.* IEEE Sensors Journal, 2010. **10**(3): p. 693-698.

51. Gulati, K.K., et al., *Real-time stand-off detection of improvised explosive materials using time-gated UV–Raman spectroscopy.* Pramana, 2019. **92**(2): p. 1-5.

52. Gautam, R., et al., *Review of multidimensional data processing approaches for Raman and infrared spectroscopy.* EPJ Techniques and Instrumentation, 2015. **2**(1): p. 1-38.

53. Reisner, L.A., A. Cao, and A.K. Pandya, *An integrated software system for processing, analyzing, and classifying Raman spectra.* Chemometrics and Intelligent Laboratory Systems, 2011. **105**(1): p. 83-90.

54. *Peak Finding and Measurement.* Available from: https://terpconnect.umd.edu/~toh/spectrum/PeakFindingandMeasurement.htm.

55. Yang, C., Z. He, and W. Yu, *Comparison of public peak detection algorithms for MALDI mass spectrometry data analysis.* BMC bioinformatics, 2009. **10**(1): p. 1-13.

56. Du, P., W.A. Kibbe, and S.M. Lin, *Improved peak detection in mass spectrum by incorporating continuous wavelet transform-based pattern matching.* bioinformatics, 2006. **22**(17): p. 2059-2065.

57. Zhang, Z.M., et al., *An intelligent background‑correction algorithm for highly fluorescent samples in Raman spectroscopy.* Journal of Raman spectroscopy, 2010. **41**(6): p. 659-669.

58. Wee, A., et al., *A continuous wavelet transform algorithm for peak detection.* Electrophoresis, 2008. **29**(20): p. 4215-4225.

59. Kandjani, A.E., et al., *A new paradigm for signal processing of Raman spectra using a smoothing free algorithm: Coupling continuous wavelet transform with signal removal method.* Journal of Raman Spectroscopy, 2013. **44**(4): p. 608-621.

60. Grossmann, A., R. Kronland-Martinet, and J. Morlet, *Reading and understanding continuous wavelet transforms*, in *Wavelets*. 1990, Springer. p. 2-20.

61. R.J.E., M., *Wavelet Theory and Applications*. 2005, Eindhoven University of Technology.

62. Xi, Y., et al., *A novel pre-processing algorithm based on the wavelet transform for Raman spectrum.* Applied spectroscopy, 2018. **72**(12): p. 1752-1763.

63. Chung, J.H. and S.G. Cho, *Nanosecond gated raman spectroscopy for standoff detection of hazardous materials.* Bulletin of the Korean Chemical Society, 2014. **35**(12): p. 3547-3552.

64. Gares, K.L., et al., *Review of explosive detection methodologies and the emergence of standoff deep UV resonance Raman.* Journal of Raman Spectroscopy, 2016. **47**(1): p. 124-141.

65. Hokr, B.H., et al., *Single-shot stand-off chemical identification of powders using random Raman lasing.* Proceedings of the National Academy of Sciences, 2014. **111**(34): p. 12320-12324.

66. Bykov, S.V., et al., *Compact solid-state 213 nm laser enables standoff deep ultraviolet Raman spectrometer: measurements of nitrate photochemistry.* Applied spectroscopy, 2015. **69**(8): p. 895-901.

67. Forest, R., et al. *Use of a spectroscopic lidar for standoff explosives detection through Raman spectra.* in *Chemical, Biological, Radiological, Nuclear, and Explosives (CBRNE) Sensing XIII.* 2012. International Society for Optics and Photonics.

68. Pettersson, A., et al., *Explosives standoff detection using Raman spectroscopy: from bulk towards trace detection.* SPIE Defense, Security, and Sensing. Vol. 7664. 2010: SPIE.

69. Reichardt, T.A., S.E. Bisson, and T.J. Kulp, *Standoff ultraviolet raman scattering detection of trace levels of explosives.* Sandia National Labs, 2011.

70. Tuschel, D.D., et al., *Deep ultraviolet resonance Raman excitation enables explosives detection.* Applied spectroscopy, 2010. **64**(4): p. 425-432.

71. Gares, K.L., et al., *Solution and solid hexahydro-1, 3, 5-trinitro-1, 3, 5-triazine (RDX) ultraviolet (UV) 229 nm photochemistry.* Applied spectroscopy, 2015. **69**(5): p. 545-554.

72. Gares, K.L., et al., *Solution and solid trinitrotoluene (TNT) photochemistry: persistence of TNT-like ultraviolet (UV) resonance Raman bands.* Applied spectroscopy, 2014. **68**(1): p. 49-56.

73. Parisi, A.V., et al., *The effects of body size and orientation on ultraviolet radiation exposure.* Photodermatology, photoimmunology & photomedicine, 1996. **12**(2): p. 66-72.

74. Reichrath, J., et al., *Biologic effects of light: An enlighting prospective.* Anticancer research, 2016. **36**(3): p. 1339-1343.

75. Gulia Sanjay, Gambhir Vijayeta, and R.M. N, *Detection of 1,3,5-trinitrobenzene using Raman Spectroscopy up to 2 meter.*, in *High Energy Materials Conference and Exhibit (HEMCE)*. 2009: High Energy Materials Research Laboratory, Pune, India.

76. Gulia Sanjay, et al., *Stand-off Detection of p-nitrobenzoic acid through translucent plastic bottles using Spatially- offset Raman Spectroscopy (SORS)*, in *National Laser Symposium (NLS-2014)*, A. Sri Venkateswara University, Editor. 2014.

77. Santos, P. and N. Goncalves, *Resonance Raman investigation of meisenheimer complexes derived from 1, 3, 5-trinitrobenzene.* Journal of Raman spectroscopy, 1989. **20**(8): p. 551-554.

78. Sakamoto, K., G. Mizutani, and S. Ushioda, *Absolute Raman-scattering cross section of a surface-adsorbed layer: Amorphous nitrobenzene on Ni (111).* Physical Review B, 1993. **48**(12): p. 8993.

79. Yang, X., et al., *Examination of the photoreaction of p-nitrobenzoic acid on electrochemically roughened silver using surface-enhanced Raman imaging (SERI).* The Journal of Physical Chemistry B, 1998. **102**(25): p. 4933-4943.

80. Al-Saidi, W., S.A. Asher, and P. Norman, *Resonance Raman spectra of TNT and RDX using vibronic theory, excited-state gradient, and complex polarizability approximations.* The Journal of Physical Chemistry A, 2012. **116**(30): p. 7862-7872.

81. Hatab, N.A., et al., *Detection and analysis of cyclotrimethylenetrinitramine (RDX) in environmental samples by surface-enhanced Raman spectroscopy.* Journal of Raman Spectroscopy, 2010. **41**(10): p. 1131-1136.

82. Emmons, E.D., et al., *Characterization of polymorphic states in energetic samples of 1, 3, 5-trinitro-1, 3, 5-triazine (RDX) fabricated using drop-on-demand inkjet technology.* Applied Spectroscopy, 2012. **66**(6): p. 628-635.

83. Wynn, C., et al., *Noncontact detection of homemade explosive constituents via photodissociation followed by laser-induced fluorescence.* Optics express, 2010. **18**(6): p. 5399-5406.

84. Eliasson, C., N. Macleod, and P. Matousek, *Non-invasive detection of powders concealed within diffusely scattering plastic containers.* Vibrational Spectroscopy, 2008. **48**(1): p. 8-11.

85. Guicheteau, J. and R. Hopkins. *Applications of spatially offset Raman spectroscopy to defense and security.* in *Chemical, Biological, Radiological, Nuclear, and Explosives (CBRNE) Sensing XVII.* 2016. International Society for Optics and Photonics.

86. Matousek, P., *Deep non-invasive Raman spectroscopy of living tissue and powders.* Chemical Society Reviews, 2007. **36**(8): p. 1292-1304.

87. Matousek, P., et al., *Numerical simulations of subsurface probing in diffusely scattering media using spatially offset Raman spectroscopy.* Applied spectroscopy, 2005. **59**(12): p. 1485-1492.

88. Matousek, P. and A. Parker, *Non‐invasive probing of pharmaceutical capsules using transmission Raman spectroscopy.* Journal of Raman Spectroscopy: An International Journal for Original Work in all Aspects of Raman Spectroscopy, Including Higher Order Processes, and also Brillouin and Rayleigh Scattering, 2007. **38**(5): p. 563-567.

89. Wilcox, P.G. and J.A. Guicheteau. *Comparison of handheld Raman sensors through opaque containers.* in *Chemical, Biological, Radiological, Nuclear, and Explosives (CBRNE) Sensing XIX.* 2018. International Society for Optics and Photonics.

90. Afseth, N.K., et al., *A novel approach for subsurface through-skin analysis of salmon using spatially offset Raman spectroscopy (SORS).* Applied spectroscopy, 2014. **68**(2): p. 255-262.

91. Chao, K., et al., *A spatially offset Raman spectroscopy method for non-destructive detection of gelatin-encapsulated powders.* Sensors, 2017. **17**(3): p. 618.

92. Keller, M.D., S.K. Majumder, and A. Mahadevan-Jansen, *Spatially offset Raman spectroscopy of layered soft tissues.* Optics letters, 2009. **34**(7): p. 926-928.

93. Loeffen, P.W., et al. *Chemical and explosives point detection through opaque containers using spatially offset Raman spectroscopy (SORS).* in *Chemical, Biological, Radiological, Nuclear, and Explosives (CBRNE) Sensing XII.* 2011. International Society for Optics and Photonics.

94. Matousek, P., et al., *Subsurface probing in diffusely scattering media using spatially offset Raman spectroscopy.* Applied spectroscopy, 2005. **59**(4): p. 393-400.

95. Olds, W.J., et al., *Spatially offset Raman spectroscopy (SORS) for the analysis and detection of packaged pharmaceuticals and concealed drugs.* Forensic science international, 2011. **212**(1-3): p. 69-77.

96. Qin, J., K. Chao, and M.S. Kim, *Nondestructive evaluation of internal maturity of tomatoes using spatially offset Raman spectroscopy.* Postharvest biology and technology, 2012. **71**: p. 21-31.

97. Qin, J., et al., *A line-scan hyperspectral Raman system for spatially offset Raman spectroscopy.* Journal of Raman Spectroscopy, 2016. **47**(4): p. 437-443.

98. Stone, N., et al., *Subsurface probing of calcifications with spatially offset Raman spectroscopy (SORS): future possibilities for the diagnosis of breast cancer.* Analyst, 2007. **132**(9): p. 899-905.

99. Hopkins, R., L. Lee, and N. Shand, *Correcting transmission losses in short-wave infrared spatially offset Raman spectroscopy measurements to enable reduced fluorescence through-barrier detection.* Analyst, 2017. **142**(19): p. 3725-3732.

100. Hopkins, R.J., S.H. Pelfrey, and N.C. Shand, *Short-wave infrared excited spatially offset Raman spectroscopy (SORS) for through-barrier detection.* Analyst, 2012. **137**(19): p. 4408-4410.

101. Emmons, E.D., et al., *Ultraviolet resonance Raman spectroscopy of explosives in solution and the solid state.* The Journal of Physical Chemistry A, 2013. **117**(20): p. 4158-4166.

102. Sackey, S.S., et al., *Spectroscopic study of UV transparency of some materials.* Environment and Pollution, 2015. **4**(4).

103. Izake, E.L., et al., *Deep Raman spectroscopy for the non-invasive standoff detection of concealed chemical threat agents.* Talanta, 2012. **94**: p. 342-347.

104. Sundarajoo, S., et al., *Non‑invasive depth profiling by space and time‑resolved Raman spectroscopy.* Journal of Raman Spectroscopy, 2013. **44**(7): p. 949-956.

105. Zachhuber, B., et al., *Stand-off spatial offset Raman spectroscopy for the detection of concealed content in distant objects.* Analytical chemistry, 2011. **83**(24): p. 9438-9442.

106. Tuschel, D., *Photoluminescence spectroscopy using a Raman spectrometer.* Spectroscopy, 2016. **31**(9): p. 14-21.

107. Frisby, A., et al. *Spatially offset Raman spectroscopy (SORS) for through-barrier proximal chemical and explosive detection.* in *Optics and Photonics for Counterterrorism and Crime Fighting VII; Optical Materials in Defence Systems Technology VIII; and Quantum-Physics-based Information Security.* 2011. International Society for Optics and Photonics.

108. Tripathi, A., et al., *Semi-automated detection of trace explosives in fingerprints on strongly interfering surfaces with Raman chemical imaging.* Applied Spectroscopy, 2011. **65**(6): p. 611-619.

109. Hargis Jr, P.J., et al., *Studies of the laser-induced fluorescence of explosives and explosive compositions.* 2006, Sandia National Laboratories.

110. Martelo, L.M., et al., *Towards the development of a low-cost device for the detection of explosives vapors by fluorescence quenching of conjugated polymers in solid matrices.* Sensors, 2017. **17**(11): p. 2532.

111. *CCD Spectral Response (QE), Andor.* Available from: http://www.andor.com/learning-academy/ccd-spectral-response-(qe)-defining-the-qe-of-a-ccd.

112. *ATF EXPLOSIVES Industry Newsletter.* 2016.

113. Matousek, P., et al., *Modelling of spatially offset Raman spectroscopy effects.* Central Laser Facility Annual Report, 2005: p. 195-198.

114. Zachhuber, B., et al. *Stand off spatial offset Raman spectroscopy: a distant look behind the scenes*. in *Optics and Photonics for Counterterrorism and Crime Fighting VII; Optical Materials in Defence Systems Technology VIII; and Quantum-Physics-based Information Security*. 2011. International Society for Optics and Photonics.

115. Maher, J.R. and A.J. Berger, *Determination of ideal offset for spatially offset Raman spectroscopy*. Applied spectroscopy, 2010. **64**(1): p. 61-65.

116. *CCD Saturation and Blooming, Hamamatsu*. Available from: http://www.hamamatsu.magnet.fsu. edu/articles/ccdstandblooming.html.

117. Drugs, U.N.O.o. and Crime, *Amphetamines and Ecstasy: 2008 Global ATS Assessment*. 2008: United Nations Publications.

118. Meyer, J.S., *3, 4-methylenedioxymethamphetamine (MDMA): current perspectives*. Substance abuse and rehabilitation, 2013. **4**: p. 83.

119. Tanner-Smith, E.E., *Pharmacological content of tablets sold as "ecstasy": results from an online testing service*. Drug and alcohol dependence, 2006. **83**(3): p. 247-254.

120. Vogels, N., et al., *Content of ecstasy in the Netherlands: 1993–2008*. Addiction, 2009. **104**(12): p. 2057-2066.

121. Wood, D.M., et al., *Variability in the 3, 4-methylenedioxymethamphetamine content of 'ecstasy' tablets in the UK*. Emergency Medicine Journal, 2011. **28**(9): p. 764-765.

122. Shulgin, A. and A. Shulgin, *PiHKAL*. A chemical love story. Transform, Berkeley, CA, 1991.

123. Sumnall, H.R., J.C. Cole, and L. Jerome, *The varieties of ecstatic experience: an exploration of the subjective experiences of ecstasy*. Journal of Psychopharmacology, 2006. **20**(5): p. 670-682.

124. Brunt, T.M., et al., *Linking the pharmacological content of ecstasy tablets to the subjective experiences of drug users*. Psychopharmacology, 2012. **220**(4): p. 751-762.

125. Rodgers, J., et al., *Differential experiences of the psychobiological sequelae of ecstasy use: quantitative and qualitative data from an internet study.* Journal of Psychopharmacology, 2006. **20**(3): p. 437-446.

126. Soar, K., J. Turner, and A.C. Parrott, *Problematic versus non-problematic ecstasy/MDMA use: the influence of drug usage patterns and pre-existing psychiatric factors.* Journal of Psychopharmacology, 2006. **20**(3): p. 417-424.

127. Wu, L.T., et al., *The variety of ecstasy/MDMA users: results from the National Epidemiologic Survey on alcohol and related conditions.* The American Journal on Addictions, 2009. **18**(6): p. 452-461.

128. Bexis, S. and J.R. Docherty, *Effects of MDMA, MDA and MDEA on blood pressure, heart rate, locomotor activity and body temperature in the rat involve α-adrenoceptors.* British journal of pharmacology, 2006. **147**(8): p. 926-934.

129. Carvalho, M., et al., *Metabolism is required for the expression of ecstasy-induced cardiotoxicity in vitro.* Chemical research in toxicology, 2004. **17**(5): p. 623-632.

130. West, M.J. and M.J. Went, *Detection of drugs of abuse by Raman spectroscopy.* Drug testing and analysis, 2011. **3**(9): p. 532-538.

131. Bell, S.E., et al., *Composition profiling of seized ecstasy tablets by Raman spectroscopy.* Analyst, 2000. **125**(10): p. 1811-1815.

132. Izake, E.L., *Forensic and homeland security applications of modern portable Raman spectroscopy.* Forensic science international, 2010. **202**(1-3): p. 1-8.

133. de Oliveira Penido, C.A.F., et al., *Raman spectroscopy in forensic analysis: identification of cocaine and other illegal drugs of abuse.* Journal of Raman Spectroscopy, 2016. **47**(1): p. 28-38.

134. Bell, S.E., et al., *Development of sampling methods for Raman analysis of solid dosage forms of therapeutic and illicit drugs.* Journal of Raman spectroscopy, 2004. **35**(5): p. 409-417.

135. Farquharson, S., et al., *Rapid detection and identification of overdose drugs in saliva by surface-enhanced Raman scattering using fused gold colloids.* Pharmaceutics, 2011. **3**(3): p. 425-439.

136. Ebrahimi, Z.F., *An ab initio study on 3, 4-methylenedioxymethamphetamine, MDMA (ecstasy) and its derivatives.* International Journal of Computational Biology and Drug Design, 2016. **9**(1-2): p. 149-161.

137. Milhazes, N., et al., *Electrochemical and spectroscopic characterisation of amphetamine-like drugs: application to the screening of 3, 4-methylenedioxymethamphetamine (MDMA) and its synthetic precursors.* Analytica chimica acta, 2007. **596**(2): p. 231-241.

138. Zapata-Torres, G., et al., *Quantum-chemical, NMR and X-ray diffraction studies on (±)-1-[3, 4-(methylenedioxy) phenyl]-2-methylaminopropane.* Journal of Molecular Graphics and Modelling, 2008. **26**(8): p. 1296-1305.

139. Sundaraganesan, b.N., et al., *FT-Raman and FT-IR spectra, vibrational assignments and density functional studies of 5-bromo-2-nitropyridine.* Spectrochimica Acta Part A: Molecular and Biomolecular Spectroscopy, 2005. **61**(13-14): p. 2995-3001.

140. Kesharwani, M.K., B. Brauer, and J.M. Martin, *Frequency and zero-point vibrational energy scale factors for double-hybrid density functionals (and other selected methods): can anharmonic force fields be avoided?* The Journal of Physical Chemistry A, 2015. **119**(9): p. 1701-1714.

141. Morimoto, B.H., S. Lovell, and B. Kahr, *Ecstasy: 3, 4-methylenedioxymeth-amphetamine (MDMA).* Acta Crystallographica Section C: Crystal Structure Communications, 1998. **54**(2): p. 229-231.

142. Ramachandran, S. and G. Velraj, *FT-IR, FT-Raman spectral analysis and density functional theory calculations studies of 3-chloro-2-nitrobenzyl alcohol.* Rom. Journ. Phys, 2012. **57**(7-8): p. 1128-1137.

143. Murray, J.S. and K. Sen, *Molecular electrostatic potentials: concepts and applications.* 1996: Elsevier.

144. Scrocco, E., J. Tomasi, and P. Lowdin, *Advances in quantum chemistry.* Edited by, 1978.

145. Šponer, J. and P. Hobza, *DNA base amino groups and their role in molecular interactions: Ab initio and preliminary density functional theory calculations.* International Journal of Quantum Chemistry, 1996. **57**(5): p. 959-970.

146. Dana, K., et al., *Rapid analysis of cocaine in saliva by surface-enhanced Raman spectroscopy.* Journal of analytical & bioanalytical techniques, 2015. **6**(6): p. 1.

147. Dies, H., et al., *Rapid identification and quantification of illicit drugs on nanodendritic surface-enhanced Raman scattering substrates.* Sensors and Actuators B: Chemical, 2018. **257**: p. 382-388.

Signal processing of Raman signatures and real-time identification of hazardous molecules using continuous wavelet transformation (CWT)

A. Parmar[a], S. Gulia[a], S. Bajaj[a], V. Gambhir[a], R. Sharma[b] and M N Reddy[a]

[a] Laser Science & Technology Centre, Delhi
[b] Delhi Technological University, Delhi
sanjay-gulia@lastec.drdo.in

Abstract—**Continuous use of explosives by terrorists throughout the world has led to the great necessity in explosives detection technology, especially in technologies that have potential for stand-off detection. The Raman vibrational spectrum of molecules provides an excellent fingerprint for species identification. Analysis of Raman signatures manually is time-consuming and cannot be afford by security personal in real scenario. Automation of detection, acquisition and analysis of Raman signal is required for operations in real scenario. In this work, we have developed software which caters all these process automatically and finally mentions name of material under observation for stand-off detection. This is based on continuous wavelet transformation (CWT). This algorithm/ software is capable of identifications/ discrimination of very similar chemicals like trinitrobenzene (TNB), trinitrotoluene (TNT) and dinitrotoluene (DNT).**

INTRODUCTION

Terrorism has emerged as a prominent threat to the society. Terrorism and detonation of explosives or mines have become the common most dreaded daily news now days. Early detection is one of key factors required for protection from such explosives and mines. However explosives detection still continues to be one of the most critical tasks that security forces both military and civil of almost all the countries must confront in a wide variety of situations.

First, different types of capabilities are required in field of explosive detection depending on real scenario. In some scenario, security personal may require very compact and light weight explosive detector and in other scenario, explosive detection may require long range of detection and high sensitivity for detection of buried landmine etc. so that causality may be avoided. Second, they must have quick response time to screen the long queues of passengers and luggage or fast moving vehicles, and then easy and safe deployability. Thirdly, the detectors should have enough resolving power to identify the type of explosive contents to take necessary action to quickly neutralize them before exploding. Well while there are several technologies available commercially or in research labs, but no single technology or sensor is proved to be reliable enough to detect the explosives unambiguously.

Most of the laser-based methods are very promising for the selective and sensitive detection of explosives in both scenario of point detection and stand-off detection because they do not need any sample preparation and they can be operate in-situ and online. Certain limitations and the scenarios in which they are effective are technique dependent. The most versatile and potential laser-based technique for the standoff detection of explosives is based on Raman Spectroscopy due to its capability of finger printing i.e. it can detect and discriminate very similar molecules**.** Other commercially available techniques can categories target material like nitrogroup, nitroamine etc. But there may be many medicines and other safe materials which may fall under these categories. So, pointing out name of target material specifically is utmost required in field of explosive detection.

In this work, we have developed software which caters all process automatically and finally mentions name of material under observation for stand-off detection. In case of stand-off detection, sample is not in closed chamber so extra signal processing like background correction etc. is required. Software developed under this study is required to process Raman signals and based on continuous wavelet transform (CWT). This software is capable of identification/ discrimination of very similar chemicals like trinitrobenzene (TNB), trinitrotoluene (TNT) and dinitrotoluene (DNT).

WAVELET TRANSFORM

Raman spectrum with adequate resolution gives unique signatures for various chemical compounds. Analysis and processing of these signatures helps identification of various chemical compounds. Spectra peaks at various wavenumber for given spectrometer resolution are unique and can be considered finger prints of that chemical. Thus peak detection is central to algorithm for Raman spectroscopy based reliable chemical identification. There are various methods to detect peaks, such as SNR, intensity, threshold, slopes of peaks, local maximum, peak width, etc. Relative amplitude and intensity threshold based algorithms are not very reliable for standoff detection due to fluctuation in spectra intensity and container effect and change in ambient conditions.

The wavelet domain representation expands the dimensionality of the functional signal. For a one-dimensional time series, the Fourier domain representation provides energy as a function of frequency. The wavelet domain representation includes the energy over both time and scale (or frequency) axes.

Thus wavelet transform offers the substantial advantages for analyzing nonlinear, transient responses and non-stationary signals for which the conventional Fourier transform failed to provide meaningful results. It provides better result as it correlates mother wavelet with pattern of Raman spectra for various scales and wave number positions. It localizes the peaks with wave numbers. Thus algorithm proposed uses CWT based ridge lines method and SNR reported in literature [1, 2].

Continuous Wavelet Transform (CWT)

The continuous wavelet transform of a continuous function x (t) at a scale $a \in R$ and translational value $b \in R$ is expressed by the following integral

$$X_w(a,b) = \frac{1}{|a|} \int_{-\infty}^{\infty} x(t)\psi\left(\frac{t-b}{a}\right)dt$$

where ψ(t) is a continuous function in both the time domain and the frequency domain called the mother wavelet .The main purpose of the mother wavelet is to provide a source function to generate the daughter wavelets which are simply the translated and scaled versions of the mother wavelet. In other words CWT is defined as the sum over all time of the signal multiplied by scaled, shifted versions of the wavelet function ψ.

The wavelet transform decomposes signals over dilated and translated functions, which transform a continuous function into a highly redundant function

The Mexican Hat wavelet was selected as the mother wavelet in the analysis of Raman spectrum, which can be mathematically described as follows:

$$\psi(x) = \left(\frac{2}{\sqrt{3}}\pi^{-1/4}\right)\left(1-x^2\right)e^{-x^2/2}$$

CWT based software developed for automated identification

CWT based peak detection method for analysis of Raman spectra computes CWT coefficients for various scales and wave number . CWT coefficients at each scale have a local maximum around the peak center. The local maximum increases corresponding to the CWT scale, which reaches its maximum when the scale best matches the peak

width.To visualize cwt coefficients for various scales and wave number a ridge like figure emerges after plotting the 2D CWT coefficients with the amplitude of the CWT coefficients taken as third dimension .The peak detection is achieved by finding the ridges over the 2D CWT coefficient matrix.
thus the peak detection algorithm consists of three steps:

- computing 2D CWT for various scales

- identifying the ridges by linking the local maxima

- identifying the peaks based on the ridges lines length thresholding

In addition to CWT analysis spectrum is preprocessed for background removal to nullify the effect of ambient conditions and translucent/transparent container for standoff detection of chemical. Algorithm is implemented on atom based Single board computer and code has been developed in QT on Linux platform.Gui program controls the complete setup including spectrometer parameters, laser module, spectra data acquisition, background subtraction, peak identification, signature matching and thresholding. The complete process is automated and operates and logs data through single button operation. Stand off detection and identification from sample at 30 cm takes about 10 sec. The flow chart of process for automatic identification of chemicals based on Raman signatures is depicted below:
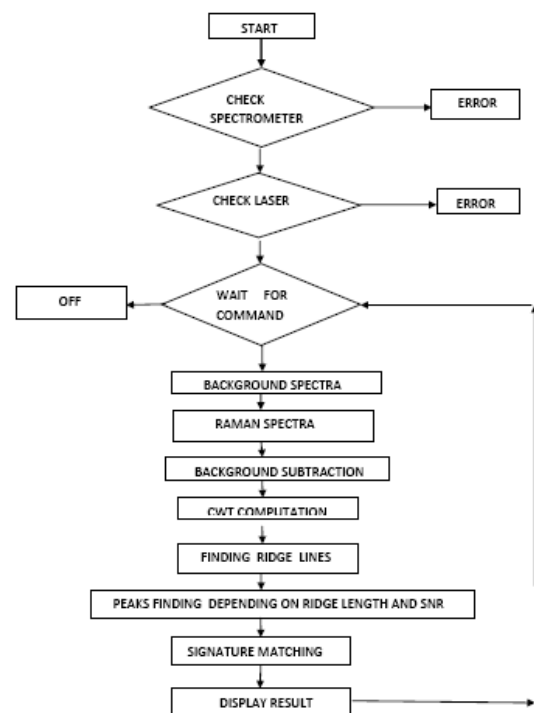
The snap shot of GUI during detection of similar molecules are shown below:
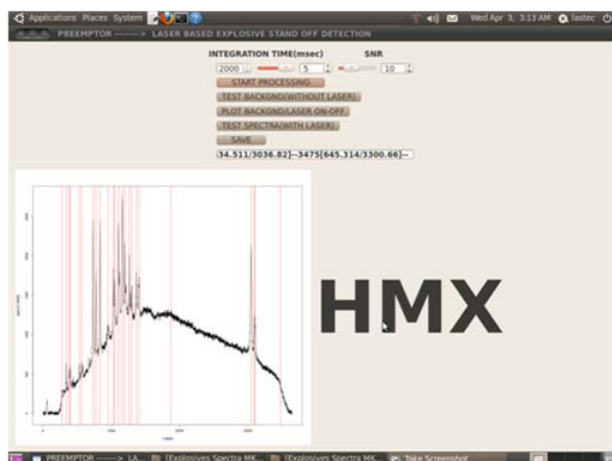
GUI of Software developed for online analysis and Identification
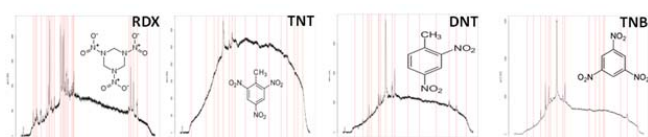
REFERENCES

1. P.Du, W. A. Kibbe, S. M. Lin, *Bioinformatics* **2006**, *22*, 2059.

2. Zhi-Min Zhang, Shan Chen, Yi-Zeng, Liang Zhao-Xia Liu, Qi-Ming Zhang, Li-Xia Ding, Fei Ye and Hu Zhouc. *An intelligent background-correction algorithm for highly fluorescent samples in Raman spectroscopy.* Journal of Raman Spectroscopy (2009).
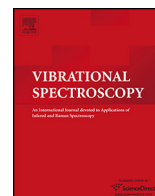
Trace detection of explosive and their derivatives in stand-off mode using time gated Raman spectroscopy

Sanjay Gulia[a,b,*], Kamal K. Gulati[a], Vijayeta Gambhir[a], Rinku Sharma[b], M.N. Reddy[a]

[a] Laser Science and Technology Centre, Delhi, 110054, India
[b] Delhi Technological University, Delhi, 110042, India

ABSTRACT

Trace detection is utmost important for detection of concealed explosive materials in form of IEDs. Surfaces of suspicious objects may be scanned for contamination of explosives. Sensitivity and selectivity are two main concerns in field of explosive detection. Raman spectroscopy provides remarkable selectivity. Time-gated Raman spectroscopy also has potential of providing sensitivity for trace detection. In present study, time-gated Raman spectroscopy investigated for detection of ppm level concentration of explosives. To achieve better sensitivity, various parameters of the experimental set-up like gain of intensifier, number of pulse accumulated and pulse energy of laser were optimised. The trend of change in intensity of Raman scattering (background subtracted) was observed by varying values of these above mentioned parameters. Followed by optimization of these parameters for better sensitivity, Raman spectra of RDX samples at lower concentrations (prepared by mixing RDX with KBr) were recorded. The corrected intensity increased in linear fashion with increase in gain of intensifier, number of pulses accumulated and pulse energy. After that, Raman spectra of RDX were recorded from a stand-off distance of 5 m in backscattered mode with concentrations down to 100 ppm.

© 2016 Elsevier B.V. All rights reserved.

1. Introduction

Since last two decades, terrorism has evolved as the most challenging menace against humanity. Most of the terrorist attacks have been noticed for use of explosives materials stored in some concealed form like metal container etc. Such types of bombs are known as improvised explosive devices (IEDs).Till today the methods used require approaching the suspicious object in order to perform the analysis with a great risk to the operator. Therefore, a new technique, need to be developed to detect and identify target object with acceptable level of confidence maintaining safe distance for the operator [1–4].

Standoff explosive detection involves methods for sensing the presence of explosive devices when vital assets and those individuals monitoring, operating, and responding to the means of detection are physically separated from the explosive device. The zone of severe damage varies with scenario and bomb type, it may vary from 10 m for a pedestrian suicide bomber and 100 m for a vehicle-based bomb [5]. Standoff detection and identification of

such explosive materials is one of the most unavoidable but greatest challenging tasks for researchers and engineers.

The detection at large distances involves physical difficulties like i. the intensity of the return light decreases inversely with the distance squared and ii. absorption & scattering losses in air lead to significant compromise in sensitivity.

Laser-based spectroscopic techniques such as laser-induced breakdown spectroscopy (LIBS), Raman spectroscopy (RS), resonant Raman spectroscopy (RRS), photo-dissociated/laser-induced fluorescence (PD/LIF) and laser-based photo-acoustic spectroscopy (LPAS) have the potential to detect minute amount of explosive materials on contaminated surfaces left by handling etc. [6–9].

LIBS technique involves power density of the order of GW/cm^2 to generate plasma of the target sample [10–12]. This level of power density is achievable with short, high peak power laser pulses and tight focusing of the laser beam by transmitting optics (usually spot size of the order of few microns). LIBS signal comprises elemental information i.e. spectral lines in LIBS spectra gives information of elements presents in the test sample whereas explosive detection requires molecular information [13,14]. It is destructive technique and hence not suitable to examine people and vehicles. Since laser beamis tightly focused into a small spot, it is difficult and time-taking to scan large objects in real conditions

---

[15]. Photo-dissociation Laser-induced fluorescence (PD-LIF) involvesdecomposition (dissociation) of polyatomic molecules into characteristic fragments [16–18]. PF-LIF method can be used to detect only nitrogen-containing explosives. In addition, the dissociation of different molecules may require different level of energy and wavelengths. In addition, absorption characteristics of species generated in dissociation process of different molecules shall be different. Thus, PD-LIF requires a tunable laser source. In addition, it involves excitation with UV wavelength and hence thermal degradation of the sample may occur [19,20]. Laser-photo acoustic spectroscopy (LPAS) involves the vibrational absorption and hence requires the tunable laser source in mid IR range i.e. 5–12 μm which corresponds to 830–2000 cm^{-1}. Quantum-cascade lasers are the main contestant for LPAS due to their compactness and light weight [21–25]. The main concerns with QCLs are their requirement of cooled environment and limited tenability [26]. In addition, detection of suspicious materials through even transparent glass and plastic containers is not possible. The sensitivity is adversely affected by humidity.

Raman spectroscopy is one of the effective techniques for detection and identification of explosive materials [27–30]. This technique is suitable for detecting both organic and inorganic explosive materials in form of solid, liquid and powder. A single-wavelength laser is sufficient to generate Raman scattering of all the molecules of interest. Raman spectroscopy is a molecular spectroscopy that provides direct information about the molecular structure and composition of the material. The potential of this technique lies in its ability to locate and identify unequivocally many different compounds at a time. The process is non-destructive, sensitive, fast, and repeatable. The vibrational spectrum provided by Raman spectroscopy is a unique molecular 'fingerprint', that is capable of differentiating very similarly structured molecules from one another with great level of specificity in real-scenario [31–34]. Conventional Raman spectroscopy in back-scattered mode, resonance-Raman spectroscopy (RRS) [35,36], surface-enhanced Raman spectroscopy (SERS) [37–39], spatially-offset Raman spectroscopy (SORS) [40–42], time-gated Raman spectroscopy [21,27,29] are being explored for detection of explosives. Time-gated Raman spectroscopy is the most suitable technique for stand-off detection of explosive materials. It involves pulse laser source and intensifier-charge coupled device (ICCD). ICCD is being synchronized with optical laser pulse with appropriate delay depending upon mainly stand-off distance [21,36,43].

In stand-off Raman spectroscopy, a pulsed laser source of nanosecond or shorter pulse is preferred as excitation source as it provides high peak power (few MW). In addition, pulse laser enables gated-detection which in turn ensures the rejection of ambient light between consecutive laser pulses and collection of Raman photons (photons generated in inelastic scattering) only during laser pulse. In this way, high power pulse with gated detection results in better signal-to-noise ratio (SNR). Raman photons are collected with a receiving optics, and then coupled to dispersive spectrograph directly or using optical fiber. Intensified CCD coupled with spectrograph is used to detect and produce Raman spectrum of the sample under study [28,44,45]. Dry sand samples having explosive concentrations 4–8% have been investigated using 532 nm as excitation laser wavelength [29]. Visibly excited stand-off detection may face fluorescence of samples and impurity. However, using pulse laser as excitation source and gated detection can be utilized to reduce contribution fluorescence and ambient light [9]. Random Raman lasing using 532 nm as excitation is being reported for stand-off explosive detection. The occurrence of Random Raman laser depends on beam-quality which is difficult to maintain at large stand-off distances [46].

Raman spectroscopy promises better sensitivity with visible wavelength as excitation compared to that in near infrared range as the Raman scattering cross-section depends inversely on the fourth power of the wavelength [31]. So far, stand-off UV Raman systems reported in the literature have been applied mainly to detection of explosives and chemicals (chemical and biological contaminants) [27,47–51]. Though, UV range excitation theoretically offers further better sensitivity, high energy UV photons exhibit potential risk of sample degradation and burning [31,52–54]. UV excitation in absorption bands of explosives causes photolysis which decreases concentration of the explosive molecules (51). Explosives exhibit problem of sample burning remarkably due to their absorption in deep UV range [55,56]. Photo-degradation of sample with UV excitation may be reduced remarkably by following two methods: (a) either sample should be in motion like open-stream flow or magnetic stirring [47] so that point of interaction of laser with samples may be varied during investigating target material (not possible in real scenario) or (b) use of pulse energy of level of micro-joule (not sufficient for stand-off detection).UV excitation based methods do not promise the detection of explosives through normal transparent glass and plastic containers. Though UV excitation promises higher maximum permissible energy (MEP) for eye safety, it may generate other irreversible biological effects in operator body [57,58]. Hence, UV excitation is not practical in stand-off where high pulse energy has to be transmitted.

Despite of several advancements in Raman spectroscopy has been achieved in the area of explosive detection, however Raman spectroscopy in the visible range remained to be investigated for trace detection of explosives. Trace detection targets surfaces of suspicious objects where there is probability of contamination like door handle of vehicles, handles of brief-case etc. The level of contamination may vary from few ng/cm^2 to μg/cm^2(i.e. ppm to ppb level) depending on the way of handling the explosives in making IED etc and adhesive nature of explosives. In addition, the effect of various parameters of the set-up of time-gated Raman spectroscopy on the sensitivity remains to be explored. Here, the effect of various parameters like gain of intensifier of intensified charge-coupled device (ICCD), number of pulses used in accumulation and pulse energy of laser on sensitivity was investigated thoroughly. After optimization of these parameters in terms of sensitivity, RDX was detected at lower concentrations. Stand-off detection of 1,3,5-trinitroperhydro-1,3,5-triazine(RDX) up to 100 ppm level using visible Raman spectroscopy i.e. 532 nm as excitation laser beam was demonstrated.

2. Experimentation

An experimental set-up used in the present study was developed according to the schematic depicted in Fig. 1. This prototype mainly involves a pulse laser excitation source, ICCD-coupled spectrograph and a compact receiving optics. The pulse laser was a 2nd harmonic of Flash lamp-pumped Nd:YAG laser (Make: Quantel, France, model: Brilliant). It has maximum pulse energy of about 160 mJ at 532 nm, pulse duration of the order of 6 ns and beam divergence of about 1mrad. It has variable pulse repetition rate of 1–10 Hz. In these measurements, pulse repetition rate of 10 Hz was used.

The collection optics was very compact having diameter of 1 inch and consisted of collimating optics (C), long pass filter (LPF) and finally focusing optics (F). The revived backscattered Raman signal was collected and collimated with collimating optics (C). Long pass filter (LPF) at 532 nm with very steep transition width ~225 cm^{-1} and high optical density (O.D.) of the order of 6 (Make: Semrock, USA) was used to reject Rayleigh scattered photons. Finally focusing optics (F) was used to focus the remaining signal
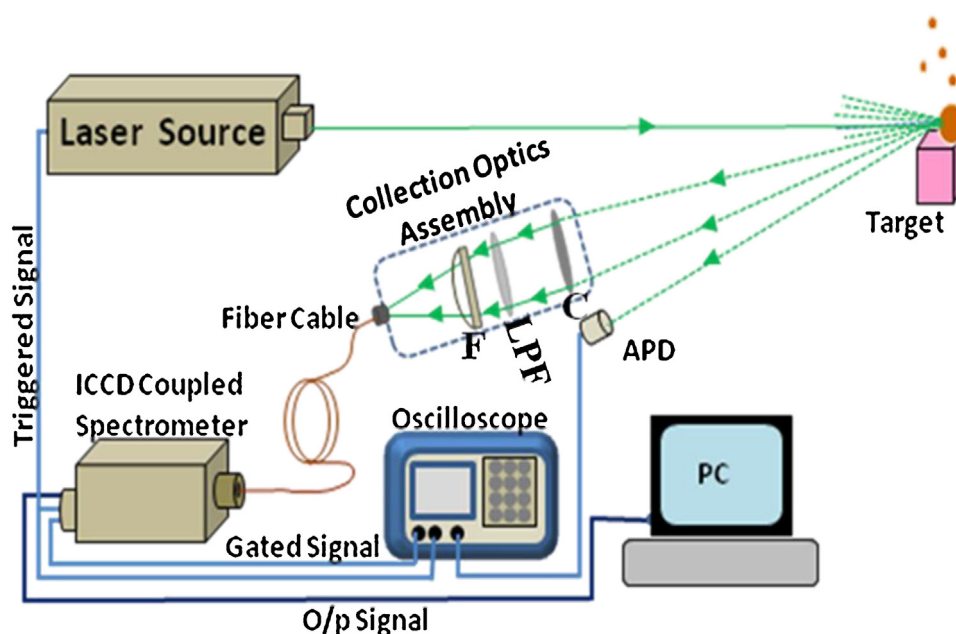
Fig. 1. Schematic of ICCD based pulse Raman Stand-off detection system. C: Collimating optics, LPF: Longpass Filter, F: Focusing optics, ICCD: Intensified Charge Coupled Device, APD: Avalanche photodiode.

i.e. Raman signal at fiber-tip of an optical fiber bundle of core diameter of 200 μm (make: M/s ANDOR, USA & model: SR-OPT-8024. This bundle has 19 fibers arranged in circular manner at one end where Raman signal was focused, and in linear way at other end coupled to spectrograph. The optical fiber bundle was used to couple the Raman signal to spectrograph (Make: ANDOR, USA, model: SR303i) attached with the intensified charge coupled Device (ICCD). The spectrograph has motorized entrance slit with a variable width varying from 10 μm–2.5 mm. In present study, silt width of 20 μm was used. This spectrograph has 303 mm focal length and f/4 aperture ratio. It consists of grating having 300 lines/mm blazed in visible range having efficiency greater than 65%. Its resulting spectral resolution is $\sim$20 cm^{-1}.

Intensified charge-coupled device (ICCD) (make: ANDOR, USA and model: iStar720-25-U) coupled with spectrograph (SR303) was used to record Raman spectra. The ICCD has thermo-electrically cooling (TEC) mechanism and array of 1024 × 256 pixels. The operational temperature of ICCD was set at −20 °C in these experiments. The ICCD may be gated 3 ns to 25 s with resolution of 25 ps. Vertical binning was performed in the measurements. Its various parameters like intensifier gain, gate width, number of pulses to be accumulated were varied to observe their effects on intensity of Raman peaks. Present study was carried out in ambient conditions i.e. day-light conditions.

There are various sources of noise including solar-noise, thermal noise of CCD and fluorescence of the samples as well as substrates. The samples like p-nitrobenzoic acid (PNBA), dinitro-benzene (TNB) and RDX mixed with KBr do not exhibit remarkable fluorescence. In addition, samples were prepared in form of pellets and hence no fluorescence from the substrate. Though, the effect of other noise sources as mentioned above may be observed separately, the idea behind current study was to simulate the experiment in real scenario where all the noise sources may exist together.

2.1. Synchronizing of optical pulse with gate width

Matching the timings for optical pulse and gate width is one of critical aspects in experiments of time-gated Raman spectroscopy.

As Raman scattering takes place without any delay, detector should be switched ON as soon as the optical pulse reaches at the detector. But still some delay has to be introduced to cater the travelling time of incident photons from laser to sample and Raman photons from sample to detection end. The difference between travelling time of photons from molecule to molecule or layer to layer (in order of sub ns) may be neglected as compared to longer laser pulses (6 ns) and gate widths ($\geq$10 ns) used in this work.

The triggering TTL signal of laser system was fed to the ICCD detector. The laser pulse detected using APD, which was kept near the receiver. The synchronization achieved by monitoring gate output of ICCD and APD signal on oscilloscope for accurate overlapping of both signals in time-domain by inserting proper delay. ICCD has inbuilt electronic card that controls gate width, gate delay and gain of the intensifier of ICCD. These parameters may be varied by the user by inserting the required values in software of ICCD.

3. Sample preparation

In current study, 1,3,5-trinitrobenzene (TNB), p-nitro benzoic acid (PNBA) and 1,3,5-trinitroperhydro-1,3,5-triazine (RDX) were used. Samples of p-nitro benzoic acid and RDX were prepared by mixing with potassium bromide (KBr) at different ratio (w/w) in the form of pallets. Aqueous solution of diluted concentration of 1,3,5-trinitrobenzene (TNB) deposited uniformly on aluminum sheet (100 mg of TNB in 1 l of water). Then mass of TNB per unit area estimated and found approximately 100 μg/cm^2.

4. Results and discussion

Initial experiments were started with benzene and 1,3,5-trinitrobenzene which share common benzene ring with many explosives like 2,4,6-trinitrotoluene (TNT), 2,4-dinitrotoluene (DNT), 2,4,6-triamino-1,3,5-trinitrobenzene (TATB), picric acid, 2,4,6-trinitrophenylmethylnitroamine (commonly known as tetryl) etc. [59,60]. Further Raman spectra of RDX and p-nitrobenzoic acid were recorded in stand-off mode from a distance of 5 m and effect of various parameters was investigated to optimize

Table 1
Assignment of the most intense peak of Raman spectra of TNB, PNBA & RDX.

Molecule	Transition (most-intense)	Assignment	Intrinsic Raman scattering cross-section
TNB	$1354\,cm^{-1}$	NO_2 symmetric stretching + NO_2 i.p. deformation + CN stretching [61]	3.7×10^{-28} [65]
PNBA	$1368\,cm^{-1}$	NO_2 symmetric stretching [62]	–
RDX	$887\,cm^{-1}$	Ring-breathing mode [63,64]	1.8×10^{-29} [66]

experimental set-up for better sensitivity. Finally, Raman spectra of RDX were recorded in lower concentrations at 1000 ppm, 500 ppm and 100 ppm level in stand-off mode from 5 m using optimised experimental parameters. The peak assignments corresponding to the most intense peak in Raman spectra of 1,3,5-trinitrobenzene (TNB), p-nitrobenzoic acid (PNBA) and 1,3,5-trinitroperhydro-1,3,5-triazine (RDX) are summarized in Table 1.

Raman scattering Raman cross-section is wavelength dependent used as excitation. For example, Raman scattering cross-section of RDX is 1.8×10^{-29}, 5.8×10^{-30} and 2.1×10^{-30} with excitation wavelength at 532 nm, 633 nm and 785 nm respectively for the peak at $887\,cm^{-1}$ [66].

4.1. Gated-Raman signal and normal Raman signal

In case of standoff detection, scattered Raman signal is accompanied by strong background noise available from other sources. This unwanted background noise can be solar or from any other light source near to targeted materials. Depending on conditions, this noise may be much strong and does not provide any information about targeted materials. Raman signal, having molecular information of targeted materials, may be easily obscured by this unwanted strong background noise. Gated detection opens the path to detect suspicious materials from stand-off distances in daytime by reducing effect of ambient light and fluorescence. This technique provides increased the signal-to-noise ratio of the Raman signal. A gated detector also improves the Raman signal by decreasing the fluorescence background [27].

Gated-Raman spectroscopy where detector synchronized with pulse laser, was used in the current study and therefore weak Raman signal of 1,3,5-trinitrobenzene at low concentration ($\mu g/cm^2$) was measured from the stand-off distance of 5 m as shown in Fig. 2. Raman signal of 1,3,5-trinitrobenzene was recorded in stand-off backscattered mode from a distance of 5 m by using ICCD in CW mode as well as in synchronized mode. The aqueous sample of diluted concentration (100 mg of TNB in 1 l of water) of 1,3,5-trinitrobenzene (TNB) deposited uniformly on aluminum sheet. The quantity of the chemical was approximately $100\,\mu g/cm^2$. In case of CW mode, intensifier of ICCD was kept continuously ON. Whereas it was synchronized with optical pulse of laser in synchronized mode. In both measurements pulse energy of laser, gain (G) of intensifier and gate width were kept at 15 mJ, 100 and 20 ns respectively. In CW mode, weak Raman signal (due to quantity at trace level $\sim100\,\mu g/cm^2$) was completely obscured by background noise which also gets amplified by intensifier continuously and hence molecular information cannot be extracted from scattered light collected at receiver (Fig. 2). However, in synchronized mode, weak Raman signal easily detected and molecular information in terms of Raman stokes lines was clearly observed as shown in Fig. 2.
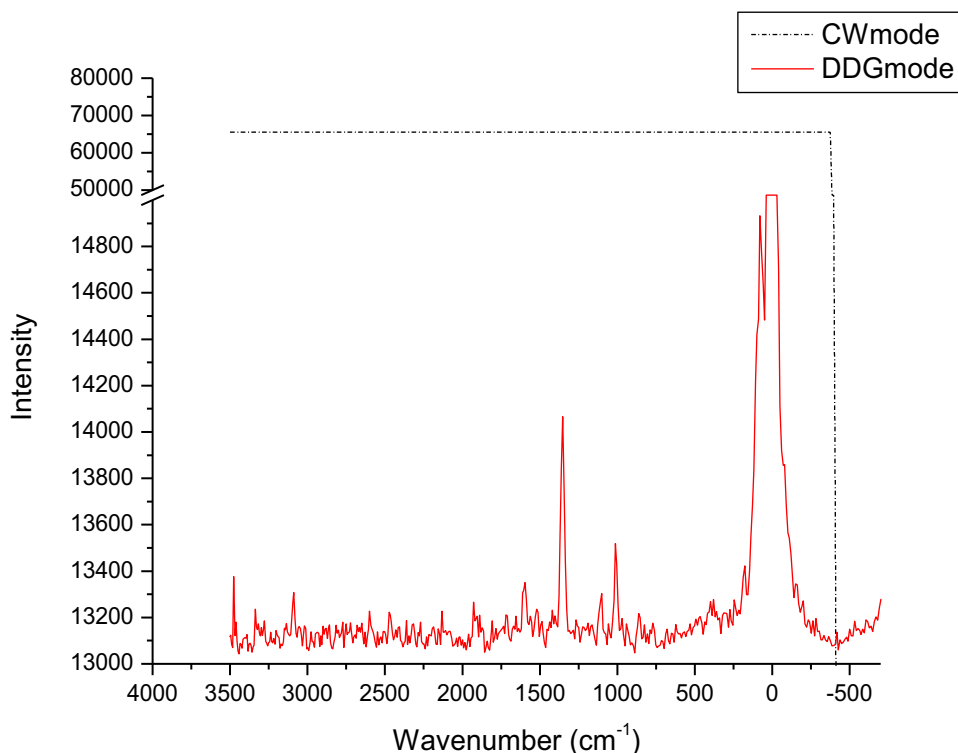
Fig. 2. Raman spectra of 1,3,5 – trinitrobenzene at low concentration ($100\,\mu g/cm^2$) recorded using ICCD in CW mode and gate mode. Pulse energy of laser, gain (G) of intensifier and gate width kept at 15 mJ, 100 and 20 ns respectively.

4.2. ICCD gain effect on Raman spectra

Photons entering to an ICCD strike a photocathode plate where they are converted to electrons which are directed towards microchannel plate (MCP). At MCP, electrons are multiplied by applying a high voltage. Gain of the ICCD depends on this multiplication and hence the applied voltage to MCP. Therefore, by controlling the voltage at MCP, gain of ICCD can be controlled.

To analyze the effect of gain of intensifier on intensity of Raman scattering, Raman spectra of 1,3,5-trinitrobenzene in stand-off mode from a distance of 5 m was recorded by varying the gain 0 to 200. Pulse energy of laser and gate width were kept at 15 mJ and 20 ns respectively. These Raman spectra were recorded with accumulation over 100 number of laser pulses.

Results of the study revealed a significant improvement in SNR of Raman peaks with increasing gain of intensifier as shown in Fig. 3. Raman spectra of 1,3,5-trinitrobenzene at gain of 0, 50, 100 and 200 are shown in Fig. 3A.The improvement in SNR of Raman peak at 1354 cm^{-1} (NO$_2$ symmetric stretching) can be easily visualized. In addition, due to increase in sensitivity with increasing gain, less intense peaks e.g. peaks at 1007 cm^{-1} and 3076 cm^{-1} which did not exist with lower gain, start appearing in Raman spectra. It was observed that the intensity of Raman peak at 1354 cm^{-1} increased with increase in gain as shown in Fig. 3B. The background subtracted intensity of Raman scattering at 1354 cm^{-1} increased gradually with gain upto 80 and beyond it increased rapidly. The signal-to-noise ratio (SNR) of Raman peak at 1354 cm^{-1} was 30 and 85 in case of gain of intensifier at 50 and 200 respectively.

Raman signal and noise both go under process of amplification. Raman signal appears in phase wise manner and keeps adding on during accumulation of pulses. Whereas, noise is a random process and therefore can be averaged out when accumulated over a number of pulses and thus improved SNR was observed in present study.

4.3. Pulse accumulation effect on Raman spectra

To study the effect of pulse accumulation on Raman spectra, pulse energy, gain (G) of intensifier and gate width were kept at 30 mJ, 100 and 20 ns respectively. The test sample i.e. p-nitrobenzoic acid mixed with KBr at 1000 ppm (w/w) was in pellet form. Raman spectra of p-nitrobenzene were recorded in stand-off mode from a distance of 5 m by accumulating number of pulses in range 10–2000. Raman spectra of p-nitrobenzoic acid mixed with KBr (at 1000 ppm) recorded using accumulation of 10, 100, 1000 and 2000 pulses in Fig. 4A. A significant increase in intensity of Raman signal was observed with increasing number of pulses accumulated. Experimental results indicated that less intense peaks i.e. 1368 cm^{-1} (NO$_2$ symmetric stretching) that was almost invisible with 10 numbers of pulses started appearing at 100 numbers of pulses. Further, improvement in SNR of Raman peaks was observed visually as the pulses increased. Fig. 4B shows the trend of change in background subtracted intensity of Raman peak at 1368 cm^{-1} with increase in accumulated pulse number. It was further observed that the intensity improves in a linear fashion with increase in number of pulses accumulated. The signal-to-noise ratio (SNR) of Raman peak at 1368 cm^{-1} was 17 and 40 in case of number of pulses accumulated is 100 and 1000 respectively. These results reveal that better sensitivity achievable by accumulating Raman spectra corresponding to more and more optical pulses of laser. However, at the same time, it is not possible to keep adding large number of pulses as this process is time consuming. In real time scenario, explosive detection and identification should be completed within a few seconds. This imposes a limit on the number of pulses to be accumulated. For

(A)

(B)
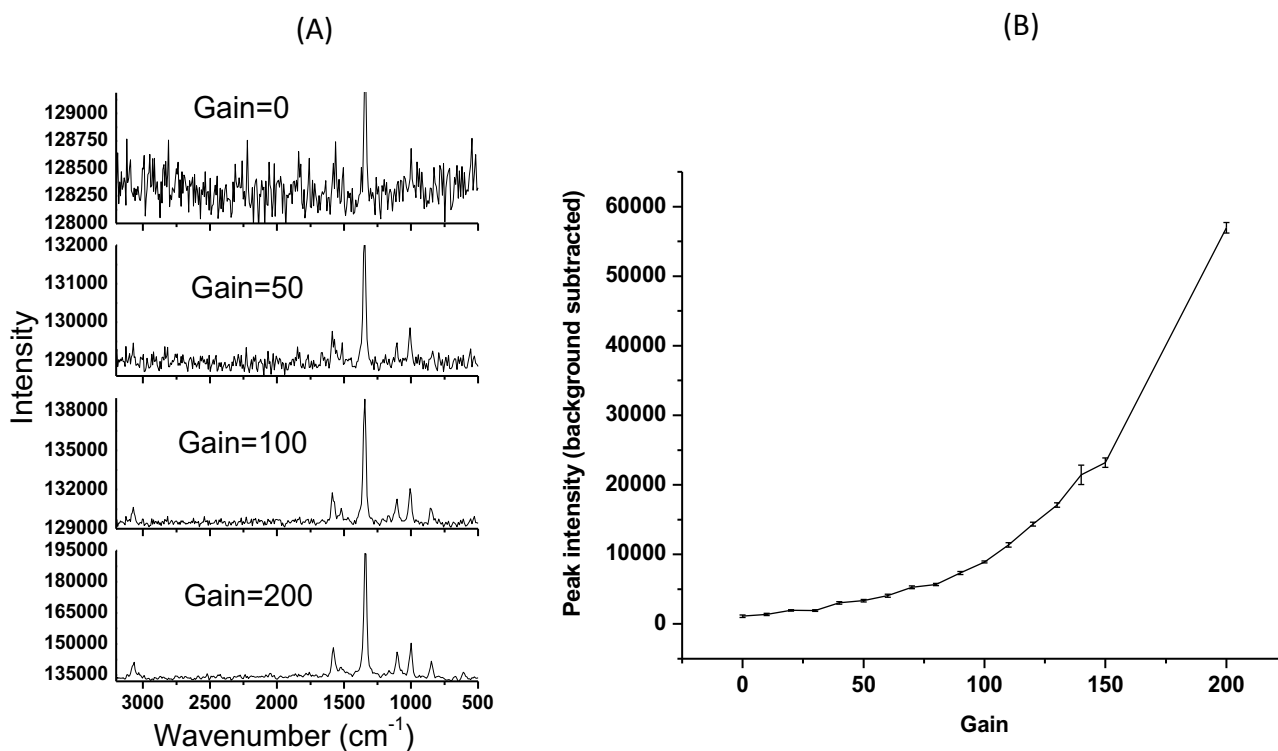
Fig. 3. A: Raman spectra of 1,3,5 – trinitrobenzene recorded using gain of intensifier of ICCD detector at 0, 50, 100 and 200. In both measurements pulse energy of laser, gain (G) of intensifier and gate width were kept at 15 mJ, 100 and 20 ns respectively and B: Variation in peak intensity (background subtracted) of Raman peak at 1354 cm^{-1} w.r.t. gain of intensifier when gain value is varied 0 to 200. The error bars represent the standard deviation (SD) of three time measurement.

Fig. 4. A: Raman spectra of p-nitrobenzoic acid recorded with accumulation of 10, 100, 1000 and 2000 pulses. Pulse energy of laser, gain (G) of intensifier and gate width at 30 mJ, 100 and 20 ns respectively and B: Variation of SNR of peak at 1368 cm^{-1} w.r.t. number of pulses accumulated. The error bars represent the standard deviation (SD) of three time measurement.

example it takes 100 s for accumulation of 1000 number of pulses in case of repetition rate of 10 Hz. The detection process can be made faster by using laser of high repetition rate. However, it may induce thermal effects and damage the target material. So, there has to be a trade-off between number of pulses accumulated, detection-analysis time and pulse repetition rate.

4.4. Pulse energy effect

Pulse energy of laser is one of the critical parameters which decide the maximum achievable sensitivity. The effect of pulse energy on intensity of Raman peaks i.e. on sensitivity was carried out. Gain of intensifier, gate width and number of pulses
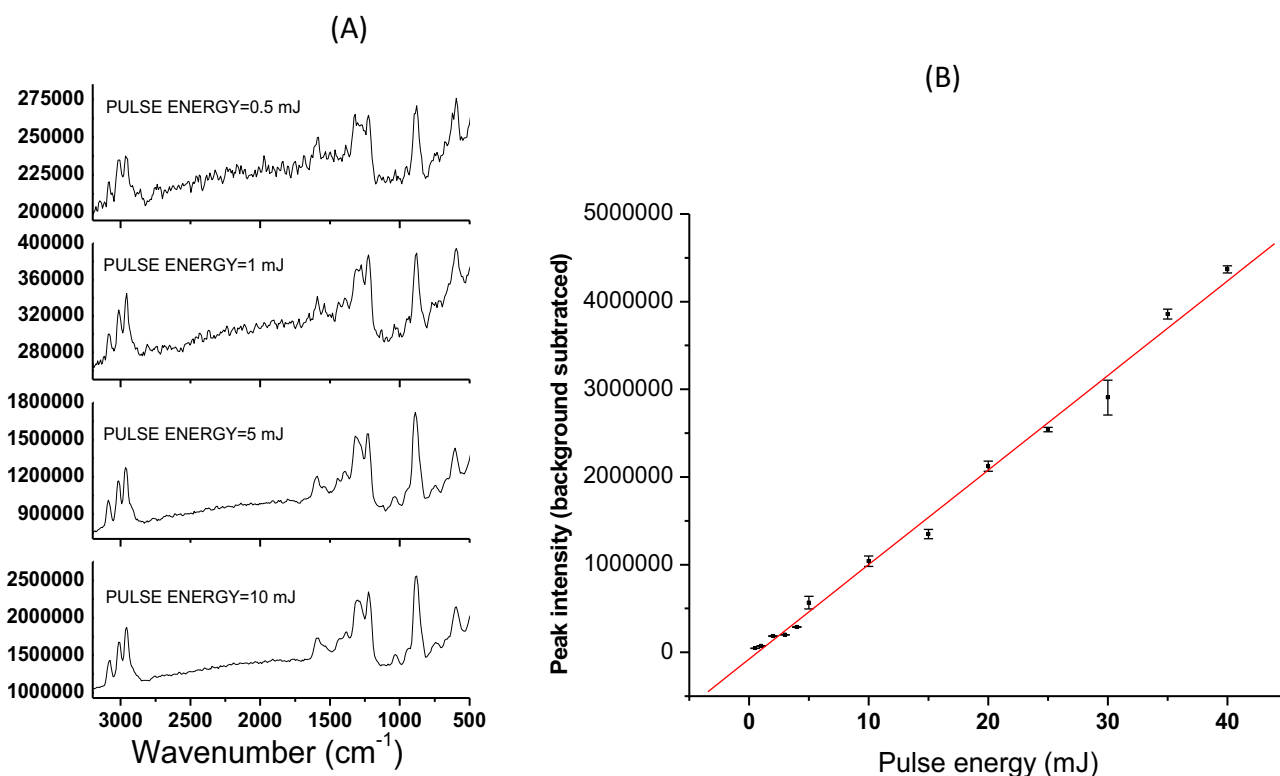
Fig. 5. A: Raman spectra of RDX with pulse energy of 0.5 mJ, 1 mJ, 5 mJ and 10 mJ. Intensifier, gate width, pulses accumulated are kept at 100, 20 ns and 1000 respectively and B: Variation of SNR of peak at 887 cm^{-1} w.r.t. pulse energy. The error bars represent the standard deviation (SD) of three time measurement.

accumulated were kept at 100, 20 ns and 1000 respectively. The sample was a pellet of RDX mixed with KBr at 1000 ppm (w/w). Fig. 5A shows recorded Raman spectra of RDX mixed with KBr (at 1000 ppm) were recorded with pulse energy varying in range 0.5–45 mJ. Raman spectra of RDX (at 1000 ppm) with pulse energy at 0.5 mJ, 1.0 mJ, 5.0 mJ and 10 mJ were shown in Fig. 5A. Significant improvement in SNR of Raman peaks was easily observed when pulse energy increased. The background subtracted intensity of Raman peak at 887 cm^{-1} (ring breathing mode) was found to be increased linearly with increase in pulse energy of laser as shown in Fig. 5B. The signal-to-noise ratio (SNR) of Raman peak at 887 cm^{-1} was observed to be increases from 35 at pulse energy of 1 mJ to 211 at pulse energy of 10 mJ respectively.

4.5. Raman spectra of explosives at ppm concentrations in stand-off mode

The effects of experimental parameters like gain of intensifier, number of pulses used in accumulation and pulses energy on the sensitivity were studied. Raman spectra of RDX mixed in KBr at concentrations 1000 ppm, 500 ppm and 100 ppm were recorded in stand-off mode from distance of 5 m as shown in Fig. 6.For achieving good sensitivity and recording of Raman spectra at these low concentrations, experimental parameters were set at optimised values. In recording of these Raman spectra, pulse energy of 20 mJ, repetition rate of 10 Hz, ICCD gain at 200, gate width of 100 ns were used and 1000 nos. of scans accumulated. Pulse energy of 20 mJ was found sufficient for detection of RDX at concentration of 100 ppm and hence higher pulse energy was not used.Raman spectra of RDX were successfully recorded at lowest tested concentration level i.e. 100 ppm in stand-off mode from distance of 5 m (Fig. 6). The intensity of Raman peaks decreased almost linearly as the concentration of sample came down from 1000 ppm to 500 ppm and then 100 ppm. Further the limit of detection (LoD) was estimated using Raman spectrum of RDX (peak at 887 cm^{-1}) of 100 ppm. In estimation of the detection limit, the intensity has to be atleast three times the standard deviation (STD) of the background [29]. By determining the standard deviation and applying a scaling factor to reduce the background-subtracted Raman signal to three times the calculated background STD, we estimated that the detection limit of RDX is approximately 10

parts-per-million. As the background-subtracted Raman intensity is linear to pulse energy and number of pulses used in accumulations, the limit of detection reaches at 1000 ppb using pulse energy of 100 mJ and accumulation of 2000 pulses.

5. Conclusion

This study illustrates that time-gated Raman spectroscopy has great potential in detecting explosives in trace mode i.e. on contaminated surfaces. The effect of various parameters i.e. pulse energy, repetition rate, ICCD gain and number of pulses on sensitivity was observed. Further the system was optimised for sensitivity at lower concentrations in terms of laser pulse energy, repetition rate, ICCD gain as well as number of pulses. Raman spectra of explosives and their derivatives were recorded in stand-off mode at a distance of 5 m. Raman spectra of RDX recorded with different concentrations down to 100 ppm with optimised experimental parameters and estimated limit of detection is 1000 ppb which is the requirement in trace detection. This study also gives a fare idea of optimised value of different specifications of laser, ICCDs, optics etc. and envisages design of time-gated Raman spectroscopy based compact and portable explosive detector for trace detection of explosive materials.

References

[1] J.S. Caygill, F. Davis, S.P.J. Higson, Talanta 88 (2012) 14–29.
[2] Z. Bielecki, J. Janucki, A. Kawalec, J. Mikołajczyk, N. Pałka, M. Pasternak, T. Pustelny, T. Stacewicz, J. Wojtas, Metrol. Meas. Syst. 19 (1) (2012) 3–28.
[3] D.J. Brenner, Radiology 259 (1) (2011) 6–10.
[4] M. Tourne, J. Forensic Res. S12 (2013) S12–002, doi:http://dx.doi.org/10.4172/2157-7145.
[5] S. Wallin, A. Pettersson, H. Ostmark, A. Hobro, Anal. Bioanal. Chem. 395 (1) (2009) 259–274.
[6] L.A. Skvortsov, Laser methods for detecting explosive residues on surfaces of distant objects, Quantum Electron. 42 (1) (2012) 1–11.
[7] K.E. Brown, M.T. Greenfield, S.D. McGrane, D.S. Morre, Advances in explosives analysis- part II: photon and neutron methods, Anal. Bioanal. Chem. 408 (2016) 49–65.
[8] E.L. Izake, Forensic and homeland security applications of modern portable Raman spectroscopy, Forensic Sci. Int. 202 (2010) 1–8.
[9] K.L. Gares, K.T. Hufziger, S.V. Bykov, S.A. Asher, Review of explosive detection methodologies and the emergence of standoff deep UV resonance Raman, J. Raman Spectrosc. 47 (2016) 124–141.
[10] J.L. Gottfried, F.C. De Lucia, Anal. Bioanal. Chem. 395 (2) (2009) 283–300.
[11] D.A. Cremers, L.J. Radziemski, Handbook of Laser-Induced Breakdown Spectroscopy, J. Wiley & Sons, Berlin, 2006.
[12] A.M. Popov, T.A. Labutin, N.B. Zorov, Moscow Univ. Chem. Bull. 64 (6) (2009) 366–377.
[13] D.W. Hahn, N. Omenetto, Appl. Spectrosc. 64 (12) (2010) 335–366.
[14] D.W. Hahn, N. Omenetto, Appl. Spectrosc. 66 (4) (2012) 347–419.
[15] J.L. Gottfried, F.C. De Lucia, C.A. Munson, A.W. Miziolek, J. Anal. At. Spectrom. 23 (2008) 205–216.
[16] C.M. Wynn, S. Palmacci, R.R. Kunz, M. Aernecke, Optical Express 19 (19) (2011) 18671–18677.
[17] J.D. White, F.A. Akin, H. Oser, D.R. Crosley, Appl. Opt. 50 (1) (2011) 74–81.
[18] C.M. Wynn, S. Palmacci, K. Clow R.R. Kunz, M. Rothshild, Proc. SPIE Int. Soc. Opt. Eng. 6954 (2008) 695407.
[19] C.M. Wynn, S. Palmacci, R.R. Kunz, K. Clow, M. Rothschild, Appl. Opt. 47 (31) (2008) 5767–5776.
[20] C. Wynn, S. Palmacci, R.R. Kunz, M. Rothschild, Opt. Express 18 (6) (2010) 5399–5406.
[21] X. Chen, L. Cheng, D. Guo, Y. Kostov, F.S. Choa, Opt. Express 19 (2011) 20251–20257.
[22] S. Gulia, DRDO Sci. Spectr. 86 (2015).
[23] J.B. Johnson, S.D. Allen, J. Merten, L. Johnson, D. Pinkham, S.W. Reeve, J. Spectrosc. (2014) 1–13.
[24] N. Petra, J. Zweck, A.A. Kosterev, S.E. Minkoff, D. Thomazy, Appl. Phys. B 94 (4) (2009) 673–680.
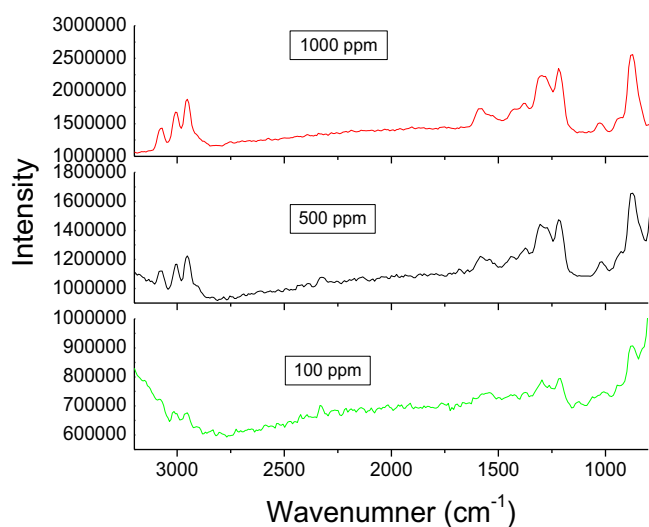
Fig. 6. Raman spectra of RDX at concentrations 1000 ppm, 500 ppm and 100 ppm. Pulse energy of 20 mJ, repetition rate of 10 Hz, ICCD gain at 200, gate width of 100 ns and accumulation of 1000 nos. of pulses.

[25] X. Chen, L. Cheng, D. Guo, Y. Kostov, F. Choa, Opt. Express 19 (21) (2011) 20251–20257.
[26] J.P. Waclawek, R. Lewicki, H. Moser, M. Brandstetter, F.K. Tittel, B. Lendl, Appl. Phys. B Lasers Opt. (2014), doi:http://dx.doi.org/10.1007/s00340-014-5809-y.
[27] M. Gaft, L. Nagli, Opt. Mater. 30 (11) (2008) 1739–1746.
[28] A.K. Misra, S.K. Sharma, C.H. Chio, P.G. Lucey, B. Lienert, Spectrochim. Acta A 61 (2005) 2281–2287.
[29] J.C. Carter, S.M. Angel, M.L. Snyder, J. Scaffidi, R.E. Whipple, J.G. Reynolds, Appl. Spectrosc. 59 (6) (2005) 769–775.
[30] S.A. Oladepo, K. Xiong, Z. Hong, S.A. Asher, J. Handen, I.K. Lednev, Chem. Rev. 112 (5) (2012) 2604–2628.
[31] E. Smith, G. Dent, Modern Spectroscopy -A Raman Practical Approach, John Wiley & Ltd. Sons, 2005.
[32] J.R. Ferraro, K. Nakamoto, C.W. Brown, Introductory Raman Spectroscopy, Academic Press, London, 2003.
[33] D.A. Long, The Raman Effect −A Unified Treatment of the Theory of Raman Scattering by Molecules, John Wiley & Sons, 2002.
[34] S.A. Asher, Handbook of Vibrational Spectroscopy, J. Wiley & Sons, 2002.
[35] W.A. Al-Saidi, S.A. Asher, P. Norman, J. Phys. Chem. 116 (2012) 7862–7872.
[36] A. Ehlerding, I. Johansson, S. Wallin, H. Ostmark, Int. J. Spectrosc. 2012 (2012) Article ID 158715.
[37] Z. Gong, H. Du, F. Cheng, C. Wang, C. Wang, M. Fan, ACS Appl. Mater. Interfaces 6 (24) (2014) 21931–21937.
[38] P.M. Mercado, S.P. Rivera, Int. J. Spectrosc. 2012 (2012) Article ID 716527.
[39] H. Syed, G.K. Podagatlapalli, M.A. Mohiddon, V.R. Soma, Adv. Mater. Lett. 6 (12) (2015) 1073–1080.
[40] P. Matousek, I.P. Clark, E.R. Draper, M.D. Morris, A.E. Goodship, N. Everall, M. Towrie, W.F. Finney, A.W. Parker, Appl. Spectrosc. 59 (4) (2005) 393–400.
[41] J. Guicheteau, R. Hopkins, Proc. SPIE 9824, Chemical, Biological, Radiological, Nuclear, and Explosives (CBRNE) Sensing XVII, 98240G (May 12, 2016); 10.1117/12.2229157.
[42] B. Zachhuber, H. Ostmark, T. Carlsson, Spatially offset hyperspectral stand-off Raman imaging for explosive detection inside containers, Proc. SPIE 9073 (2014), doi:http://dx.doi.org/10.1117/12.2053251.
[43] J.H. Chung, S.G. Cho, Bull. Korean Chem. Soc. 35 (12) (2014) 3547–3552.
[44] S.K. Sharma, S.M. Angel, M. Ghosh, H.W. Hubble, P.G. Lucey, Appl. Spectrosc. 56 (6) (2002) 699–705.
[45] J.H. Chung, S.G. Cho, Bull. Korean Chem. Soc. 34 (6) (2013) 1668–1672.
[46] B.H. Hokr, J.N. Bixler, G.D. Noojin, R.J. Thomas, B.A. Rockwell, V.V. Yakovlev, M.O. Scully, Proc. Natl. Acad. Sci. 111 (34) (2014) 12320–12324.
[47] D.D. Tuschel, A.V. Mikhonin, B.E. Lemoff, S.A. Asher, Appl. Spectrosc. 64 (4) (2010) 425–432.
[48] A. Pettersson, S. Wallin, H. Östmark, A. Ehlerding, I. Johansson, M. Nordberg, H. Ellis, A. Khalili, Proc. SPIE. 7664 (2010) (76641K).
[49] R. Forest, F. Babin, D. Gay, N. Ho, O. Pancrati, S. Deblois, S. Desilets, J. Maheux, Proc. SPIE 8358 (2012) (83580M.).
[50] T.A. Reichardt, S.E. Bisson, T.J. Kulp, Sandia National Labs (2011) SAND2011-7955.
[51] S.V. Bykov, M. Mao, K.L. Gares, S.A. Asher, Appl. Spectrosc. 69 (8) (2015) 895–901.
[52] R.L. McCreery, Raman Spectroscopy for Chemical Analysis, John Wiley & Sons Inc., New York, 2005.
[53] T.L. Andrew, T.M. Swager, J. Org. Chem. 76 (9) (2011) 2976–2993.
[54] R.R. Kunz, K.E. Gregory, M.J. Aernecke, M.L. Clark, A. Ostrinskaya, A.W. Fountain 3rd, J. Phys. Chem. A 116 (14) (2012) 3611–3624.
[55] K.L. Gares, S.V. Bykov, B. Godugu, S.A. Asher, Appl. Spectrosc. 68 (1) (2014) 49–56.
[56] K.L. Gares, S.V. Bykov, B. Godugu, S.A. Asher, Appl. Spectrosc 69 (5) (2015) 545–554.
[57] A.V. Parisi, M.G. Kimlin, J.C.F. Wong, R.A. Fleming, Photodermatol. Photoimmunol. Photomed. 12 (2) (1996) 57–65.
[58] M.F. Holick, Anticancer Res. 36 (3) (2016) 1397–1401.
[59] S. Gulia, V. Gambhir, M.N. Reddy, High Energy Materials Conference and Exhibit (HEMCE), High Energy Materials Research Laboratory, DRDO, 2009.
[60] S. Gulia, M.N. Reddy, V. Gambhir, R. Sharma, National Laser Symposium (NLS-23), Sri Venkateswara University, India, 2014.
[61] P.S. Santos, N.S. Goncalves, J. Raman Spectrosc. 20 (1989) 551–554.
[62] X.M. Yang, D.A. Tryk, K. Hashimoto, A. Fujishima, J. Phys. Chem. B 102 (1998) 4933–4943.
[63] W.A. Al-Saidi, S.A. Asher, P. Norman, J. Phys. Chem. A 116 (2012) 7862–7872.
[64] Nahla A, Hatab b, GyulaEres, Paul Hatzinger and BaohuaGu, J. Raman Spectrosc. 41 (2010) 1131–1136.
[65] K. Sakamoto, G. Mizutani, S. Ushioda, Phys. Rev. B Condens. Matter 48 (12) (1993) 8993–9005.
[66] E.D. Emmons, J.A. Guicheteau, A.W. Fountain III, S.D. Christesen, Appl. Spectrosc. 66 (6) (2012) 628–635.

Detection of explosive materials and their precursors through translucent commercial bottles using spatially offset Raman spectroscopy using excitation wavelength in visible range

Sanjay Gulia
Kamal K. Gulati
Vijayeta Gambhir
Rinku Sharma

Detection of explosive materials and their precursors through translucent commercial bottles using spatially offset Raman spectroscopy using excitation wavelength in visible range

Sanjay Gulia,[a,b,*] Kamal K. Gulati,[a] Vijayeta Gambhir,[a] and Rinku Sharma[b]
[a]Laser Science and Technology Centre, New Delhi, India
[b]Delhi Technological University, New Delhi, India

Abstract. The detection and analysis of hazardous materials through opaque barriers is important for law enforcement agencies. Conventional Raman spectroscopy provides fingerprint signatures of materials but lacks the ability to detect materials through opaque containers. Spatially offset Raman spectroscopy (SORS) overcomes the limitation of conventional Raman spectroscopy and allows the detection of materials through most commercial bottles and packaging materials. Moreover, SORS has the potential to detect hazardous materials through colored glass bottles, high-density polyethylene (HDPE) bottles, Teflon layers, etc., which is required in the screening of commercial packaging at airports and other vital facilities. SORS was investigated in the visible range with a 532-nm excitation source for the detection of urea and sodium nitrate through commercial packaging, i.e., a white HDPE bottle with a thickness of 1 mm. The effects of the spatial offset and integration time on the Raman spectra of the contents and container were evaluated. The trend of the change in the relative contributions from the contents and container was studied by varying the offset and integration time. P-nitrobenzoic acid was detected through the colored bottles in the study of reduction of fluorescence in the SORS effect. © 2019 Society of Photo-Optical Instrumentation Engineers (SPIE) [DOI: 10.1117/1.OE.58.12.127102]

Keywords: spatially offset Raman spectroscopy; explosive detection; translucent containers.

Paper 190690 received May 21, 2019; accepted for publication Dec. 5, 2019; published online Dec. 28, 2019.

1 Introduction

The detection of explosives, hazardous chemicals, and biological agents through opaque packages is required by law enforcement agencies.[1–6] The development of a reliable technique with minimal false alarms is necessary. Various spectroscopic techniques, such as laser-induced breakdown spectroscopy (LIBS), Raman spectroscopy, cavity ring-down spectroscopy (CRDS), and laser photoacoustic spectroscopy (LPAS), are used to analyze the signatures of materials.[7–11] The LIBS technique involves the generation of plasma, and therefore, requires a high power density on the sample, resulting in permanent mass loss of the sample. Furthermore, it does not provide molecular information regarding the sample; rather, it indicates the elemental composition of the sample material.[12,13] Other spectroscopy techniques, such as CRDS,[14,15] LPAS,[16–18] and photothermal imaging,[19] require tunable laser sources. Therefore, a material can only be screened if its vibrational absorption spectra are within the tunable range of the laser.

Raman spectroscopy techniques, such as conventional Raman spectroscopy, time-gated Raman spectroscopy, and surface-enhanced Raman spectroscopy (SERS), have the ability to screen for explosives and other hazardous materials, as they require no tunable light source and provide a high level of selectivity.[20–23] SERS is being investigated by scientists for the detection of low concentrations of explosives in the vapor phase in air. It has been used to detect

vapors of materials with a high vapor pressure, such as 2,4-dinitrotolune, in a controlled laboratory environment.[24] However, in practice, the detection of extremely low vapor concentrations is necessary in the case of hidden and buried explosive objects because of the low vapor pressure of explosive materials.[25,26]

Conventional Raman spectroscopy has been extensively investigated for bulk detection as it provides fingerprint signatures of materials but has limitations for the detection of explosives through opaque containers.[27,28] In the real scenario of screening of materials at airports, railway stations, and other checkpoints, materials must be detected through different types of containers and packages, such as colored glass, transparent plastic bottles, high-density polyethylene (HDPE) bottles, and tetra packing. Spatially offset Raman spectroscopy (SORS) offers a solution for the detection of materials through most nonmetallic containers, such as colored glass bottles, HDPE bottles, and Teflon layers.[29–34] SORS is based on the collection of Raman signals from spatial regions offset from the point of illumination on the sample surface, as depicted in Fig. 1.

The majority of photons in an excitation beam undergo multiple Rayleigh scattering in the probed medium such as random walk, and produce Raman photons that again randomly migrate. This process is referred to as Raman photon migration.[29] Thus, a Raman scattering signal may be collected at a particular offset distance from the illuminating point, and the intensity of the Raman signal of the contents and container depends on the offset distance. The spatial

*Address all correspondence to Sanjay Gulia, E-mail: sanjay-gulia@lastec.drdo.in
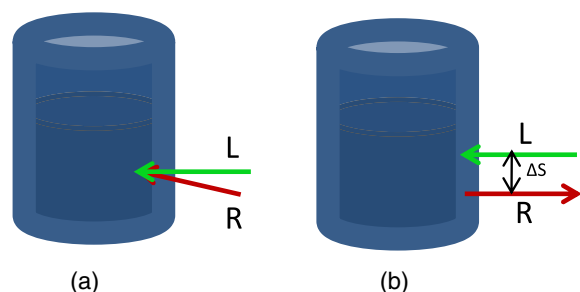
Fig. 1. Geometrical configurations. (a) Conventional back-scattering Raman; (b) SORS. L, Laser beam; R, Raman scattering; and ΔS, spatial offset.

offset reduces the interfering Raman and fluorescence signals from the container.[35–43] The interfering Raman and fluorescence signals from the container are strongest at the illuminating point and decrease in strength with an increase in the spatial offset between the illuminating and collection points.[44,45]

The SORS technique has been investigated in the near-infrared (NIR) region using different excitation wavelengths, e.g., 785,[37,41,42,44] 830,[30,32,35,36,38,40,45] and 1064 nm.[46,47] Though studies with excitation in the ultraviolet (UV) range were also reported for explosive detection,[48–51] no SORS study reported with UV excitation, being low transmission of UV wavelengths through glass containers, translucent containers, etc.[52] The excitation wavelength of 532 nm in the visible region has also been employed for long-range stand-off SORS using expensive pulsed lasers and intensified charge-coupled device (CCD) detectors for depth profiling of target samples, which is important for medical applications.[53–55] However, detection using 532 nm as the excitation wavelength with a CCD has not been extensively investigated in SORS studies and is avoided in conventional Raman spectroscopy owing to a fluorescence problem.[56] For small ranges, a continuous-wave (CW) laser could be used with a CCD without any appreciable effect of ambient light.[57]

Commercial bottles, particularly those made of HDPE, exhibit no fluorescence or weak fluorescence, and in addition, explosives inherently exhibit hardly any fluorescence,[58,59] though different fluorescence-based techniques, such as photodissociation-cum-laser-induced fluorescence technique[60] and amplified fluorescence polymers-based technique,[61] were reported for detection of explosive materials. Therefore, SORS may offer better sensitivity with excitation in the visible region compared with the NIR region, owing to the inversely proportional relationship of the Raman cross section with the fourth power of the wavelength[27,28] and the high quantum efficiency of CCD detectors in the visible region.[62]

In this study, we developed a stand-off SORS system capable of detecting a variety of hazardous materials through commercial containers (i.e., an HDPE bottle) with an excitation wavelength of 532 nm using a CW laser and a CCD detector. The effects of the integration time and spatial offset on the Raman spectra of urea and sodium nitrate, which were recorded through a bottle, were examined. The intensities (background-subtracted) of the Raman spectra of the contents (urea and sodium nitrate) and container were plotted with respect to the offset. The SORS ratio was also calculated and plotted for different offset values. The intensity of the peaks for both the contents and the container decreased with

an increase in the offset. The photon diffusion in the container was smaller than that in the contents due to the large volume of interaction of the contents. Therefore, the intensity of the Raman signal decreased quickly in the case of the container. The effects of the diffusion characteristics of the content materials on the SORS ratio were also investigated. Further, the variation of the peak intensity with respect to the integration time was examined while keeping the offset constant. P-nitrobenzoic acid (PNBA) was detected through colored bottles in the study of reduction of fluorescence in the SORS effect.

2 Experimental Details and Materials

A schematic of the SORS-based experimental setup is depicted in Fig. 2(a). The setup included a CW laser, a CCD-coupled spectrometer, transreceiver (TR) optics, a mirror, and filters. The laser was a commercially available CW 532-nm second-harmonic Nd:YAG laser (SDL-532-LN-400T, M/s Shanghai Dream Lasers Technology, China) with variable optical power in the range of 0 to 400 mW. An optical power of 150 mW was used for the experiments. The TR optics had a 70-mm diameter. A longpass filter (LPF, M/s Semrock) was used to filter out the Rayleigh scattering at a 532-nm wavelength. The laser beam was guided to the sample container by a high reflective (HR) mirror, the LPF with an angle of incidence of 45 deg, and the TR optics. The backscattered Raman signal was collected and collimated using the TR optics. The collimated beam comprised a Rayleigh-scattered optical signal (532 nm) and a Raman scattered optical signal (>532 nm). The Rayleigh signal was filtered out by LPFs. The desired optical signal, i.e., the Raman scattered signal, was coupled to a spectrometer (HR4000, Ocean Optics) by using focusing optics. The required offset between the laser beam and the receiving axis could be inserted by using the tilting mechanism in the mount of the HR mirror. The experiments were conducted in the stand-off mode at a distance of 30 cm. SORS studies were performed on two content materials—urea and sodium nitrate (Loba Chemie Pvt. Ltd., India)—using their respective commercial containers [white HDPE bottles with a thickness of ~1 mm, as shown in Fig. 2(b)]. In addition, PNBA (Sigma Aldrich) was used in the study of fluorescence reduction by the SORS effect.

3 Results and Discussion

The stand-off detection of the content materials was performed at a distance of 30 cm. The optical power of the laser was kept at 150 mW. The integration time and spatial offset used for recording the Raman spectra were varied, as described herein. Urea was used in this study because it is a precursor of explosive materials such as urea nitrate. Sodium nitrate was employed because it can be mixed with potassium nitrate to produce explosive materials.[63] First, the Raman spectra of pure urea and sodium nitrate were recorded, as shown in Fig. 3.The potential of the SORS technique for detecting the materials through translucent containers was demonstrated. The effects of the spatial offset and integration time on the Raman signatures recorded through the container were examined. The intensities (background-subtracted) of the most intense Raman peaks of the content materials (peaks at 1011 and 1068 cm^{-1} for urea and sodium nitrate, respectively) and the container (peak at 2890 cm^{-1})

(a)

(b)　　　　　　(c)
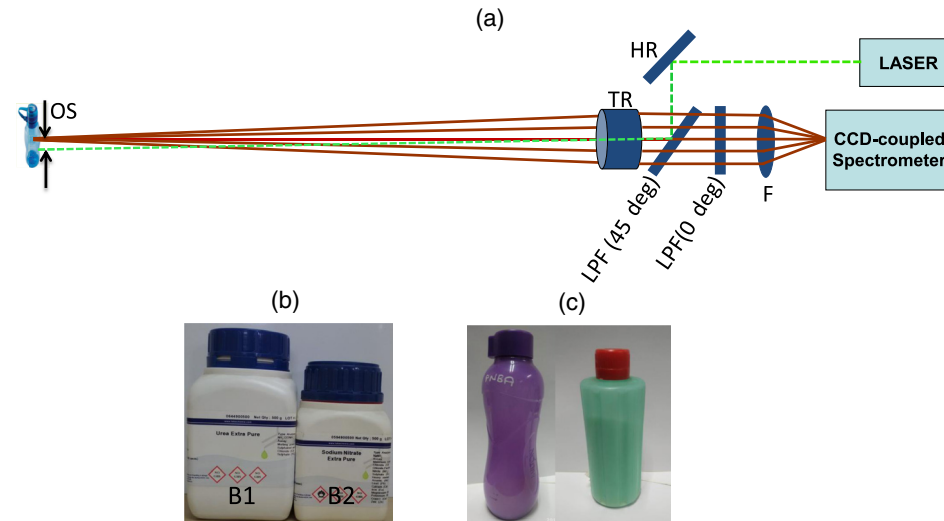
Fig. 2 (a) Schematic of SORS-based experimental setup for stand-off detection through translucent containers. Laser beam and Raman scattered signal represented by dotted lines (green) and solid lines (dark red). HR: High reflecting mirror with AOI = 45 deg. LPF (45 deg): Longpass filter with AOI = 45 deg. TR: Trans-receiver optics. LPF (0 deg): Longpass filter with AOI = 0 deg. F: Focusing optics. OS: Offset inserted. (b) Commercial bottles containing sample material urea (B1) and sodium nitrate (B2); (c) violet coloured bottle (C1) and green coloured bottle (C2) used for experiments of fluorescence reduction by SORS effect.
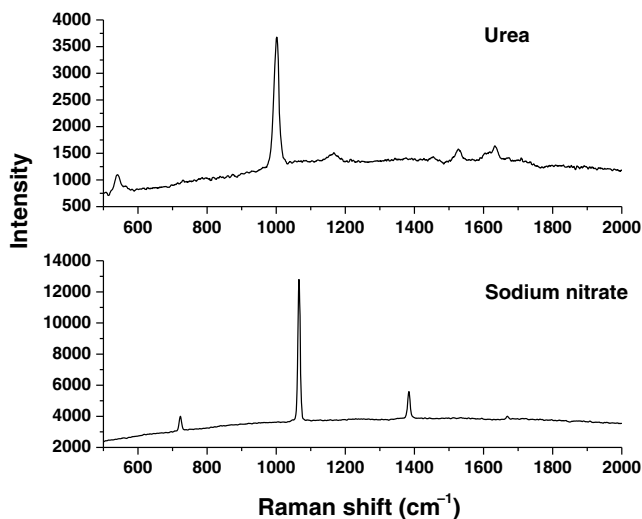
Fig. 3 Raman spectra of pure urea and sodium nitrate recorded at integration times of 10 and 2 s, respectively.

were plotted with respect to the spatial offset and integration time for both materials. Depending on the diffusion characteristics of urea and sodium nitrate, different trends were observed in the variation of the intensity with respect to the offset.

3.1 Spatially Offset Raman Spectroscopy Effect

The capability of SORS for the detection of explosive materials concealed in plastic containers was investigated, as shown in Fig. 4. Reference Raman spectra of the plastic containers and the content materials (urea and sodium nitrate) are shown at the top and bottom in Figs. 4(a) and 4(b), respectively. Both the reference spectra were recorded in the stand-off mode with a distance of 30 cm and an integration time of 2 s. The Raman spectra of the content

materials were recorded through the container in two modes: conventional Raman spectroscopy (laser incident spot and collection spot coinciding) and SORS (spatial offset of 6 mm between laser incident spot and collection point). The spectra recorded using conventional Raman spectroscopy were dominated by the Raman signatures of the container, and the signatures of the content materials were suppressed and not clearly observable. In contrast, the Raman spectra recorded in the SORS mode clearly exhibited the Raman signatures of urea and sodium nitrate, as shown in Fig. 4. Thus, SORS facilitated the recording of the weak Raman signatures of the content materials by suppressing the strong Raman signatures of the containers.

3.2 Effect of Spatial Offset

The effect of the spatial offset on the Raman spectra of the content materials, i.e., urea and sodium nitrate, recorded through plastic containers (both containers had the same parameters) was examined, as shown in Figs. 5 and 6, respectively. The Raman spectra were recorded while varying the spatial offset from 0 to 10 mm in steps of 2 mm for both content materials. The stand-off distance and integration time were kept at 30 cm and 4 s, respectively. These spectra comprised the Raman signatures of the content materials and the container. However, their relative contributions changed with respect to the spatial offset. At zero spatial offset, the Raman signatures of the contents were almost obscured by those of the container. As the spatial offset increased, all the Raman peaks of the container decreased significantly faster than those of the content materials, as shown in Figs. 5(a) and 6(a). This was because of the diffusion of both excitation photons and Raman scattered photons in the content materials, e.g., random walk, along the diffusion path.[30] Consequently, the interaction volume of the excitation photons and the distribution of "produced Raman photons" in the lateral direction in the content material increased, which
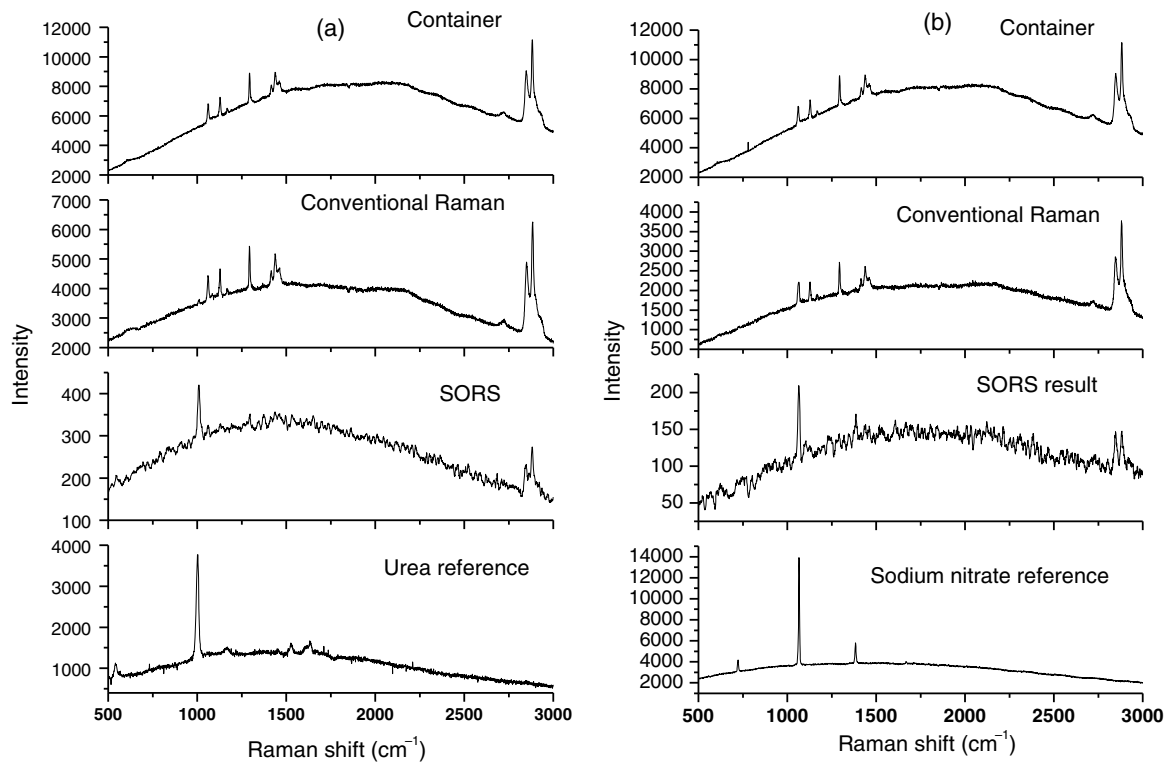
Fig. 4 Conventional Raman and SORS spectra of (a) urea and (b) sodium nitrate in HDPE white bottles (B1 and B2), whereas the top and bottom show reference spectra of the container and pure (a) urea and (b) sodium nitrate, respectively.
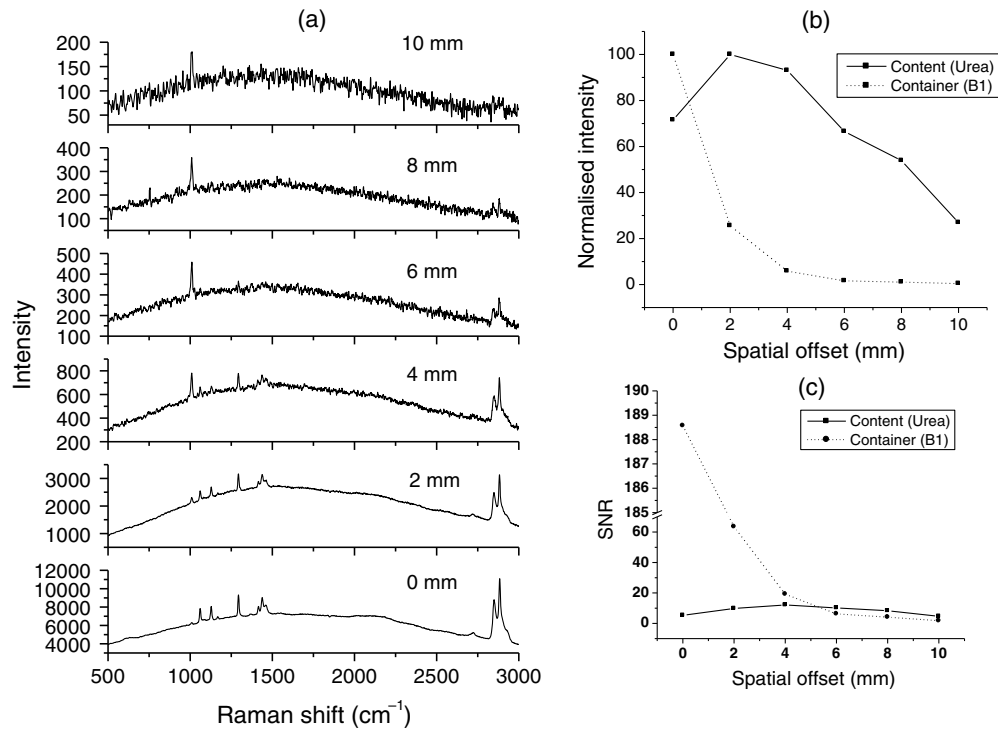
Fig. 5 (a) SORS spectra of urea recorded through a plastic container in the stand-off mode at different values of spatial offset. Spatial offset varied from 0 to 10 mm in steps of 2 mm. Stand-off distance is kept at 30 cm and integration at 4 s. (b) The background-corrected intensity of Raman peaks of urea at 1011 cm^{-1} and container at 2890 cm^{-1} plotted with respect to the spatial offset C. (c) The intensity of both bands normalized (maximum set to 100%) and plotted with respect to the spatial offset.

was not the case for the container. Figures 5(b) and 6(b) show the trend of the change in the normalized intensity (background-subtracted) of the most intense Raman peaks of the content materials, i.e., the peak at 1011 cm^{-1} for urea and 1068 cm^{-1} for the sodium nitrate and container (2890 cm^{-1}), with an increase in the spatial offset. The signal-to-noise ratios (SNRs) of the most intense peaks of urea and sodium nitrate were plotted with respect to the spatial offset, as shown in Figs. 5(c) and 6(c), respectively. The plots of the normalized intensity revealed the trends of the change in the intensity of the Raman peaks of the contents and container. The SNR plots also indicated the sensitivity of the experimental setup for the Raman signatures of the contents and container. The SNRs of the Raman peaks of the contents were lower than that of the container at zero offset. With an increase in the offset, this trend of the SNR of the Raman peaks for the contents and container was reversed, i.e., the SNR was higher for the contents than for the container with an offset of >4 mm (for sodium nitrate) and >5 mm (for urea). The difference between the SNRs of the Raman peaks of the contents and container increased up to an offset of 10 mm and then started decreasing. The SNRs of the Raman peaks were calculated based on the baseline-subtracted intensity of the respective peak in the Raman spectrum divided by the root-mean-square (RMS) noise. The RMS noise was estimated by taking one-fifth of the peak-to-peak variation for the flattest region of the Raman spectra between 1850 and 2000 cm^{-1}.[21]

3.3 Diffusion-Dependent Trend in Intensity Variation with Respect to Spatial Offset

The dependence in the normalized intensities of the most intense Raman peaks of urea (at 1011 cm^{-1}) and the container (at 2890 cm^{-1}), as well as sodium nitrate (at 1068 cm^{-1}) and the container (at 2890 cm^{-1}), were plotted with respect to the spatial offset, as shown in Figs. 5(b) and 6(b), respectively. The intensities of the peaks of the content materials and container were normalized by setting the maximum intensity to 100%. The trend of the change in the intensity (normalized) was clearly depicted for both content materials. There was a difference between the trends of the change in intensity with respect to the spatial offset for the two content materials. With an increase in the spatial offset, the intensity of the Raman peak of urea first increased and then decreased [Fig. 5(b)], whereas the intensity of the Raman peak of sodium nitrate only decreased [Fig. 6(b)]. The different trends of the variation in intensity were due to the different photon-diffusion efficiencies of the urea and sodium nitrate. The Raman peak intensity for urea initially increased due to its higher diffusion efficiency. The intensity of the Raman peak of the container decreased continuously with an increase in the spatial offset. As the thickness of the container was significantly smaller than that of the contents, the diffusion mainly occurred in the contents, with no appreciable diffusion due to the container wall.[64] Thus, the intensity of the Raman peaks of the container decreased sharply with the increasing spatial offset.
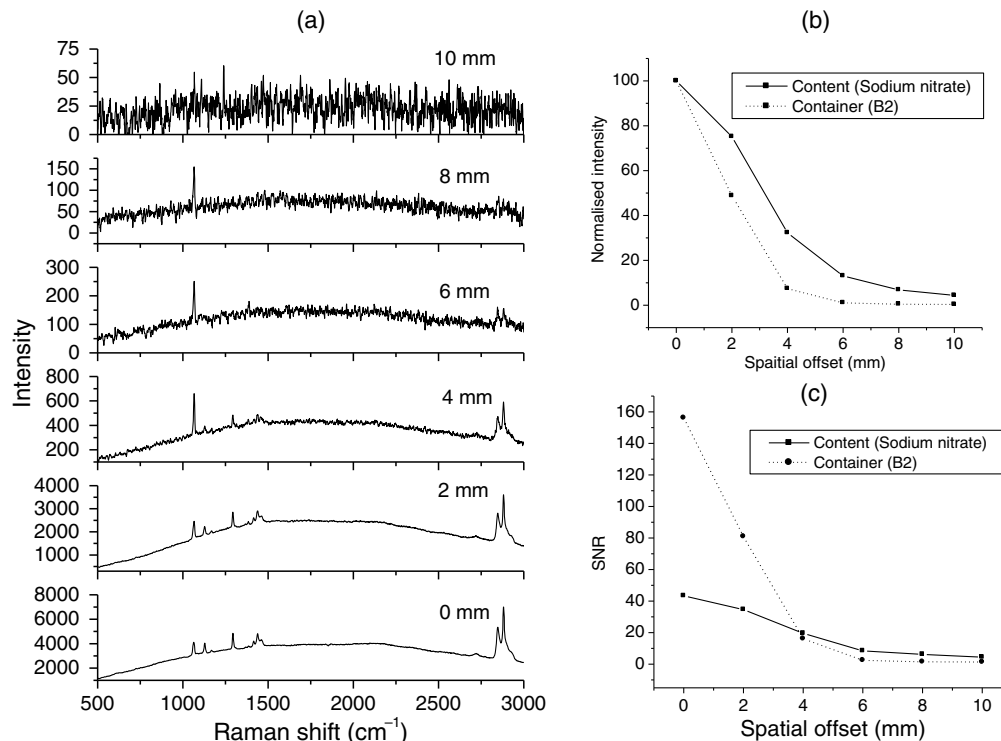
Fig. 6 (a) SORS spectra of sodium nitrate recorded through a plastic container in the stand-off mode at different values of spatial offset. Spatial offset varied from 0 to 10 mm in steps of 2 mm. Stand-off distance is kept at 30 cm and integration at 4 s. (b) The background-corrected intensity of Raman peaks of urea at 1068 cm^{-1} and container at 2890 cm^{-1} plotted with respect to the spatial offset C. (c) The intensity of both bands normalized (maximum set to 100%) and plotted with respect to the spatial offset.

3.4 Spatially Offset Raman Spectroscopy Ratio

The SORS ratio indicated the relative rate of decay of the intensities of the Raman peaks of the contents and container. This is defined as the ratio of the intensity of the Raman peak of the contents at a particular spatial offset(s) to that of the container at the same spatial offset(s) divided by the intensity ratio of the contents to the container at zero spatial offset[64] and is given by the following equation:

$$\text{SORS ratio}\,(s) = \frac{I_{\text{content}}(s)/I_{\text{container}}(s)}{I_{\text{content}}(0)/I_{\text{container}}(0)}. \qquad (1)$$

Here, $I_{\text{content}}(s)$ and $I_{\text{container}}(s)$ are the Raman signal intensities of the contents and container, respectively, at the spatial offset s and $I_{\text{content}}(0)$ and $I_{\text{container}}(0)$ are those at zero offset.

The equation of SORS ratio shows that SORS ratio is dependent on the intensities of both the contents and container materials. The intensity of Raman peaks of container will again mainly depend on its material and thickness. Here, we have used different content materials, i.e., urea and sodium nitrate in same type of container, i.e., HDPE bottles. In calculations of the SORS ratio, the intensities (background-subtracted) of the Raman peaks of urea, sodium nitrate, and the containers at 1011, 1068, and 2890 cm^{-1}, respectively, were used. The SORS ratio was calculated for different values of the spatial offset in the range of 0 to 10 mm, with increments of 2 mm. The calculated SORS ratios were plotted with respect to the spatial offset, as shown in Fig. 7.

With the increasing spatial offset, the SORS ratio initially (up to 2 mm) increased slowly and subsequently increased almost linearly. At small spatial offsets, the diffusion was mainly due to the container. Therefore, the relative contribution of the Raman signal from the contents increased slowly with the increasing spatial offset. The SORS ratio increased at a higher rate for urea than for sodium nitrate. This is attributed to the higher diffusion efficiency of urea, which resulted in a slower intensity decay of the Raman
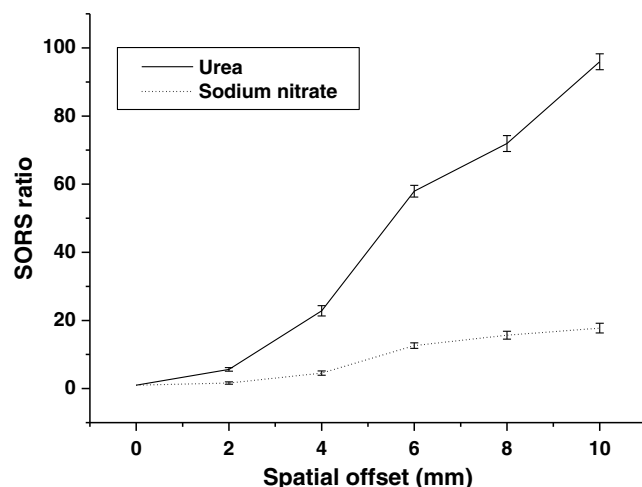
peaks of urea compared with those of sodium nitrate. The SORS ratio initially, i.e., at low offset values, varies at slow rate and this slow rate is attributed to the thickness of the container.[65]

3.5 Effect of Integration Time

The effect of the integration time (i.e., the time during which the Raman signal was acquired) on the Raman spectra of the content materials, i.e., urea and sodium nitrate, was examined in the range of 2 to 10 s with steps of 2 s, as depicted in Figs. 8(a) and 9(a), respectively. The stand-off distance and spatial offset were kept at 30 cm and 6 mm, respectively. The Raman peaks of the content materials were relatively strong compared with those of the container at a spatial offset of 6 mm (Figs. 5 and 6). These spectra included the Raman signatures of both the contents and the container. However, their relative contributions did not change as the integration time was varied; rather, the relative contributions were dependent on the spatial offset. The trends of the change in intensity (background-corrected) for the most intense Raman peaks of the content materials (at 1011 cm^{-1} for urea and 1068 cm^{-1} for sodium nitrate) and the container (2890 cm^{-1}) with an increase in the integration time are shown in Figs. 8(b) and 9(b). The intensities of the Raman signals of the content materials and container increased almost linearly with respect to the integration time. At a large spatial offset, i.e., 6 mm, the Raman signal intensity of the contents was not appreciable with a short integration time, i.e., 2 s, although it was higher than that of the container. Therefore, the spatial offset and integration time must be carefully optimized to achieve the desired result and these parameters are related.[66] The optimized values of both parameters depend on the nature of the contents and container.

3.6 Fluorescence Reduction by Spatially Offset Raman Spectroscopy Offset

Because SORS is a potential technique for detecting explosive through translucent containers, it has to be explored for fluorescence reduction that is caused by the colored containers as the explosive materials themselves do not exhibit the fluorescence. The colored containers used exhibited the fluorescence in the case of conventional Raman spectroscopy. The NIR excitation surely helps in the reduction of fluorescence in conventional Raman spectroscopy but at the cost of sensitivity.[62]

Here, the fluorescence reduction is explored with the SORS technique even with excitation in visible range (532 nm). In this study, conventional Raman spectra and SORS spectra of PNBA contained in two colored bottles, i.e., violet bottle (C1) and green bottle (C2), were recorded, as shown in Figs. 10(a) and 10(b), respectively. In addition, reference Raman spectra of PNBA and both the colored bottles were also recorded. Both the bottles (C1 and C2) exhibited intense fluorescence as could be observed in the spectra at the top of Figs. 10(a) and 10(b). It could also be observed that the conventional Raman spectra recorded through both bottles C1 and C2 exhibited fluorescence too intense to observe the Raman lines of the contents, i.e., PNBA. The CCD of the spectrometer got saturated due to high strength of fluorescence of the container and produced a flat portion in spectra due to the blooming effect of the CCD.[67] Raman peaks of PNBA were obscured by the strong fluorescence.

Fig. 7 SORS ratio with respect to the spatial offset. SORS ratio calculated using the background-corrected intensity of Raman peaks of urea at 1011 cm^{-1}, sodium nitrate at 1068 cm^{-1}, and container at 2890 cm^{-1}.
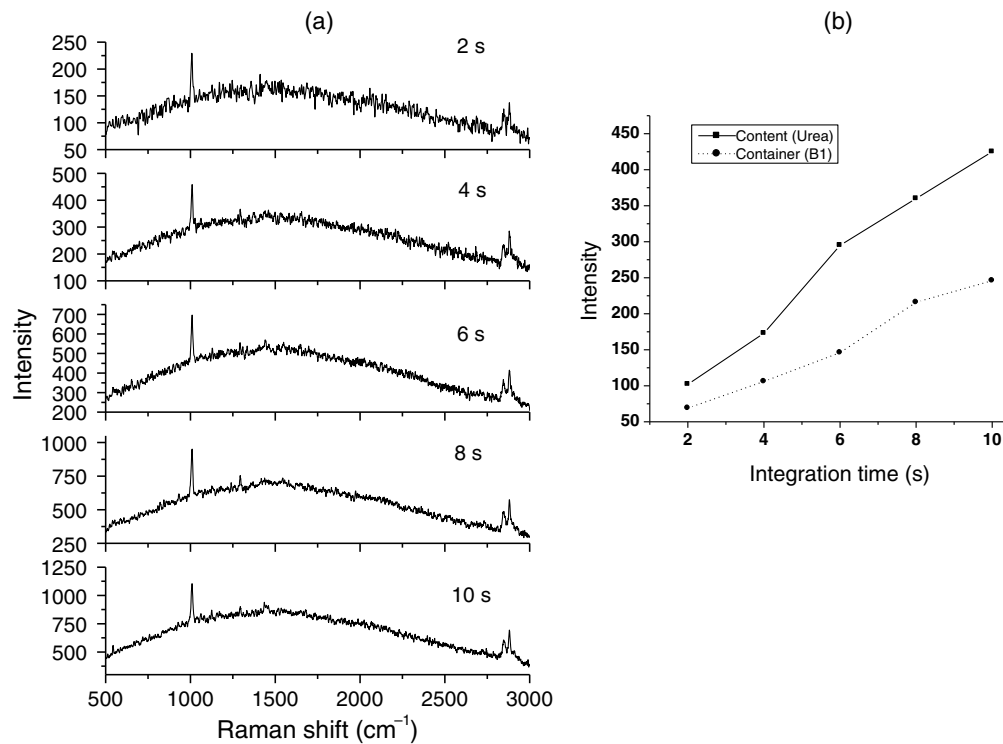
Fig. 8 (a) SORS spectra of urea recorded through a plastic container in the stand-off mode at different integration times. Integration times varied from 2 to 10 s in steps of 2 s. Stand-off distance is kept at 30 cm and spatial offset at 6 mm. (b) The background-corrected intensity of Raman peaks of urea at 1011 cm^{-1} and container at 2890 cm^{-1} plotted with respect to the integration time spatial offset.
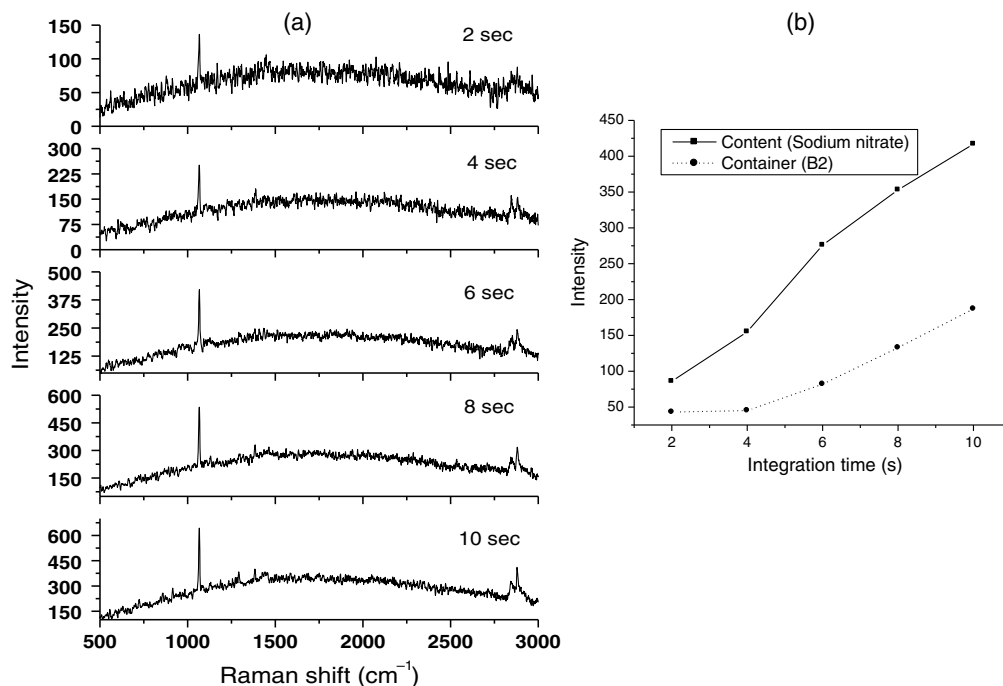
Fig. 9 (a) SORS spectra of sodium nitrate recorded through a plastic container in the stand-off mode at different integration times. Integration times varied from 2 to 10 s in steps of 2 s. Stand-off distance is kept at 30 cm and spatial offset at 6 mm. (b) The background-corrected intensity of Raman peaks of urea at 1068 cm^{-1} and container at 2890 cm^{-1} plotted with respect to the integration time spatial offset.

After inserting an offset of 10 mm, SORS spectra of PNBA were recorded through these fluorescent bottles, i.e., C1 and C2, using integration times of 6 and 10 s, respectively. SORS spectra exhibited an appreciable reduction in the fluorescence and all the intense Raman peaks could be clearly observed. SORS spectra recorded by inserting the offset were generated from the depth of the contents, i.e., PNBA, rather than from the container, i.e., the colored
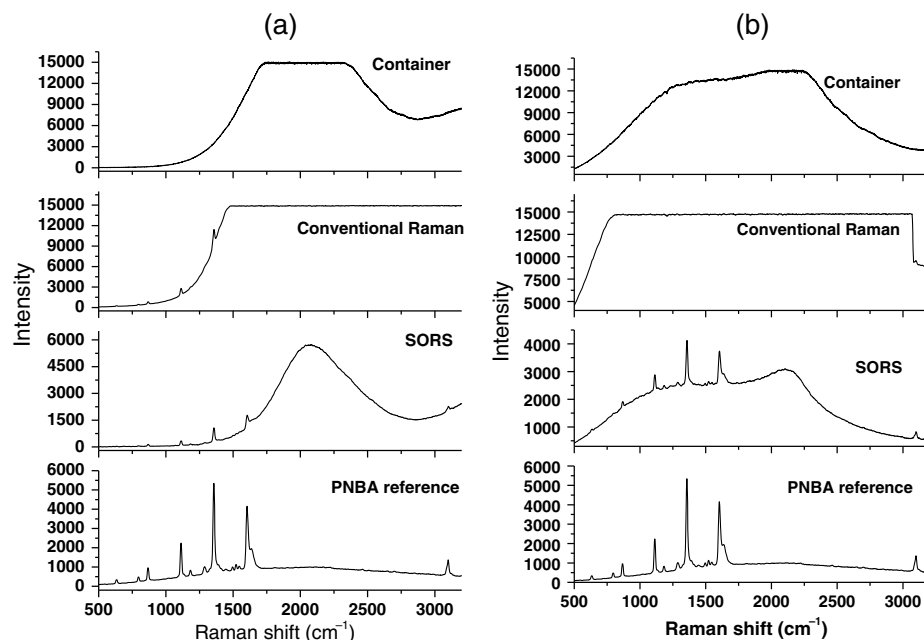
Fig. 10 Conventional Raman and SORS spectra of PNBA in (a) violet-colored bottle (C1) and (b) green-colored bottle (C2), whereas the top and bottom show reference spectra of the container and pure PNBA, respectively. SORS spectra of PNBA were recorded at an offset of 10 mm and integration times of 6 and 10 s in bottles C1 and C2, respectively.

fluorescent bottles, C1 and C2, as is the case with the conventional Raman spectra and hence exhibited a drastic decrease in the fluorescence. Thus, it was clearly shown that SORS could play a role in reducing the fluorescence of containers even with excitation in the visible range and hence without compromising the sensitivity.

4 Conclusion

This study demonstrated the potential application of SORS for detecting explosives and their precursors concealed in plastic commercial packages, such as HDPE bottles and colored bottles. The contribution of the Raman signatures of the contents relative to that of the container increased with the spatial offset. This was confirmed by the variation in the SNRs of the Raman peaks of the content materials and the container. The SNR of the content materials improved over that of the container as the spatial offset increased. At a large spatial offset ($\sim$10 mm), the SNRs of the Raman peaks of the contents approached those of the container. The changes in the relative contributions of the Raman signals of the contents and container (and hence the SORS ratio) with an increase in the spatial offset were elucidated. We experimentally investigated the effect of the diffusion efficiency of the contents on the trend of the variation in intensity with respect to the spatial offset. The capability of the SORS technique in reduction of fluorescence was demonstrated by recording the Raman signatures of content material, i.e., PNBA through colored bottles in the presence of a strong fluorescence signal from the colored bottles. This study gives a fair idea about the potential of SORS techniques in the visible range and contributes toward the development of an effective SORS system for the detection of explosives concealed in plastic packages with excitation in the visible range and hence with reasonable better sensitivity.

References

1. J. S. Caygill, F. Davis, and S. P. J. Higson, "Current trends in explosive detection techniques," *Talanta* **88**, 14–29 (2012).
2. Z. Bielecki et al., "Sensors and systems for the detection of explosive devices—an overview," *Metrol. Meas. Syst.* **19**(1), 3–28 (2012).
3. D. J. Brenner, "Are x-ray backscatter scanners safe for airport passenger screening? For most individuals, probably yes, but a billion scans per year raises long-term public health concerns," *Radiology* **259**(1), 6–10 (2011).
4. M. Tourne, "Developments in explosives characterization and detection," *J. Forensic Res.* **S12**, 002 (2013).
5. "Country reports on terrorism: annex of statistical information," National Consortium for the Study of Terrorism and Responses to Terrorism (START), 2015, https://www.state.gov/documents/organization/239628.pdf
6. "Global terrorism database," National Consortium for the Study of Terrorism and Responses to Terrorism (START), 2018, https://www.start.umd.edu/research-projects/global-terrorism-database-gtd.
7. S. Wallin et al., "Laser-based standoff detection of explosives: a critical review," *Anal. Bioanal. Chem.* **395**(2), 259–274 (2009).
8. J. B. Johnson et al., "Standoff methods for the detection of threat agents: a review of several promising laser-based techniques," *J. Spectrosc.* **2014**, 1–13 (2014).
9. P. M. Pellegrino, E. L. Holthoff, and M. E. Farrell, *Laser-Based Optical Detection of Explosives*, CRC Press (2015).
10. S. Gulia, "Laser based spectroscopic techniques for explosive detection," *DRDO Sci. Spectr.* **86**, 97–110 (2015).
11. K. L. Gares et al., "Review of explosive detection methodologies and the emergence of standoff deep UV resonance Raman," *J. Raman Spectrosc.* **47**, 124–141 (2016).
12. J. L. Gottfried and F. C. DeLucia, "Laser-induced breakdown spectroscopy: capabilities and applications," ARL-TR-5238, Army Research Laboratory, 2010, https://apps.dtic.mil/dtic/tr/fulltext/u2/a528756.pdf
13. J. J. Brady et al., "Laser-induced breakdown spectroscopy: a review of applied explosive detection," ARL-TR-6649, Army Research Laboratory, 2013, https://apps.dtic.mil/dtic/tr/fulltext/u2/a585868.pdf.

14. T. Stacewicz et al., "Cavity ring down spectroscopy: detection of trace amounts of substance," *Opto-Electron. Rev.* **20**(1), 53–60 (2012).

15. C. Dhiman, M. S. Khan, and M. N. Reddy, "Phase-shift cavity ring down spectroscopy set-up for NO_2 sensing: design and fabrication," *Defence Sci. J.* **65**(1), 25–30 (2015).

16. X. Chen et al., "Quantum cascade laser based standoff photoacoustic chemical detection," *Opt. Express* **19**(21), 20251–20257 (2011).

17. L. S. Marcus, E. L. Holthoffand, and P. M. Pellegrino, "Standoff photoacoustic spectroscopy of explosives," *Appl. Spectrosc.* **71**(5), 833–838 (2017).

18. J. S. Li et al., "Contributed review: quantum cascade laser based photoacoustic detection of explosives," *Rev. Sci. Instrum.* **86**(3), 031501 (2015).

19. R. Furstenberg et al., "Stand-off detection of trace explosives via resonant infrared photothermal imaging," *Appl. Phys. Lett.* **93**(22), 224103 (2008).

20. G. Mogilevsky et al., "Raman spectroscopy for homeland security applications," *Int. J. Spectrosc.* **2012**, 808079 (2012).

21. J. C. Carter et al., "Standoff detection of high explosive materials at 50 meters in ambient light conditions using a small Raman instrument," *Appl. Spectrosc.* **59**(6), 769–775 (2005).

22. S. Gulia et al., "Trace detection of explosive and their derivatives in stand-off mode using time gated Raman spectroscopy," *Vib. Spectrosc.* **87**, 207–214 (2016).

23. J. A. Guicheteau et al., "Surface-Enhanced Raman Scattering (SERS) evaluation protocol for nanometallic surfaces," *Appl. Spectrosc.* **67**, 396–403 (2013).

24. S. B. Jaber et al., "Sensitive and specific detection of explosives in solution and vapour by surface-enhanced Raman spectroscopy on silver nanocubes," *Nanoscale* **9**, 16459–16466 (2017).

25. F. Zapata, M. L. Lopez, and C. G. Ruiz, "Detection and identification of explosives by surface enhanced Raman scattering," *Appl. Spectrosc. Rev.* **51**(3), 227–262 (2016).

26. C. Muehlethaler, M. Leona, and J. R. Lombardi, "Review of surface enhanced Raman scattering applications in forensic science," *Anal. Chem.* **88**(1), 152–169 (2016).

27. E. Smith and G. Dent, "*Modern Spectroscopy—a Raman Practical Approach*," John Wiley & Ltd. Sons (2005).

28. J. R. Ferraro, K. Nakamoto, and C. W. Brown, "*Introductory Raman Spectroscopy*," Academic Press (2013).

29. P. Matousek et al., "Numerical simulations of subsurface probing in diffusely scattering media using spatially offset Raman spectroscopy," *Appl. Spectrosc.* **59**(12), 1485–1492 (2005).

30. P. Matousek and A. W. Parker, "Non-invasive probing of pharmaceutical capsules using transmission Raman spectroscopy," *J. Raman Spectrosc.* **38**(5), 563–567 (2007).

31. P. Matousek, "Deep non-invasive Raman spectroscopy of living tissue and powders," *Chem. Soc. Rev.* **36**(8), 1292–1304 (2007).

32. C. Eliasson, N. A. Macleod, and P. Matousek, "Non-invasive detection of powders concealed within diffusely scattering plastic containers," *Vib. Spectrosc.* **48**(1), 8–11 (2008).

33. J. Guicheteau and R. Hopkins, "Applications of spatially offset Raman spectroscopy for defence and security," *Proc. SPIE* **9824**, 98240G (2016).

34. P. G. Wilcox and J. A. Guicheteau, "Comparison of handheld Raman sensors through opaque containers," *Proc. SPIE* **10629**, 106290M (2018).

35. P. W. Loeffen et al., "Chemical and explosives point detection through opaque containers using spatially offset Raman spectroscopy (SORS)," *Proc. SPIE* **8018**, 80181E (2011).

36. P. Matousek et al., "Subsurface probing in diffusely scattering media using spatially offset Raman spectroscopy," *Appl. Spectrosc.* **59**(4), 393–400 (2005).

37. W. J. Olds et al., "Spatially offset Raman spectroscopy (SORS) for the analysis and detection of packaged pharmaceuticals and concealed drugs," *Forensic Sci. Int.* **212**, 69–77 (2011).

38. N. Stone et al., "Subsurface probing of calcifications with spatially offset Raman spectroscopy (SORS): future possibilities for the diagnosis of breast cancer," *Analyst* **132**(9), 899–905 (2007).

39. M. D. Keller et al., "Spatially offset Raman spectroscopy of layered soft tissues," *Opt. Lett.* **34**(7), 926–928 (2009).

40. N. K. Afseth et al., "A novel approach for subsurface through-skin analysis of salmon using spatially offset Raman spectroscopy (SORS)," *Appl. Spectrosc.* **68**(2), 255–262 (2014).

41. J. Qin, K. Chao, and M. S. Kim, "Nondestructive evaluation of internal maturity of tomatoes using spatially offset Raman spectroscopy," *Postharvest Biol. Technol.* **71**, 21–31 (2012).

42. J. Qin et al., "A line-scan hyperspectral Raman system for spatially offset Raman spectroscopy," *J. Raman Spectrosc.* **47**(4), 437–443 (2016).

43. K. Chao et al., "A spatially offset Raman spectroscopy method for non-destructive detection of gelatin-encapsulated powders," *Sensors (Basel)* **17**(3), 618 (2017).

44. W. J. Olds et al., "Noninvasive, quantitative analysis of drug mixtures in containers using spatially offset Raman spectroscopy (SORS) and multivariate statistical analysis," *Appl. Spectrosc.* **66**(5), 530–537 (2012).

45. M. D. Hargreaves and P. Matousek, "Threat detection of liquid explosive precursor mixtures by spatially offset Raman spectroscopy (SORS)," *Proc. SPIE* **7486**, 74860B (2009).

46. R. J. Hopkins, L. Lee, and N. C. Shand, "Correcting transmission losses in short-wave infrared spatially offset Raman spectroscopy measurements to enable reduced fluorescence through-barrier detection," *Analyst* **142**(19), 3725–3732 (2017).

47. J. H. Rebecca, H. P. Suzanne, and N. C. Shand, "Short-wave infrared excited spatially offset Raman spectroscopy (SORS) for through-barrier detection," *Analyst* **137**, 4408–4410 (2012).

48. E. D. Emmons et. al., "Ultraviolet resonance Raman spectroscopy of explosives in solution and the solid state," *J. Phys. Chem. A* **117**, 4158–4166 (2013).

49. K. L. Gares et. al., "Solution and solid Trinitrotoluene (TNT) photochemistry: persistence of TNT-like ultraviolet (UV) resonance Raman," *Appl. Spectrosc.* **68**(1), 49–56 (2014).

50. K. L. Gares et. al., "Solution and solid hexahydro-1, 3, 5-trinitro-1, 3, 5-triazine (RDX) ultraviolet (UV) 229 nm photochemistry," *Appl. Spectrosc.* **69**(5), 545–554 (2015).

51. D. D. Tuschel et. al., "Deep ultraviolet resonance Raman excitation enables explosives detection," *Appl. Spectrosc.* **64**(4), 425–432 (2010).

52. S. S. Sacket et al., "Spectroscopic study of UV transparency of some materials," *Environ. Pollut.* **4**(4), 1–17 (2015).

53. B. Zachhuber et al., "Stand-off spatial offset Raman spectroscopy—a distant look behind the scenes," *Proc. SPIE* **8189**, 818904 (2011).

54. S. Sundarajoo et al., "Non-invasive depth profiling by space and time-resolved Raman spectroscopy," *J. Raman Spectrosc.* **44**(7), 949–956 (2013).

55. E. L. Izake et al., "Deep Raman spectroscopy for the non-invasive stand-off detection of concealed chemical threat agents," *Talanta* **94**, 342–347 (2012).

56. D. Tuschel, "Photoluminescence spectroscopy using a Raman spectrometer," *Spectroscopy* **31**(9), 14–21 (2016).

57. A. Frisby et. al., "Spatially offset Raman spectroscopy (SORS) for through-barrier proximal chemical and explosive detection," *Proc. SPIE* **8189**, 81890B (2011).

58. A. Tripathi et. al., "Semi-automated detection of trace explosives in fingerprints on strongly interfering surfaces with Raman chemical imaging," *Appl. Spectrosc.* **65**, 611–619 (2011).

59. C. C. Phifer et al., "Studies of laser-induced fluorescence of explosives and explosives compositions," Sandia Report SAND2006-6697 (2006).

60. C. M. Wynn et al., "Noncontact detection of homemade explosive constituents via photodissociation followed by laser-induced fluorescence," *Opt. Express* **18**(6), 5399–5406 (2010).

61. L. M. Martelo et al., "Towards the development of a low-cost device for the detection of explosives vapors by fluorescence quenching of conjugated polymers in solid matrices," *Sensors* **17**(11), 2532 (2017).

62. CCD Spectral Response (QE), Andor. http://www.andor.com/learning-academy/ccd-spectral-response-(qe)-defining-the-qe-of-a-ccd.

63. "Annual list of explosive materials," *ATF EXPLOSIVES Industry Newsletter*, U.S. Department of Justice Bureau of Alcohol, Tobacco, Firearms and Explosives, 2016, https://www.atf.gov/explosives/docs/newsletter/explosives-industry-newsletter-june-2016/download.

64. P. Matousek et al., "Modelling of spatially offset Raman spectroscopy effects," Central Laser Facility Annual Report, pp. 195–198, 2005/2006, https://www.clf.stfc.ac.uk/Pages/ar05-06_s7_lsf_modelling_sors.pdf.

65. B. Zachhuber et al., "Stand-off spatial offset Raman spectroscopy for the detection of concealed content in distant objects," *Anal. Chem.* **83**(24), 9438–9442 (2011).

66. J. R. Maher and A. J. Berger, "Determination of ideal offset for spatially offset Raman spectroscopy," *Appl. Spectrosc.* **64**(1), 61–65 (2010).

67. CCD Saturation and Blooming, Hamamatsu, http://www.hamamatsu.magnet.fsu.edu/articles/ccdstandblooming.html.

Sanjay Gulia obtained his MSc (physics) degree from Maharishi Dayanand University, Rohtak, Haryana. Currently, he is working as a scientist-"E" at LASTEC, DRDO, Delhi. His area of interest is detection of explosive and hazardous chemical materials using laser-based spectroscopic techniques. He has been instrumental in conceptualizing, designing, and developing explosive point and stand-off detection systems based on techniques such as normal-Raman and time-gated Raman spectroscopy, SORS, and amplified-fluorescent polymers.

Kamal K. Gulati obtained his MSc (physics) degree from IIT, Roorkee, Uttrakhand. Currently, he is working as a scientist-"E" at LASTEC, DRDO, Delhi. His area of interest is detection of explosive and hazardous chemical materials using laser-based spectroscopic techniques, such as Raman spectroscopy, laser-induced breakdown spectroscopy, and cavity ring-down spectroscopy.

Vijayeta Gambhir obtained her MSc (electronic science) degree from University of Delhi, Delhi. Currently, she is working as a scientist-"G" at LASTEC, DRDO, Delhi and heads the explosive agent detection

group. She contributed toward finalization of the design and concept of prototype development.

Rinku Sharma obtained her MSc (physics) degree from University of Delhi, Delhi. Currently, she is working as a professor and heads the Department of Applied Physics at Delhi Technological University (DTU), Delhi. She has vast experience in fields such as interaction of superintense, femto-second laser fields with atoms, and molecule-involving multiphoton processes, collisions in intense short laser pulses, atomic structure calculations for multielectron atoms and ions using configuration interaction technique, electron impact excitation collision strengths, and rate coefficients having application in astrophysics, plasma physics, and nuclear fusion reactors, photo-ionization of complex ions and atoms, plasma physics/plasma applications, nanotechnology, THz radiation emission, and Raman spectroscopy.

Computation of vibrational and thermal characteristics with their interpretation of [3,4-(methylenedioxy) phenyl]-2-methylaminopropane (MDMA)

Sanjay Gulia[a, b], Manuj Ahuja[b], Ajay Kumar[a] and Rinku Sharma[b]

[a]Instruments Research and Development Establishment, Dehradun-248008
[b]Delhi Technological University, Delhi-110042

Abstract: Geometry optimization of [3,4-(methylenedioxy) phenyl]-2-methylaminopropane (MDMA) was performed using density functional theory (DFT) and ab initio HF methods with different basis sets. Mullikan charge and molecular electrostatic potential (MEP) were studied for negative and positive sites of molecule. Molecular orbital characteristics like HOMO-LUMO energies, energy gap, ionization potential, electron affinity, global hardness and chemical potential were investigated. Thermal properties like SCF, zero-point energy, rotational constants, dipole moments were estimated. Enthalpy, specific heat and entropy were investigated in terms of temperature effect in range 50 K – 700 K. UV-visible spectrum of MDMA was investigated with gas, chloroform, DMSO and water as solvent. Vibrational analysis was performed on optimized geometries of MDMA with different levels of theory. The scaled values of vibrational frequencies were found in an excellent agreement with experimental values.

Key words: MDMA, ab initio calculations, DFT, Raman & IR spectra, thermal properties

1. Introduction

Illicit drugs are common to be used for recreational ecstasy throughout the world [1]. [3,4-(methylenedioxy)phenyl]-2-methylaminopropane (MDMA) is one of main constituent in tables sold for recreational ecstasy [2-6] and belongs to class of amphetamine compounds [7]. MDMA is sometimes called a "club drug" due to its frequent use at dance parties, especially "raves". However, some users take this chemical at regular house parties, small social gatherings with friends, or with a sexual partner [8].

Regular users also report various problems that they relate to their drug use. Examples of such problems include poor concentration and memory; fluctuating mood; increased feelings of anxiety, depression, and/or irritability; difficulty sleeping; weight loss; and tremors or twitches [9-12]. In addition, MDMA increases heart rate, blood pressure and myocardial oxygen consumption in both humans [13] and animals [14]. In fact, MDMA doses greater than 180 mg were found to produce only adverse responses in users [12].

The quick and reliable methods of drug identification are utmost required by forensic scientists and the law enforcement agencies as part of the fight against drugs [15]. New emerging challenges from organised crime and terrorist groups underline the vital need for sensitive and selective rapid identification of illicit drugs. Using NIR laser excitation, it was possible to discriminate the spectra of the illicit substances based on differences in the position of vibrational bands, even in the presence of adulterants and diluents. Optical techniques, particularly Raman spectroscopy, have been used for qualitative and quantitative analyses of illegal drugs and adulterants [16-19].

Experimentally spectral characteristics of MDMA have been well investigated using Raman spectroscopy [20-22]. In addition, theoretical studies have also been carried out on MDMA molecule [23-25]. Zapata-Torres, G et al. (2008) [25] investigated the conformational space of MDMA as the free and protonated base in D_2O and $CDCl_3$. Z F Ebrahimi et al. (2016) [24] carried out the theoretical study, ab initio, for the MDMA molecule and its derivatives to characterize the key parameters such as quadrupole coupling constant (QCC), NQR, chemical shift (δ), chemical shift anisotropy (CSA) and asymmetry parameters of MDMA and its derivatives. Nuno Milhazes et al. (2007) [23] investigated theoretically the synthesis pathway of MDMA and its synthetic precursors like MDA, 3,4-methylenedioxybenzaldehyde (piperonal) and 3,4-methylenedioxy-β-methyl-β-nitrostyrene. In addition geometric optimization and frequency calculation of MDMA and MDA were carried out using methods RHF/6-31G (d,p), B3LYP/6-31G(d,p) and B3LYP/ cc-pVDZ.

The present work reports the extensive theoretical studies of MDMA on the spectroscopic and thermodynamic properties and its electronic structure. The geometry optimization and calculation of vibrational frequencies were carried out using Hartree Fermi (HF) and DFT methods. The basis set 6-31G(d,p) was used in HF method and 6-31G(d,p), 6-311G++(d,p) and cc-pVDZ along with DFT/ B3LYP. The calculated scaled values of vibrational frequencies were compared with experimental and theoretical values reported in literature. The values calculated with method B3LYP/ 6-311G++(d,p) were in better agreement with experimental values in comparision to the studies reported by Nuno Milhazes et al. (2007). Further the thermodynamic properties like thermal energy, zero-point vibrational energy, enthalpy, specific heat capacity, entropy, rotational constants, and dipole moment of MDMA molecule were estimated. In addition, electronic structure of MDMA was also studied.

2.   Quantum Mechanical calculations

The reported quantum mechanical calculations have been performed at ab-initio HF method with 6-31G(d,p) basis set and DFT with three parameter hybrid functional of Beek's B3 with 6-31G(d,p), 6-311++G(d,p) and cc-pVDZ basis sets using the Gaussian 09 program. The calculations of vibrational frequencies were carried on the optimized structures at different levels of theories and a variety of basis sets. True minimum of the potential energy surface was obtained as no imaginary frequency mode appeared. In order to improve the calculated values in agreement with the experimental values, the vibrational frequencies calculated were scaled by 0.89 for HF/6-31G(d,p), 0.9668 for B3LYP/6-31G(d,p), 0.983 (for the range of wavenumbers upto 1700 cm-1) & 0.958 (for above 1700 cm-1) for B3LYP/6-311G++(d,p) [26] and 0.9721for B3LYP/cc-Pvdz [27]. The values of calculated frequencies, after scaling, were found in good agreement with experimental values with deviation of less than 10 cm^{-1}. The assignments of the calculated normal modes have been made on the basis of the corresponding Total Energy Distribution (TEDs).

3.   Results and discussion

3.1   Molecular geometry

The theoretically optimized geometric structure optimized using B3LYP method with base set 6-311G++(d,p) and the scheme of numbering the atoms of MDMA is shown in Fig.1. This molecule has nine C-C bond length, fourteen C-H bond lengths, four C-O bond lengths, two C-N bond lengths and one N-H bond length.
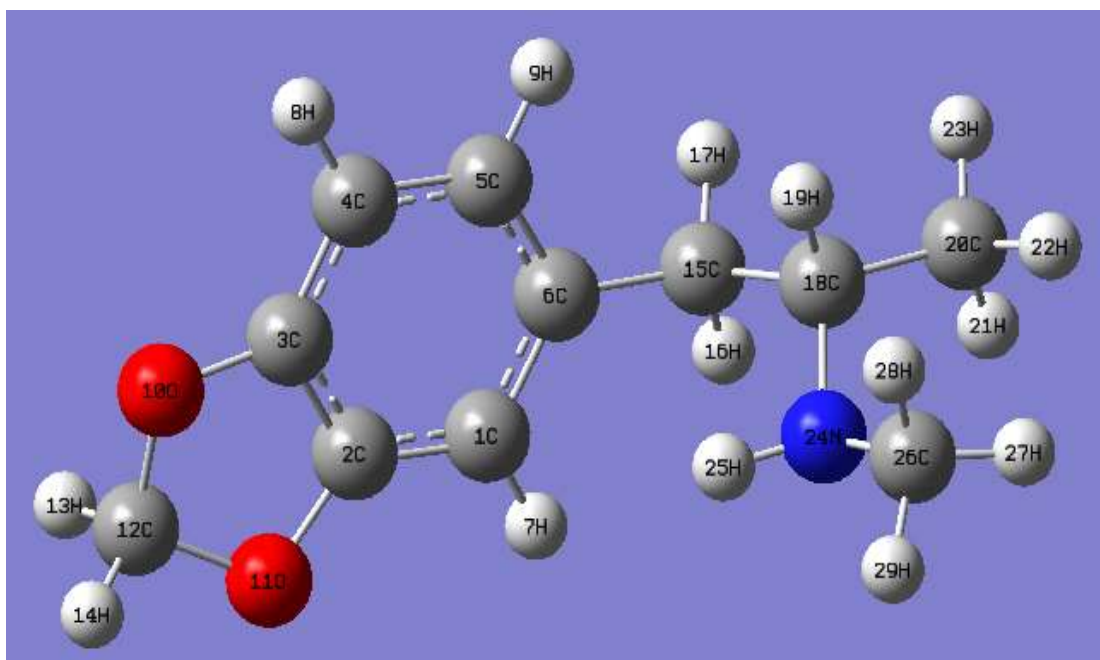
Figure-1: The theoretical optimised geometric structure with atoms numbering of MDMA using B3LYP method with base set 6-311G++(d,p).

The geometry of MDMA molecule was optimized using at ab-initio HF method with 6-31G(d,p) basis set and DFT with three parameter hybrid functional of Beek's B3 with 6-31G(d,p), 6-311++G(d,p) and cc-pVDZ basis sets. The optimized bond lengths and bond angles calculated by various methods were summarized in table-1. The relaxation of all parameters in calculation was used to ensure achieving of true energy minima as indicator of optimized geometries and revealed by no imaginary frequency calculated.

The estimated values of bond-length and bond angles were compared with the experimental values reported in literature [28]. The values calculated using B3LYP with 6-311G++(d,p) are found in agreement with high accuracy with experimental values. The values calculated using HF with 6-31G(d,p) were found towards lower side whereas using B3LYP with 6-31G(d,p) & cc-pVDZ towards higher side when compared with experimental values. The theoretical values of bond-length and bond-angles of MDMA have been already reported in literature [24] and included in table-1. It could be easily observed from table-1 that the estimated values in the present study clearly gave much better agreement with experimental values than reported values in literature.

Table-1: Optimized parameters of MDMA (bond lengths (Å) and bond angle (°))

	HF	B3LYP			Theoretical values (B3LYP;6-31G+) [24]	Experimental values [28]
	6-31G(d,p)	6-31G(d,p)	6-311G++(d,p)	cc-pVDZ		
Bond lengths (Å)						
C12H13	1.08501	1.09988	1.09773	1.10816		
C12H14	1.07981	1.09394	1.08904	1.10073		
C12O10	1.40765	1.43204	1.43226	1.43165	1.407	1.430
C12O11	1.40851	1.43252	1.43317	1.43221	1.408	1.429
O10-C3	1.35968	1.37671	1.37747	1.37594		1.385
O11-C2	1.35809	1.37615	1.37652	1.37540		1.373
C1C2	1.36708	1.38110	1.37908	1.38358	1.366	1.373
C2C3	1.37882	1.39159	1.38883	1.39413		1.384
C3C4	1.36580	1.38062	1.37817	1.38298		1.363
C4C5	1.39874	1.40580	1.40382	1.40835		1.408
C5C6	1.38629	1.40074	1.39924	1.40268		1.392
C6C1	1.40512	1.41381	1.41067	1.41608		1.402
C1H7	1.07437	1.08476	1.08331	1.09108		
C4H8	1.07395	1.08412	1.08261	1.09052		
C5H9	1.07605	1.08635	1.08465	1.09262		
C6C15	1.51659	1.51548	1.51482	1.51541		1.507
C15H16	1.08551	1.09593	1.09428	1.10229		
C15H17	1.08600	1.09606	1.09445	1.10224		
C15C18	1.53857	1.54646	1.54463	1.54583		1.535
C18H19	1.09612	1.10943	1.10705	1.11668		
C18C20	1.52827	1.53247	1.53140	1.53179		1.517
C20H21	1.08551	1.09503	1.09388	1.10258		
C20H22	1.08406	1.09368	1.09219	1.10061		
C20H23	1.08584	1.09498	1.09370	1.10194		
C18N24	1.45399	1.46492	1.46530	1.46437	1.456	1.497
N24H25	0.99915	1.01701	1.01452	1.02100	1.001	1.013
N24C26	1.44929	1.45969	1.46069	1.45849	1.447	1.490
C26H27	1.08363	1.09452	1.09247	1.10199		
C26H28	1.09349	1.10593	1.10397	1.11389		
C26H29	1.08418	1.09407	1.09219	1.10126		
Bond angle (°)						
H13C12H14	110.846	110.830	118.819	110.833		
H13C12O10	109.663	109.518	109.343	109.522		
H13C12O11	109.583	109.465	109.259	109.460		
H14C12O10	109.675	109.471	109.514	109.507		
H14C12O11	109.623	109.447	109.479	109.484		
O10C12O11	107.384	108.061	107.320	107.984	107.414	108.5
C12O10C3	106.211	105.433	104.822	105.280	106.192	105.6
C12O11C2	106.313	105.502	104.901	105.355	106.283	105.8
O10C3C2	109.169	109.719	109.540	109.642	109.155	109.5
C4C3O10						128.0
O11C2C3	109.087	109.628	109.460	109.540		110.2
C1C2C3	122.238	122.121	122.140	122.099		121.9
C1C2O11						127.9
C2C3C4	121.570	121.549	121.499	121.441		122.5
C3C4C5	116.860	116.841	116.886	116.946		116.3
C4C5C6	122.256	122.345	122.335	122.350		121.9
C5C6C1	119.412	119.451	119.383	119.351		120.3
C6C1C2	117.664	117.692	117.757	117.812		117.2
C2C1H7	120.996	121.118	121.000	120.928		
C6C1H7	121.340	121.189	121.243	121.259		
C3C4H8	121.454	121.363	121.410	121.263		
C5C4H8	121.685	121.795	121.704	121.790		

C4C5H9	118.571	118.681	118.584	118.618		
C6C5H9	119.171	118.972	119.078	119.030		117.9
C1C6C15	120.173	120.179	120.208	120.167		
C5C6C15	120.415	120.363	120.405	120.477		121.8
C6C15H16	109.607	109.877	109.765	109.755		
C6C15H17	108.896	109.389	109.324	109.303		
C6C15C18	114.476	114.425	114.522	114.612		111.1
H16C15C18	108.170	107.971	108.073	107.952		
H17C15C18	108.150	107.867	107.838	107.833		
C15C18H19	107.846	107.496	107.636	107.549		
C15C18C20	109.733	110.119	110.181	110.066		113.0
C15C18N24	109.486	109.271	109.513	109.287		
N24C18C20						107.9
H19C18C20	107.950	107.928	107.971	107.880		
H19C18N24	110.952	111.200	110.570	111.185		
C18C20H21	110.267	110.221	110.303	110.239		
C18C20H22	111.852	111.816	111.763	111.846		
C18C20H23	110.539	110.589	110.500	110.662		
H21C20H22	108.108	108.012	108.067	107.980		
H21C20H23	108.637	108.681	108.679	108.637		
H22C20H23	107.322	107.408	107.416	107.356		
C18N24H25	108.906	107.939	108.703	107.711	110.103	106.3
C18N24C26	115.598	114.775	115.115	114.804	116.339	115.3
N24C26H27	110.861	110.646	110.664	110.831		
N24C26H28	113.652	114.160	113.589	114.190		
N24C26H29	108.980	109.104	109.071	109.222		
H27C26H28	107.874	107.525	107.845	107.355		
H27C26H29	107.213	107.138	107.236	107.004		
H28C26H29	108.029	108.006	108.216	107.956		

3.2   Atomic Charges

Mulliken charge distribution has its importance in the field of theoretical calculations based on quantum theories. Different properties of molecule like dipole moment, polarizability, electrostatic structure are influenced by Mulliken charge distribution. It is based on the linear combinations of atomic orbitals molecular orbital method. It has been calculated for MDMA molecule using HF and DFT with different basis sets and summarized in table-2. The structural charge distributions of MDMA, calculated with different combinations of methods and basis sets, were shown in figure-2 and charge at each atomic site was summarized in table-2. It could be observed that the charge at C1, O10, O11 & N24 is negative whereas at C3, H13, H14, H16, H17, H21, H22, H23, H25, H27 & H29 is positive with all methods of calculation. The charge at other sites of molecules shows change in polarity i.e. changes from positive to negative or vice-versa in case of different methods. The charge at C4, C5, C15, C20 & C26 and H7, H8, H9, H19 & H28 is found to be positive and negative respectively whereas negative and positive respectively in case of other methods. The change in charge with basis set is attributed to polarization.
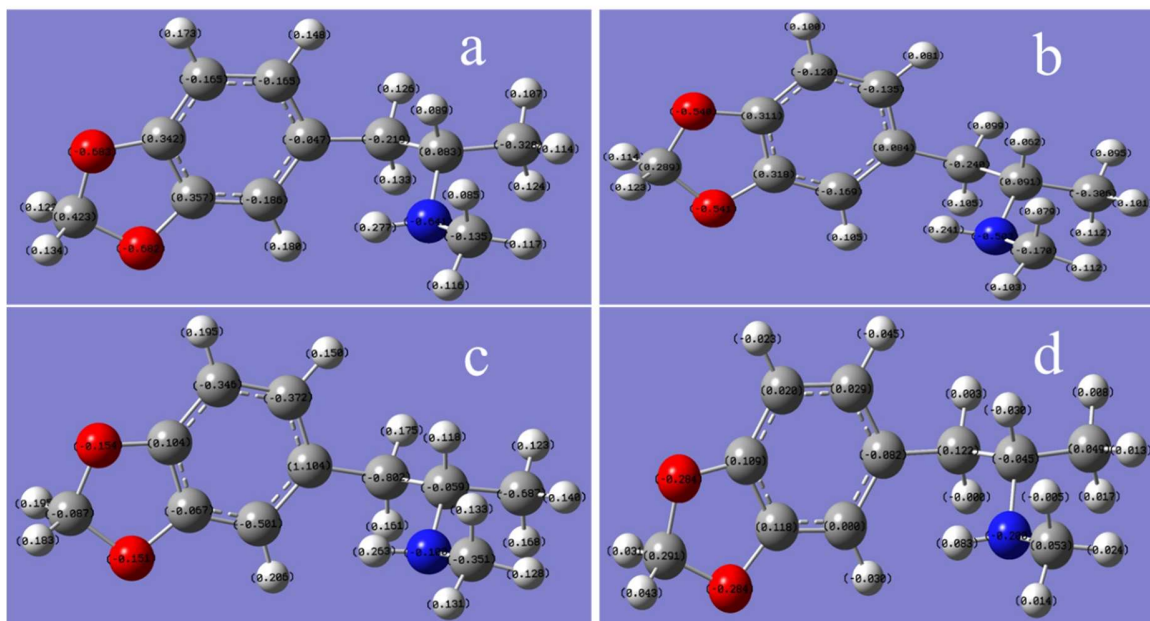
Figure-2: The Mulliken charge distribution molecular structure of MDMA by using (a)HF/6-31G(d,p) (b)B3LYP/6-31G(d,p) (c) B3LYP/6-311++G(d,p) and (d) B3LYP/cc-pVDZ

Table-2: Mulliken charges of MDMA with different basis sets.

Atom	HF	B3LYP		
	6-31G(d,p)	6-31G(d,p)	6-311G++(d,p)	cc-pVDZ
C1	-0.186	-0.169	-0.501	0.000
C2	0.357	0.318	-0.067	0.118
C3	0.342	0.311	0.104	0.109
C4	-0.165	-0.120	-0.346	0.020
C5	-0.165	-0.135	-0.372	0.029
C6	-0.047	0.084	1.104	-0.082
H7	0.180	0.105	0.205	-0.030
H8	0.173	0.100	0.195	-0.023
H9	0.148	0.081	0.150	-0.045
O10	-0.683	-0.540	-0.154	-0.284
O11	-0.682	-0.541	-0.151	-0.284
C12	0.423	0.289	-0.087	0.291
H13	0.122	0.114	0.195	0.031
H14	0.134	0.123	0.183	0.043
C15	-0.219	-0.240	-0.802	0.122
H16	0.133	0.105	0.161	0.000
H17	0.126	0.099	0.175	0.003
C18	0.083	0.091	-0.059	-0.045
H19	0.089	0.062	0.118	-0.030
C20	-0.328	-0.306	-0.687	0.049
H21	0.124	0.112	0.168	0.017
H22	0.114	0.101	0.140	0.013
H23	0.107	0.095	0.123	0.008
N24	-0.641	-0.503	-0.100	-0.200
H25	0.277	0.241	0.263	0.083
C26	-0.135	-0.170	-0.351	0.053
H27	0.117	0.112	0.128	0.024
H28	0.085	0.079	0.133	-0.005
H29	0.116	0.103	0.131	0.014

3.3   Estimation of Frontier molecular orbitals

The calculation of HOMO and LUMO of MDMA was carried out using 6-311G++(d,p) basis set. Further their energy gap was estimated which is a measure of chemical activity of molecule. The frontier molecular orbitals are depicted in figure-2 along with their atomic orbital compositions for the gas phase.

Electronic structure calculation has been done for MDMA using TD-DFT B3LYP/6-3111++ and the electronic excited states were obtained for MDMA in its gas phase and by adding the polar solvents (DMSO, chloroform, Water) using the SCRF (Self-Consistent Reaction Field) methods.

Further the energy of second-highest occupied molecular orbital (HOMO-1) and second-lowest unoccupied molecular orbital (LUMO+1) were estimated. In addition, different parameters like ionization energy, electron affinity, global hardness, chemical hardness, electrophilicity and transition dipole moment were estimated and summarized in table-3 including formulas used for gas phase and other solvents.
UV-Visible spectral studies were carried out on MDMA in gas phase and with different solvents i.e., DMSO, chloroform and water. Theoretically estimated UV-Visible spectra for the title molecule were shown in figure-3 in its gas phase and other solvents.
The electronic energy (E), oscillation strength (f_{osc}) and wavelength(λ) corresponding to first three strong transitions were summarized in table-4.
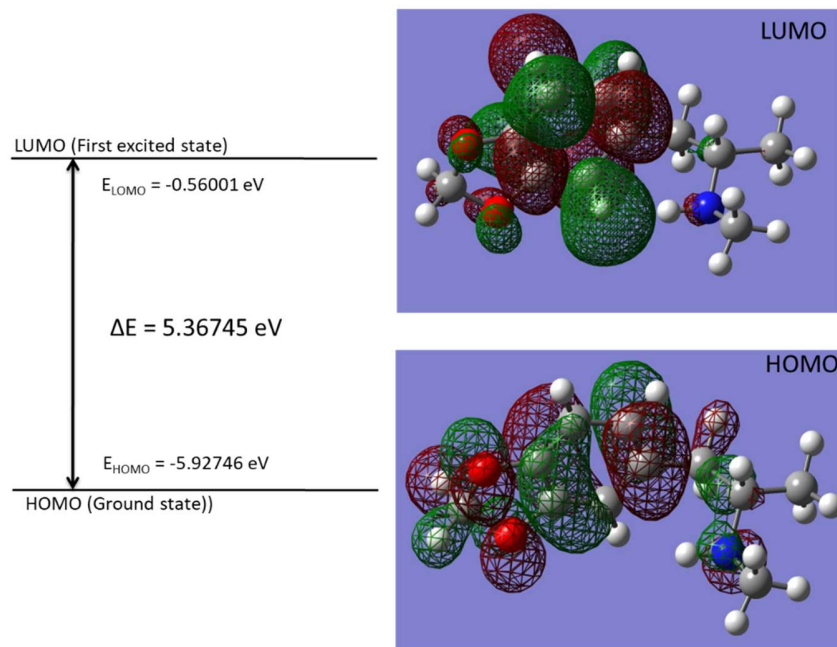

Figure-2: The frontier molecular orbitals and energies of HOMO and LUMO of MDMA calculated at B3LYP/6-311G++(d,p) level

Table-3: Calculated energies values of MDMA in gas phase and other solvents at B3LYP/6-311G++(d,p) level

| Parameter	Formula [29]	Gas	Water	DMSO	Chloroform
E_{HOMO} (eV)		-5.92744	-5.99005	-5.98868	-5.96311
E_{LUMO} (eV)		-0.56001	-0.62069	-0.61906	-0.59266
$\Delta E_{HOMO\text{-}LUMO}$ (eV)		5.36743	5.36936	5.36962	5.37045
E_{HOMO-1} (eV)		-6.18241	-6.345877	-6.34206	-6.2789
E_{LUMO-1} (eV)		-0.30885	-0.335239	-0.334155	-0.31674
$\Delta E_{(HOMO-1)\text{-}(LUMO+1)}$ (eV)		5.87356	6.0106	6.0079	5.9621
Ionisation potential (I)	$I = -E_{HOMO}$	5.92744	5.99005	5.98868	5.96311
Electron affinity (A)	$A = -E_{LUMO}$	0.56001	0.62069	-0.61906	0.59266
Global hardness (η)	$\eta = 1/2$ $(\Delta E_{HOMO\text{-}LUMO})$	2.68372	2.68468	2.68481	2.685225
Chemical potential (μ)	$\mu = 1/2(E_{HOMO} + E_{LUMO})$	-3.24373	-3.30537	-3.30387	-3.277885
Global electrophilicity (ω)	$w = \mu^2/2\eta$	1.96029845	2.034780837	2.032836025	2.000675935
Transition Dipole Moment		0.6156	0.8229	0.8638	0.8735
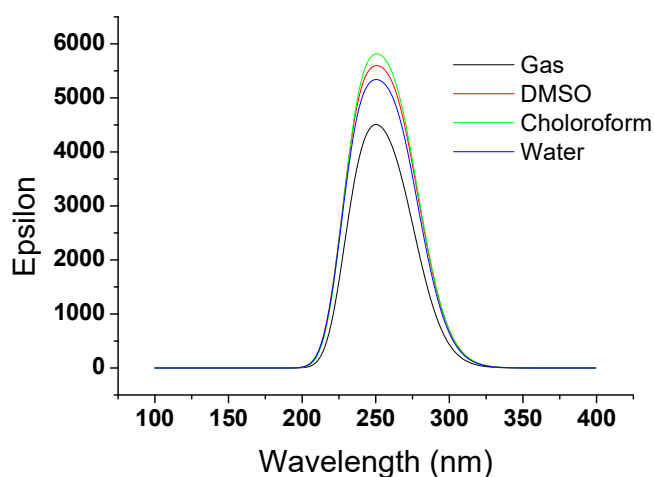
Figure-3: UV-Visible Spectrum of MDMA in gas phase and with different solvents

Table-4: Calculated electronic energy (E), oscillation strength (fosc) and wavelength(λ) corresponding to first three strong transitions in gas phase and different solvents

Solvents	λ (nm)	Energy(eV)	f_{osc}	Major contribution
Gas	264.65	4.6849	0.0707	H to L (86%)
	242.12	5.1208	0.0446	H-1 to L+1 (42%) H to L+2 (21%) H to L+1 (25%)
	235.88	5.1974	0.0177	H-1 to L+2 (56%) H-1 to L+3 (23%)
Chloroform	265.91	4.6626	0.0998	H to L (87%)
	240.61	5.15291	0.0766	H to L+2 (47%) H to L+1 (30%)
	245.05	5.0596	0.0170	H to L+1 (37%) H to L+2 (47%)
DMSO	265.87	4.6633	0.0987	H to L (87%)
	239.97	5.1667	0.0762	H to L+1(52%) H to L+2 (31%)
	244.15	5.0781	0.0177	H to L+1(33%) H to L+2 (49%)
Water	265.65	4.6672	0.0941	H to L (87%)
	239.78	5.1708	0.0734	H to L+1(53%) H to L+2 (30%)
	244.04	5.0805	0.0163	H to L+1(32%) H to L+2 (50%)

3.4 Molecular electrostatic potential (MEP)

MEP of target molecule MDMA is depicted in figure-4. The MEP helps to study reactivity of the molecule. In the MEPs, maximum negative region where an approaching electrophilic will attack is represented as red colour whereas maximum positive region where a nucleophilic will attack is represented as blue colour. MEP itself consists of the molecular information like its size & shape as well as positive, negative and neutral electrostatic potential regions in terms of colour coding and so is important in studies of molecular structure with its physiochemical characteristic [30-32]. The value of potential ranges from -0.0385 a.u. (deepest red) to 0.02335 a.u. (deepest blue) and increases in the order red < orange < yellow < green < blue.
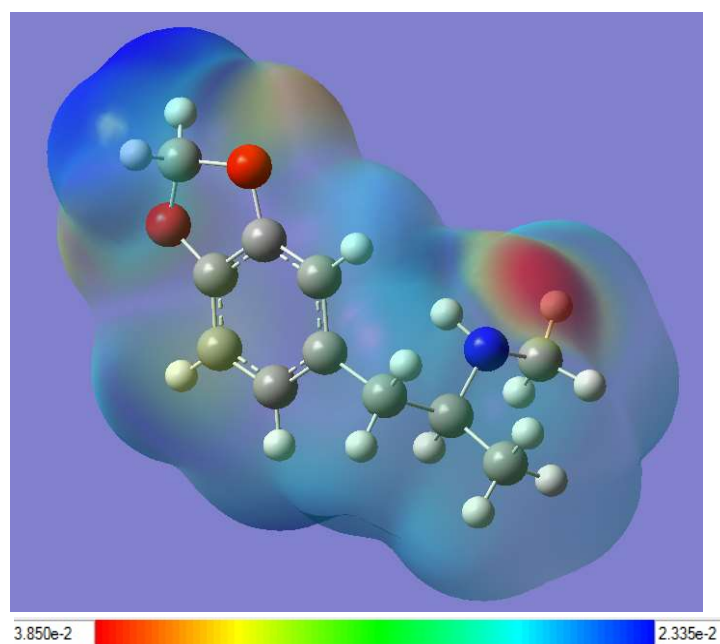
Figure-4: Molecular electrostatic potential (ESP) map of MDMA

3.5   Thermodynamic properties

Thermodynamic properties like SCF energy, vibrational energy, heat capacity (Cv), entropy (S), enthalpy (H), zero-point vibrational, rotational constants, and dipole moments were computed at standard temperature i.e. 298.15 K using methods HF with basis set 6-31G (d,p) and DFT with basis sets 6-31G(d,p), 6-311G++(d,p) and cc-pVDZ and summarized in table-5. The minimum energy estimated for optimized MDMA structure was found to be -633 a.u. using DFT method with 6-31G(d,p), 6-311G++(d,p) and cc-pVDZ and -629 a.u. (lower by 4 a.u.) using HF method with 6-31G(d,p). The heat capacity and entropy were also found to be lowest whereas vibrational energy, zero-point energy and rotational constants highest in case of HF method. The vibrational energy, zero-point energy, rotational constants and dipole moment showed trends of decrease with DFT method from lower to higher basis set.

Table-5: The calculated thermodynamic parameters of MDMA

Thermodynamic parameters (298.15 K)	HF	B3LYP		
	6-31G(d,p)	6-31G(d,p)	6-311G++(d,p)	cc-pVDZ
SCF energy (a.u.)	-629.452645814	-633.395856449	-633.549888298	-633.406086164
Vibrational energy, E_{vib} (kcal mol^{-1})	172.000	161.335	160.473	160.254
Heat capacity at const. volume, Cv (cal mol^{-1} K^{-1})	40.770	44.636	44.805	44.786
Entropy, S (cal mol^{-1} K^{-1})	39.610	43.049	42.319	42.910
Zero-point vibrational energy, E_0 (kcal mol-1)	165.89543	154.70709	153.87833	153.62888
Rotational constants (GHz)				
A	1.58615	1.5429537	1.55984	1.54160

B	0.33855	0.3387186	0.33599	0.33821
C	0.31718	0.3158813	0.31694	0.31515
Dipole moment (Debye)				
μ_x	0.3192	0.7083	0.5450	0.8022
μ_y	-0.6297	-0.3851	-0.6115	-0.2158
μ_z	0.5542	0.4756	0.4178	0.3899
μ_{total}	0.8975	0.9360	0.9196	0.9177

The standard thermodynamic parameters i.e. Enthalpy changes (H), specific heat capacity (Cv) and Entropy (S) were studied at different temperatures in range 50 K to 700 K using DFT method with 6-311G++(d,p) and values obtained were summarized in table-6.

Table-6: Thermodynamic properties at different temperatures using method B3LYP with basis set 6-311G++(d,p)

Temp, T (K)	E(thermal) (kcal mol^{-1})	Specific heat, Cv (cal mol^{-1}K^{-1})	Entropy, S (cal mol^{-1}K^{-1})
50	154.044	7.36	5.319
100	154.608	15.154	12.823
150	155.548	22.35	20.355
200	156.842	29.465	27.751
250	158.503	37.068	35.123
298.15	160.473	44.805	42.319
350	163.015	53.227	50.162
400	165.875	61.086	57.786
450	169.116	68.458	65.412
500	172.711	75.243	72.982
600	180.844	87.035	87.777
700	190.049	96.757	101.947

The values of these parameters were found to be increased as temperature was increased from 50 K to 700 K. It is attributed to increased vibrational intensities with increase in temperature (J. Bevan 2000). The correlation equations of enthalpy changes (ΔH_m^o), heat capacities ($C_{p,m}^o$) and entropies (S_m^o) in function of temperature were derived using method of curve fitting with quadratic formulas and the corresponding fitting factors (R^2) were found to be 0.9999, 0.9986 and 0.9999, respectively. The derived relations were written below and the curve fitted graphs of corresponding parameters are shown in figure-5.

$$\Delta H_m^o = 153.70161 + 0.00148\,T + 7.24447 \times 10^{-5}\,T^2$$

$$C_{p,m}^o = -2.52611 + 0.17553\,T - 4.54168 \times 10^5\,T^2$$

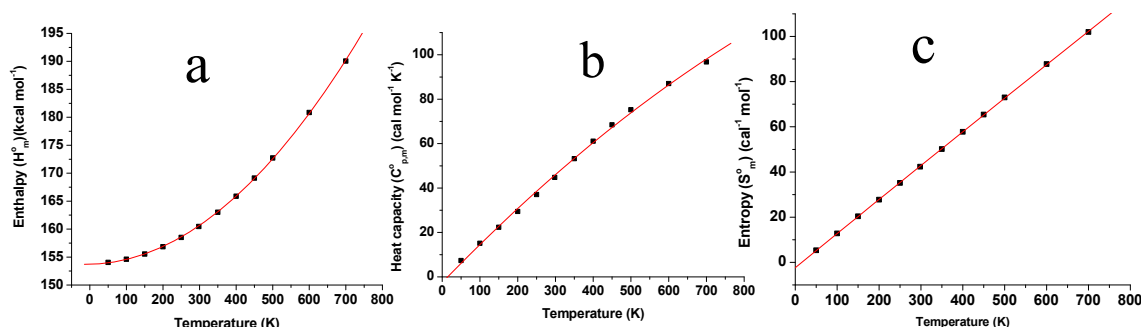$$S_m^o = -2.37919 + 0.15164\,T - 3.06255 \times 10^{-6}\,T^2$$

Figure-5: Curve fitted graphs of (a) enthalpy, (b) heat capacity and (c) entropy w.r.t. temperature for MDMA molecule

3.6   Vibrational analysis

The frequency of normal vibrations of MDMA molecules were estimated using HF and DFT methods with basis set 6-31G(d,p) and basis sets 6-31G(d,p), 6-311G++(d,p) & cc-pVDZ respectively. Being consisting of 29 molecules, MDMA exhibited 81 numbers of normal mode of vibrations. The vibrational frequencies calculated were scaled by 0.89 for HF/6-31G(d,p), 0.9668 for B3LYP/6-31G(d,p), 0.983 (for the range of wavenumbers upto 1700 cm-1) & 0.958 (for above 1700 cm-1) for B3LYP/6-311G++(d,p) [26] and 0.9721for B3LYP/cc-pVDZ [27]. The calculated frequencies after applying the scaling factor have been summarized in table-7 and compared with experimental values reported in literature. The scaled frequencies estimated at level B3LYP/6-31G++(d,p) have exhibited the lowest deviation when compared with the experimental values. Theoretically estimated Raman spectra and IR spectra using HF and DFT methods with basis set 6-31G(d,p) and basis sets 6-31G(d,p), 6-311G++(d,p) & cc-pVDZ were shown in figure-6(a) and 6(b) respectively.
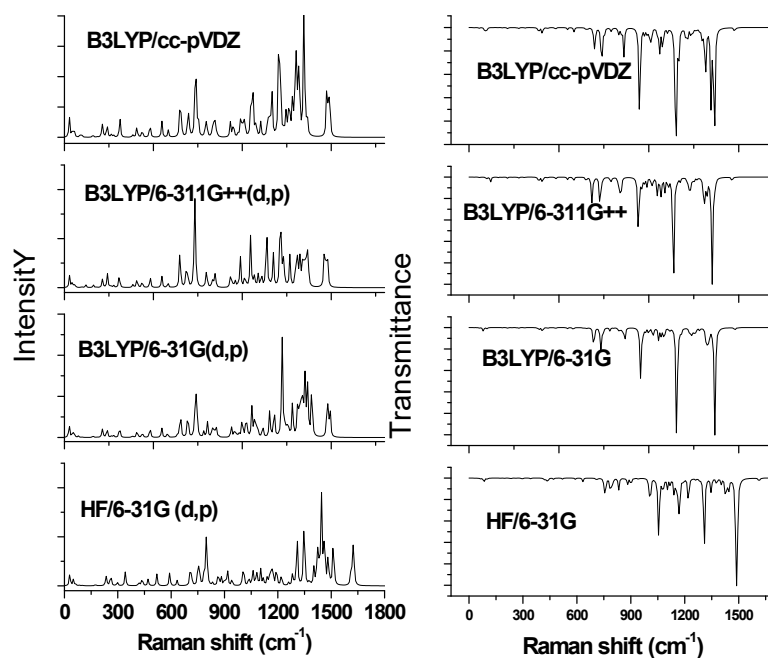
Figure-6: Theoretical Raman and IR spectra estimated using HF and DFT methods with basis set 6-31G(d,p) and basis sets 6-31G(d,p), 6-311G++(d,p) & cc-pVDZ respectively.

Table-7: Comparision of estimated scaled frequencies with different method and basis sets with experimental values.

Modes	Experimental values [23, 33, 34]	HF/ 6-31G(d,p)	B3LYP			Assignments
			6-31G(d,p)	6-311G++(d,p)	cc-pVDZ	
ν1	346	346	336	341	340	$\tau(CCC)$
ν2	521	521	523	533	525	$\beta(CCC)$
ν3	716	715	709	717	720	$\beta(OCCC)$
ν4	774	787	756	766	762	$\tau(HNCC)$
ν5	812	799	812	811	806	$\tau(HCCC)$
ν6	1036	1037	1035	1041	1039	$\nu_a(C-C)$
ν7	1102	1104	1107	1092	1100	$\nu_a(C=C)$
ν8	1233	1220	1211	1224	1245	$\nu_s(C=C)$
ν9	1253	1260	1253	1255	1254	$\beta(C-H)$
ν10	1366	1377	1371	1362	1360	$\beta(C-H)$
ν11	1444	1446	1442	1444	1439	$\beta(C-H)$
ν12	1501	1512	1511	1499	1487	$\beta(C-H)$
ν13	1607	1613	1606	1615	1609	$\nu_a(C=C)$

4. Conclusion

The geometry optimization MDMA molecule were performed completely using HF method with basis set 6-31G(d,p) and DFT-B3LYP method with basis sets 6-31G(d,p), 6-311G++(d,p) and cc-pVDZ. The estimated values of bond lengths and bond angles from optimized MDMA molecular structure were found very close to the experimental ones. Mulliken charges on atomic sites and then MEP map revealed that negative charge/ potential sites were on oxygen atoms whereas positives charge/ potential sites on hydrogen atoms. HOMO-LUMO molecular orbital energies and other properties of MDMA like ionisation potential, electronic affinity, molecular hardness, molecular potential, electrophilicity and transition dipole moment were estimated. Also, UV-Visible spectrum, oscillation strength, excited energy and wavelength were obtained and compared for gas phase and different solvents. Further thermodynamic properties of target molecule were studied and correlated relation between enthalpy; specific heat and entropy with temperature were derived. Finally vibrational analysis was performed on MDMA optimized geometries using HF and DFT methods. The estimated values of vibrational frequencies were found matched with experimental ones in excellent agreement.

Acknowledgement

References

1. United Nations Office on Drugs, and Crime. *Amphetamines and Ecstasy: 2008 Global ATS Assessment*. United Nations Publications, 2008.
2. Tanner-Smith, Emily E. "Pharmacological content of tablets sold as "ecstasy": results from an online testing service." *Drug and alcohol dependence* 83, no. 3 (2006): 247-254.
3. Vogels, Neeltje, Tibor M. Brunt, Sander Rigter, Peter Van Dijk, Hylke Vervaeke, and Raymond JM Niesink. "Content of ecstasy in the Netherlands: 1993–2008." *Addiction* 104, no. 12 (2009): 2057-2066.
4. Wood, David Michael, Vasoulla Stribley, Paul Ivor Dargan, Susannah Davies, David W. Holt, and John Ramsey. "Variability in the 3, 4-methylenedioxymethamphetamine content of 'ecstasy'tablets in the UK." *Emergency Medicine Journal* 28, no. 9 (2011): 764-765.
5. EcstasyData.org [homepage on the Internet]. *Available from: http:// www.ecstasydata.org. Accessed April 28, 2013.*
6. Meyer, Jerrold S. "3, 4-methylenedioxymethamphetamine (MDMA): current perspectives." *Substance abuse and rehabilitation* 4 (2013): 83-99.
7. Shulgin, Alexander Theodore, and Ann Shulgin. *TIHKAL: the continuation*. Vol. 546. Berkeley, CA: Transform press, 1997.
8. Sumnall, Harry R., Jon C. Cole, and Lisa Jerome. "The varieties of ecstatic experience: an exploration of the subjective experiences of ecstasy." *Journal of Psychopharmacology* 20, no. 5 (2006): 670-682.
9. Rodgers, Jacqui, Tom Buchanan, Carol Pearson, Andy C. Parrott, Jon Ling, Tom Heffernan, and Andrew B. Scholey. "Differential experiences of the psychobiological sequelae of ecstasy use: quantitative and qualitative data from an internet study." *Journal of Psychopharmacology* 20, no. 3 (2006): 437-446.
10. Soar, K., J. J. D. Turner, and Andy C. Parrott. "Problematic versus non-problematic ecstasy/MDMA use: the influence of drug usage patterns and pre-existing psychiatric factors." *Journal of psychopharmacology* 20, no. 3 (2006): 417-424.
11. Wu, Li-Tzy, Andy C. Parrott, Christopher L. Ringwalt, Chongming Yang, and Dan G. Blazer. "The variety of ecstasy/MDMA users: results from the National Epidemiologic Survey on alcohol and related conditions." *The American Journal on Addictions* 18, no. 6 (2009): 452-

461.

12. Brunt, Tibor M., Maarten W. Koeter, Raymond JM Niesink, and Wim van den Brink. "Linking the pharmacological content of ecstasy tablets to the subjective experiences of drug users." *Psychopharmacology* 220, no. 4 (2012): 751-762.

13. Carvalho, Márcia, Fernando Remiao, Nuno Milhazes, Fernanda Borges, Eduarda Fernandes, Maria do Céu Monteiro, Maria José Gonçalves et al. "Metabolism is required for the expression of ecstasy-induced cardiotoxicity in vitro." *Chemical research in toxicology* 17, no. 5 (2004): 623-632.

14. Bexis, Sotiria, and James R. Docherty. "Effects of MDMA, MDA and MDEA on blood pressure, heart rate, locomotor activity and body temperature in the rat involve α-adrenoceptors." *British journal of pharmacology* 147, no. 8 (2006): 926-934.

15. West, Matthew J., and Michael J. Went. "Detection of drugs of abuse by Raman spectroscopy." *Drug testing and analysis* 3, no. 9 (2011): 532-538.

16. Bell, Steven EJ, D. Thorburn Burns, Andrew C. Dennis, Lindsay J. Matchett, and James S. Speers. "Composition profiling of seized ecstasy tablets by Raman spectroscopy." *Analyst* 125, no. 10 (2000): 1811-1815.

17. Izake, Emad L. "Forensic and homeland security applications of modern portable Raman spectroscopy." *Forensic science international* 202, no. 1-3 (2010): 1-8.

18. de Oliveira Penido, Ciro Augusto Fernandes, Marcos Tadeu Tavares Pacheco, Igor K. Lednev, and Landulfo Silveira Jr. "Raman spectroscopy in forensic analysis: identification of cocaine and other illegal drugs of abuse." *Journal of Raman Spectroscopy* 47, no. 1 (2016): 28-38.

19. Mogilevsky, Gregory, Laura Borland, Mark Brickhouse, and Augustus W. Fountain III. "Raman spectroscopy for homeland security applications." *International Journal of Spectroscopy* 2012 (2012).

20. Farquharson, Stuart, Chetan Shende, Atanu Sengupta, Hermes Huang, and Frank Inscore. "Rapid detection and identification of overdose drugs in saliva by surface-enhanced Raman scattering using fused gold colloids." *Pharmaceutics* 3, no. 3 (2011): 425-439.

21. Bell, Steven EJ, D. Thorburn Burns, Andrew C. Dennis, Lindsay J. Matchett, and James S. Speers. "Composition profiling of seized ecstasy tablets by Raman spectroscopy." *Analyst* 125, no. 10 (2000): 1811-1815.

22. Bell, Steven EJ, J. Renwick Beattie, John J. McGarvey, K. Laota Peters, N. M. S. Sirimuthu, and S. James Speers. "Development of sampling methods for Raman analysis of solid dosage forms of therapeutic and illicit drugs." *Journal of Raman spectroscopy* 35, no. 5 (2004): 409-417.

23. Milhazes, Nuno, Pedro Martins, Eugenio Uriarte, Jorge Garrido, Rita Calheiros, M. Paula M. Marques, and Fernanda Borges. "Electrochemical and spectroscopic characterisation of amphetamine-like drugs: application to the screening of 3, 4-methylenedioxymethamphetamine (MDMA) and its synthetic precursors." *Analytica chimica acta* 596, no. 2 (2007): 231-241.

24. Ebrahimi, Zahra Fallah. "An ab initio study on 3, 4-methylenedioxymethamphetamine, MDMA (ecstasy) and its derivatives." *International Journal of Computational Biology and Drug Design* 9, no. 1-2 (2016): 149-161.

25. Zapata-Torres, Gerald, Bruce K. Cassels, Julia Parra-Mouchet, Yvonne P. Mascarenhas, Javier Ellena, and A. S. De Araujo. "Quantum-chemical, NMR and X-ray diffraction studies on (±)-1-[3, 4-(methylenedioxy) phenyl]-2-methylaminopropane." *Journal of Molecular Graphics and Modelling* 26, no. 8 (2008): 1296-1305.

26. Sundaraganesan, B. N., S. Ilakiamani, H. Saleem, Piotr M. Wojciechowski, and Danuta Michalska. "FT-Raman and FT-IR spectra, vibrational assignments and density functional studies of 5-bromo-2-nitropyridine." *Spectrochimica Acta Part A: Molecular and Biomolecular Spectroscopy* 61, no. 13-14 (2005): 2995-3001.

27. Kesharwani, Manoj K., Brina Brauer, and Jan ML Martin. "Frequency and zero-point vibrational energy scale factors for double-hybrid density functionals (and other selected methods): can anharmonic force fields be avoided?." *The Journal of Physical Chemistry A* 119, no. 9 (2015): 1701-1714.

28. Morimoto, Bruce H., Scott Lovell, and Bart Kahr. "Ecstasy: 3, 4-methylenedioxymethamphetamine (MDMA)." *Acta Crystallographica Section C: Crystal Structure Communications* 54, no. 2 (1998): 229-231.

29. Ramachandran, S., and G. Velraj. "DFT, FT-IR AND FT-RAMAN INVESTIGATIONS OF 2-CHLORO-5-NITROBENZYL ALCOHOL." *ROMANIAN JOURNAL OF PHYSICS* 58, no. 3-4 (2013): 305-318.

30. Murray, Jane S., and Kalidas Sen, eds. *Molecular electrostatic potentials: concepts and applications*. Elsevier, 1996.
31. Lowdin, Per-Olov. *Advances in quantum chemistry*. Academic Press, 1979.
32. Šponer, Jiří, and Pavel Hobza. "DNA base amino groups and their role in molecular interactions: Ab initio and preliminary density functional theory calculations." *International Journal of Quantum Chemistry* 57, no. 5 (1996): 959-970.
33. Dana, Kathryn, Chetan Shende, Hermes Huang, and Stuart Farquharson. "Rapid analysis of cocaine in saliva by surface-enhanced Raman spectroscopy." *Journal of analytical & bioanalytical techniques* 6, no. 6 (2015): 1.
34. Dies, Hannah, Joshua Raveendran, Carlos Escobedo, and Aristides Docoslis. "Rapid identification and quantification of illicit drugs on nanodendritic surface-enhanced Raman scattering substrates." *Sensors and Actuators B: Chemical* 257 (2018): 382-388.